# Spectral Analyses of Wolf-Rayet Stars in the Triangulum-Galaxy (M33)

## Master Thesis

submitted to the

### Institut für Physik und Astronomie

of the

### Mathematisch-Naturwissenschaftlichen Fakultät

of the

### Universität Potsdam

from

## Max Pritzkuleit

maxpri@astro.physik.uni-potsdam.de

Potsdam, 15 December 2020

First supervisor: Prof. Dr. Wolf-Rainer Hamann
Second supervisor: Prof. Dr. Stephan Geier

# Contents

# Deutsche Zusammenfassung

Massereiche Sterne mit mehr als anfänglich 10 Sonnenmassen spielen eine besondere Rolle in der Entwicklung des Kosmos. Durch ihre hohen Temperaturen und Leuchtkräfte von bis zu einigen Millionen Sonnenleuchtkräften lieferten sie einen signifikanten Beitrag zur Reionisation des Universums. Des Weiteren haben sie starke Winde, die mit dem sie umgebenden Material interagieren und so die Bildung von weiteren Sternen anregen können. Die massereichsten von ihnen ($M_{\mathrm{Anfang}} > 22\,M_\odot$) sind in der Lage ihre wasserstoffreichen Hüllen durch ihre Winde komplett abzustoßen. In diesem Stadium werden sie dann als Wolf-Rayet Sterne bezeichnet und können Temperaturen von bis zu $200\,\mathrm{kK}$ erreichen. Durch ihre starken Winde und daraus resultierenden Massenverlustraten erhalten sie ein Spektrum, das von Emissionslinien dominiert ist. Die Massenverlustrate hängt dabei von verschiedenen Parametern ab, wovon einer die Metallizität ist (genauer gesagt die Häufigkeit der Eisengruppenelemente). Je geringer die Metallizität ist, desto geringer ist auch die Massenverlustrate, da die Winde durch eisenähnliche Elemente getrieben werden. Allerdings ist der genaue Zusammenhang zwischen diesen beiden Parametern nicht genau bekannt und Objekt aktueller Forschung. Um aber zu verstehen, wie sich Sterne im frühen, metallarmen Universum entwickelt haben, sind genauere Kenntnisse notwendig. Deshalb ist es wichtig massereiche Sterne in solchen Regionen zu identifizieren und analysieren.

In meiner Arbeit werte ich die Spektren von 74 Wolf-Rayet Sternen in der Triangulum Galaxie, auch bekannt als M33, aus. Die meisten von ihnen befinden sich in den äußeren Bereichen der Galaxie, wo die Metallizität ungefähr ein drittel so groß ist wie der solare Wert ($Z_\odot = 0.014$). Somit ist sie eingeordnet zwischen der metallärmeren Kleinen Magellanschen Wolke ($Z \approx 1/5\,Z_\odot$) und der etwas metallreicheren Großen Magellanschen Wolke ($Z \approx 1/2\,Z_\odot$). Die Resultate vergleiche ich mit Analysen von Wolf-Rayet Sternen in diesen beiden Galaxien und der Milchstraße. Die Daten werden eingeordnet in die Relation für Massenverlust und Metallizität von Hainich et al. (2015). Mein Ergebnis ist in sehr guter Übereinstimmung mit ihrer Vorhersage und bestätigt deren Resultate. Zukünftige Analysen von Wolf-Rayet Sternen in Regionen noch metallärmer als die Kleine Magellansche Wolke werden zeigen, ob sich dieser Trend so weiterentwickelt oder ob er noch stärker abfällt wie es neueste theoretische Modelle vorhersagen.

# 1 Introduction

Massive stars (initially more massive than ten solar masses) are cosmic power houses playing an important role in the evolution of the universe. The most massive of them ($M_{\mathrm{ini}} > 20\,M_\odot$) are of special interest because they have temperatures between 30 and $50\,\mathrm{kK}$ and luminosities up to a few million solar luminosities. Therefore, they produce the majority of UV photons seen in star forming galaxies and contributed a major part to the reionisation of the early universe (Barkana 2006; Latif & Ferrara 2016). During their evolution they have the potential to shed off their entire hydrogen envelope through their winds and strong mass-loss rates turning them into a so-called Wolf-Rayet (WR) star.

This special class of stars was first described by Charles Wolf and Georges Rayet in 1867 (Wolf & Rayet 1867). To their surprise, they observed emission lines in the spectra but were unable to identify the elements nor to explain the mechanism behind their creation. Only in 1929 it was Carlyle Smith Beals, who compared the spectra of Wolf-Rayet stars with spectra of novae, to realise that these stars must have strong mass-loss rates (Beals 1929). Since then many more Wolf-Rayet stars were discovered. Today, there are currently 667 known Wolf-Rayet stars in our own Galaxy[1]. Because of their high luminosity, they were also observed in other galaxies like the Magellanic Clouds, M31 or M33.

The Wolf-Rayet phase marks the final evolutionary stage of a massive star. Since Wolf-Rayet stars represent the core region of their progenitors, they can reach temperatures up to $200\,\mathrm{kK}$ (Sander et al. 2019) making them strong emitters of ionising UV photons. Through their strong stellar winds they can induce shocks into the surrounding interstellar medium possibly triggering further star formation. However, the mass-loss rate depends on different quantities, one of them being the metallicity. It is the subject of current research to find an accurate relation between mass-loss rate and metallicity making it important to observe and analyse Wolf-Rayet stars in especially metal poor regions where the conditions are closer to the ones in the early universe. Furthermore, recent events have shown the importance of this problem. Liu et al. (2019) claimed the discovery of a 70 solar mass black hole surrounded by a B type star in the Milky Way. However, to our current understanding, it is not possible to form such a massive black hole in a metal rich region. Several authors questioned this result and found that the star belongs more likely to another class of helium stars (Eldridge et al. 2019; Irrgang et al. 2020; Shenar et al. 2020a). Thus, it is not a 70 solar mass black hole. Nevertheless, we know from gravitational wave measurements that such massive black holes exist. Abbott et al. (2020) reported the detection of a merging event between a 60 and 80 solar mass black hole. So far it cannot be excluded that they do not have a stellar origin but the other observed events involve black holes with masses of more than 20

---

[1]List of Galactic WR stars: `http://pacrowther.staff.shef.ac.uk/WRcat/`

solar masses challenging our current understanding of stellar evolution. However, so far we just do not know how stars behave at very low metallicities making it crucial to observe and analyse them in metal poor regions.

In this work, the spectra of 74 Wolf-Rayet stars located in the spiral galaxy M33 are analysed using the Potsdam Wolf-Rayet (PoWR) stellar atmosphere code to deduce their stellar parameters. The majority of the analysed stars are located in the outer parts of the galaxy, which is a metal poor region with a reported metallicity of $Z = 0.3 Z_\odot = 0.0042$ (U et al. 2009) placing it between the Small Magellanic ($Z_{\mathrm{SMC}} = 0.14 Z_\odot$) and Large Magellanic ($Z_{\mathrm{LMC}} = 0.43 Z_\odot$) Clouds. The results will be compared to previous analyses from other galaxies and they will be integrated in the results from Hainich et al. (2015) to test their derived mass-loss versus metallicity relation.

The work is organised as follows. In Chapter 2 the current understanding of the evolution of massive stars is described for single and binary stars. The properties of Wolf-Rayet stars are summarised in Chapter 3. The Potsdam Wolf-Rayet atmosphere models and the spectral fitting procedure are explained in Chapter 4. In Chapter 5.3 the programme stars are introduced. The analyses and results are discussed in Chapter 6. In the Appendix there is a comment for each star of the sample, the spectral fits of the stars and a list of all known Wolf-Rayet stars in M33.

# 2 Evolution of massive stars

## 2.1 Single star evolution

### 2.1.1 Hydrogen core burning

The evolution of massive stars is still not completely understood[1]. Like all other stars, they form out of a collapsing cloud where a protostar accretes more and more material. The protostar contracts such that temperature and density increase in its centre until the fusion of hydrogen sets in. This marks the beginning of the Main Sequence evolution, which is the longest lasting period in the evolution of a star. Our Sun will spend about eight billion years on the Main Sequence but for stars with more than 20 solar masses, this phase will only last for a few million years because the timescale $t_\mathrm{H}$ for core hydrogen burning has a strong dependence on the stellar mass $M$:

$$t_\mathrm{H} \propto M^{1-\eta} \tag{2.1}$$

with an average value of $\eta = 3.5$ one obtains $t_\mathrm{H} \propto M^{-2.5}$ which means that there is a strong decrease of $t_\mathrm{H}$ for higher masses. The value for $\eta$ is not a uniform value and declines towards higher masses. Still, determining the exact time of core hydrogen burning is dependent on numerous parameters whose range is still uncertain as we will see in the following.

There exist two different reaction chains that are responsible for the transformation of hydrogen into helium. The first one is called proton-proton chain which is performed by stars with less than 1.5 solar masses and will thus not be discussed here in detail. In more massive stars, hydrogen is transformed into helium via the so-called CNO cycle where the elements carbon, nitrogen and oxygen work as catalysts. The individual steps of the cycle are shown in Fig. 2.1, which is taken from Adelberger et al. (2007). In the first step, a proton merges with a $^{12}$C core to $^{13}$N, which is unstable and decays rapidly to $^{13}$C via a $\beta^+$ decay. Then another proton is added creating a $^{14}$N core. This nucleus is stable such that another proton has to merge with it to continue the cycle. However, $^{14}$N has the highest potential wall of the stable nuclei in the CNO cycle making it the bottle neck in that reaction. Thus, nearly all the initial carbon is transformed into nitrogen such that the carbon mass fraction relative to the one of nitrogen is about $1/60$ (Schaerer et al. 1993). The enhancement of nitrogen is later seen in the spectra of Wolf-Rayet stars of the nitrogen sequence. In the next step of the cycle, the $^{14}$N core merges with another

---

[1]The following explanations are mainly based on the book:"Stellar Structure and Evolution" from Kippenhahn et al. (2012)
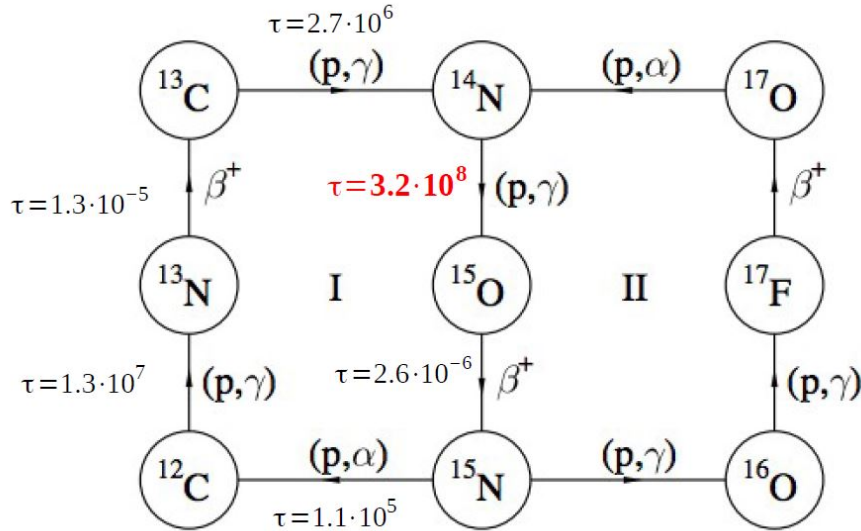
**Fig. 2.1** The figure is taken from Adelberger et al. (2007) and presents the two branches of the CNO cycle. For the first branch, the average timescales are shown for each step in seconds.

proton to form $^{15}$O. This again is unstable and via a $\beta^+$ decay it creates $^{15}$N. From here there are two different options. In the first case, the first cycle is finished by merging with another proton but then the energy is too high and the nucleus decays to $^{12}$C and an alpha particle and the cycle can start anew. Four protons were transformed into one helium core through this whole cycle. The second option is about 1000 times less likely but by merging a proton with $^{15}$N a stable $^{16}$O core is created. This one merges again with a proton to form $^{17}$F, which is radioactive and decays to $^{17}$O. The second cycle is then completed by merging with another proton leading to an unstable configuration that decays into an $\alpha$ particle and $^{14}$N. Thus, even the original oxygen is mainly transformed into nitrogen.

When a star is massive enough to burn hydrogen via the CNO cycle, its inner structure is changing. While low mass stars like our sun have a degenerate radiative core and a convective envelope, massive stars have a non degenerate convective core and a radiative envelope. In contrast to the proton-proton chain, the nuclear reaction rates of the CNO cycle have a much higher temperature dependency. For the CNO cycle, it is sensitive to $T^\mu$ with $\mu$ covering a range of $\mu = 23...13$ for core temperatures between 8 and 50 MK. Thus, more massive stars burn their hydrogen faster. Due to the strong temperature dependence, the helium production is concentrated towards the centre of the core but the strong convection keeps it fully mixed. The convective motion leads to an effect known as convective overshooting. This means that some of the material is reaching into the regions outside the core where the criterion for convective instability is not fulfilled anymore. This is known as Schwarzschild criterion, which is defined via the adiabatic ($\nabla_{\mathrm{ad}}$) and radiative temperature gradient ($\nabla_{\mathrm{rad}}$). If $\nabla_{\mathrm{rad}} < \nabla_{\mathrm{ad}}$, then a layer is stable against convection. The strength of the convective overshooting effect is highly uncertain. However, it can have a strong impact on the evolution of a star because it effectively increases the size of the core as more material is available for hydrogen fusion. More hydrogen means that the Main Sequence duration is extended as demonstrated in Fig. 2.2 from Kippenhahn et al.

(2012)[p.352]. Since massive stars have strong stellar winds with mass-loss rates on the order of $10^{-6}$ to $10^{-7}$ solar masses per year $(M_\odot/\mathrm{yr})$ slowly reducing their hydrogen envelope, a longer time in that phase would mean that they can remove more of their initial mass before entering the next evolutionary phase. The effect of
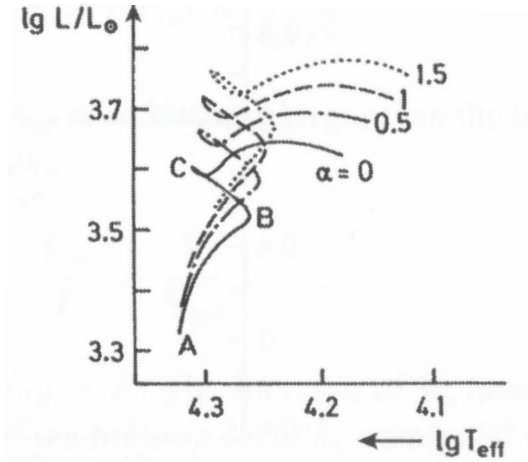


**Fig. 2.2** The diagram from Kippenhahn et al. (2012)[p.352] shows the evolution of a massive star on the Main Sequence for different values of the overshooting parameter. $\alpha = 0$ means that no overshooting is applied.

overshooting is described by the parameter $\alpha$, which is the ratio between the mixing length $l_\mathrm{m}$ a blob of matter has in a convective region before it dissolves and the scale height of pressure $(H_P)$ in that region, so $\alpha = l_\mathrm{m}/H_P$. Fig. 2.2 shows a Hertzsprung - Russell diagram where the logarithm of the stellar luminosity is plotted over the logarithm of the effective temperature of a star. It includes different evolutionary tracks for a star with an initial mass of $7\,M_\odot$. No overshooting is applied for the track with $\alpha = 0$ and the strongest overshooting has the track with $\alpha = 1.5$. As can be seen, overshooting can have a strong impact on the position of a star in the Hertzsprung-Russell diagram. The letters A, B and C mark the beginning of hydrogen core burning (A), the minimum of the effective temperature on the Main Sequence (B) and the exhaustion of central hydrogen (C). Overshooting is not the only uncertain parameter in our understanding of stellar evolution. During core hydrogen burning nuclear fusion is concentrated more and more towards the centre creating regions with partly processed material. The Schwarzschild criterion assumes that everything is homogeneously mixed but when the burning region decreases it can introduce a gradient of the mean molecular weight $(\nabla_\mu)$. If overshooting is rather weak, this creates a gradient in the mean molecular weight, which can lead to a phenomenon called semiconvection. The Schwarzschild criterion needs to be extended by an additional term that includes $\nabla_\mu$. It is then called Ledoux criterion which is:

$$\nabla_\mathrm{rad} < \nabla_\mathrm{ad} + \frac{\phi}{\delta}\nabla_\mu \tag{2.2}$$

where $\phi$ and $\delta$ are both positive. The gradient increases towards the centre giving $\nabla_\mu > 0$. This can lead to a stabilising effect such that a radiative region is established right above the core although it would be unstable according to the Schwarzschild criterion. Now diffusion processes try to remove this gradient by mix-

ing hydrogen rich material into deeper layers. This has no influence for the Main Sequence evolution but for later evolutionary phases.

## 2.1.2 Evolution through helium core burning and beyond

After hydrogen is depleted in the core, it starts to contract and in the layer above it conditions are fulfilled to ignite hydrogen shell burning. At the same time the envelope expands which, significantly reduces the surface temperature. Thus, in the Hertzsprung-Russell diagram the star moves to the right side towards the so-called Hayashi line and becomes a Red Supergiant. At this point, the star cannot cool down further and it becomes nearly fully convective. Since massive stars have high core temperatures, helium burning already starts before approaching the Hayashi-line. Via the triple $\alpha$ reaction three helium cores are fused to one $^{12}$C core. Compared to the CNO cycle the nuclear reaction rate is even more sensitive to the core temperature where the exponent reaches a value of up to $\mu = 40$. Thus, helium is burned even faster and this stage lasts only for about $10\,\%$ of the total lifetime of a star. When more and more carbon is built up in the centre, reactions forming $^{16}$O and $^{20}$Ne become more likely. Furthermore, some neon is already produced at the onset of helium core burning from the nitrogen of the CNO cycle. By capturing an $\alpha$ particle the leftover $^{14}$N is transformed into radioactive $^{18}$F, which decays to $^{18}$O. This captures another $\alpha$ particle and creates $^{22}$Ne (Iben & Tutukov 1985). Thus, during central helium burning two different isotopes of neon are created.

After reaching the Hayashi line, the mass-loss rate determines the further evolution of a star. However, this is another uncertain parameter in the stellar evolution models. Moreover, it is strongly dependent on the metallicity of the star because the winds are driven by radiation pressure intercepted by iron like metals. If the mass-loss is high enough, the star can get rid of its hydrogen rich envelope and the hotter inner part is unveiled. Then the star evolves to higher temperatures again and its strong stellar winds create an emission line dominated spectrum. The star enters the Wolf-Rayet phase, which is the final stage before core collapse. For our Galaxy, it is assumed that a star needs an initial mass of at least 22 solar masses to reach the Wolf-Rayet phase only via wind stripping (Hamann et al. 2006). Less massive stars are not able to remove their hydrogen envelope and they end up as Red Supergiants. At lower metallicities this shifts to higher masses but the exact behaviour is not well known.

There is evidence that stars with initially more than $\sim$40 solar masses are not becoming Red Supergiants because at some point they reach the Humphreys-Davidson limit (Humphreys & Davidson 1979), which is related to the Eddington limit. The outwards acting radiative force exceeds the gravitational force of the stars which leads to an unstable configuration where the stars have very high mass-loss rates. This helps to remove a big part of the envelope within a short period of time. The stars are called Luminous Blue Variables (LBVs). Crowther (2007) divides the evolution of massive stars with solar metallicity that reach the Wolf-Rayet phase in three different mass ranges:

**25-40 $M_\odot$**

$$O \rightarrow RSG/LBV \rightarrow WN(H-poor) \rightarrow SN\,Ic$$

**40-75 $M_\odot$**

$$O \rightarrow LBV \rightarrow WN(H-poor) \rightarrow WC \rightarrow SN\,Ic$$

**>75 $M_\odot$**

$$O \rightarrow WN(H-rich) \rightarrow LBV \rightarrow WN(H-poor) \rightarrow WC \rightarrow SN\,Ic$$

The symbols WN and WC denote two of the three different categories of Wolf-Rayet stars. WN stars show emission lines of nitrogen, helium and sometimes hydrogen in their spectra if the envelope is not completely removed. Since we see material processed by the CNO cycle, it is clear why there are strong nitrogen lines. So WN stars are the observational proof of the CNO cycle. Consequently, WC stars are the proof of the triple $\alpha$ reaction because their spectra include strong lines of carbon and oxygen, the products of helium burning. If even more material can be removed through the Wolf-Rayet winds, oxygen lines become more prominent because more oxygen is produced at the end of helium burning. These stars are denoted as WO stars, which are the best candidates for stars that are in their carbon burning stage, which follows after core helium burning. This phase lasts only for a few hundred years and is the last one we could in principle notice. All following burning stages do not last long enough to have an influence on the appearance of the star because the star is not fast enough to adapt to the changes in its core. Silicon burning is the last burning phase, which is finished after a few hours. Then the core consists completely of $^{56}$Fe and no further nuclear reactions are possible because this is the isotope with the highest binding energy per nucleon such that more energy would be needed than the reaction gives in return. At this point, gravity takes over and the star collapses as supernova of type Ib/c leaving a neutron star or black hole. In the helium core mass range between about 60 to around 80 solar masses, so-called pair instability supernovae are predicted that completely destroy the star and leave no remnant behind. However, recent gravitational wave observations question this because black hole mergers in this mass range were observed. Due to their dense cores it might even be questionable whether a supernova is even possible. It could be that the stars are just directly collapsing into black holes (Yoon 2015). In that case a star would just disappear from the sky. A possible candidate was reported recently by Allan et al. (2020) but it could just be due to dust obscuration. At some point in the future, we should be able to see clear evidence because some of the known Wolf-Rayet stars should be in their carbon core burning stage. Maybe we will be "lucky" to not see one of them anymore since every day could be their last one.

### 2.1.3 Quasi chemically homogeneous evolution

So far the standard evolutionary path for massive stars was described. When a massive star is formed, it should have a high rotational speed due to the conservation of

angular momentum from the cloud. Through stellar winds this angular momentum is lost and the rotational speed decreases. However, in environments with very low metallicities the stars should, in theory, retain their fast rotation. A fast rotation is believed to induce a mixing process which comprises the major part of the stellar mass. Thus, the star would have a very extended hydrogen core burning phase and only a small envelope where the stellar wind should be sufficient enough to remove it during this phase. Therefore, the star would not become an LBV or RSG but directly enter the Wolf-Rayet stage (Maeder & Meynet 2000; Brott et al. 2011). In that case, a star would not drastically increase its radius such that interactions with close companions are more unlikely. Furthermore, it retains more of its initial mass resulting in a higher mass during the final core collapse and for the resulting black hole. Thus, it allows the formation of a pair of massive black holes, which are observed from gravitational wave events. There is also observational evidence for stars in the SMC that an evolution similar to quasi chemically homogeneous scenario might be possible (Ramachandran et al. 2019). Now there is only one big problem for this explanation because the observed stars are not fast rotators although this is the underlying assumption for these models. Thus, there are presumably different reasons besides rotation as to why the observed stars follow a quasi homogeneous evolution, and it will be the task of future studies to shed light on this topic.

## 2.2 Impact of binarity

So far only the evolution of single stars was discussed but Sana et al. (2012) showed that the majority of massive stars in our Galaxy are part of a double or multiple system. Furthermore, they found that small separations are favoured, which means that it is very likely that the stars interact at least once during their evolution. Binary star interactions can significantly change the evolution of a star and lead to special incidents. Numerous binary evolution products are observationally confirmed (e.g. blue straggler, extremely low mass white dwarfs, neutron star and black hole mergers...). Thus, the question arises whether it has a non-negligible impact on the formation of Wolf-Rayet stars.

Binary interactions are divided in three different cases. In case A, the stars already interact during their Main Sequence evolution. In case B, they start to interact when the more massive component finished its hydrogen core burning and drastically increases its radius. In case C, the more massive star already evolved to a Red Supergiant, which slowly increases its radius even further. In all cases, the originally more massive star, which is denoted as the primary, loses mass when it fills its Roche lobe. The mass can be transferred to the secondary star if the mass transfer is stable leading to a rejuvenation. If the mass transfer is unstable, it cannot be accreted by the secondary. The outcome can be two stars in a very small orbit but it can also lead to the merger of both objects. The spectrum of the stripped star should be enriched in helium and nitrogen. Since the envelope of the primary is removed, it should help to form Wolf-Rayet stars, especially at low metallicities where it is much more difficult for the stars to remove it solely via stellar winds. Thus, one would expect to find Wolf-Rayet stars at low metallicities whose initial mass would not be sufficient enough to enter this stage. Because of its low metallicity

of about a fifth of the solar metallicity, the Small Magellanic Cloud (SMC) seems to be an ideal place to test this. However, Shenar et al. (2016) found no clear indication that binary evolution would be needed to explain the existence of the observed Wolf-Rayet stars in binaries because their initial masses are high enough such that their winds are sufficient to reach this phase on their own. They also reported that there is no difference in the spectra of these stars compared to that of presumably single Wolf-Rayet stars. On the first glance this seems to be very counterintuitive because there is no reason to assume why those stars should not interact and why it should not have an influence on the formation of Wolf-Rayet stars. A possible explanation is provided by Shenar et al. (2020b). Although a star might have been stripped by its companion, it still needs a mass-loss rate that is sufficiently high enough to create a Wolf-Rayet like spectrum. This is problematic in a metal poor region like the SMC because the winds are mainly driven by iron like ions. Shenar et al. (2020b) calculated that a star needs a luminosity of at least $\log L/L_\odot = 5.6$ to show a Wolf-Rayet spectrum. For the Milky Way, they calculated a lower luminosity limit of around $\log L/L_\odot \approx 4.9$. The estimated lower limit for the SMC is in line with the known presumably single Wolf-Rayet stars, which were analysed by Hainich et al. (2015). In their work, no star with a luminosity significantly below $\log L/L_\odot = 5.6$ is listed. However, this means that those stars should still exist but they just do not show a typical Wolf-Rayet spectrum. These stars are then denoted as stripped envelope stars which are the link between hot subdwarfs, the low mass form of a helium star, and Wolf-Rayet stars. However, so far only a handful of them are known. If the system has undergone mass transfer, it would be very hard to detect it in the optical spectrum because the originally less massive star would outshine them. As the stripped stars are believed to be hotter than their companion, it is assumed that they should create an excess in UV light, which cannot be explained by their companion alone.

The metallicity is not only affecting the mass-loss rate of a massive star but also its evolution as a whole. In metal poor regions, stars remain more compact during their evolution. This not only leads to an extension of the Main Sequence duration but even when hydrogen is depleted in the core, they are not expanding as fast as stars in metal rich regions. In comparison to metal rich stars, they have higher core temperatures and densities, and lower opacities in their envelopes. Thus, they remain hotter after hydrogen is depleted, which results in smaller radii meaning that interactions with a companion become more unlikely. Klencki et al. (2020) show that the stars spend already a long time in their helium burning phases before interactions set in. Even if a Wolf-Rayet star is formed, it would have a lifetime that is about one order of magnitude smaller compared to normal Wolf-Rayet stars. Furthermore, not all hydrogen will be removed because due to semiconvection some hydrogen is mixed into layers that become visible when the envelope is removed. Thus, at low metallicities Wolf-Rayet stars of the nitrogen sequence are expected to always show hydrogen in their spectra. Indeed, there is no known WN star in the SMC that is hydrogen free (Hainich et al. 2015; Shenar et al. 2016). Klencki et al. (2020) found that mass transfer happens at the end of core helium burning for metallicities below the SMC value such that not enough time would be left to form a Wolf-Rayet star. All in all it seems that binarity might not be a main driver for the creation of Wolf-Rayet stars, and even if it supports the removal of the hydrogen rich envelope, it still needs a luminosity sufficiently high enough to create

an emission line spectrum otherwise they only appear as helium stars, which are difficult to identify.

# 3 Properties of Wolf-Rayet stars

## 3.1 Classification

The optical spectra of Wolf-Rayet stars are dominated by emission lines. Depending on their evolutionary phase hydrogen, helium, nitrogen, carbon or oxygen lines are visible in their spectra. Thus, the emission lines of these elements were used to divide them in three different groups. Wolf-Rayet stars with strong helium and nitrogen lines belong to the nitrogen sequence and are denoted as WN stars. Thus, at this stage the products of hydrogen burning are visible. Wolf-Rayet stars showing strong carbon, helium and also oxygen lines in their spectra belong to the carbon sequence, which is represented by the abbreviation WC. At this stage, the products of helium burning are observed in their spectra. At the beginning of helium burning, mainly carbon is produced and only a bit of oxygen but at later stages the weight shifts to oxygen. With the rise of the oxygen abundance, the oxygen lines might, in theory, become more prominent in the spectrum and then the star is classified as WO. However, for WO stars the oxygen abundance is not the only definitive parameter. At higher temperatures the spectrum changes in favour of the oxygen lines because it has more optical transitions whereas the carbon lines become depleted. Thus, WO stars could, in principle, just be hot WC type stars.

The different spectral types are further divided into subtypes. In the past, two slightly different classification schemes were established and both of them are commonly used. The classification applied here was introduced by van der Hucht (2001), which is based on earlier schemes of Smith (1968a,b). The criteria are presented in the Tables 3.1 - 3.3. For the WN sequence the following lines are used to classify the stars:

**He** I **at:** 3888, 4027, 4471, 4921 and 5875 Å
**He** II **at:** 4200, 4340, 4541, 4686, 4861, 5411 and 6560 Å
**N** II **at** 3995 Å
**N** III **at:** 4634-4641 and 5314 Å
**N** IV **at:** 3479-3484 and 4058 Å
**N** V **at:** 4603, 4619 and 4933-4944 Å.

For the classification of the WC sequence the lines used are:
**C** II **at:** 4267 Å
**C** III **at:** 4650 and 5696 Å
**C** IV **at:** 4650 and 5801-5812 Å
**O** V **at:** 5572-5598 Å.

For WO stars the following lines are used:
**C** IV **at:** 5801-5812 Å
**O** IV **at:** 3400 Å

**O** v **at:** 5572-5598 Å
**O** vi **at:** 3811-3834 Å
**O** vii **at:** 5670 Å
**O** viii **at:** 6068 Å.

**Table 3.1** Classification of the WN stars (van der Hucht 2001)

| WN-type | Ratio of nitrogen emission lines | other criteria |
|---------|----------------------------------|----------------|
| WN2 | N v weak or absent | strong He ii |
| WN2.5 | N v visible, N iv absent | |
| WN3 | N iv ≪ N v, N iii weak or absent | |
| WN4 | N iv ≈ N v, N iii weak or absent | |
| WN4.5 | N iv > N v, N iii weak or absent | |
| WN5 | N iii ≈ N iv ≈ N v | |
| WN6 | N iii ≈ N iv, N v weak or absent | |
| WN7 | N iii > N iv, N iii < He ii 4686 | weak He i P-Cyg profile |
| WN8 | N iii ≫ N iv, N iii ≈ He ii 4686 | strong He i P-Cyg profile |
| WN9 | N iii > N ii, N iv absent | He i P-Cyg profile |
| WN10 | N iii ≈ N ii | Balmer lines, He i P-Cyg profile |
| WN11 | N ii ≈ He ii, N iii weak or absent | Balmer lines, He i P-Cyg profile |

**Table 3.2** Classification of the WC stars (van der Hucht 2001)

| WO-Typ | Ratio of oxygen emission lines | other criteria |
|--------|--------------------------------|----------------|
| WO1 | O vii ≥ O v, O viii present | C iii absent |
| WO2 | O vii < O v | C iv < O vi, C iii absent |
| WO3 | O vii weak or absent | C iv ≈ O vi, C iii absent |
| WO4 | | C iv ≫ O vi, C iii absent |

**Table 3.3** Classification of the WO stars (van der Hucht 2001)

| WC-Typ | Ratio of carbon emission lines | other criteria |
|--------|--------------------------------|----------------|
| WC4 | C iv strong, C ii weak or absent | O v moderate |
| WC5 | C iii ≪ C iv | C iii < O v |
| WC6 | C iii ≪ C iv | C iii > O v |
| WC7 | C iii < C iv | C iii ≫ O v |
| WC8 | C iii > C iv | C ii absent, |
| | | O v weak or absent |
| WC9 | C iii > C iv | C ii present, |
| | | O v weak or absent |

The other commonly applied classification scheme is from Smith et al. (1996) and only available for WN stars. It is a bit more complex and is based on the line ratios of He ii 5411/He i 5875, N v 4604/N iii 4640, N iv 4057/N v,iii 4604-4640, C iv 5801/He ii 5411 and C iv 5801/He ii 5875. Moreover, other criteria were introduced to describe the spectral appearance. Only the ones important for this work will be mentioned. For a complete list see Smith et al. (1996). WN stars showing the presence of hydrogen in their spectra are additionally flagged with the letter h (e.g. WN3h). How hydrogen is identified without performing a spectral analysis is described in Smith et al. (1996) and depicted in Fig. 3.1. For this the smaller He ii lines at 4200, 4340, 4541, 4861 and 5411 Å are used. Since the lines at 4340

and 4861 Å are blended with hydrogen lines they will exceed a straight line drawn between the unblended lines. In this work, the designation h was only used for stars with spectral type WN5 or earlier because all observed late type WN have hydrogen in their spectrum. The second sub criteria applied here is +abs which is used to mark WN stars showing absorption lines of unknown origin in their spectrum. In some cases, it is caused by an unknown companion or another star located in the line of sight but it could also come from the Wolf-Rayet star itself. In any case, this would require a more detailed analysis and cannot be solved by just taking a look at the spectrum.

In the last years, a new class of early type WN stars was identified in the LMC and reported by Neugent et al. (2017). A few examples for the spectra of these stars are shown in Fig. 3.2 taken from Neugent et al. (2017). As can be seen, their emission lines are fairly weak and only a few lines appear in emission. All of the smaller He II lines are in absorption mimicking the spectral type O3. However, the observed luminosities are far too faint for an O3 star. Therefore, the lines must have their origin in the Wolf-Rayet star. Since their emission line spectrum is similar to that of a WN3 star, they received the unfortunate designation WN3/O3. This class is only mentioned for the sake of completeness but no such star was identified in the analysed sample.
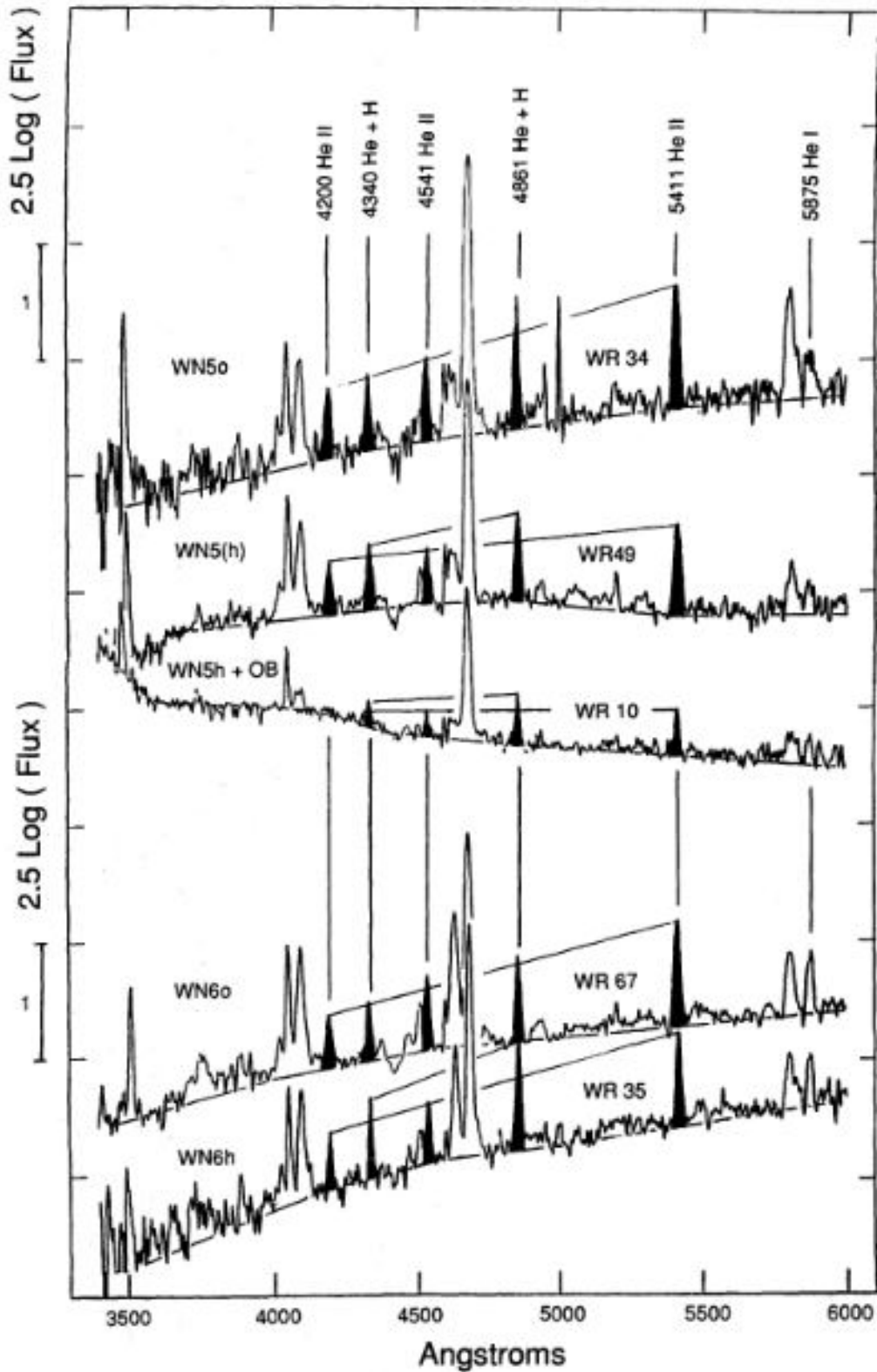
**Fig. 3.1** The diagram from Smith et al. (1996) shows how hydrogen is detected in the spectra of WN stars. This method was first employed by Conti et al. (1983). The He II lines at 4340 and 4861 Å are blended with hydrogen lines. Thus, when hydrogen is present these lines exceed a straight line drawn between the He II line at 4200, 4541 and 5411 Å.

16
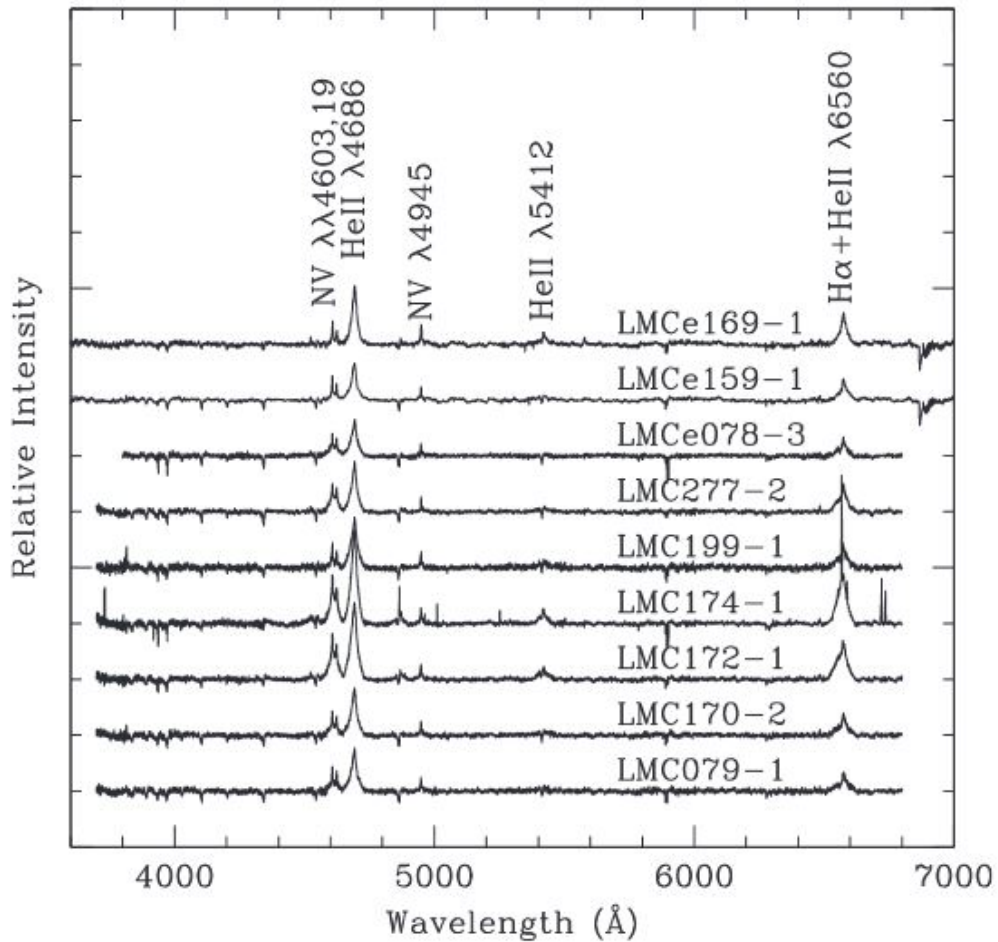
**Fig. 3.2** Example spectra of WN3/O3 stars observed in the Large Magellanic Cloud taken from Neugent et al. (2017). They are similar to the spectra of WN3 stars but they only have very few emission lines, which are rather weak. The observed absorption features fit to a O3 star but such a star would be too bright for the luminosity that is observed for the stars.

## 3.2 Radiation driven winds

The wind of a massive star is accelerated by radiation. Ions absorb photons, which are re-emitted after some time. When a photon is absorbed, it transfers its momentum to the ion but the energy is lost again when the photon is re-emitted. The re-emission is random and can point in any direction but the momentum of the absorbed photon is always radially pointing away from the star such that the ion is accelerated in the same direction. Now it is important to note that not all ions have the same driving potential due to their different opacities. In fact, the most abundant elements in Wolf-Rayet stars, which are hydrogen, helium and nitrogen for WN and helium, carbon and oxygen for WC/WO stars, contribute only a small part. Albeit their low abundance, the winds of Wolf-Rayet stars are mainly driven by iron-like elements (Sander et al. 2020) because they have much more possible transitions in the extreme UV where the stars have their highest radiation flux allowing them to absorb huge amounts of photons. Thus, they collect a lot of momentum which accelerates the iron-like ions into space. Through Coulomb interactions, elastic collisions transfer the momentum to other ions making them to move together. Thus, the metallicity plays an important role because in metal poor regions the amount of iron-like metals is reduced leading to a smaller mass-loss rate.

## 3.3 Parameters

In the Hertzsprung-Russell diagram Wolf-Rayet stars are located in the upper part between luminosities of $\log L/L_\odot \sim 5.0$ up to $\log L/L_\odot \sim 6.7$ in extreme cases. Their temperatures range from about $25\,\mathrm{kK}$ for late type WN stars up to $200\,\mathrm{kK}$ for the hottest WO type stars (Sander et al. 2012). Most of them are located between the Zero Age Main Sequence (ZAMS) and He-ZAMS. Due to their high mass-loss rates they have an optical spectrum that is dominated by emission lines. The observed values for the mass-loss rates range between $\sim 10^{-4}$ to $\sim 10^{-6}$ $M_\odot/\mathrm{yr}$. It strongly depends on the metallicity because the main wind driver are iron-like elements. The exact relation between mass-loss rate and metallicity is not completely understood. The results from theoretical predictions suggest a power law with $\dot{M} \sim Z^m$. Vink & de Koter (2005) found a value of $m = 0.86$ but this is not supported by observational results from Hainich et al. (2015) who found a value of $m = 1.2$. Recent theoretical predictions from Sander et al. (2020) found a result similar to the one of Hainich et al. (2015) and their analysis suggest that it gets even steeper for very low metallicities.

The stellar winds of Wolf-Rayet stars are non-stationary and inhomogeneous leading to a phenomenon known as clumping. This is accounted for by introducing the clumping parameter $D$. Clumping has an impact on the mass-loss rate of a star. Compared to a model without clumping, a model with clumping has a smaller mass-loss rate by a factor of $\sqrt{D}$ (Hamann & Koesterke 1998). Usually clumping is determined by the strength of the electron scattering wings but this can be difficult to estimate in the optical spectrum due to the choice of the continuum and blends (Hillier 1991).

The terminal velocities of Wolf-Rayet winds cover a range between $\sim 200$ to about $5000\,\mathrm{km\,s^{-1}}$. Usually, late type WN have the smallest terminal velocities between 300 and $1000\,\mathrm{km\,s^{-1}}$. This is followed by the early type WN stars having terminal wind speeds between 1000 and $2000\,\mathrm{km\,s^{-1}}$. WC and WO stars have the fastest winds with up to $5000\,\mathrm{km\,s^{-1}}$. Their higher carbon and oxygen abundance leads to an increase in opacity in the wind, which helps to accelerate it even further compared to the WN stars (Sander et al. 2020).

# 4 Potsdam Wolf-Rayet atmosphere code

## 4.1 The models

The spectral analyses was performed using the Potsdam Wolf-Rayet (PoWR) atmosphere code that allows calculating synthetic spectra for expanding atmospheres. The basic assumptions are spherical symmetry and a stationary mass-loss. The models account for non-local thermodynamic equilibrium (non-LTE) effects and solve the radiative transfer equation in the co-moving frame together with the equations of statistical and radiative equilibrium to ensure the energy conservation. Furthermore, the effects of iron line blanketing and wind clumping are accounted for. The elements of the iron group are treated in a super level approach where $10^7$ line transitions between $\sim 10^5$ energy levels are summarised in super levels. A more detailed description is given in Gräfener et al. (2002); Hamann & Gräfener (2004); Sander et al. (2015).

The models use a predefined velocity field that has the form of a single beta law in the supersonic part of the wind:

$$v(r) = v_\infty \left( 1 - \frac{R_0}{r} \right)^\beta \tag{4.1}$$

where $v_\infty$ is the terminal wind speed and $R_0 \approx R_*$. For all models $\beta = 1$ was adopted. For some of the WC star fits a "double beta law" was adopted:

$$v(r) = v_\infty \left[ 0.6 \left( 1 - \frac{r_0}{r} \right)^{\beta_1} + 0.4 \left( 1 - \frac{r_1}{r} \right)^{\beta_2} \right] \tag{4.2}$$

The parameters $r_0$ and $r_1$ correspond roughly to the stellar radius $R_*$. For the $\beta$s the following values were chosen $\beta_1 = 1$ and $\beta_2 = 50$ because it should in principle result in a better fit (Gräfener & Hamann 2005). In the subsonic region the velocity field is calculated self-consistently such that the hydrostatic equation is fulfilled.

The inner boundary is defined at an optical depth of $\tau_{\mathrm{Ross}} = 20$ which defines the position of the stellar radius $R_*$ and the effective stellar temperature $T_*$. Both are related to the luminosity $L$ via the Stefan-Boltzmann law:

$$L = 4\pi\sigma R_*^2 T_*^4 \tag{4.3}$$

where $\sigma$ is the Stefan-Boltzmann constant. In the model, two out of the three quantities need to be given and the third one is then calculated.

Another useful parameter is the so-called transformed radius that was introduced by Schmutz et al. (1989). It depends on the mass-loss rate $\dot{M}$, the terminal wind speed $v_\infty$, the stellar radius $R_*$ and the so-called clumping parameter $D$:

$$R_\mathrm{t} = R_* \left[ \frac{v_\infty}{2500\,\mathrm{km\,s^{-1}}} \bigg/ \frac{\dot{M}\sqrt{D}}{10^{-4} M_\odot\,\mathrm{yr^{-1}}} \right]^{2/3}$$

Models sharing the same transformed radius have similar spectra. The clumping parameter $D$ accounts for wind inhomogeneities where it is assumed that optically thin clumps fill a volume $f_\mathrm{V}$ while the medium between the clumps is empty. The clumping parameter is then the inverse of the volume filling factor $D = 1/f_\mathrm{V}$. For nearly all models, depth dependent clumping was applied using the approach of Martins et al. (2009). In the models, clumping starts at the sonic point and reaches its maximum value of $D = 10$ at the terminal velocity.

Detailed model atoms of H, He, N and C were included for the calculation of the WN stars. In a few cases also Si and O were included to check whether some features are created by these elements. For the WC stars He, C and O were included and in some cases Ne but the majority of the models was calculated without Ne due to convergence issues.

During the calculation of a model the code executes different steps. In the first step, the parameters are read in. Then a start approximation is calculated for the predefined velocity field $v(r)$, the density stratification $\rho(r)$ and the radiation field $J_\nu$. The velocity is used to calculate an approximation of the density stratification from the continuity equation:

$$\rho(r) = \frac{\dot{M}}{4\pi r^2 v(r)} \tag{4.4}$$

The radiation field is defined as:

$$J_\nu = \frac{1}{2} \int_{-1}^{1} I_\nu d\mu \tag{4.5}$$

where $I_\nu$ is the the frequency dependent intensity, which is defined as energy $\mathrm{d}E$ per time interval $\mathrm{d}t$ and frequency $\mathrm{d}\nu$ from a solid angle $\mathrm{d}\omega$ going through a surface $\mathrm{d}A$:

$$I_\nu = \frac{\mathrm{d}^4 E}{\mathrm{d}\nu\,\mathrm{d}t\,\mathrm{d}\omega\,\mathrm{d}A} \tag{4.6}$$

This is done in the so-called co-moving frame because of the expansion of the atmosphere. When integrating Equation 4.5 additionally over ($\mu$, $\mu^2$ and $\mu^3$) the first, second and third moment of $J_\nu$ can be calculated:

$$[H_\nu, K_\nu, N_\nu] = \frac{1}{2} \int_{-1}^{1} I_\nu[\mu, \mu^2, \mu^3]d\mu \tag{4.7}$$

These quantities are needed to calculate the Eddington factors $f = K/J$ and $g = N/H$, which are needed to solve the radiative transfer equation and temperature

stratification. In spherical coordinates $\mu = \cos\vartheta$. On this basis, the occupation numbers $\vec{n}$ are calculated.

The next step consists of iterative processes that are executed until the applied changes drop below a certain limit called $\epsilon$, which is defined in the model. Furthermore, there is also a limit for the flux consistency, which was set to 1 and sometimes up to 2 %. Since occupation numbers and radiation field depend on each other, a system of coupled differential equations needs to be solved numerically. This is done via the so-called *approximated/accelerated lambda iteration* (ALI) operation. For more details see Hubeny & Mihalas (2015)[p.421-424]. After five repetitions $I_\nu$ and the Eddington factors are updated because they are needed to solve the equations for $J_\nu$ and $\vec{n}$. This is repeated until everything is converged. In the last step, the emergent spectrum is calculated in the formal integral.

## 4.2 Spectral fitting

Achieving a good spectral fit requires the execution of many different steps. For a first estimate, the spectrum was compared to a model from the LMC Grid (Todt et al. 2015). When a good model was found, it was compared to neighbouring models to delimit the range of the transformed radius and temperature. Then the best fitting model was selected and adjusted. Since quite a lot of stars were analysed at the same time, a document was created were every modification to a model was recorded. The luminosity was adjusted such that the optical photometric magnitudes were covered by the spectral energy distribution. For WN stars, temperatures and transformed radii were adjusted such that the helium lines were fitted. For WC stars, the small lines were taken as anchor points because the He II/C III/C IV blend at around 4686 Å and C IV at 5801 Å features react extremely sensitively to these parameters. Unfortunately, in some spectra only those two features are visible leading to high uncertainties.

Abundances were determined via an iterative process. In the first step, a model was calculated that reproduces most of the He II lines. Then the abundances of carbon and nitrogen were adjusted until they matched the observed line profiles. However, this can slightly change the ionisation structure such that temperature and transformed radius needed to be adapted to the new conditions. Determining the hydrogen abundance follows the same steps but all lines are blended with He II lines. Additionally, there are nebula emission lines which are easy to distinguish from stellar lines for early type WN stars as these have high wind velocities resulting in broad emission lines. However, the same cannot be said for late type WN stars as it gets far more difficult to distinguish between stellar and nebular emission. Unfortunately, these are exactly the stars that have a much higher probability to show hydrogen in their spectra leading to a higher uncertainty. In the case of WC stars, the determination of the individual abundances was much more difficult because their spectra are not so easy to reproduce as in the case of WN stars. Therefore, the abundance give only a very rough estimate.

All but one star are analysed here for the first time. Only for M33-WR205 (Romano's star) a spectral analysis was available (see for example Clark et al. (2012);

Maryeva et al. (2019)). As an example the spectral fit of this star is shown in Fig. 4.1. The plot includes a lot of different information. In the upper left corner is the identifier of the star as used in this work and in the upper right corner is the classification. The first box shows the SED fit, which has some basic stellar parameters printed on top of it. In the right side of the box, the luminosity, reddening parameters and abundances are given. All spectra were corrected for the radial velocity of M33, which is $v_{\mathrm{rad,M33}} = 180\,\mathrm{km\,s^{-1}}$ (Karachentsev et al. 2004). In some cases, an additional shift was observed that was compensated. In the fit, this is given as $v_{\mathrm{rad}}$, which is the radial velocity on top of the radial velocity of M33. The abbreviation CWD in the upper right corner stands for crowding index as given by Neugent & Massey (2011). There are four different gradings. They mark the "Crowding, measured by the greatest contamination by neighbours in U, B, V, R, or I with a 1″5 slit in 1″ seeing"[1]. The gradings are separated into I (contamination is less than 5 %), S (contamination between 5 and 20 %), C (contamination is between 20 and 80 %) and X (contamination is more than 80 %). Stars with a crowding index of X show in many cases absorption lines in their spectra. To account for the contamination, an OB star model from the LMC grid was used (Hainich et al. 2019) to reproduce the absorption lines. However, these models were not refined any further because they mainly served to account for the contamination and their parameters should not be seen as a very accurate determination. In most cases, the secondary component is probably not connected to the analysed Wolf-Rayet star and is just a star within the slit.

---

[1]Description from the "Revised LGGS UBVRI photometry of M31 and M33 stars" in VizieR
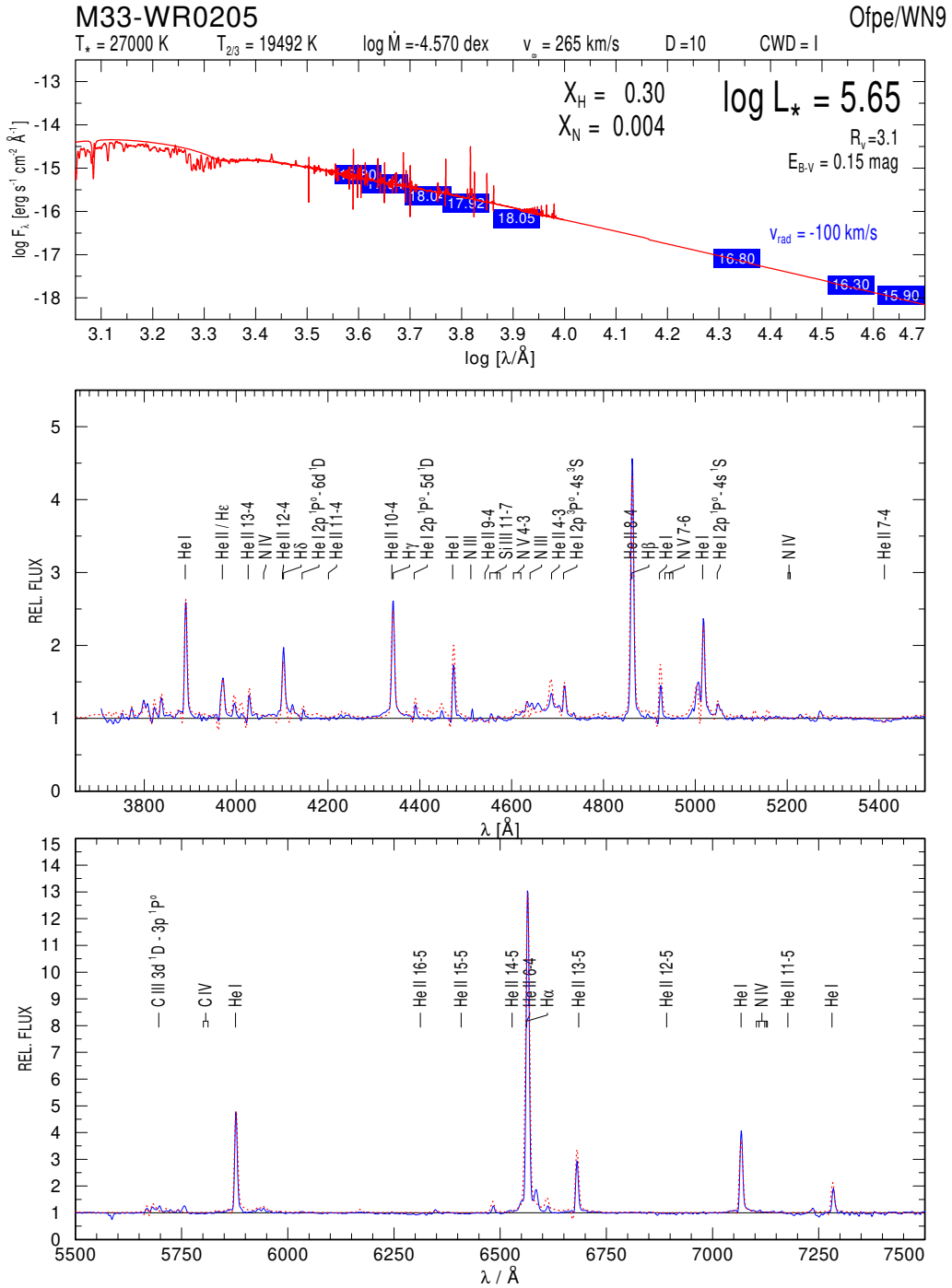
**Fig. 4.1** The final spectral fit for M33-WR205 (Romano's star). The solid blue line is the observed spectrum whereas the dotted red line represents the best fitting model.

# 5 The data

## 5.1 Identification of candidates

The identification of Wolf-Rayet star candidates is the first step needed on the road to obtain their spectra in a distant galaxy like M33. Since their first detection in 1867, different techniques have been used for their identification. The most effective method is the use of narrowband interference filter imaging, which exploits the prominent emission lines in the spectra of Wolf-Rayet stars. The region of interest is observed in three different filters. To identify WN stars, a narrowband filter is used centred at the prominent He II line at 4686 Å. For WC stars a different narrowband filter is used with a central wavelength of 4650 Å covering the prominent C III line in their spectra. The third filter covers a region where no emission lines are expected and is therefore denoted as continuum filter (CT), which is centred at 4750 Å. All filter have a bandwidth of around 50 Å. Wolf-Rayet star candidates are then identified by blinking between the WN and continuum or WC and continuum filter. Already with the naked eye candidates can be identified as demonstrated in Fig. 5.1.
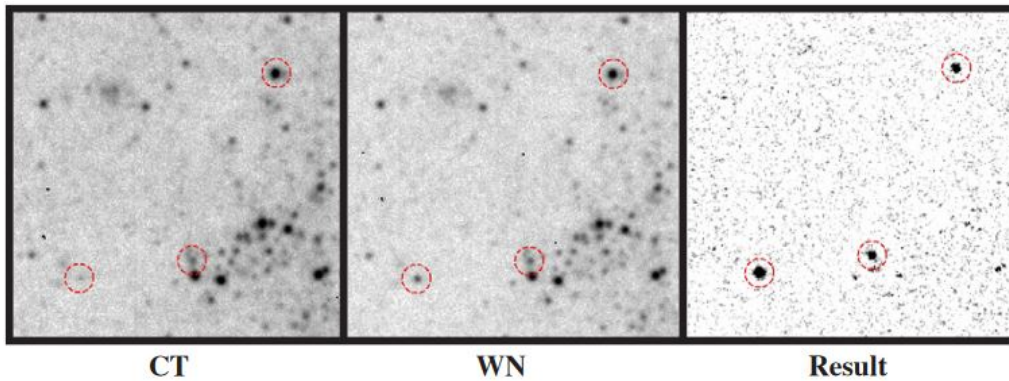


**Fig. 5.1** This image from Neugent & Massey (2011) demonstrates the image sub-
straction technique. Already by eye the Wolf-Rayet star in the lower left
corner can be identified by just comparing its brightness in the CT and
WN filter. The other two Wolf-Rayet stars show only up in the right image
which is the result when the CT image is substracted from the WN image.

Additionally, Neugent & Massey (2011) used an image substraction software that substracted the CT image from the WN and WC image respectively such that candidates are easier to identify.

The photometry was obtained on 2000 September 21, 23 and 24 with the Kitt Peak 4 m Mayall telescope. The galaxy was covered by three overlapping $36' \times 36'$ fields that extended out to a radius of around 8.5 kpc. The seeing conditions

varied between 1″.1 and 1″.5. Stars with a magnitude difference more negative than $-0.10$ mag and a significance level greater than $3\sigma$ were considered resulting in 1693 candidates. However, from a simple approximation that compares the absolute visual magnitudes of the LMC ($M_V = -18.5$) and M33 ($M_V = -18.9$) (van den Bergh 2000) around 190 Wolf-Rayet stars are then expected for M33. Thus, Neugent & Massey (2011) adjusted the criteria and kept only candidates with a significance level of more than $5\sigma$. This reduced the number of candidates to 382. This was further reduced by applying the mentioned image substraction software, which removed anomalies, and in the end 330 candidates were left. As a last note, it should be mentioned that the choice of the continuum filter has a small downside because stars with spectral type of M3 and later have a TiO molecular absorption band at 4760 Å making them appear brighter in the Wolf-Rayet filters such that some of them were listed as possible candidates.

## 5.2 The spectroscopic observations

To clearly confirm a candidate as Wolf-Rayet star, a spectrum has to be taken. This was done by Neugent & Massey (2011) with the 300 fiber-fed spectrometer Hectospec mounted on the 6.5 m MMT observatory upon Mount Hopkins in Arizona, USA. Observations were performed on 2010 October 9 and 11 using the 270 line mm$^{-1}$ grating blazed at 5000 Å resulting in a moderate resolution of around 6 Å (FWHM). The covered wavelength range starts at 3700 Å and reaches up to 9000 Å. Due to the configuration of the spectrograph it can happen that the spectrum beyond 7500 Å is contaminated by second-order blue light. Therefore, the spectra are only analysed up to this point. The instrument has a field of view of 1° in diameter allowing to observe extended objects like M33. The fibers have a diameter of 250 $\mu$m, which translates to 1″.5 on the sky (Fabricant et al. 2005). Assuming a distance of 830 kpc to M33, the 1″.5 corresponds to a region with a radius of around 6 pc within the galaxy. Moreover, the seeing conditions increase this value even further. Stars located in crowded regions or with bright sources in the line of sight are therefore effected by contamination.

## 5.3 The sample

The analysed sample consists of 74 Wolf-Rayet stars listed in Table 5.3. In the first column the identifier for the stars is given, which can be used to find the stars in the Simbad database[1]. Because of the length the identifier has, a new identification is introduced in the second column, which will be used in this work. The stars are numbered in ascending Right Ascension. A complete table including all 206 Wolf-Rayet stars from Neugent & Massey (2011) in M33 is given in the Appendix extended by the 5 stars that were additionally confirmed by Neugent & Massey (2014).

---

[1] http://simbad.u-strasbg.fr/

In the analysed sample, 64 of the 74 stars belong to the nitrogen sequence (WN), 9 have strong emissions of carbon and oxygen (WC) and one object is a transition type star WN/C. There is no known WO star in M33. Of the WN stars, 52 have a spectral type of WN5 or earlier such that they are considered as early type WN (WNE) stars. Consequently, there are 12 remaining stars of the nitrogen sequence with spectral type WN6 or later, which are called late type WN (WNL) stars. Thus, about two-thirds of the analysed Wolf-Rayet stars are WNE stars. The majority of these stars are of spectral subtype WN3 (27 stars) and WN4 (17 stars) giving us the opportunity to study the properties of these stars in detail.

Fig. 5.2 shows the position of all analysed Wolf-Rayet stars in the Triangulum galaxy (M33). The blue circles represent distances of 1, 2, 4, 6 and 8 kpc to the centre of the galaxy under the assumption that the galaxy has a distance of 830 kpc (Massey et al. 2007) and an inclination of its plane against the line of sight of 56° (Zaritsky et al. 1989). The red circles represent the WN stars and the blue circles the WC type stars. Only a few of the analysed stars are located inside the inner 2 kpc of the galaxy. A big fraction of the programme stars lie even more than 4 kpc away from the centre where the metallicity measured from blue supergiants is found to drop to a value of $Z = 0.0042 = 0.3 Z_\odot$ (U et al. 2009) making it a perfect environment to study Wolf-Rayet stars at low metallicities.

Due to the distance of M33, the spectra do not always show only the Wolf-Rayet star but also contributions from one or more sources. Since Wolf-Rayet stars belong to the young stellar population, they are often located in regions where star formation is still going on such that there are bright O and B type stars in their proximity. However, it could also be that the star is part of a real binary. Observations have shown that in our Galaxy the binary fraction of O type stars is more than 70% (Sana et al. 2012). Thus, it could be possible that nearly all O stars are formed as a component of a binary system. Therefore, it can be interesting to know if an additional source in the spectrum could be a binary companion of the Wolf-Rayet star. However, with only one spectrum it is not possible to draw a clear conclusion. Only a difference between the radial velocities could give a small hint but could also be attributed to the movement of the individual stars inside their cluster. Fortunately, Neugent & Massey (2014) reobserved many of the stars analysed here to estimate if the close binary frequency is metallicity dependent. Their analysis of Wolf-Rayet stars in M31 and M33 suggests that it is independent of metallicity. For M31 and M33 they found a binary frequency of about (45 ±12) %.

For Wolf-Rayet stars it is not trivial to search for a close companion especially when located in a galaxy like M33 where most of the Wolf-Rayet stars have a V band magnitude of 19 or even more. Additionally, the broad emission lines make it challenging to get a good estimate of the radial velocity, but on top of that, Wolf-Rayet stars show also variability in the strength of their lines as reported in e.g.Moffat et al. (1988).

**Table 5.1**  List of analysed stars

| Identifier | Abbreviation | Right ascension (J2000) | Declination (J2000) | Classification[a] |
| --- | --- | --- | --- | --- |
| | | (deg) | (deg) | |
| [NM2011] J013232.07+303522.4 | M33-WR001 | 023.13362 | +30.58956 | WN2 |
| [NM2011] J013232.13+303514.3 | M33-WR002 | 023.13387 | +30.58731 | WN3+neb |

**Table 5.1** continued.

| Identifier | Abbreviation | Right ascension (J2000) (deg) | Declination (J2000) (deg) | Classification[a] |
|---|---|---|---|---|
| [NM2011] J013233.24+302652.3 | M33-WR003 | 023.13850 | +30.44786 | WN2+abs |
| [NM2011] J013241.39+303416.2 | M33-WR007 | 023.17246 | +30.57117 | WN3h |
| [NM2011] J013245.41+303858.3 | M33-WR009 | 023.18921 | +30.64953 | Ofpe/WN9 |
| [NM2011] J013245.74+303854.4 | M33-WR010 | 023.19058 | +30.64844 | WN2+O7 |
| [NM2011] J013245.84+302019.5 | M33-WR011 | 023.19100 | +30.33875 | WC4+neb |
| [NM2011] J013256.35+303535.4 | M33-WR013 | 023.23479 | +30.59317 | WN6+abs |
| [NM2011] J013257.32+304418.1 | M33-WR015 | 023.23883 | +30.73836 | WN3+neb |
| [NM2011] J013257.88+303549.8 | M33-WR016 | 023.24117 | +30.59717 | WC4 |
| [NM2011] J013257.88+303549.8 | M33-WR016 | 023.24117 | +30.59717 | WC4 |
| [NM2011] J013302.28+301119.1 | M33-WR018 | 023.25950 | +30.18864 | WN3+neb |
| [NM2011] J013302.67+303120.1 | M33-WR019 | 023.26112 | +30.52225 | WN3 |
| [NM2011] J013303.21+303408.6 | M33-WR022 | 023.26337 | +30.56906 | WN6 |
| [NM2011] J013307.50+304258.5 | M33-WR026 | 023.28125 | +30.71625 | WN2 |
| [NM2011] J013307.68+303315.4 | M33-WR027 | 023.28200 | +30.55428 | WN4 |
| [NM2011] J013310.77+302734.2 | M33-WR032 | 023.29487 | +30.45950 | WN4 |
| [NM2011] J013311.29+303146.9 | M33-WR034 | 023.29704 | +30.52969 | WN4+B2I |
| [NM2011] J013312.44+303848.0 | M33-WR038 | 023.30183 | +30.64667 | WN3+neb |
| [NM2011] J013312.54+303900.3 | M33-WR039 | 023.30225 | +30.65008 | WN/C+abs |
| [NM2011] J013312.61+304531.0 | M33-WR040 | 023.30254 | +30.75861 | WN4 |
| [NM2011] J013314.56+305319.6 | M33-WR043 | 023.31067 | +30.88878 | WN3+neb |
| [NM2011] J013315.43+302300.1 | M33-WR046 | 023.31429 | +30.38336 | WN3 |
| [NM2011] J013315.55+304514.1 | M33-WR047 | 023.31479 | +30.75392 | WN3+neb |
| [NM2011] J013315.82+305644.8 | M33-WR048 | 023.31592 | +30.94578 | WN4.5+O |
| [NM2011] J013316.17+304751.8 | M33-WR049 | 023.31737 | +30.79772 | WC4 |
| [NM2011] J013324.04+305030.7 | M33-WR052 | 023.35017 | +30.84186 | WN8 |
| [NM2011] J013326.60+303550.3 | M33-WR053 | 023.36083 | +30.59731 | WN6 |
| [NM2011] J013330.36+303128.6 | M33-WR057 | 023.37650 | +30.52461 | WN4 |
| [NM2011] J013334.93+310042.8 | M33-WR070 | 023.39554 | +31.01189 | WN4 |
| [NM2011] J013335.23+310037.6 | M33-WR071 | 023.39679 | +31.01044 | WN3 |
| [NM2011] J013336.67+304302.6 | M33-WR074 | 023.40279 | +30.71739 | WN4+O |
| [NM2011] J013337.34+303527.1 | M33-WR075 | 023.40558 | +30.59086 | WN4 |
| [NM2011] J013337.81+302831.9 | M33-WR076 | 023.40754 | +30.47553 | WN4 |
| [NM2011] J013340.32+304600.9 | M33-WR088 | 023.41800 | +30.76692 | WN3+neb |
| [NM2011] J013343.33+304450.5 | M33-WR096 | 023.43054 | +30.74736 | WN4 |
| [NM2011] J013350.71+305636.7 | M33-WR115 | 023.46129 | +30.94353 | WN3+neb |
| [NM2011] J013352.43+304351.7 | M33-WR119 | 023.46846 | +30.73103 | WN8 |
| [NM2011] J013355.94+302732.1 | M33-WR133 | 023.48308 | +30.45892 | WN3+B2I |
| [NM2011] J013356.33+303420.8 | M33-WR136 | 023.48471 | +30.57244 | WN3 |
| [NM2011] J013359.60+303435.4 | M33-WR143 | 023.49833 | +30.57650 | WN5 |
| [NM2011] J013359.79+305150.0 | M33-WR144 | 023.49912 | +30.86389 | WN2+O9I |
| [NM2011] J013402.93+305126.2 | M33-WR151 | 023.51221 | +30.85728 | WN3+neb |
| [NM2011] J013406.80+304727.0 | M33-WR152 | 023.52833 | +30.79083 | WN7+neb |
| [NM2011] J013408.23+305234.2 | M33-WR154 | 023.53429 | +30.87617 | WN4 |
| [NM2011] J013408.90+304732.0 | M33-WR155 | 023.53708 | +30.79222 | WN3 |
| [NM2011] J013410.72+305240.7 | M33-WR157 | 023.54467 | +30.87797 | WN3 |

**Table 5.1** continued.

| Identifier | Abbreviation | Right ascension (J2000) (deg) | Declination (J2000) (deg) | Classification[a] |
|---|---|---|---|---|
| [NM2011] J013411.14+304637.5 | M33-WR158 | 023.54642 | +30.77708 | WC4 |
| [NM2011] J013415.85+305522.9 | M33-WR162 | 023.56604 | +30.92303 | WN4 |
| [NM2011] J013416.07+303642.1 | M33-WR163 | 023.56696 | +30.61169 | Ofpe/WN9 |
| [NM2011] J013416.28+303646.4 | M33-WR164 | 023.56783 | +30.61289 | WC6+neb |
| [NM2011] J013418.37+303837.0 | M33-WR168 | 023.57654 | +30.64361 | Ofpe/WN9 |
| [NM2011] J013419.16+303127.7 | M33-WR170 | 023.57983 | +30.52436 | WN3 |
| [NM2011] J013419.58+303801.5 | M33-WR171 | 023.58158 | +30.63375 | WN7 |
| [NM2011] J013419.68+303343.0 | M33-WR172 | 023.58200 | +30.56194 | WN3-4+neb |
| [NM2011] J013421.21+303758.2 | M33-WR173 | 023.58837 | +30.63283 | WN5+neb |
| [NM2011] J013421.97+303314.3 | M33-WR174 | 023.59154 | +30.55397 | WN4 |
| [NM2011] J013422.37+303313.7 | M33-WR175 | 023.59321 | +30.55381 | WN3+abs |
| [NM2011] J013423.02+304650.0 | M33-WR177 | 023.59592 | +30.78056 | WN4 |
| [NM2011] J013425.11+301950.3 | M33-WR178 | 023.60462 | +30.33064 | WN3 |
| [NM2011] J013426.96+305256.7 | M33-WR179 | 023.61233 | +30.88242 | WNN4.5 |
| [NM2011] J013427.30+305229.2 | M33-WR180 | 023.61375 | +30.87478 | WN3+neb |
| [NM2011] J013429.56+304145.0 | M33-WR181 | 023.62317 | +30.69583 | WC4 |
| [NM2011] J013431.45+305716.7 | M33-WR182 | 023.63104 | +30.95464 | WN3+neb |
| [NM2011] J013433.22+310019.3 | M33-WR191 | 023.63842 | +31.00536 | WN7+neb |
| [NM2011] J013433.82+304656.3 | M33-WR193 | 023.64092 | +30.78231 | WC4 |
| [NM2011] J013438.18+304953.2 | M33-WR195 | 023.65908 | +30.83144 | WN5 |
| [NM2011] J013440.42+304321.9 | M33-WR197 | 023.66842 | +30.72275 | WN4+neb |
| [NM2011] J013443.51+304919.4 | M33-WR198 | 023.68129 | +30.82206 | WN4 |
| [NM2011] J013444.28+303757.2 | M33-WR199 | 023.68450 | +30.63256 | WN3 |
| [NM2011] J013444.61+304445.4 | M33-WR200 | 023.68587 | +30.74594 | WC5-6 |
| [NM2011] J013447.32+310748.8 | M33-WR201 | 023.69717 | +31.13022 | WN3 |
| [NM2011] J013507.24+304500.9 | M33-WR204 | 023.78017 | +30.75025 | WC5 |
| [NM2011] J013509.73+304157.3 | M33-WR205 | 023.79054 | +30.69925 | Ofpe/WN9 |
| [NM2011] J013510.27+304522.9 | M33-WR206 | 023.79279 | +30.75636 | WN2pec |

**Notes.** [a] classification from Neugent & Massey (2011)
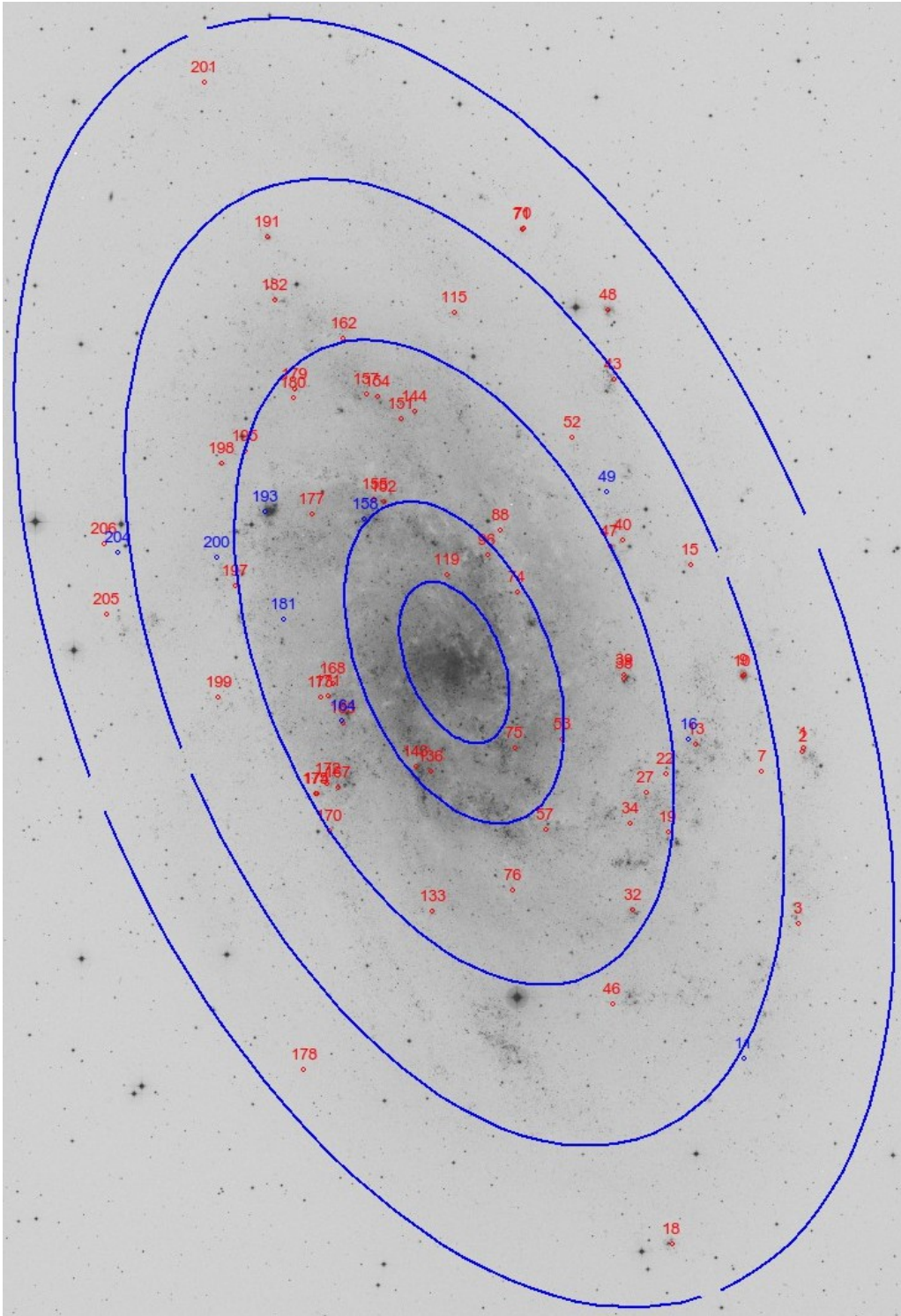
**Fig. 5.2** The image shows the position of the stars in M33 that were analysed in this work. The blue circles represent distances of 1, 2, 4, 6 and 8 kpc to the centre of M33 Red: WN stars; Blue: WC stars

# 6 Results

## 6.1 Stellar analysis: Composite spectrum or single star - M33-WR040 as test case

M33-WR040 is classified as WN4 where the spectrum is shown in Fig. 8.23. In addition to the emission lines, it exhibits small absorption features. As a test case, a single star model and a composite star fit are created. As can be seen in Fig. 8.23 some of the absorption features can be replicated by the single star fit. From this a temperature of 55 kK and a luminosity of $\log(L/L_\odot) = 5.75$ are derived.

The composite star fit is shown in Fig. 8.24 where the companion is best fitted using a B star model from the PoWR LMC grid with a temperature of 26 kK. However, even in this case not all absorption lines are perfectly reproduced. The Wolf-Rayet model has a temperature of 71 kK. This value is much higher than that of the single star model demonstrating that it can sometimes be very difficult to infer accurate stellar parameters for some of the stars. Especially the derived luminosities and mass-loss rates are affected. To reproduce the observed emission line spectrum in these fits, a higher mass-loss rate is needed on average compared to the single star fits. Since only one spectrum is available in this work, no statement can be made about a possible binary nature of the stars. If the Wolf-Rayet star is part of a cluster, it is possible that other cluster members contributed light to the spectrum, which means that there can be more than one additional source. Thus, in some cases the employed O or B star model can just be an approximation to account for the contamination. On top of that, another difficulty can be seen in the spectrum of M33-WR040. Most spectra show nebula emissions of hydrogen, which can partly or completely fill some of the absorption features reducing the amount of lines that can be reproduced. However, it is not always obvious whether an absorption line is filled due to a nebula emission because a possibly underlying Wolf-Rayet emission could have the same effect. The H$\epsilon$ absorption in the spectrum of M33-WR040 is deformed in its line core and there are at least three different possible explanations. First, it could be filled by a nebula hydrogen emission line because there are other lines visible in the spectrum. Second, it could be due to an emission of the Wolf-Rayet star. Third, it is just the result of a low signal-to-noise, which usually decreases at the blue end of the spectrum. Due to all these difficulties that can arise, stars were, in doubt, analysed as single stars. Only in cases where no appropriate single star fit could be found or where the contamination is obvious because the relative strength of the emission lines is very low, a composite fit was applied. Furthermore, it is not the goal of this work to accurately describe the properties of the secondary source. Thus, these results should be taken with care. However, that does not mean that an accurate analysis of a composite spectrum is impossible. Shenar et al. (2018)

were able to decouple a system containing four different sources but in contrast to this work, they could rely on a much better data base. For the future it might be interesting to study some of the objects flagged as composite spectra in more detail to see how good my estimates are and to get an understanding which spectral features are suited to describe or approximate the secondary component. With the advance of telescopes, we will be able to observe Wolf-Rayet stars at even further distances where the issue of crowding becomes even more pronounced.

## 6.2 Stellar parameters

With the help of the Potsdam Wolf-Rayet (PoWR) stellar atmosphere code, the spectra were analysed to derive the fundamental parameters of the stars. The results are listed for each star in Table 6.2.3. In Sect. 8.1 of the Appendix every star is discussed individually and the spectral fits are provided. The position of all analysed stars in the $\log T_*$-$\log R_t$ plane is shown in Fig. 6.1. Because of the large fraction of early WN type stars, in particular stars of subtype WN3 and WN4, they are clustering in the diagram. With the exception of a few stars, the subtypes WN3 and WN4 are well separated. In most cases, WN3 stars have higher temperatures compared to stars of subtype WN4. As can be seen in the diagram, with increasing temperature the transformed radius decreases. The hottest stars are located in a region of parameter degeneracy where the stars can be shifted parallel to the grey lines without changing the spectrum significantly. For very dense winds, $R_t$ and $T_*$ are not independent parameters determining the spectrum anymore because all radiation we receive, including the continuum, is formed in wind layers that already move with nearly the terminal wind speed. Because the grey lines are nearly aligned with $R_t \propto T_*^{-2}$, the spectrum depends only on the mass-loss rate for given luminosity, terminal wind speed and clumping factor. Thus, the grey lines represent regions of constant $R_t T_*^2$ (Hamann et al. 2003).

The late type WN stars are located in the left part of the diagram due to their lower temperatures. The subtypes WN6 and WN7 follow the trend that smaller temperatures are accompanied by bigger transformed radii. However, stars with spectral types WN8 or WN9/Of are the coolest stars in this sample but their transformed radii decrease again. This behaviour occurs also for the Galatic WN stars (Hamann et al. 2006) and for the LMC WN stars (Hainich et al. 2014). The turnoff point is located at spectral type WN7. This could point to an LBV like nature for these stars although it is expected to occur at higher luminosities. However, Ramachandran et al. (2019) conclude from their analysis of OB stars in the SMC that the Humphreys-Davidson limit shifts to lower luminosities for lower metallicities. For the more massive stars, they suggest a quasi chemically homogeneous evolution. This could be the reason why there are no extremely luminous WN late stars with luminosities exceeding $\log L/L_\odot = 6.0$ in the analysed sample here, which is in strong contrast to what is observed in our Galaxy where many WNL stars have luminosities close to or even higher than $\log L/L_\odot = 6.0.$. For M33-WR205, also known as Romano's star, it is known that the star was very active during the last decades (Maryeva et al. 2019). If the more massive stars evolve quasi chemically
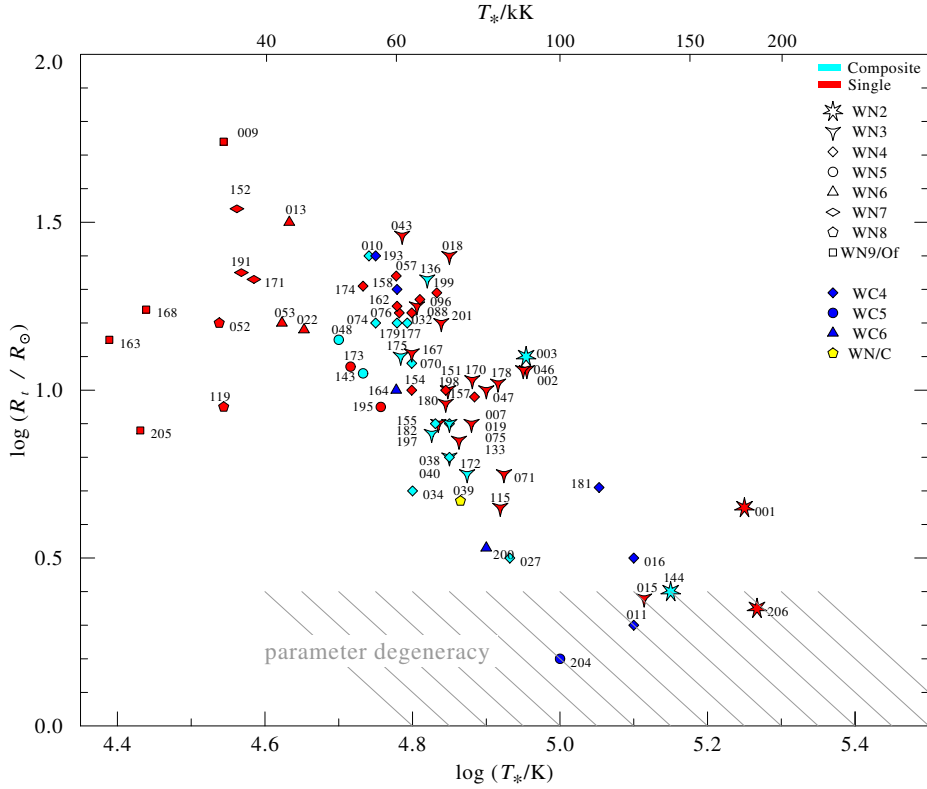
**Fig. 6.1** The diagram shows the position of all analysed Wolf-Rayet stars in the $\log R_{\mathrm{t}}$-$\log T_*$ plane. The WN stars that were analysed using a two component fit are plotted in turquoise, while the red symbols refer to the stars that were analysed as single stars. The grey lines at the bottom represent the region where the parameter space is degenerate. There the winds are very thick and the stars can be shifted parallel to the lines without changing the spectrum significantly.

homogeneous, than they should directly evolve to early type WN stars showing hydrogen in their spectra. However, these stars are not observed in this sample such that the question regarding the stellar evolution remains open.

The WC stars are spread across the diagram. According to Sander et al. (2012), there is a tight correlation between the subtypes and temperature. This behaviour is not observed for the stars displayed in Fig. 6.1. Compared to their work, this sample includes only a few WC stars and many of the spectra suffer from strong contamination making it challenging to find an accurate fit. An extreme case is the putative WC4 M33-WR193 in Fig. 8.70 showing very strong nebula emissions but only a weak Wolf-Rayet spectrum. Thus, in this case the derived parameters are questionable and should be treated with caution.

For all stars, the luminosity was derived by fitting the model to optical U, B, V, R, I observations from Neugent & Massey (2011) in the SED plot. For some stars GALEX UV measurements were available but these observations often include many different contributions aside the Wolf-Rayet star due to the low spatial resolution of 4.2″ in the FUV and 5.3″ in the NUV band (Morrissey et al. 2007). Additionally, the stars were cross matched with the *Spitzer* infrared catalogue from Khan et al.

(2015), which lists nearly 79 000 point sources in M33. In their analysis, they used an extraction aperture of 2.4″. Thus, UV, optical and infrared photometry is available in an ideal case such that luminosity and reddening can be determined very accurately. In reality, most stars have only optical photometry available limiting the accuracy of the estimate of the colour excess $E(B-V)$, which has a direct influence on the determination of the luminosity. Nevertheless, for the majority of the stars the luminosity should be accurate to around $\pm 0.2$ dex. Using the derived luminosities, the masses of the WN stars can be constructed by applying the mass-luminosity relation for chemically homogeneous stars from Gräfener et al. (2011). Their Eq. 9 is used for stars showing hydrogen in their spectra, while Eq. 10 is used for the hydrogen free stars. It should be pointed out again that these relations are for chemically homogeneous stars, but if a WN star is showing hydrogen in its spectrum, it does not necessarily mean that it is still hydrogen burning in the core. Thus, the derived masses are upper limits. For WC stars the relation from Langer (1989) is used.

For the WN stars, it should be noted that the observed nitrogen fraction is, in general, higher than expected. Since the metallicity of the stars is in the range between an SMC and LMC like level, the nitrogen fraction should be at maximum half the solar value of the sum of carbon, oxygen and nitrogen as most of the carbon and oxygen are transformed into nitrogen in the CNO cycle. This should lead to an observed nitrogen mass fraction of about 0.004 assuming a metallicity of $Z = 0.5Z_\odot \approx 0.007$ (Hainich et al. 2014). Nevertheless, the observed value is, in general, higher even when accounting for the uncertainty which is about 50%. A possible explanation could be that some of the produced carbon during core helium burning was mixed into a hydrogen burning shell where it was transformed into nitrogen before the hydrogen envelope was ejected from the star. If the stars have a radiative envelope, there should not be a strong mixing process which should result in an overall smaller nitrogen abundance for late type WN stars as these still have not lost their hydrogen envelope. Although some of the late type WN stars here show indeed a smaller nitrogen abundance, the size of the sample is not big enough to confirm this hypothesis. This would require a much more detailed analysis, which is beyond the scope of this work. As a last note it should be mentioned that Hainich et al. (2014) also found that the nitrogen abundance is enhanced for some of the WN stars in the LMC.

## 6.2.1 Mass-loss rates

The mass-loss rate of massive stars is one of the key parameters to understand their evolutionary way. During their evolution they can lose more than 50 % of their initial mass (Crowther 2007). For Wolf-Rayet stars it determines by how much they enrich their surroundings with products from hydrogen or even helium burning. Furthermore, it dictates spectral appearance of the supernova if the star is not just directly collapsing to a black hole (Heger et al. 2003). However, as already explained in Sect. 3.3 the mass-loss rate has a strong metallicity dependence, which is not yet completely understood. Therefore, it is required to observe and analyse massive stars in very metal poor regions.

The empirical mass-loss rates are given in Table 6.2.3. Because Wolf-Rayet winds are clumped (Moffat et al. 1988), the mass-loss rate as derived from recombination lines scales with the square root of the clumping factor $D$ (Hamann & Koesterke 1998). The depth dependent clumping factor was chosen such that it reaches $D = 10$ when the terminal wind speed is achieved. Nevertheless, it can differ for each star individually. Previous analyses from electron-scattering line wings found that clumping factors between four and ten are usual (Liermann & Hamann 2008). For early type WN stars, models with depth dependent clumping do not differ significantly compared to models with a fixed clumping parameter. Only the N IV feature at around $7110\,\text{Å}$ is slightly weaker compared to models without depth dependent clumping. In contrast, for late type WN stars it has a strong influence on the appearance of the spectrum. Additionally, Table 6.2.3 includes the wind efficiency $\eta$, which the ratio between the wind momentum $\dot{M}v_\infty$ and the momentum of the radiation field defined as $L/c$:

$$\eta = \frac{\dot{M}vc}{L} \tag{6.1}$$

This quantity describes how often a photon is typically scattered in the wind. Thus, for values exceeding unity photons are scattered on average by this value before they leave the wind. Since the wind efficiency depends on the mass-loss rate, it depends also on metallicity. For early type WN stars, an average value of 5.9 was found for the Galactic sample (Hamann et al. 2006), whereas it is only 2.1 in the LMC (Hainich et al. 2014). For the SMC stars it is even below unity and has a value of 0.3 (Hainich et al. 2015). In this analysis, stars modelled using a composite spectrum fit are excluded in the calculation of the average value because many of them have outstandingly high wind efficiencies compared to the rest of the early type WN stars, which is most likely due to underestimated luminosities. When calculating the average wind efficiencies for the early type WN stars, one obtains a value of 1.0, which is below the LMC but higher than SMC value. Due to some outliers, the smallest value is 0.2 while the highest is 3.2, it might be more appropriate to use the median resulting in the slightly smaller value of 0.8. In contrast, when only calculating the average value for the stars analysed using a composite spectrum this leads to a much higher average of 1.9 and median of 1.4.

## 6.2.2 Error estimations

Some error sources were already briefly touched on in previous sections but here they will be discussed in more detail. Beginning with the luminosity, there is always the uncertainty of the distance for Galactic sources. Over the last years, the situation improved because there are now exact trigonometric parallaxes available measured by the Gaia satellite. In contrast, the distance uncertainty for M33 is rather small and therefore the resulting uncertainty is small compared to other error sources. Thus, it is neglected here. The luminosity is determined by fitting the observed SED. For the majority of the stars, there is only optical photometry available where some of the filters include strong emission lines. Additionally, it is challenging to estimate an accurate value for the extinction. Thus, in total an uncertainty of $\pm 0.2\,\text{dex}$ is assumed for the luminosity. Nevertheless, this is only the error when fitting the SED,

but in addition to that there is also another source where the distance of M33 is indirectly playing a role. Due to its distance of around 830 kpc, it is most likely that not only the light of the Wolf-Rayet component was measured, thus the luminosity is slightly overestimated. Stars located in clusters are probably more affected as isolated sources but statistically seen, the luminosities are overestimated.

Mass-loss rate and temperature are obtained by fitting the model to the observed spectrum. The resulting temperature has an uncertainty of $\pm 1000$ K for the coolest stars and up to $\pm 5000$ K for the hottest stars. This is also affecting the luminosity because the bolometric correction is also temperature dependent. The mass-loss rate is usually determined via the transformed radius, which can be determined to an accuracy of $\pm 0.05$ dex, but it is also coupled to the luminosity uncertainty because $\log \dot{M} \propto 0.75 \cdot \log L$. In some cases, lines of the Balmer and Pickering series are clearly visible in the spectra and these were then analysed using a two component fit when it was clear that these are created by the second source. However, not in all spectra a contamination might be obvious but it can still cause a dampening of the lines. In total, this leads statistically to an underestimation of the mass-loss rate due to the seemingly weaker emissions.

So far only the errors for the single star analyses were discussed. For the two component fits, it is much more difficult to provide an error estimate. A problem that was already mentioned is the underestimation of the luminosity of the Wolf-Rayet component, which results in an overestimation of the mass-loss rate. A clear indicator is the overall higher wind efficiency compared to the single star fits. However, this is not due to the quality of the fits as can be seen by taking a look at the plot for M33-WR034 in Fig. 8.19. The strength of the OB star component is determined by fitting the Balmer and He II Pickering lines in the blue part of the spectrum but in many cases the signal-to-noise ratio declines towards the blue end. A good example is M33-WR172 in Fig. 8.60 which was only fitted using two components because it has a crowding index of X and the emission lines are clearly diluted. There the signal is so noisy that absorption features are not unambiguously identifiable and the fit of the secondary is debatable. However, in the case of M33-WR034 the quality of the fit looks reasonable. Only the H$\beta$ line is clearly overestimated demonstrating another issue. Nearly all spectra show nebula emission lines of hydrogen. Those can partly or completely fill some of the absorption lines making it even harder to find an appropriate fit for the second component. The H$\beta$ line in the spectrum of M33-WR034 might be affected by a nebula emission because it also has an H$\alpha$ emission on top of the stellar line. Additionally, it cannot be ruled out that more than one additional source is contributing to the spectrum. If the star is embedded in a cluster, there can be in principle more than just one star in the vicinity of the target. However, different hot stellar components are in this case not recognisable due to the low resolution and missing information like magnesium or silicon lines. In general, more spectral information like UV observations or a better resolution with higher signal-to-noise ratio would help to find a unique solution. Thus, the results from these spectra should be viewed carefully and in many cases the given luminosity is rather a lower limit.

Abundances are determined via an iterative process as described in Sect. 4.2. The spectra of WN stars display mostly two or even three different ionisation stages of nitrogen (N III & IV for WNL and N IV & V for WNE). Nevertheless, often the

prediction of the N v feature at around 4604 Å is weaker than observed for early type WN stars. This could point to an underestimated temperature but it could also be a problem in the normalisation because it is difficult to define the continuum due to the wings of the He II line at 4686 Å. Thus, the remaining nitrogen lines received a higher priority, which are the N IV lines at 4060 and 7103 Å and the N v line at 4934 Å but the N IV lines react more sensitive to mass-loss rate, temperature and a change of the nitrogen abundance while changing the abundance is not affecting the N v line that much in comparison. For this line, the temperature has a stronger impact. Thus, the derived abundances are more likely upper limits.

### 6.2.3 Hertzsprung-Russell diagram

All analysed stars of this work are displayed in the Hertzsprung-Russell diagram in Fig. 6.2. The majority of them are located between the Zero Age Main Sequence (ZAMS) and the He-ZAMS. In contrast to analyses from the LMC and Galactic WN stars, there is only one extremely luminous WR star in the sample, which is most likely located in a crowded region where other sources contribute a lot of light. There are a few stars with luminosities slightly above $\log L/L_\odot = 6.0$ but these also have conspicuous spectra. Since only a subsample of all known Wolf-Rayet stars in M33 is covered in this analysis, it cannot be ruled out that there are extremely luminous Wolf-Rayet stars located elsewhere. Nearly the whole central region of the galaxy is not covered in this work.

Compared to the analyses of the LMC WN stars, most of the WN3 and WN4 stars are located within a small temperature range between 60 and 80 kK. With M33-WR015 there is only one outlier where the temperature exceeds 100 kK. In the LMC even exist some WN4 stars whith temperature above 100 kK (Hainich et al. 2014). For some of these stars, round line profiles are reported but this effect is also observed for some of the cooler stars. However, M33-WR015 is not showing round line profiles. Nevertheless, there are some stars showing this kind of line shape in their spectrum but their temperatures are comparable to the other WN3 and WN4 stars. The hottest object in this work is the peculiar WN2 star M33-WR206, which has a strong O VI in its spectrum. Its temperature of nearly 180 kK is comparable to the temperature of the two Galactic WO stars analysed in Sander et al. (2012).

The majority of the analysed WC stars are classified as WC4, which is the hottest spectral type in that class. Thus, most of them are located around the He-ZAMS. In contrast to the analysed WN stars, many of the WC star spectra show clear indications of contamination but due to the absence of absorption lines from other hot stellar sources it is difficult to estimate the impact. Only for M33-WR016 a composite spectrum could be identified. Thus, the derived parameters for the WC stars have in general higher uncertainties.

All of the low luminosity stars have composite spectra and it was already discussed that their luminosity is most likely underestimated. The faintest stars, which were analysed as single stars, have a luminosity of $\log L = 5.3$. This is similar to the Wolf-Rayet stars in the LMC (Hainich et al. 2014). In contrast, there are a few examples in our own Galaxy having luminosities below this value (Hamann et al. 2019). This could be due to several reasons like distance uncertainties or metallicity
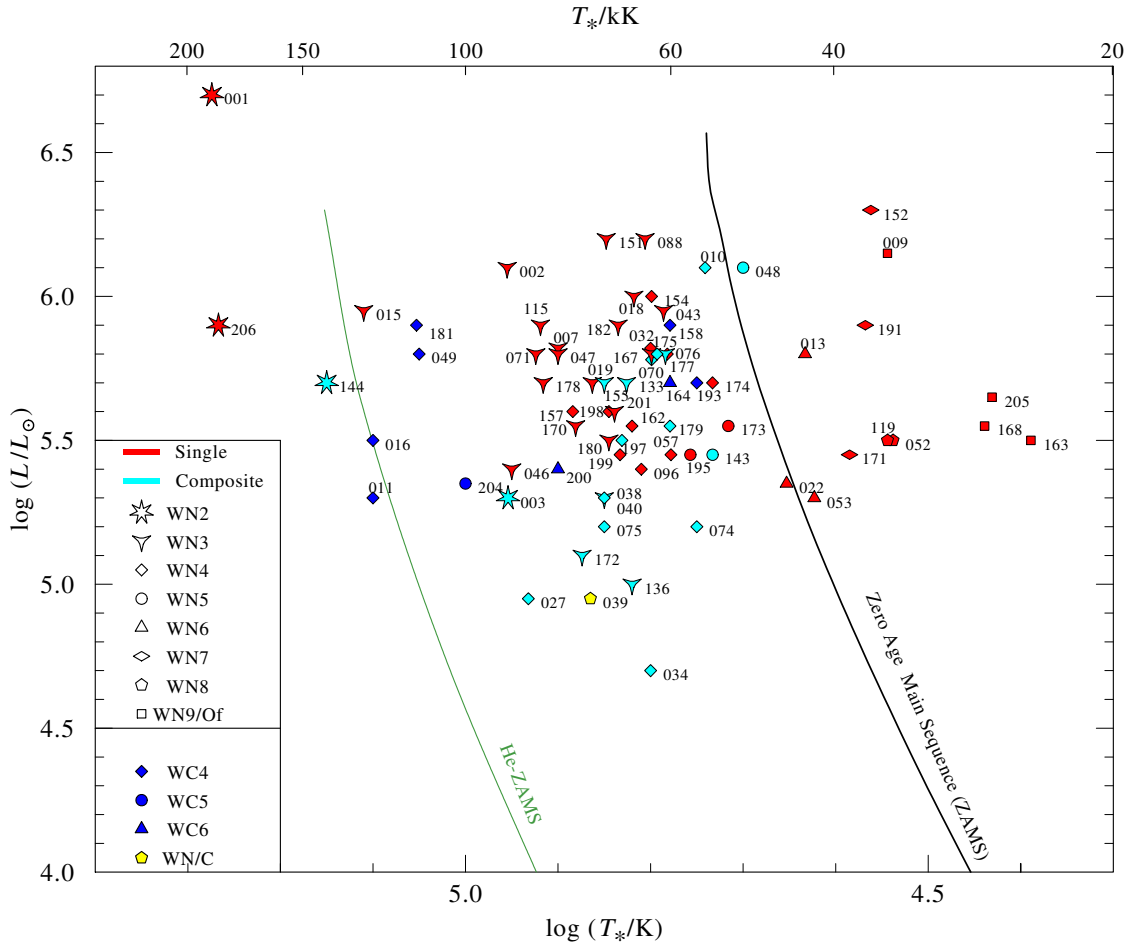
**Fig. 6.2** Hertzsprung-Russell diagram including all analysed stars. The WN are divided into stars that were analysed with a single star fit (red) and into the ones where a composite spectrum was applied (turquoise). The WC stars are shown in blue and the transition type WN/C in yeollow.Most of the WNE are located between ZAMS and He-ZAMS while the WNL are located at cooler temperatures on the right side of the ZAMS.

effects. These stars are probably the result of binary evolution. Interestingly, Shenar et al. (2019) found for the binary Wolf-Rayet stars in the LMC also a minimum luminosity of $\log L = 5.2$, which is very similar to the observed limit from the single star analyses from Hainich et al. (2014). In Shenar et al. (2019) the authors had a much better data base including several epochs and UV spectra. This opens the question how Wolf-Rayet stars are formed in metal poor regions and what the impact of binarity is. These topics will be discussed in the following section.

**Table 6.1** Parameters of the Wolf-Rayet stars in M33

| M33-WR | Subtype | $T_*$ [kK] | $M_{\mathrm{spec}}$ [$M_\odot$] | $\log L$ [$L_\odot$] | $\log \dot{M}$ [$M_\odot$/yr] | $\log R_{\mathrm{t}}$ [$R_\odot$] | $R_*$ [$R_\odot$] | $\eta$ | $M_{\mathrm{V}}$ [mag] |
|---|---|---|---|---|---|---|---|---|---|
| 001 | WN2 | 178 | 103.2 | 6.70 | -5.03 | 0.65 | 2.4 | 0.2 | -4.3 |
| 002 | WN3 | 90 | 37.1 | 6.1 | -5.29 | 1.06 | 4.6 | 0.3 | -4.6 |
| 003 | WN2+abs | 90 | 12.02 | 5.30 | -5.95 | 1.10 | 1.8 | 0.4 | -2.8 |
| 007 | WN3h | 76 | 29.9 | 5.65 | -5.21 | 0.90 | 3.9 | 0.9 | -4.2 |
| 009 | Ofpe/WN9 | 35 | 75.2 | 6.15 | -5.24 | 1.74 | 32.4 | 0.2 | -7.4 |
| 010 | WN4+O7[b] | 55 | 55.0 | 6.1 | -5.08 | 1.40 | 12.3 | 0.6 | -7.0 |
| 011 | WC4+neb | 126 | 11.6 | 5.3 | -5.09 | 0.30 | 0.9 | 4.0 | -4.7 |
| 013 | WN6+abs | 43 | 41.6 | 5.80 | -5.41 | 1.50 | 14.4 | 0.3 | -6.0 |
| 015 | WN3+neb | 130 | 29.5 | 5.95 | -4.81 | 0.38 | 1.9 | 1.5 | -3.9 |
| 016 | WC4 | 89 | 11.6 | 5.30 | -4.79 | 0.40 | 1.2 | 4.0 | -5.4 |
| 018 | WN3+neb | 66 | 31.8 | 6.0 | -5.46 | 1.40 | 7.7 | 0.3 | -5.5 |
| 019 | WN3 | 73 | 20.6 | 5.70 | -4.90 | 0.85 | 4.4 | 2.5 | -4.2 |
| 022 | WN6 | 45 | 20.7 | 5.35 | -5.13 | 1.18 | 7.8 | 1.6 | -4.1 |
| 027 | WN4 | 85 | 7.8 | 4.95 | -5.33 | 0.50 | 1.4 | 3.3 | -3.6 |
| 032 | WN4 | 63 | 23.7 | 5.80 | -5.30 | 1.23 | 6.7 | 0.6 | -4.0 |
| 034 | WN4+B2I | 63 | 5.8 | 4.70 | -5.33 | 0.70 | 1.9 | 7.3 | -6.2 |
| 038 | WN3+neb | 71 | 12.0 | 5.30 | -5.18 | 0.8 | 3.0 | 2.6 | -5.8 |
| 039 | WN/C+abs | 73 | 7.8 | 4.95 | -5.30 | 0.67 | 1.9 | 4.5 | -5.2 |
| 040 | WN4 | 55 | 22.1 | 5.75 | -5.31 | 1.33 | 8.3 | 0.7 | -4.5 |
| 043 | WN3+neb | 61 | 29.5 | 5.95 | -5.49 | 1.46 | 8.4 | 0.3 | -5.1 |
| 046 | WN3 | 89 | 13.7 | 5.40 | -5.80 | 1.06 | 2.1 | 0.5 | -2.9 |
| 047 | WN3+neb | 79 | 23.7 | 5.80 | -5.25 | 1.0 | 4.2 | 0.7 | -3.8 |
| 048 | WN4.5+O | 50 | 37.1 | 6.10 | -4.56 | 1.15 | 14.9 | 2.1 | -8.2 |
| 049 | WC4 | 66 | 22. | 5.8 | -4.92 | 0.40 | 6.1 | 1.9 | -4.5 |
| 052 | WN8 | 34.5 | 30.8 | 5.50 | -5.12 | 1.20 | 15.8 | 0.7 | -5.9 |
| 053 | WN6 | 42 | 17.9 | 5.30 | -5.35 | 1.20 | 8.5 | 1.0 | -4.9 |
| 057 | WN4 | 60 | 14.6 | 5.45 | -5.67 | 1.34 | 4.9 | 0.6 | -4.0 |
| 070 | WN4 | 63 | 23.7 | 5.80 | -5.13 | 1.08 | 6.7 | 0.8 | -5.9 |
| 071 | WN3 | 84 | 23.7 | 5.80 | -4.98 | 0.75 | 3.8 | 1.2 | -4.1 |
| 074 | WN4+O | 56 | 10.6 | 5.20 | -5.56 | 1.20 | 4.2 | 1.4 | -5.7 |
| 075 | WN4 | 71 | 10.6 | 5.20 | -5.41 | 0.90 | 2.7 | 1.9 | -3.9 |
| 076 | WN4 | 61 | 23.7 | 5.80 | -5.25 | 1.23 | 7.2 | 0.7 | -3.6 |
| 088 | WN3+neb | 64 | 43.4 | 6.20 | -4.86 | 1.25 | 10.3 | 1.1 | -3.2 |
| 096 | WN4 | 65 | 13.7 | 5.40 | -5.70 | 1.27 | 4.0 | 0.6 | -3.9 |
| 115 | WN3+neb | 81 | 23.7 | 5.80 | -4.60 | 0.71 | 4.3 | 3.2 | -4.9 |
| 119 | WN8 | 35 | 30.8 | 5.50 | -4.85 | 0.95 | 15.3 | 1.1 | -5.9 |
| 133 | WN3+B2I | 67 | 20.6 | 5.70 | -4.92 | 0.87 | 5.3 | 1.9 | -4.4 |

**Table 6.1** continued.

| M33-WR | Subtype | $T_*$ [kK] | $M_{\mathrm{spec}}$ [$M_\odot$] | $\log L$ [$L_\odot$] | $\log \dot{M}$ [$M_\odot$/yr] | $\log R_{\mathrm{t}}$ [$R_\odot$] | $R_*$ [$R_\odot$] | $\eta$ | $M_{\mathrm{V}}$ [mag] |
|---|---|---|---|---|---|---|---|---|---|
| 136 | WN3 | 66 | 8.3 | 5.00 | -6.08 | 1.33 | 2.4 | 0.7 | -4.1 |
| 143 | WN5 | 54 | 14.6 | 5.45 | -5.19 | 1.05 | 6.1 | 1.5 | -5.6 |
| 144 | WN2+O9I | 141 | 20.6 | 5.70 | -5.18 | 0.40 | 1.2 | 1.0 | -6.1 |
| 151 | WN3+neb | 70 | 43.4 | 6.20 | -4.64 | 1.00 | 8.5 | 1.6 | -5.7 |
| 152 | WN7+neb | 36 | 83.7 | 6.30 | -4.88 | 1.54 | 35.5 | 0.3 | -7.8 |
| 154 | WN4 | 63 | 31.8 | 6.00 | -4.81 | 1.00 | 8.4 | 1.2 | -4.7 |
| 155 | WN3 | 71 | 20.6 | 5.70 | -4.94 | 0.90 | 4.7 | 2.3 | -3.4 |
| 157 | WN3 | 77 | 17.9 | 5.60 | -5.33 | 0.98 | 3.6 | 0.9 | -3.7 |
| 158 | WC4 | 60 | 26.9 | 5.90 | -5.11 | 1.30 | 1.9 | 2.7 | -4.2 |
| 162 | WN4 | 66 | 16.7 | 5.55 | -5.58 | 1.25 | 4.6 | 0.6 | -4.2 |
| 163 | Ofpe/WN9 | 24.5 | 32.9 | 5.50 | -4.95 | 1.15 | 31.3 | 0.5 | -7.0 |
| 164 | WC6+neb | 60 | 19.8 | 5.70 | -4.87 | 1.00 | 6.5 | 2.6 | -5.0 |
| 167 | WN3+neb | 63 | 23.7 | 5.80 | -5.15 | 1.11 | 6.7 | 0.8 | -4.7 |
| 168 | Ofpe/WN9 | 27.5 | 32.7 | 5.55 | -5.2 | 1.24 | 26.3 | 0.2 | -7.0 |
| 170 | WN3 | 76 | 16.7 | 5.55 | -5.43 | 1.03 | 3.4 | 0.8 | -3.7 |
| 171 | WN7 | 39 | 25.2 | 5.45 | -5.58 | 1.33 | 12.0 | 0.2 | -4.8 |
| 172 | WN3+neb$^c$ | 75 | 9.3 | 5.1 | -5.23 | 0.75 | 2.1 | 4.6 | -4.3 |
| 173 | WN5+neb | 52 | 16.7 | 5.55 | -5.00 | 1.07 | 7.4 | 2.2 | -3.9 |
| 174 | WN4 | 54 | 20.6 | 5.7 | -5.30 | 1.31 | 8.1 | 0.8 | -4.3 |
| 175 | WN3+abs | 61 | 23.7 | 5.80 | -5.06 | 1.10 | 7.2 | 1.1 | -6.9 |
| 177 | WN4 | 62 | 23.7 | 5.8 | -5.24 | 1.20 | 6.9 | 0.7 | -5.5 |
| 178 | WN3 | 83 | 20.6 | 5.70 | -5.38 | 1.02 | 3.5 | 0.7 | -4.0 |
| 179 | WN4.5 | 60 | 16.7 | 5.55 | -5.44 | 1.20 | 5.5 | 0.7 | -5.2 |
| 180 | WN3+neb | 70 | 15.6 | 5.50 | -5.29 | 0.96 | 3.8 | 1.2 | -3.7 |
| 182 | WN3+neb | 68 | 27.4 | 5.90 | -4.74 | 0.90 | 6.4 | 2.2 | -4.9 |
| 191 | WN7+neb | 37 | 47.4 | 5.90 | -5.07 | 1.35 | 21.8 | 0.4 | -6.8 |
| 193 | WC4 | 56 | 19.8 | 5.70 | -5.39 | 1.40 | 7.5 | 0.8 | -5.4 |
| 195 | WN5 | 64 | 16.70 | 5.55 | -4.96 | 0.95 | 5.4 | 2.7 | -4.1 |
| 197 | WN4+neb | 68 | 15.6 | 5.50 | -5.22 | 0.90 | 4.1 | 1.2 | -5.7 |
| 198 | WN4 | 70 | 17.9 | 5.60 | -5.27 | 1.00 | 4.3 | 1.0 | -4.1 |
| 199 | WN3 | 68 | 14.6 | 5.45 | -5.75 | 1.29 | 3.8 | 0.5 | -3.6 |
| 200 | WC5-6 | 79 | 13.2 | 5.4 | -4.76 | 0.53 | 2.7 | 6.9 | -4.7 |
| 201 | WN3 | 69 | 28.1 | 5.60 | -5.50 | 1.20 | 4.4 | 0.7 | -4.2 |
| 204 | WC4-5 | 100 | 12.2 | 5.35 | -4.60 | 0.20 | 1.6 | 11.0 | -4.7 |
| 205 | Ofpe/WN9 | 27 | 34.5 | 5.45 | -4.57 | 0.88 | 30.6 | 0.8 | -6.9 |
| 206 | WN2+Oxy | 185 | 27.4 | 5.90 | -5.21 | 0.35 | 0.9 | 0.8 | -3.2 |

**Notes.** $^{(a)}$ classification from Neugent & Massey (2011) $^{(b)}$ previously WN2+O7 $^{(c)}$ previously WN3-4

## 6.3 Stellar evolution

The evolution of massive stars is not yet completely understood. Therefore, it is necessary to observe them in their different stellar evolutionary phases to get better constraints. In particular, their behaviour in metal poor regions is of great interest due to their ability to generate a lot of ionising photons. Nowadays it is believed that massive stars contributed a major part to the re-ionisation of the universe (Barkana 2006). When massive stars reach the Wolf-Rayet phase, their temperatures can exceed the ones of O type Main Sequence stars, which means that they produce more ionising photons. However, at low metallicities only the most massive stars will be able to remove their hydrogen rich envelope through stellar winds and enter the Wolf-Rayet phase. Thus, binary interactions could play a significant role to increase the number of Wolf-Rayet stars. Therefore, the analysed sample of this work will be compared to single star and binary star evolution tracks, which were calculated with the BPASS[1] code and are described in Eldridge et al. (2017); Stanway & Eldridge (2018).

Figure 6.3 shows the same HRD as in Fig. 6.2 but now extended by BPASS single star evolution tracks. The tracks are using a metallicity of $Z = 0.006$ and do not account for rotational mixing. There are various other stellar evolution codes on the market using different assumptions leading to different results. For now, the BPASS tracks are used to allow for a better comparison to the binary stellar evolution models.

The Wolf-Rayet stars are now divided into early and late type WN, and WC stars. The red symbols represent all WN stars showing hydrogen at their surface. In contrast to the Galactic Wolf-Rayet stars, all late type WN contain hydrogen in their spectra. In the tracks different Wolf-Rayet stages are highlighted with different colours reflecting the change of the surface abundances. The black line represents the pre-WR phase. At the point where the tracks turn red, the surface hydrogen mass fraction sinks below 40 % marking the beginning of the WNL phase. When the hydrogen fraction shrinks below 5 % the star enters the WNE phase shown in green. Finally, stars with a carbon surface abundance exceeding 20 % are considered as WC/WO stars.

When comparing these tracks to the observed sample, one can immediately see that not all stars are covered. According the the stellar evolution models, the initial mass of a star must be higher than $30 \, M_\odot$ in order to reach the Wolf-Rayet phase. However, this does not cover the stars having luminosities less than $\log L/L_\odot = 5.7$ which is more than half of all analysed sample. Furthermore, the predicted WNL phase reaches nearly to the beginning of the He-ZAMS but most of the observed early type Wolf-Rayet stars have no signatures of hydrogen in their spectra. This is also observed in other analyses e.g. Hainich et al. (2014) and is known as "radius problem" because the derived radii of Wolf-Rayet stars from spectral analyses are larger compared to the radii predicted from stellar evolution models. A possible solution is the existence of a subphotospheric layer where radiation pressure might lead to an inflation of the envelope (Gräfener et al. 2012). This would lead to a

---

[1]bpass.auckland.ac.nz
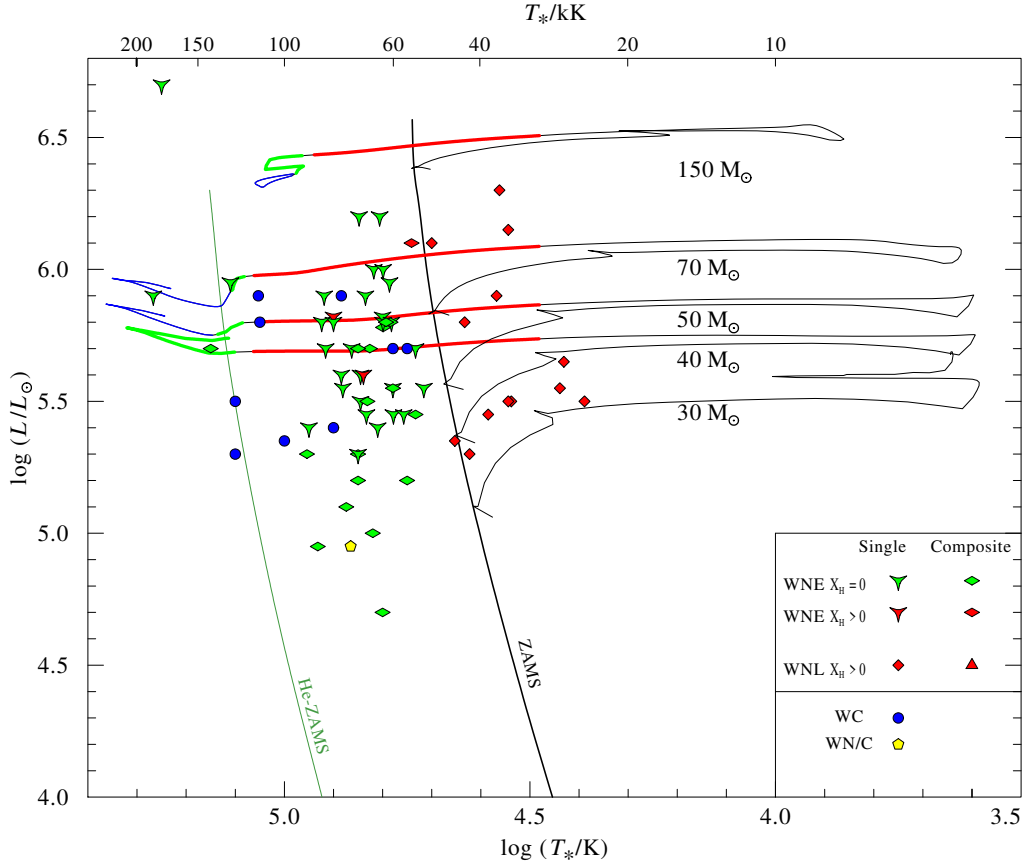
**Fig. 6.3** This plot shows the same HRD as before but now the stars are divided into early and late type WN, and WC. Symbols with a red colour represent WN stars showing hydrogen in their spectra. Additionally, different symbols are used for stars analysed using a single star fit and a composite star fit. The stellar tracks predict the evolution for single stars with an initial metallicity of $Z = 0.006$ from Stanway & Eldridge (2018). The initial masses are given on the right side below each track. For reaching the Wolf-Rayet stage, stars need an initial mass exceeding 30 solar masses according to the tracks. The colours of the tracks represent the different Wolf-Rayet phases. Red: late WN; Green: Early WN; Blue: WC and WO

decrease in effective temperature particularly in the upper parts of the Hertzsprung-Russell diagram including the WC stars (Gräfener et al. 2012; Sanyal et al. 2017). However, this phenomenon is not completely resolved yet and future studies will hopefully shed light on the topic. Therefore, it is not included in the current BPASS models (Eldridge et al. 2017). For the WC stars, it should be mentioned that they are found to have a more complex wind structure due to their extremely dense winds but the models were calculated using a simple single beta law. Self-consistent hydrodynamic atmosphere models lead to much better results (Gräfener & Hamann 2005) at the cost of longer calculation times.

Ramachandran et al. (2019) found indicators that massive stars are evolving quasi chemically-homogeneously at low metallicities. In their analyses of massive stars in the SMC, they could not find any Red Supergiant with initially more than $30\,M_\odot$. Therefore, the analysed sample is compared to BPASS quasi chemically-homogeneous evolution tracks in Fig. 6.4. The utilised symbols and notations are the same as in Fig. 6.3. The tracks use a smaller metallicity of $Z = 0.004$ compared to the other tracks presented here because Eldridge et al. (2017) suspect that a quasi chemically-homogeneous evolution occurs at higher metallicities. It can be seen
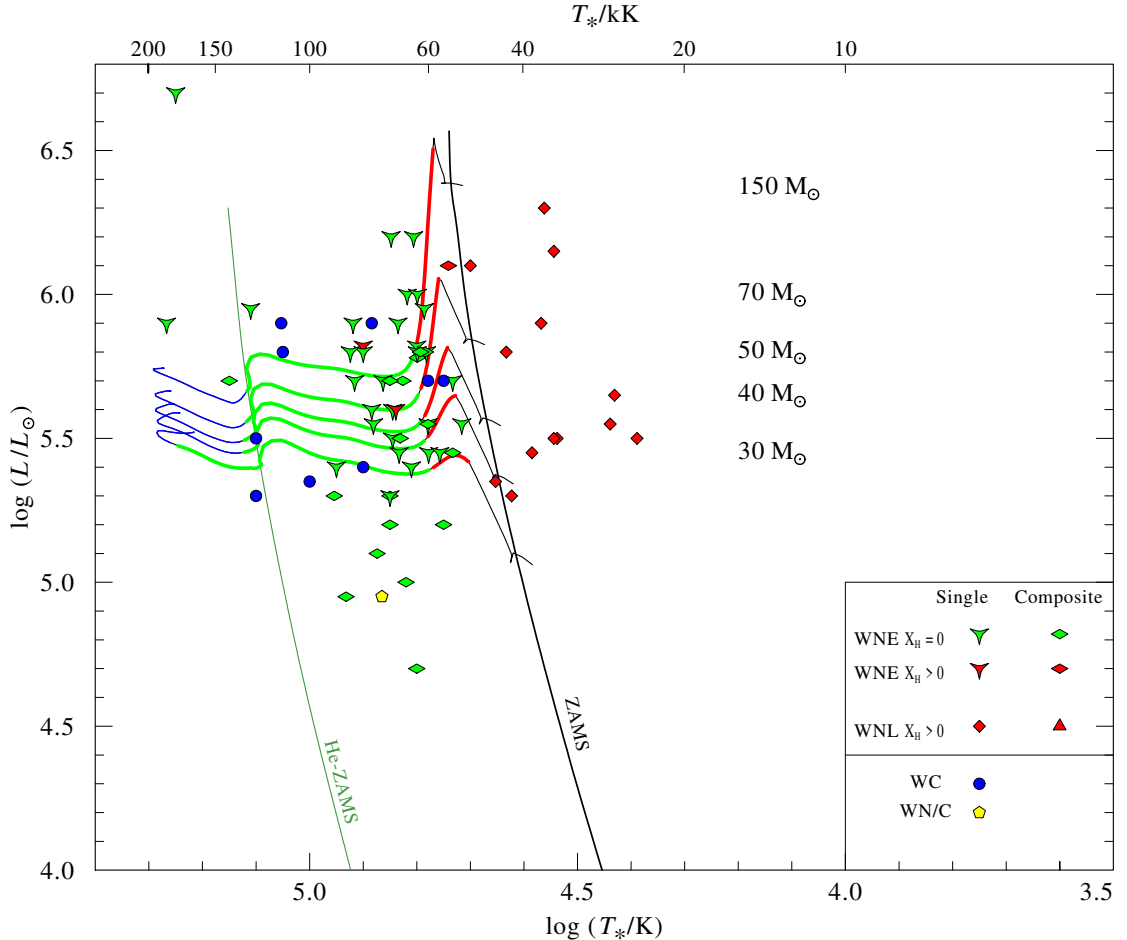


**Fig. 6.4** Symbols and notations are the same as in Fig. 6.3 but the stellar evolution tracks from Stanway & Eldridge (2018) are for a quasi chemically-homogeneous evolution.

that the stars are only evolving towards higher temperatures. When comparing the tracks to the observation, it seems unlikely that the stars evolved like this because the majority of the late type WN stars are not covered. However, in Ramachandran et al. (2019) there are still some Blue Supergiants observed up to luminosities of $\log L/L_\odot = 6.0$. Very recently Massey et al. (2020) published an analysis of the Red Supergiant content in M33. In their work, they found Red Supergiants only to initial masses of up to $40\,M_\odot$ whereas for the SMC, Red Supergiants seem to disappear at initial masses of $30\,M_\odot$ (Ramachandran et al. 2019). However, only a handful of Red Supergiants are observed above an initial mass of $30\,M_\odot$ in M33 and the analysis includes also the more metal rich centre of the galaxy. A more detailed analysis would be needed for a better comparison between the results from Ramachandran et al. (2019) and the findings of Massey et al. (2020). As a last note one should keep in mind that it is more unlikely to observe Red Supergiants at higher masses because the stars have higher mass-loss rates at this stage reducing the evolutionary time they stay in that phase.

So far the stars from this work were only compared to single star tracks. Analyses of Galactic O stars revealed an intrinsic binary fraction of around $70\,\%$ and a preference to small orbital separations, which means that most of the stars should interact at least once with their companion during their evolution (Sana et al. 2012). Thus, most of the Wolf-Rayet stars should be the result of binary interactions. Neugent & Massey (2014) found a close binary fraction of around $45\,\%$ for the Wolf-Rayet stars in the outer regions of M33. Similar values were found for WN stars in the SMC ($\approx 40\,\%$) and LMC ($\approx 30\,\%$) (Foellmi et al. 2003; Schnurr et al. 2008). Also for the Milky Way a binary fraction of around $40\,\%$ is reported (van der Hucht 2001) but recently Dsilva et al. (2020) reported an observed binary fraction of nearly $60\,\%$ for a small sample of Galactic WC stars. From their analyses, they conclude that the intrinsic Wolf-Rayet binary fraction is around $70\,\%$. If this value holds for future analyses including more stars, it points to the fact that the binary fraction for the most massive stars is nearly $100\,\%$. Thus, it should be a factor that needs to be taken into account when analysing Wolf-Rayet stars.

In Fig. 6.5 BPASS binary evolution tracks are shown for a mass ratio of 0.5 (primary is initially twice as massive as secondary). For the tracks with masses of 150, 60 and $25\,M_\odot$ an initial period of 1000 days is used whereas the 20 and $15\,M_\odot$ tracks use a period of around 2.5 days because longer periods are not reaching the Wolf-Rayet phase. In contrast to the single star tracks, they are now covering the faintest Wolf-Rayet stars analysed as single stars. The $25\,M_\odot$ track has a very peculiar shape and the hydrogen envelope is not completely ejected. However, at smaller initial periods the stars would interact earlier during their evolution and the primary would still be able to lose its hydrogen. The tracks with masses of 15 and $20\,M_\odot$ are covering the stars with the lowest luminosities from the composite spectra but it is not expected that stars show a Wolf-Rayet spectrum at low metallicities there.

Shenar et al. (2019) calculated that below a luminosity of $\log L/L_\odot = 4.8$ no Wolf-Rayet spectrum is expected anymore at LMC metallicity, which would correspond to an initial mass of around $15\,M_\odot$. However, the results from Shenar et al. (2019) and from this work suggest that this limit occurs already at around $\log L/L_\odot \approx 5.2$. This value was also found by Shenar et al. (2020b) in a more

detailed analysis as discussed in Sect. 2.2. Furthermore, hydrodynamic calculations from Sander et al. (2020) have shown that the mass-loss is not linearly decreasing with the mass of the stripped star but that there is a steep drop at some point for the mass-loss rate towards smaller helium star masses as can be seen in figure 1 from Sander & Vink (2020). In our own Galaxy are a few examples known which have a luminosity of less than $\log L/L_\odot = 5.0$ like WR 120 (Hamann et al. 2019) or the so-called quasi Wolf-Rayet star HD 45166. While WR 120 is classified as WN7 with a luminosity of $\log L/L_\odot = 4.92$ (according to Gaia distance), a temperature of around 50 kK and a mass-loss rate of $\log \dot{M} = -4.9$, HD 45166 is classified as so called quasi Wolf-Rayet star with a luminosity of $\log L/L_\odot = 4.78$, a temperature of 80 kK and a mass loss-rate of $\log \dot{M} = -7.2$ (Doležalová et al. 2019). Although the stars have a similar luminosity, their mass-loss rates differ a lot. In M33 the mass-loss rates of M33-WR034 or M33-WR027 are also high compared to M33-WR136. Most likely the luminosities of M33-WR034 and M33-WR027 are heavily underestimated but with the Galactic examples in mind this cannot be completely ruled out and therefore their values were kept. Additionally, it is interesting to note that M33-WR034 and M33-WR027 are identified as close binaries by Neugent & Massey (2014) whereas for M33-WR136 no companion could be found. Thus, it is possible that the two stars were formed by binary interactions regardless of their derived luminosities, making them interesting objects for further analyses even if their low luminosity is not confirmed.

With the capability to detect gravitational waves from black hole mergers, we have an additional tool to investigate the last stages of massive star evolution. However, the observations challenge our current understanding of massive star evolution because most of the detected black holes from binary black hole mergers have masses of more than $20\,M_\odot$ with the currently most massive one known having more than $80\,M_\odot$ before it merged (Abbott et al. 2020). On the other hand, the currently most massive stellar black hole known from electromagnetic observations is a binary component in the ultra-luminous X-ray source (ULX) M33-X7, which has a mass of "only" $\approx 16\,M_\odot$ (Orosz et al. 2007). The majority of the analysed stars in this work already have masses of less than $20\,M_\odot$ and the few stars exceeding this mass are either late WN type stars, which are probably going to lose the rest of their hydrogen envelope or they have questionably high luminosities. To form such massive black holes as they are observed with gravitational wave detectors, a star must retain a high fraction of its initial mass. This should only be possible in very metal poor regions where the occurrence of so-called TWUIN (Transparent Wind Ultraviolet INtense) stars is predicted to have a very small mass-loss rate during their main sequence evolution and following a quasi chemically-homogeneous stellar evolution path (Kubátová et al. 2019).
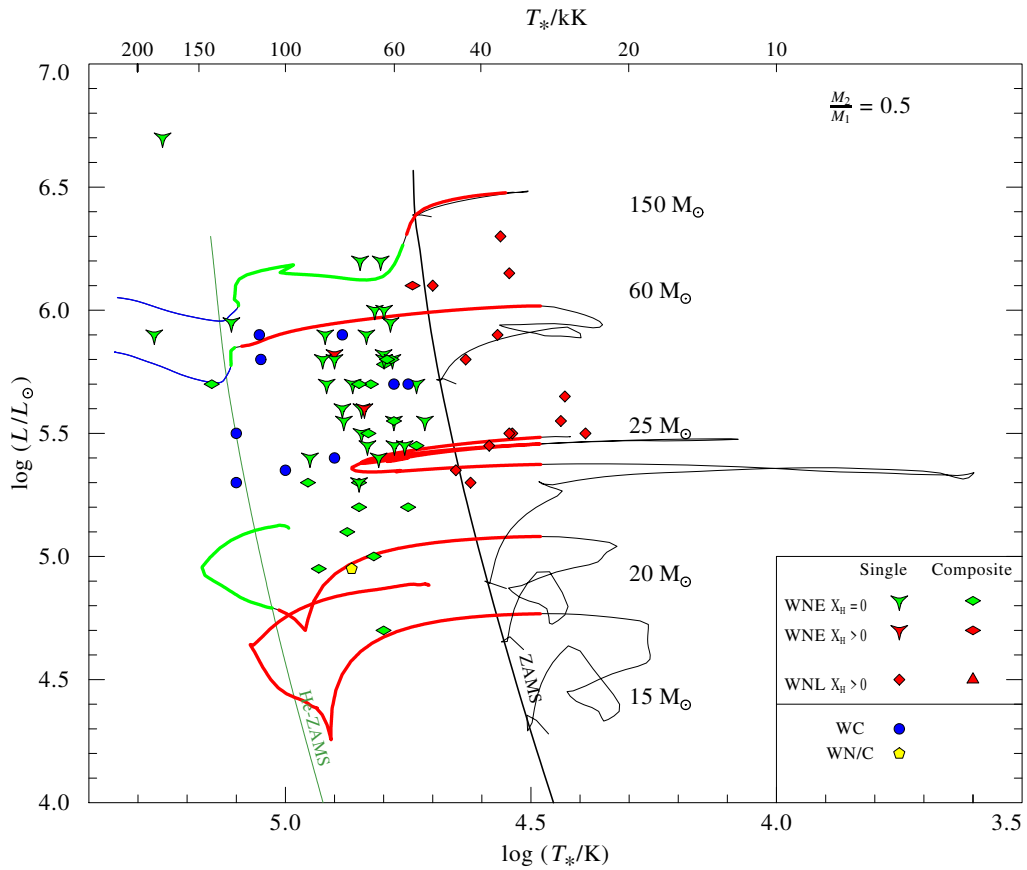
**Fig. 6.5** In this HRD BPASS binary tracks are plotted for the evolution of the initially more massive star under the assumption that the primary star is twice as massive as the secondary component. The tracks are using initial periods of 2.5 days for 15 and 20 $M_\odot$, and 1000 days for 25, 60 and 150 $M_\odot$.

## 6.4 Mass-loss luminosity relation for early type WN stars

To predict the evolution of massive stars and their evolutionary phases at various metallicities, we need a relation between mass-loss rate, luminosity and metallicity that can be implemented into stellar evolution codes. This can be achieved by using either theoretical predictions or even better empirical results. In the past, this was done by different authors for different metallicities. For the Galactic stars there are empirical results by Nugis & Lamers (2000), for the LMC by Hainich et al. (2014) and for the SMC by Hainich et al. (2015). A theoretical prescription is for example available from Vink (2017), which is used in this work. Figure 6.6 shows a mass-loss rate versus luminosity diagram including all analysed stars and the relations from Nugis & Lamers (2000), Hainich et al. (2014) and Vink (2017). The last mentioned relation is shown for an LMC and SMC like metallicity. As can be seen, there is a clear difference between the empirical relation from Hainich et al. (2014) and the theoretical description from Vink (2017). It should be mentioned that the relation from Vink (2017) is an extrapolation from the stripped star regime. Furthermore, it was already mentioned that the hydrodynamic models from Sander et al. (2020) predict a heavy drop in the mass-loss rate at low luminosities. This could be the reason why it is not in accordance with the empirical result. Moreover, in Fig. 6.6 all analysed stars are included. Most of them seem to follow a trend that is located between the relation from Hainich et al. (2014) and the LMC like metallicity relation from Vink (2017). In contrast to previous analyses of the Galactic or LMC WN stars, the hydrogen rich late type WN have higher mass-loss rates than the hydrogen free early type WN. Actually the opposite behaviour is expected due to the lower temperatures of late WN stars.

To get a mass-loss rate - luminosity relation a subsample of the early type WN stars is used. Late type WN and all WC stars are excluded as they obviously form distinct groups in the diagram. Furthermore, all stars with composite spectra are rejected because of the problems already mentioned. To keep the effect of contamination and crowding issues as low as possible, only stars with a crowding index of I are taken into account. The last criterion was the distance to the centre of M33 to decrease the effect of the metallicity gradient: only stars with a distance of more than 4 kpc are included in Fig. 6.7. Star M33-WR001 was removed from this sample because of its obviously outstanding position. In the end, only 13 stars are left but they cover a luminosity range between $\log L/L_\odot = 5.4$ and $\log L/L_\odot = 5.90$, which includes the majority of the classical Wolf-Rayet stars known. From the linear regression we obtain the following prescription for the mass-loss rate:

$$\log(\dot{M}/(M_\odot\,\mathrm{yr}^{-1})) = 1.64(\pm 0.29)\log(L/L_\odot) - 14.61(\pm 1.66) \qquad (6.2)$$

Eq. 6.2 is so far only given in terms of the luminosity but the metallicity dependence is included in the last term, which might also include a dependency of the composition. Hainich et al. (2015) combined empirical results of the Galactic, M31, LMC and SMC samples and found that $\dot{M} \propto Z^{1.2}$, which can be seen in their figure 10. Using the results from the outer region of M33 the diagram from Hainich et al. (2015) can be extended by another data point. The result is shown in Fig. 6.8 and
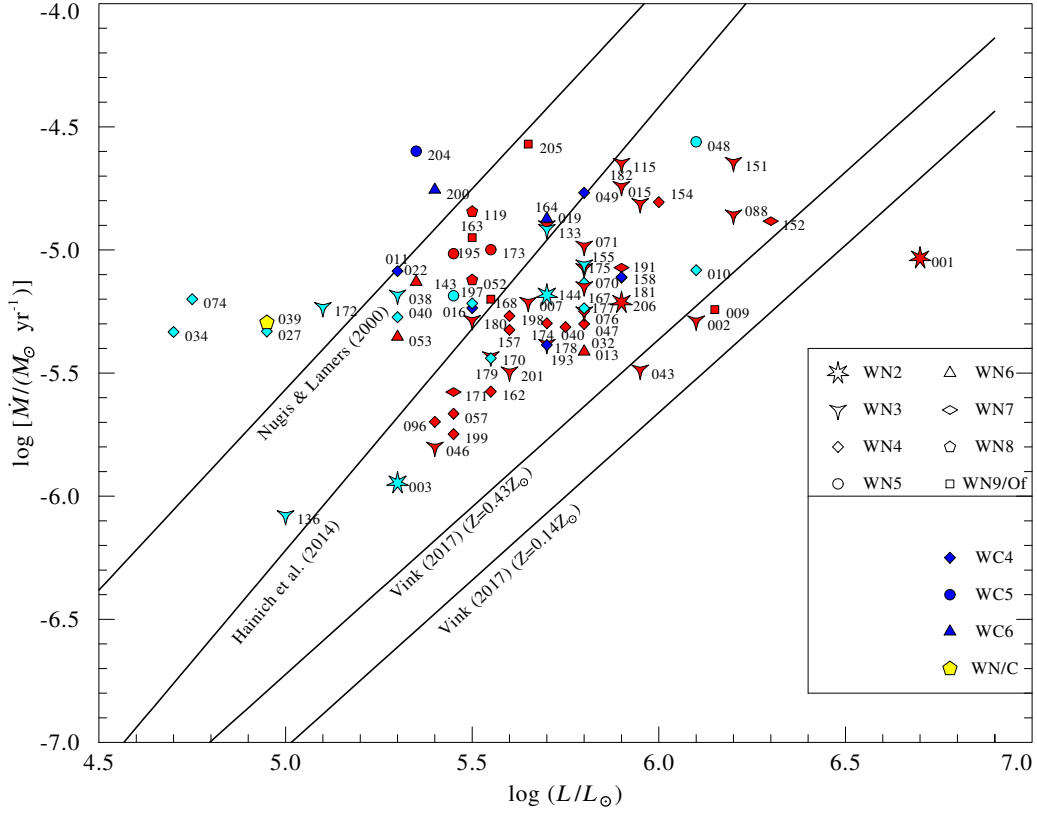
**Fig. 6.6** Mass-loss rate versus luminosity for all analysed stars. Additionally, mass-loss rate - luminosity relations from Nugis & Lamers (2000), Hainich et al. (2014) and Vink (2017) are drawn. The relation from Vink (2017) is shown for an LMC and an SMC like metallicity. The meaning of the colours and symbols is as in Fig. 6.2.

is in very good agreement with the previous analysis from Hainich et al. (2015). However, the value for the metallicity of the outer parts of M33 is not well constrained but hopefully it can be improved with the help of UV spectra, which are now available for some of the Wolf-Rayet stars in M33.
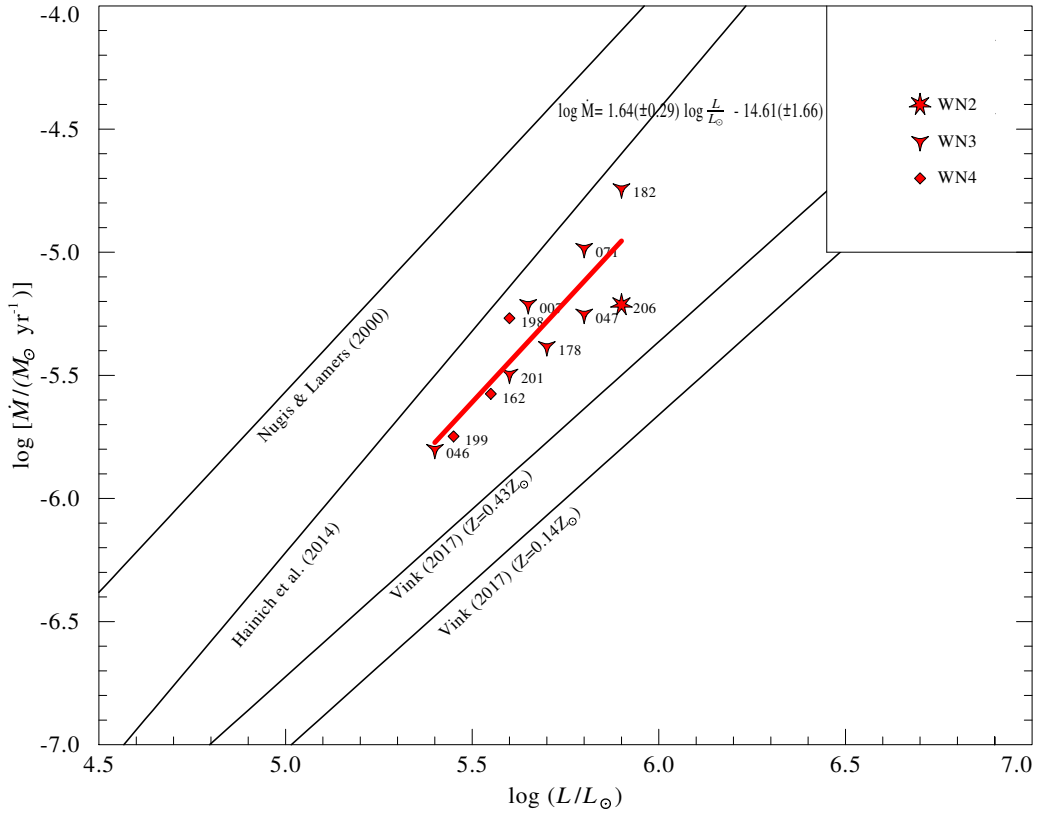
**Fig. 6.7** Mass-loss rate versus luminosity for all early WN analysed as single star with a distance of more than 4 kpc from the centre of M33. The mass-loss rate - luminosity relations are the same as in the previous figure. Excluded is M33-WR001 due to its outstlier position.
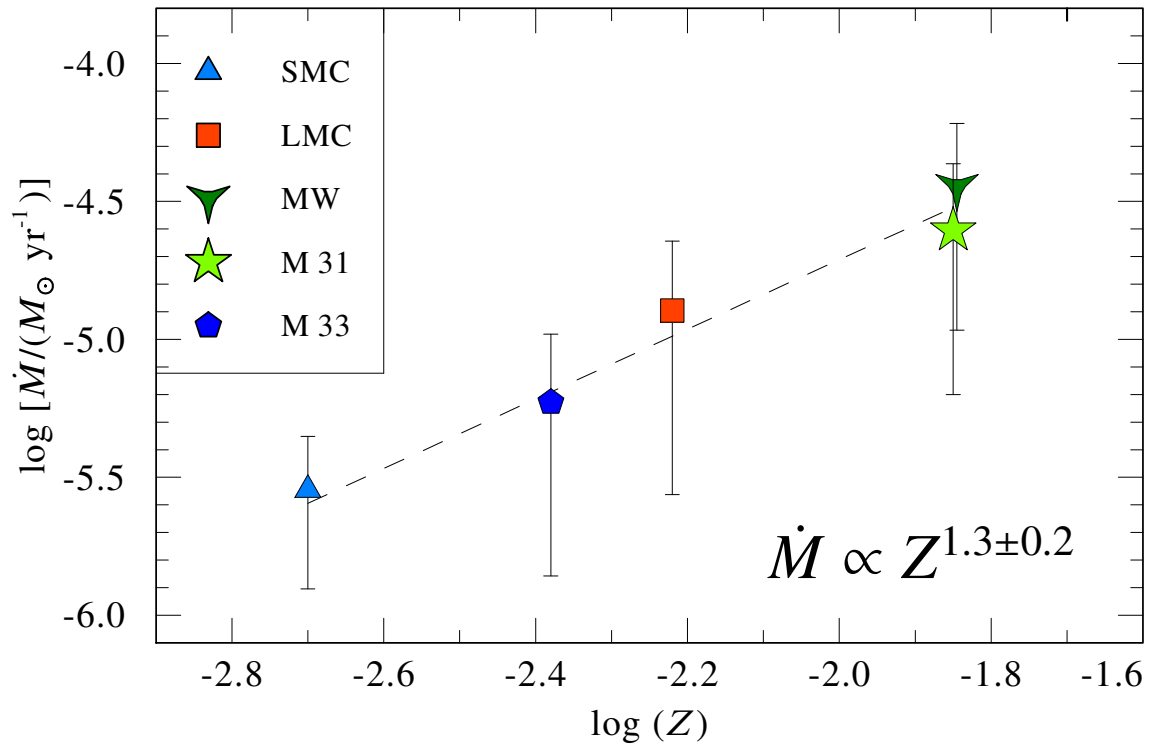
**Fig. 6.8** Average mass-loss rates of WN stars for the SMC (light blue), LMC (orange), M31 (light green), Milky Way (dark green) and the outer region of M33 (dark blue) versus metallicity. The new result from the outer region of M33 is in good agreement with the previous findings.

The obtained relation between mass-loss rate and metallicity is a bit steeper compared to Hainich et al. (2015) but it is still within their error bars. In comparison, the theoretical prediction of Vink & de Koter (2005) suggest a smaller exponent of 0.86 in the metallicity range between $10^{-3} \leq Z/Z_\odot \leq 1$. At higher metallicities the driving iron lines become saturated while at lower metallicities the elements of the CNO cycle and even hydrogen and helium are believed to drive the wind. However, Sander et al. (2020) argue that this relation cannot be described by a single power law because at metallicities below the SMC level the relation becomes steeper. Thus, the next step would be to find and analyse Wolf-Rayet stars in regions with metallicities, which are even below the SMC value.

## 6.5 Summary and Conclusions

In this work, a spectroscopic study of 74 Wolf-Rayet stars was performed using the Potsdam Wolf-Rayet (PoWR) atmosphere code. Out of the 74 stars, 64 belong to the nitrogen sequence (WN), 9 to the carbon sequence (WC) and one is a transition type object (WN/C). All analysed stars have a distance of more than 1 kpc from the centre of M33 and a big subsample is even located at distances exceeding 4 kpc where U et al. (2009) found that the metallicity reaches a value of $Z = 0.0042$. Thus, on a metallicity scale it is located between the Small and the Large Magellanic Cloud making it a perfect environment to study Wolf-Rayet stars at low metallicities. For comparison purposes with previous analyses in these galaxies, the focus was set on the early type WN stars, which form with 52 programme stars the majority of the sample. From the analysis of the early type WN stars with distances of more than 4 kpc away from the centre, a correlation in the form $\dot{M} \propto Z^{1.3}$ was found between mass-loss rate and metallicity. This result is in very good agreement with Hainich et al. (2015).

By fitting the stars in the $\log R_{\mathrm{t}}$-$\log T_*$ plane, it was observed that the transformed radius increases with decreasing temperature for the WN stars up to a certain point. At around spectral type WN7 it starts to decrease again. This effect can also be seen for the LMC and partly for the Galactic WN stars. A possible explanation could be that at lower temperatures the stars are closer to the instability region that is responsible for the LBV phenomenon causing them to have higher mass-loss rates. At least for M33-WR205 (Romano's star) it is known that it was very active during the last decades where the spectral appearance changed between WN11 and WN8.

Although the analysed WC stars range only from spectral type from WC4 to WC6 they cover a broad range of parameters. In general it seems that WC4 have higher temperatures and mass-loss rates compared to the WC6 but the parameters of the WC4 scatter a lot, which is most likely due to a strong contamination in some of the spectra and therefore their temperature and mass-loss rate are heavily underestimated. Since most of these spectra do not include absorption lines from surrounding O or B type stars, which could have served as reference points, they were analysed as single stars. Compared to the WN stars, the analyses of the WC spectra was much more challenging and in most cases only one of the very prominent C IV

features at around 4440 and 5801 Å are reproduced leading to higher uncertainties compared to the WN analyses.

All of the WNL stars in the sample still show hydrogen in their spectra. This is also observed in the LMC and SMC but some of the Galactic WNL are supposed to be hydrogen free. The higher metallicity in our Galaxy could be the reason but in M31 where the metallicity is similar to that of the Milky Way or even higher, no hydrogen free WNL stars are detected either Sander et al. (2014).

BPASS single stellar evolution tracks were not able to explain the Wolf-Rayet stars with luminosities less than $\log L/L_\odot = 5.7$. According to these tracks, a star needs an initial mass of more than $30\,M_\odot$ to become a Wolf-Rayet star via wind stripping. The stars were additionally compared to BPASS binary stellar evolution tracks because most, if not all, massive stars have at least one companion and therefore it can be assumed that binarity interactions can play a role to form Wolf-Rayet stars. However, results from Shenar et al. (2020b) and Sander et al. (2020) suggest that a stripped star needs a specific minimum luminosity, which is metallicity dependent, to develop a Wolf-Rayet spectrum. Using the binary tracks the position of nearly all stars could be reproduced suggesting that most of them had an initial mass between 25 and 60 solar masses. Nevertheless both single star and binary star evolution tracks were not able to predict the correct Wolf-Rayet star phase because even at higher temperatures than observed, hydrogen was predicted to be prominent in the atmosphere. This is not completely understood in detail but the best explanation is the existence of an inflated subphotospheric layer that leads to a bigger radius than predicted. So far this is not integrated in most of the stellar evolution codes and future studies will show if it helps to better reproduce the observations.

Throughout this work many noteworthy Wolf-Rayet stars were analysed but $[NM2011]J013510.27 + 304522.9$ (M33-WR206) stands out in particular because it has a unique spectrum that was never observed for any other Wolf-Rayet star before. It is classified as WN2 but has a very strong O VI line at 3811 Å which is much stronger than the C IV line at 5801 Å. The analysis (see Appendix) revealed an extraordinarily high temperature of nearly 180 kK, which first explains the small apparent V band magnitude of 21.81 mag despite its luminosity of nearly 1 million solar luminosities. Second, it explains the strength of the oxygen line although the estimated carbon mass fraction of 3 % is around three times higher than the oxygen abundance. At these temperatures C IV is not the leading ion anymore. Recently, a Hubble COS spectrum was taken for this star allowing us to refine the stellar parameters and to learn more about this special and possibly short-lasting evolutionary phase of a Wolf-Rayet star at a low metallicity.

# 7 Selbstständigkeitserklärung

Hiermit versichere ich, dass ich die vorliegende Arbeit selbstständig verfasst habe. Alle Passagen, die aus der Literatur oder anderen Quellen entnommen wurden, sind als solche markiert und als Quelle aufgelistet.

Potsdam, December 15, 2020, . . . . . . . . . . . . . . . . . . . . . . . . . . . . . . . . . . . . . . . . . . .
Max Pritzkuleit

# Bibliography

Abbott, R., Abbott, T. D., Abraham, S., et al. 2020, Phys. Rev. Lett., 125, 101102

Adelberger, E. G., García, A., Robertson, R. G. H., et al. 2007, Reviews of Modern Physics, 83, 195

Allan, A. P., Groh, J. H., Mehner, A., et al. 2020, MNRAS, 496, 1902

Barkana, R. 2006, Science, 313, 931

Beals, C. S. 1929, MNRAS, 90, 202

Brott, I., de Mink, S. E., Cantiello, M., et al. 2011, A&A, 530, A115

Clark, J. S., Castro, N., Garcia, M., et al. 2012, A&A, 541, A146

Conti, P. S., Leep, M. E., & Perry, D. N. 1983, ApJ, 268, 228

Corral, L. J. 1996, AJ, 112, 1450

Crowther, P. A. 2007, ARA&A, 45, 177

Doležalová, B., Kubátová, B., Kubát, J., & Hamann, W.-R. 2019, in Astronomical Society of the Pacific Conference Series, Vol. 519, Radiative Signatures from the Cosmos, ed. K. Werner, C. Stehle, T. Rauch, & T. Lanz, 197

Drissen, L., Crowther, P. A., Úbeda, L., & Martin, P. 2008, MNRAS, 389, 1033

Drissen, L., Moffat, A. F. J., & Shara, M. M. 1993, AJ, 105, 1400

Dsilva, K., Shenar, T., Sana, H., & Marchant, P. 2020, A&A, 641, A26

Duncan, J. C. 1922, PASP, 34, 290

Eldridge, J. J., Stanway, E. R., Breivik, K., et al. 2019, arXiv e-prints, arXiv:1912.03599

Eldridge, J. J., Stanway, E. R., Xiao, L., et al. 2017, PASA, 34, e058

Fabricant, D., Fata, R., Roll, J., et al. 2005, PASP, 117, 1411

Fariña, C., Bosch, G. L., & Barbá, R. H. 2012, AJ, 143, 43

Foellmi, C., Moffat, A. F. J., & Guerrero, M. A. 2003, MNRAS, 338, 1025

Gaia Collaboration, Brown, A. G. A., Vallenari, A., et al. 2018, A&A, 616, A1

Georgy, C., Meynet, G., Walder, R., Folini, D., & Maeder, A. 2009, A&A, 502, 611

Gräfener, G. & Hamann, W. R. 2005, A&A, 432, 633

Gräfener, G., Koesterke, L., & Hamann, W. R. 2002, A&A, 387, 244

Gräfener, G., Owocki, S. P., & Vink, J. S. 2012, A&A, 538, A40

Gräfener, G., Vink, J. S., de Koter, A., & Langer, N. 2011, A&A, 535, A56

Hainich, R., Pasemann, D., Todt, H., et al. 2015, A&A, 581, A21

Hainich, R., Ramachandran, V., Shenar, T., et al. 2019, A&A, 621, A85

Hainich, R., Rühling, U., Todt, H., et al. 2014, A&A, 565, A27

Hamann, W. R. & Gräfener, G. 2004, A&A, 427, 697

Hamann, W.-R., Gräfener, G., & Koesterke, L. 2003, in A Massive Star Odyssey: From Main Sequence to Supernova, ed. K. van der Hucht, A. Herrero, & C. Esteban, Vol. 212, 198

Hamann, W. R., Gräfener, G., & Liermann, A. 2006, A&A, 457, 1015

Hamann, W. R., Gräfener, G., Liermann, A., et al. 2019, A&A, 625, A57

Hamann, W. R. & Koesterke, L. 1998, A&A, 335, 1003

Heger, A., Fryer, C. L., Woosley, S. E., Langer, N., & Hartmann, D. H. 2003, ApJ, 591, 288

Hillier, D. J. 1991, A&A, 247, 455

Hubeny, I. & Mihalas, D. 2015, Theory of stellar atmospheres, 10th edn. (Princeton University Press, Princeton and Oxford)

Humphreys, R. M. & Davidson, K. 1979, ApJ, 232, 409

Humphreys, R. M. & Sandage, A. 1980, ApJS, 44, 319

Humphreys, R. M., Weis, K., Davidson, K., Bomans, D. J., & Burggraf, B. 2014, ApJ, 790, 48

Iben, I., J. & Tutukov, A. V. 1985, ApJS, 58, 661

Irrgang, A., Geier, S., Kreuzer, S., Pelisoli, I., & Heber, U. 2020, A&A, 633, L5

Ivanov, G. R., Freedman, W. L., & Madore, B. F. 1993, ApJS, 89, 85

Karachentsev, I. D., Karachentseva, V. E., Huchtmeier, W. K., & Makarov, D. I. 2004, AJ, 127, 2031

Khan, R., Stanek, K. Z., Kochanek, C. S., & Sonneborn, G. 2015, ApJS, 219, 42

Kippenhahn, R., Weigert, A., & Weiss, A. 2012, Stellar Structure and Evolution, 2nd edn. (Springer-Verlag, Berlin Heidelberg)

Klencki, J., Nelemans, G., Istrate, A. G., & Pols, O. 2020, A&A, 638, A55

Kubátová, B., Szécsi, D., Sander, A. A. C., et al. 2019, A&A, 623, A8

Langer, N. 1989, A&A, 210, 93

Latif, M. A. & Ferrara, A. 2016, PASA, 33, e051

Liermann, A. & Hamann, W.-R. 2008, in Clumping in Hot-Star Winds, ed. W.-R. Hamann, A. Feldmeier, & L. M. Oskinova, 247

Liu, J., Zhang, H., Howard, A. W., et al. 2019, Nature, 575, 618

Maeder, A. & Meynet, G. 2000, ARA&A, 38, 143

Magrini, L., Leisy, P., Corradi, R., et al. 2004, arXiv e-prints, 2006

Marchenko, S. V., Moffat, A. F. J., & Crowther, P. A. 2010, ApJ, 724, L90

Martins, F., Hillier, D. J., Bouret, J. C., et al. 2009, A&A, 495, 257

Maryeva, O. & Abolmasov, P. 2012, MNRAS, 419, 1455

Maryeva, O., Koenigsberger, G., Egorov, O., et al. 2018, A&A, 617, A51

Maryeva, O., Polcaro, V. F., Rossi, C., & Viotti, R. 2015, in Wolf-Rayet Stars, ed. W.-R. Hamann, A. Sander, & H. Todt, 361

Maryeva, O., Viotti, R. F., Koenigsberger, G., et al. 2019, Galaxies, 7, 79

Massey, P., Bianchi, L., Hutchings, J. B., & Stecher, T. P. 1996, ApJ, 469, 629

Massey, P., Neugent, K. F., Levesque, E. M., Drout, M. R., & Courteau, S. 2020, arXiv e-prints, arXiv:2011.13279

Massey, P., Neugent, K. F., & Smart, B. M. 2016, VizieR Online Data Catalog, J/AJ/152/62

Massey, P., Olsen, K. A. G., Hodge, P. W., et al. 2007, AJ, 133, 2393

Meynet, G. & Maeder, A. 2005, A&A, 429, 581

Mochejska, B. J., Kaluzny, J., Stanek, K. Z., Sasselov, D. D., & Szentgyorgyi, A. H. 2001, AJ, 122, 2477

Moffat, A. F. J., Drissen, L., Lamontagne, R., & Robert, C. 1988, ApJ, 334, 1038

Morrissey, P., Conrow, T., Barlow, T. A., et al. 2007, ApJS, 173, 682

Neugent, K. F. & Massey, P. 2011, ApJ, 733, 123

Neugent, K. F. & Massey, P. 2014, ApJ, 789, 10

Neugent, K. F., Massey, P., Hillier, D. J., & Morrell, N. 2017, ApJ, 841, 20

Nugis, T. & Lamers, H. J. G. L. M. 2000, A&A, 360, 227

Orosz, J. A., McClintock, J. E., Narayan, R., et al. 2007, Nature, 449, 872

Polcaro, V. F., Maryeva, O., Nesci, R., et al. 2016, AJ, 151, 149

Ramachandran, V., Hamann, W. R., Oskinova, L. M., et al. 2019, A&A, 625, A104

Romano, G. 1978, A&A, 67, 291

San Roman, I., Sarajedini, A., & Aparicio, A. 2010, ApJ, 720, 1674

Sana, H., de Mink, S. E., de Koter, A., et al. 2012, Science, 337, 444

Sander, A., Hamann, W. R., & Todt, H. 2012, A&A, 540, A144

Sander, A., Shenar, T., Hainich, R., et al. 2015, A&A, 577, A13

Sander, A., Todt, H., Hainich, R., & Hamann, W. R. 2014, A&A, 563, A89

Sander, A. A. C., Hamann, W. R., Todt, H., et al. 2019, A&A, 621, A92

Sander, A. A. C. & Vink, J. S. 2020, MNRAS, 499, 873

Sander, A. A. C., Vink, J. S., & Hamann, W. R. 2020, MNRAS, 491, 4406

Sanyal, D., Langer, N., Szécsi, D., -C Yoon, S., & Grassitelli, L. 2017, A&A, 597, A71

Schaerer, D., Meynet, G., Maeder, A., & Schaller, G. 1993, A&AS, 98, 523

Schmutz, W., Hamann, W. R., & Wessolowski, U. 1989, A&A, 210, 236

Schnurr, O., Moffat, A. F. J., St-Louis, N., Morrell, N. I., & Guerrero, M. A. 2008, MNRAS, 389, 806

Shenar, T., Bodensteiner, J., Abdul-Masih, M., et al. 2020a, A&A, 639, L6

Shenar, T., Gilkis, A., Vink, J. S., Sana, H., & Sand er, A. A. C. 2020b, A&A, 634, A79

Shenar, T., Hainich, R., Todt, H., et al. 2018, A&A, 616, A103

Shenar, T., Hainich, R., Todt, H., et al. 2016, A&A, 591, A22

Shenar, T., Hamann, W. R., & Todt, H. 2014, A&A, 562, A118

Shenar, T., Sablowski, D. P., Hainich, R., et al. 2019, A&A, 627, A151

Sholukhova, O. N., Fabrika, S. N., Zharova, A. V., Valeev, A. F., & Goranskij, V. P. 2011, Astrophysical Bulletin, 66, 123

Smith, L. F. 1968a, MNRAS, 138, 109

Smith, L. F. 1968b, MNRAS, 140, 409

Smith, L. F., Shara, M. M., & Moffat, A. F. J. 1996, MNRAS, 281, 163

Spiller, F. 1992, PhD thesis, -

Stanway, E. R. & Eldridge, J. J. 2018, MNRAS, 479, 75

Todt, H., Sander, A., Hainich, R., et al. 2015, A&A, 579, A75

U, V., Urbaneja, M. A., Kudritzki, R.-P., et al. 2009, ApJ, 704, 1120

Valeev, A. F., Sholukhova, O., & Fabrika, S. 2009, MNRAS, 396, L21

van den Bergh, S. 2000, PASP, 112, 529

van der Hucht, K. A. 2001, New A Rev., 45, 135

Vink, J. S. 2017, A&A, 607, L8

Vink, J. S. & de Koter, A. 2005, A&A, 442, 587

Wolf, C. J. E. & Rayet, G. 1867, Academie des Sciences Paris Comptes Rendus, 65, 292

Yoon, S.-C. 2015, PASA, 32, e015

Zaritsky, D., Elston, R., & Hill, J. M. 1989, AJ, 97, 97

Zhang, W., Todt, H., Wu, H., et al. 2020, arXiv e-prints, arXiv:2008.08205

# 8 Appendix

## 8.1 Comments on individual stars

**M33-WR001** is the first star in the list from Neugent & Massey (2011) and is classified as WN2. It is located inside a cluster lying more than 6 kpc away from the centre of M33. In Fig. 8.4, the spectrum (blue line) shows mainly He II lines and a weak N V feature at around 4604 Å but no N IV lines indicating that it should be very hot as it is expected for a WN2 star. Due to its potential cluster membership, the spectrum seems to be contaminated as indicated by the compressed shape of the He II line at 4686 Å. Neugent & Massey (2011) assigned the star a crowding index (CWD) of S, which means that the star is somewhat isolated and that the contamination lies between 5-20 %. It is a rare case where not only optical photometry is available but also UV photometry from GALEX. For the spectral modelling the star was treated as single star because there are no strong hydrogen nor helium lines visible in the blue part of the spectrum, which would be expected if the star is located in a star forming region. However, Neugent & Massey (2014) found evidence that the star could have a close companion. From the spectral energy distribution an extraordinarily high luminosity of $\log(L/L_\odot) = 6.7$ was derived. However, this is rather unlikely because it would be the most luminous early-type Wolf-Rayet star known so far. Furthermore, it has quite a low mass-loss rate compared to its luminosity making it even more unlikely that the spectrum stems from a single star. Therefore, the contamination is most likely higher than 80 % which results in a crowding index of X. It is still puzzling why there are no observed absorption features in the spectrum from O and B type stars.

Due to the strong contamination the derived stellar parameters have higher uncertainties as already discussed for the luminosity and mass-loss rate. The estimated stellar temperature of nearly 178 kK is also an upper limit because at hotter temperatures the N V component at 4604 Å would disappear. The temperature might be lower but it cannot be too cold because otherwise the N IV line at 7103 Å starts to become visible at around 100 kK. The terminal velocity is the only parameter that can be estimated with a higher accuracy because the width of the lines is not changing in a contaminated spectrum. Compared to the WNE-LMC grid models it has a slighter higher terminal velocity of 1900 km s$^{-1}$ Therefore, the classification as WN2 remains.

**M33-WR002** is classified as WN3. The spectrum in Fig. 8.5 exhibits only weak emission lines and from its crowding index of X it can be concluded that the spectrum is heavily contaminated by light from other sources. However, since there are no clear absorptions visible a single star fit was applied. For a WN star, it has a rather strong C IV line at 5801 Å, which has nearly the same strength as the He II line

located at H$\alpha$. To account for this line, the carbon abundance was increased but this had already effects on the He II line at 4686 Å. In contrast to the majority of the WN3 stars in this sample, there are no N IV lines visible in the spectrum. This points to a higher temperature and indeed the estimated temperature of 90 kK is higher than the average value for WN3. For the luminosity a value of log $L/L_\odot = 6.10$ was found but this is only the upper limit since the exact degree of contamination could not be identified.

**M33-WR003** is a star of the rare type WN2. The spectrum in Fig. 8.6 shows strong absorption lines of He I and weak emission lines. Therefore, it was analysed using a two component fit. Neugent & Massey (2014) found no evidence that the star has a close companion. Although the spectrum suffers from low signal-to-noise ratio the He II 4-3, 7-4 and 6-4 as well as the N V line at 4603 Å are clearly detectable. To reproduce the absorption lines in the blue part of the spectrum a B star model was used with a temperature of 18 kK from the LMC-OB-I grid. As can be seen from Fig. 8.6, the B star dominates the optical spectrum because the Wolf-Rayet star is much hotter with a temperature of around 90 kK. For the luminosity, a value of $\log(L/L_\odot)L = 5.3$ was derived. Although there is a degeneracy between mass-loss rate and luminosity in binary star fits, the position of M33-WR003 in the graph of Fig. 6.6 seems reasonable compared to the single WNE stars. The WN2 classification was not changed.

**M33-WR007** is an isolated WN3 star whose is shown in Fig. 8.7. Although it is an early type Wolf-Rayet star it is still showing hydrogen in its spectrum. According to the criteria of Neugent & Massey (2014), the star has no close neighbour. The best fit was achieved with a hydrogen abundance of 20 % by mass. Furthermore, it has not only GALEX UV measurements but the UV photometry is most likely solely coming from this star. From the spectral fit a luminosity of $\log(L/L_\odot) = 5.65$ and a stellar temperature of 76 kK was inferred. When comparing this star to other observed WN3h stars, it looks like a nearly perfect twin to Bat99 018 in the Large Magellanic Cloud (Hainich et al. 2014).

**M33-WR009** is classified as Ofpe/WN9 star and was already identified by Humphreys & Sandage (1980) as a Blue Supergiant. In contrast to the other Ofpe/WN9 stars in this sample, its emission lines are rather weak. However, from all these stars it is brightest with a luminosity of log $L/L_\odot = 6.15$. From the spectrum in Fig. 8.8 a temperature of 35 kK was derived. Due to its high luminosity and the fact that the emission lines are rather weak compared to the other stars of this class, the star is probably still in the core hydrogen burning phase.

**M33-WR010** was classified as WN2+O7 star by Neugent & Massey (2011) and therefore, it was analysed using a two star fit. In the spectrum in Fig. 8.9 not only the Wolf-Rayet emission and OB star absorption lines but also strong nebula emission lines of He I and even He II lines are visible, making it very difficult to find a good model for the WR star companion. The star was already identified by Humphreys & Sandage (1980) as part of an association. Moreover, it was in the sample from Neugent & Massey (2014) but they could not find evidence that the star has a close companion. For the O type component, a grid model with a temperature of 34 kK was selected to account for the contamination but this is highly uncertain. For the Wolf-Rayet star a luminosity of $\log(L/L_\odot) = 6.1$ and a temperature of 55 kK were

derived. Additionally, the model contains 20 % hydrogen to partially reproduce the Hα line but the strong nebula emissions do not allow for a further refinement. Due to its low temperature and the presence of N IV and N V lines the spectral classification is changed from WN2 to WN4(h).

**M33-WR011** is classified as WC4. The spectrum in Fig. 8.10 contains many emission lines but suffers from low signal-to-noise. When fitting the spectral energy distribution, the reddest photometry mark was used as orientation because the bands seem to be effected by the emission lines. For the luminosity a value of $\log L/L_\odot = 5.3$ was obtained. The estimated temperature of 126 kK is similar to other observed WC4 stars.

**M33-WR013** is the first late type WN star in the sample and is classified as WN6 showing absorption lines in the blue part of its spectrum. Albeit the presence of absorption lines, it was treated as single star because these features can partly be reproduced by the model as can be seen in Fig. 8.11. The model has a temperature of 43 kK and a luminosity of $\log(L/L_\odot) = 5.8$. To fit the Hα line, a hydrogen mass fraction of 30 % was assumed with an error of ±10 % because of the nebula emission.

The absorption lines in the blue part of the spectrum are not completely reproduced by the model, indicating that the star might have a companion. The star was part of the sample from Neugent & Massey (2014) but from their analysis it is unclear whether it is part of a close binary system. From Fig. 5.2 it appears that the star is located inside a cluster. This is further supported by the observed GALEX photometry because the measured UV flux is not generated by the Wolf-Rayet star alone. Thus, the estimated luminosity of the star might be a bit overestimated.

**M33-WR015** is a WN3 showing a slightly roundish profile in Fig. 8.12, indicating that the star might rotate (Shenar et al. 2014). The best fitting stellar model has a temperature of 130 kK and a luminosity of $\log(L/L_\odot) = 5.95$. It is the hottest WN3 star in the sample and it is located nearly on the He-ZAMS in the HRD in Fig. 6.2. To account for rotation, the model was calculated with a rotational velocity of $200 \, \mathrm{km \, s^{-1}}$. In contrast to the majority of the other WNE stars in the sample, it has an increased ratio between mass-loss and luminosity. This might indicate that the mass-loss rate is increased due to the rotation of the star. In addition, the star was also observed by Neugent & Massey (2014) but their analysis can neither confirm nor exclude the presence of a close companion.

**M33-WR016** is classified as WC4 and it is the only WC star showing clear evidence of contamination. Therefore, it was analysed with a composite spectrum which is shown in Fig. 8.13. The secondary component is best reproduced by a B star with a temperature of 24 kK. For the Wolf-Rayet star a luminosity of $\log(L/L_\odot) = 5.50$ and a temperature of about 126 kK were derived. Although a velocity difference of about $300 \, \mathrm{km \, s^{-1}}$ was found, Neugent & Massey (2014) could not find any evidence that the star has a close companion.

**M33-WR018** is classified as WN3 and its spectrum in Fig. 8.14 displays only very weak emissions of He II at 4686 and 6562 Å and N V at 4604 Å. The spectrum of the star is most likely contaminated but no absorption lines of a hot close companion are visible. Therefore, the star was treated as single star although there are

hints that it could have a close companion (Neugent & Massey 2014). The star was also observed by Gaia which has a much better resolution of $0\overset{''}{.}4$ in data release two. Interestingly, it has a G band magnitude of about $19.85\,\mathrm{mag}$ (Gaia Collaboration et al. 2018). This is comparable to the observed magnitudes by Neugent & Massey (2011) according to the Johnson-Cousins relationships for Gaia[1]. Thus, the contaminating source must be located within $0\overset{''}{.}4$. From the model, a stellar temperature of $66\,\mathrm{kK}$ and a luminosity of $\log(L/L_\odot) = 6.00$ are inferred but these values are highly uncertain and therefore the star was not used for further analyses.

**M33-WR019** is a WN3 star. From the spectral fit in Fig. 8.15 a temperature of $73\,\mathrm{kK}$ and a luminosity of $\log(L/L_\odot) = 5.70$ are derived. In contrast to most of the other WN3 and WN4 stars, it has a rather high terminal velocity of $2000\,\mathrm{km\,s^{-1}}$. Additionally, it has an increased ratio between its mass-loss rate and luminosity. It might also rotate with a non-negligible velocity but because the model reproduces the observed spectrum quite good it was calculate without rotation. In their search for close companions of Wolf-Rayet stars, Neugent & Massey (2014) could not find a strong evidence that the star has a close companion. Furthermore, it was observed by Gaia and there it has a G band magnitude of $20.67\,\mathrm{mag}$ (Gaia Collaboration et al. 2018), which is in line with the photometry from Neugent & Massey (2011). Thus, the observed spectrum is primarily generated by the Wolf-Rayet star.

**M33-WR022** is the second WN6 star in the sample. The spectrum is shown in Fig. 8.16. In contrast to M33-WR013, it has no strong absorption lines in the blue end of its spectrum. The best fitting model has a temperature of $45\,\mathrm{kK}$ and a luminosity of $\log(L/L_\odot) = 5.35$. To match the observed photometry a higher reddening of $E(\mathrm{B-V}) = 0.3\,\mathrm{mag}$ was used but it should be noted that the photometry could be flawed as in some other cases. For clarification more photometric data are necessary.

The hydrogen mass fraction was estimated to be $20\,\%$. Although it is a WNL star it has a pretty high mass-loss rate for its luminosity. Neugent & Massey (2014) could not find a clear indication for a close companion.

**M33-WR027** is classified as WN4 and because its He II line at $4686\,\text{Å}$ appears to have an absorption feature on top of the emission it was treated as binary star. However, because the spectrum in Fig. 8.17 suffers from a low signal-to-noise ratio, it is difficult to clearly confirm the presence of another star but Neugent & Massey (2014) found strong evidence that the star is probably part of a close binary system. The Wolf-Rayet component is best fitted using a model with a temperature of $85\,\mathrm{kK}$ and a luminosity of only $\log(L/L_\odot) = 4.95$, which is rather small for a Wolf-Rayet star. Nevertheless, there are Wolf-Rayet stars known which have luminosities below $\log(L/L_\odot) = 5.00$ (Hamann et al. 2019; Zhang et al. 2020).

It is noteworthy that it has a rather high temperature for a WN4 star but due to the high mass-loss rate, the N IV lines are getting strong again. Furthermore, its terminal velocity is $1300\,\mathrm{km\,s^{-1}}$, which is slightly smaller than the usually adopted $1600\,\mathrm{km\,s^{-1}}$.

---

[1]https://gea.esac.esa.int/archive/documentation/GDR1/Data_processing/chap_cu5phot/sec_phot_calibr.html

**M33-WR032** is classified as WN4. The spectrum in Fig. 8.18 is not only defined by its Wolf-Rayet lines but also by strong nebula emissions. To match the observed optical photometry a higher reddening of $E(B - V) = 0.3$ mag was adopted. From the GALEX UV photometry, it can be assumed that the star is part of a cluster.

The spectral analysis reveals a luminosity of $\log(L/L_\odot) = 5.80$ and a temperature of 63 kK. According to the criteria of Neugent & Massey (2014) it has most likely no close companion.

**M33-WR034** was classified as WN4+B2I by Neugent & Massey (2011). Thus, it was treated as composite spectrum. The plot is displayed in Fig. 8.19. The absorption lines of the companion are clearly identifiable and are well modelled by a B star grid model with a temperature of 26 kK. From the spectral fit a luminosity of only $\log(L/L_\odot) = 4.70$ is inferred for the Wolf-Rayet star. If this value is correct, it would be one of the faintest Wolf-Rayet stars known. However, this value should be seen as a lower limit because the mass-loss rate is most likely overestimated as can be seen in Fig. 6.6. In contrast, a smaller mass-loss rate would imply a higher luminosity for the Wolf-Rayet star but this would make it difficult to fit the absorption lines of the companion. Whatever the case is, it seems to be an interesting object for further studies. Neugent & Massey (2014) found strong evidence that the star has a close companion.

The object was first detected by Ivanov et al. (1993). Their photometry is in good agreement with the observations from Neugent & Massey (2011) indicating that the stars have not changed significantly between the two surveys. According to Ivanov et al. (1993) M33-WR034 is a member of an association that they assigned the number 17.

**M33-WR038** is a Wolf-Rayet star of spectral type WN3. The spectrum is shown in Fig. 8.20 where absorption lines in the blue part of the spectrum indicate the presence of another source. It is very unlikely that this star belongs to the WN3 stars showing strong absorption lines (WN3/O3) because it also has He II emissions bluewards of the 4686 Å line. Therefore, it was treated as two component spectrum where the proportion of the O star companion is reproduced by a grid model with a temperature of 32 kK. From the UV photometry it can be concluded that there must be more hot stars in the proximity. The star was also observed by Drissen et al. (2008) who present it as part of the H II region NGC592. Their spectrum in Fig. 8.21 was taken in 2000/2001 and is shown for comparison. As one can see, it suffers not as much from contaminating sources as the spectrum from Neugent & Massey (2011). Thus, it is a perfect case to test how good the binary analysis is in this case. In their work, Drissen et al. (2008) compare the spectrum of M33-WR038 to the spectrum of the Galactic Wolf-Rayet star WR44, which is classified as WN4. The analyses of the star by Hamann et al. (2019) revealed a temperature of 79 kK and a luminosity of $\log(L/L_\odot) = 5.60$. In comparison M33-WR038 has a luminosity of $\log(L/L_\odot) = 5.30$ and a temperature of around 71 kK. Additionally, the values for the mass-loss rates are quite similar when adjusted for the different luminosities and terminal wind velocities of the two stars. Thus, it is not very surprising that the model looks quite similar to the observed spectrum of WR44 in Hamann et al. (2019), which was used as reference in Drissen et al. (2008). Therefore, the derived parameters from the binary fit for M33-WR038 are quite certain.

For the star, Drissen et al. (2008) measured a B band flux of 19.7 mag, which is around 0.7 mag fainter than the observation from Neugent & Massey (2011). Due to the different quality of the spectra, it could be that Drissen et al. (2008) only measured the light coming from the Wolf-Rayet star. However, the star was observed by Gaia too and this measurement is consistent with the observed photometry from Neugent & Massey (2011). On the other hand, it is possible that the Gaia identification of this star is erroneous in Simbad because Gaia detected another star (Source:303381856836417408) at a distance of only 0″.58 that has a G band magnitude of 20.10 mag (Gaia Collaboration et al. 2018). Thus, this could be the Wolf-Rayet star. Additionally the star was in the sample from Neugent & Massey (2014) but from their analysis it is unclear whether the star could have a close companion.

**M33-WR039** has a very interesting spectrum because it is not only showing nitrogen lines but also a strong C IV line at 5801 Å. Therefore, it was classified as a rare transition type WN/C. Furthermore, the spectrum in Fig. 8.22 shows strong absorption lines and was therefore analysed with a two star fit. The B star component is plotted using a grid model with a temperature of 16 kK. It should be noted that the observed spectrum contains a very strong Ca II (K) line which is not reproduced by this model. The Ca K line is also very prominent in the interstellar medium but in contrast the Na D line is not well pronounced. Furthermore, the transition to a velocity space reveals that the Na D line and the Ca K line form in different regions as can be seen in Fig. 8.1. The Ca K line could consist of a stellar and an interstellar component. By comparison to the Hδ line, which should be produced by the B star, it is slightly off. However, the origin of a stellar component is puzzling because the He I absorption lines clearly demonstrate that the second component must be a B type star. The model has a temperature of about 73 kK and a lumi-
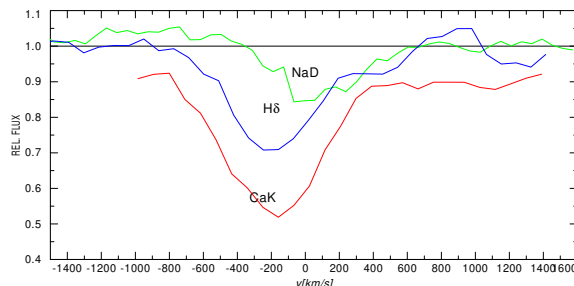


**Fig. 8.1** In this plot the velocity components of the Na D, Ca K and Hδ lines are compared. Obviously, the Na D line forms at a different velocity than the Ca K line. The Hδ absorption should be produced by the companion and is shown as comparison.

nosity of only $\log(L/L_\odot) = 4.95$. To match the optical photometry, a reddening of $E(B-V) = 0.4$ mag was adopted. The analysis reveals that the star is indeed enhanced in carbon. The carbon mass fraction is about 0.4 %±0.1 %. Recently, a similar star was discovered in our own Galaxy by Zhang et al. (2020). It has nearly the same luminosity but the temperature of 47 kK is much cooler. Another star that fits in this group is the Galactic star WR 58 which has a temperature of 79 kK and a luminosity of $\log(L/L_\odot) = 4.95$ too (Sander et al. 2019). These values are very similar and the spectrum of WR 58 is comparable to the model shown in Fig. 8.22. To have a better spectrum of M33-WR039 without the contribution of

the other component would be interesting to see if the star has indeed such a low luminosity.

**M33-WR040** was already extensively discussed in Sect. 6.1

**M33-WR043** is classified as WN3. Although the spectrum in Fig. 8.25 contains some absorption features in the blue part it was treated as single star because it was flagged as isolated by Neugent & Massey (2011) and in Neugent & Massey (2014) no close companion could be found. From the spectral fit a luminosity of $\log(L/L_\odot) = 5.95$ and a temperature of $61\,$kK were derived. The absorption lines are partly reproduced by the model but some of the He II lines are too weak. Additionally, the temperature is quite low for a WN3 star and from its position in Fig. 6.6, it seems that the mass-loss rate is underestimated. Thus, it is most likely that there is a significant contribution from another source, which would mean that the crowding index of I is erroneous.

**M33-WR046** has a very noisy spectrum especially at redder wavelengths as can be seen in Fig. 8.26. Only the He II at $4686\,$Å and the N V emission at $4604\,$Å were identified. Since there are only two lines, the estimated stellar parameters can only be seen as a rough orientation. Nevertheless, a luminosity of $\log(L/L_\odot) = 5.95$ and a temperature of $89\,$kK are reasonable for a Wolf-Rayet star of subtype WN3. For a confirmation a better spectrum is needed.

**M33-WR047** is classified as WN3. the spectrum in Fig. 8.27 is a textbook example for a WN3 star. The best fitting model has a luminosity of $\log(L/L_\odot) = 5.95$ and a temperature of about $79\,$kK.

It should be noted that the photometric entries in Simbad are not correct for this star. Furthermore, the method in Neugent & Massey (2014) suggests that the star has no close companion.

**M33-WR048** is classified as WN4.5+O where the O star component is clearly visible in the spectrum in Fig. 8.28. Thus, it was treated as composite spectrum where the O star component was fitted using a grid model with $43\,$kK. Even though it is already fitted as a binary, it belongs to one of the brighter Wolf-Rayet stars in this sample with a luminosity of $\log(L/L_\odot) = 6.10$. This star has also a Gaia entry with a G magnitude of $16.90\,$mag (Gaia Collaboration et al. 2018), which is slightly fainter than the observation from Neugent & Massey (2011).

**M33-WR049** is classified as WC4 where the spectrum in Fig. 8.29 shows a lot of small carbon and oxygen emissions. As it is quite difficult for WC stars to reproduce all of the lines, a model was selected that covers most of the smaller lines. The estimated luminosity of $\log(L/L_\odot) = 5.80$ is not only in good agreement with the optical but also with the UV photometry from GALEX. Furthermore, the optical photometry from Neugent & Massey (2011) is supported by the detected Gaia G band magnitude of $20.71\,$mag. From the analysis of Neugent & Massey (2014) it seems that the star has no close companion.

**M33-WR052** is one of the two WN8 stars in the sample. The spectral plot is displayed in Fig. 8.30. It is also a rare case where UV data from GALEX and *Spitzer* infrared measurements from Khan et al. (2015) are available. The SED suggests that the star is indeed isolated because optical, UV and part of the infrared photometry

are covered by the model. The luminosity is found to be $\log(L/L_\odot) = 5.50$. In the spectrum most of the lines are well reproduced using a model with a temperature of 34.5 kK but the He II at 4686 Å is overestimated. However, this problem also occurs for the majority of the other WNL stars. Neugent & Massey (2014) could not find an evidence that the star has a close companion.

**M33-WR053** is the second WN6 in the sample. The spectrum in Fig. 8.31 includes also nebula emissions of hydrogen making it complicate to estimate the hydrogen fraction. It has a luminosity of $\log(L/L_\odot) = 5.30$ and a temperature of 42 kK.

Additionally, the star has a Gaia G band magnitude of 20.16 mag (Gaia Collaboration et al. 2018), which is comparable to the photometry from Neugent & Massey (2011). This indicates that the star is indeed isolated. Additionally, Neugent & Massey (2014) could not identify a close companion.

**M33-WR057** is classified as WN4 where the analysis of the spectrum in Fig. 8.32 reveals a luminosity of $\log(L/L_\odot) = 5.45$ and a temperature of 60 kK. For this star, Neugent & Massey (2014) could not find indications for a close companion.

**M33-WR070** is classified as WN4 where the spectrum in Fig. 8.33 is clearly exhibiting the presence of another component. Hence, it was analysed using a two component fit. The star is in the sample from Neugent & Massey (2014) but it is unclear whether the star could have a close companion. The O star component was fitted using a grid model with a temperature of 36 kK. The Wolf-Rayet model has a luminosity of $\log(L/L_\odot) = 5.80$ and a temperature of 63 kK. Furthermore, it has a slightly smaller terminal velocity of 1400 km s$^{-1}$ compared to the Grid models.

**M33-WR071** is classified as WN3 and its spectrum is shown in Fig. 8.34. It has a luminosity of $\log(L/L_\odot) = 5.80$ and a temperature of 84 kK. The GALEX photometry cannot be reproduced by the star alone. Thus, it is probably part of a cluster. The star was also observed by Gaia measuring a G band magnitude of 20.74 mag (Gaia Collaboration et al. 2018). This value is in accordance with the observation from Neugent & Massey (2011). According to Neugent & Massey (2014), there is evidence that the star has a close companion.

**M33-WR074** is classified as WN4+O. Hence, a two component fit was used for the determination of the stellar parameter. According to the results from Neugent & Massey (2014), it is unclear if the star has a close companion. The spectrum is shown in Fig. 8.35. The O star component was fitted using a 35 kK grid model. The Wolf-Rayet star has a luminosity of $\log(L/L_\odot) = 5.20$ and a temperature of 56 kK.

**M33-WR075** is classified as WN4 and was treated as binary because its spectrum in Fig. 8.36 shows absorption lines which cannot be reproduced by a single star model. The second component is fitted using a B star grid model with a temperature of 24 kK. The Wolf-Rayet star model has a temperature of around 71 kK and a luminosity of $\log(L/L_\odot) = 5.20$. Although the model contains no hydrogen, the line located at the H$\alpha$ position is overpredicted. Furthermore, it is the only case where the observed N IV line at around 7110 Å has a higher intensity than the He II line at H$\alpha$.

For this star the Gaia satellite measured a G band magnitude of 21.08 mag (Gaia Collaboration et al. 2018). This value is in good agreement with the observation from Neugent & Massey (2011). It is noteworthy that the analyses from Neugent & Massey (2014) suggests that the star is not a close binary, which is interesting because it is difficult to explain the formation of a putatively single Wolf-Rayet star with such a low luminosity even at solar metallicity. However, since the star is located quite close to the centre of M33 (a bit more than 1 kpc away from it) it could be located in a region with enhanced metal content.

**M33-WR076** is classified as WN4. The spectrum is shown in Fig. 8.37. It is one of the few cases where the GALEX UV photometry helped to estimate a better value for the reddening because it had to be increased to match the UV observation. Compared to the other stars it has an increased value of $E(B - V) = 0.4$ mag. As a result, the star has a luminosity of $\log(L/L_\odot) = 5.80$ and a temperature of about 61 kK. From Neugent & Massey (2014) it is unclear if the star has a close companion.

**M33-WR088** is a difficult case to estimate the luminosity because the observed optical photometry marks are nearly at the same level suggesting a reddening of $E(B - V) = 0.9$ mag. As a consequence, the luminosity is $\log(L/L_\odot) = 6.20$. In this case, the observed UV photometry is not covered, which is not necessarily a problem as there might be more young stars in the proximity of M33-WR088. However, under the assumption that the optical photometry is erroneous and that the whole UV flux is generated by the star then the star would be much fainter with a luminosity of $\log(L/L_\odot) = 5.40$. Regardless of the luminosity, the temperature is 64 kK.

Moreover, the spectrum of the star in Fig. 8.38 is also outstanding because the model suggest a relatively high terminal velocity of 2500 km s$^{-1}$, which is much higher compared to the other WN3 stars in the sample. The shape of the 4686 Å He II line suggests that the spectrum is contaminated but the blue part of the spectrum is too noisy to really identify absorption lines. Therefore, the star was handled as single star. However, Neugent & Massey (2014) found strong evidence for the existence of a close companion. Additionally, the lines have a round profile, which was tried to account for by using a rotational velocity of $v_{rot} \sin i = 1500$ km s$^{-1}$.

**M33-WR096** is classified as WN4. The spectral fit is displayed in Fig. 8.39. Neugent & Massey (2014) could not find indications of a close companion. It has a luminosity of $\log(L/L_\odot) = 5.40$ and a temperature of around 65 kK.

**M33-WR115** is a very good example of a Wolf-Rayet star with round emission lines as can be seen in Fig. 8.40. It is also a perfect example of a flat top C IV profile. To fit the observation a rotational velocity of $v_{rot} \sin i = 1500$ km s$^{-1}$ was assumed. As M33-WR088 it has a higher terminal velocity of 2300 km s$^{-1}$ compared to the other WN3 stars of the sample. Most of the lines are reproduced by a model with a luminosity of $\log(L/L_\odot) = 5.90$ and a temperature of 83 kK. However, if the star is really a fast rotator it should be deformed such that spherical symmetry is not necessarily given anymore. The star was also in the sample from Neugent & Massey (2014) but from their results it is not clear if there is a close companion.

**M33-WR119** is the second WN8 in the sample. The spectral fit is shown in Fig. 8.41. With $\log(L/L_\odot) = 5.50$ it has the same luminosity as M33-WR052 but it

has a slightly higher temperature of 35 kK. Albeit the stars are looking quite similar on the first glance, their spectra differentiate because M33-WR119 has a higher mass-loss rate.

According to Ivanov et al. (1993), the star is a member of an association they attributed the number 65.

**M33-WR133** is classified as WN3+B2I and therefore it was analysed with a composite spectrum. The optical photometry is very special because the measured V flux is much fainter than the other bands. It is possible that this is just an error but maybe the seeing during the V band observation was good enough that only the Wolf-Rayet star was measured because in Fig. 8.42 the Wolf-Rayet component is scraping the V photometry mark. However, this argument is not supported by the Gaia measurement because there a value of 17.71 mag was detected for the G band (Gaia Collaboration et al. 2018), which is in line with the other photometry. Thus, it is likely just a coincidence that the Wolf-Rayet model covers the V band photometry. Furthermore, together with the B star component the detected UV photometry is covered.

The B star component is fitted using a model with 26 kK. The Wolf-Rayet has a temperature of 67 kK and a luminosity of $\log(L/L_\odot) = 5.70$.

The star was part of the sample from Neugent & Massey (2014) where they searched for close companions for some of the Wolf-Rayet stars. From their analyses, it could be a candidate for a close binary but it cannot be unambiguously excluded that it is a single star or wide binary.

**M33-WR136** is classified as WN3 and the spectrum is shown in Fig. 8.43. Although it is a composite spectrum, Neugent & Massey (2014) have not found an indicator for the existence of a close companion. The B star component is fitted by a grid model with a temperature of 24 kK, but due to nebula emissions not all lines are reproduced. The estimated value for the luminosity of the Wolf-Rayet star is $\log(L/L_\odot) = 5.00$ and can be seen as a lower limit. When taking a look at Fig. 6.6, its position is in line with most of the other single Wolf-Rayet stars indicating that the luminosity might be plausible. For the temperature, a value of 66 kK was derived.

It should be noted that Gaia measured a much brighter G band magnitude of 18.66 mag (Gaia Collaboration et al. 2018), which deviates from the optical photometry from Neugent & Massey (2011). However, this could be an erroneous identification because the revised catalogue from Massey et al. (2016) lists at least two source there at a distance of less than 1."5 away from the Wolf-Rayet star having a V magnitude of around 18.6 mag. Thus, it could be possible that the observed photometry belongs to the Wolf-Rayet star. If this is the case, the Wolf-Rayet star would have a luminosity of $\log(L/L_\odot) = 5.60$.

**M33-WR143** is classified as WN5. Its spectrum in Fig. 8.44 contains absorption features and therefore it was analysed using a two star fit. It is noteworthy that Neugent & Massey (2014) found indicators for the presence of a close companion. The B star component was fitted using a grid model with a temperature of 17 kK. However, the strengths of the absorption lines are a bit overestimated but neither hotter nor cooler models perform better. Thus, it might be that the luminosity of

$\log(L/L_\odot) = 5.45$ of the Wolf-Rayet component is underestimated but by increasing the luminosity even further the mass-loss rate must be reduced and then the nitrogen lines will be too weak. This can only be compensated by increasing the nitrogen fraction even more. However, this is very unlikely because the nitrogen fraction is already at a solar level. By taking a closer look at the absorption line cores, they are deformed, which could point to the presence of nebula emissions. It is also possible that there are even more sources contributing to the spectrum such that also the absorption lines are contaminated.

**M33-WR144** is obviously a composite spectrum and is classified as WN2+O9I. The Wolf-Rayet star is strongly contaminated and only He II lines and possibly a N V line at around 4944 Å are identifiable as can be seen in Fig. 8.45. One might think that there is a N IV component at around 7100 Å but this is only an artefact from the normalisation because the raw spectrum has a small step there. Thus, on the first glance, it should be a hot star as it expected for a WN2.

The O star was modelled using a grid model with a temperature of 30 kK. In this case, also a significant shift between the radial velocities of the two stars was measured. However, Neugent & Massey (2014) were not able to identify a close companion. This could hint to a possible runaway nature of M33-WR144. Runaway Wolf-Rayet stars are also observed in our own Galaxy (Marchenko et al. 2010).

The model Wolf-Rayet star model is presented in Fig. 8.45 has a temperature of 141 kK and a luminosity of $\log(L/L_\odot) = 5.70$.

**M33-WR151** is classified as WN3. Its spectrum in Fig. 8.46 is a perfect example of a round line star. To account for the effect the model was calculated with a rotation speed of $v \sin i = 2000 \, \text{km s}^{-1}$. This velocity exceeds the critical rotation velocity of the star but with a co-rotating wind the rotation speed of the core would be smaller because we see the rotation velocity of the co-rotating wind.

For the luminosity of the star a value of $\log L/L_\odot = 6.2$ and a temperature of 63 kK were derived. Thus it is one of the brighter stars in the sample. It has also a Gaia G band magnitude which is similar to the observed V band photometry. Neugent & Massey (2014) found evidence that the star is part of a close binary system.

**M33-WR152** is classified as WN7. Although it has some absorption features in the blue part of its spectrum in Fig. 8.47, a single star fit was applied because it reproduces the absorption lines. The star has a luminosity of $\log L/L_\odot = 6.20$ and an estimated temperature of around 36 kK. According to Ivanov et al. (1993) it is part of an association which they attributed the number 71. Furthermore, Neugent & Massey (2014) found strong evidence that it has a close companion.

**M33-WR154** is classified as WN4. By taking a look at the spectral fit in Fig. 8.48 it seems that the star is contaminated in the red part of the optical spectrum because the He II line at H$\alpha$ and the N IV line at around 7100 Å have intensities comparable to the C IV emission at around 5800 Å. This cannot be reproduced by a single star model. Furthermore, the He II lines at H$\delta$ and H$\gamma$ have very roundish profiles in contrast to the other lines in the spectrum. This could indicate that also the green part of the spectrum suffers from contamination, which would also explain why the smaller He II in the blue part of the spectrum are underestimated. However,

the optical photometry is not showing a strong excess to redder wavelengths but *Spitzer* infrared observation from the catalogue from Khan et al. (2015) contain a measurement, which is in a radius of 0″69 from the position of M33-WR154. The infrared *Spitzer* photometry is included in Fig. 8.48 and it is not covered by the star suggesting that it must come from some other source. Furthermore, Neugent & Massey (2014) analysed this star and they could not find indicators pointing to the presence of a close companion.

From the model a luminosity of $\log(L/L_\odot) = 6.00$ and a temperature of $63\,\mathrm{kK}$ were derived. It should also be noted that this is the only spectrum showing no nebula emissions besides a probably weak H$\alpha$ feature.

**M33-WR155** is classified as WN3 where the spectrum in Fig. 8.49 shows the contribution of another star. Thus, it was modelled as a composite spectrum where the B star component was fitted using a grid model with a temperature of $15\,\mathrm{kK}$. According to the method from Neugent & Massey (2014), it seems that there is no close companion. From the optical photometry a reddening of $E(\mathrm{B} - \mathrm{V}) = 0.6\,\mathrm{mag}$ was inferred. It might be possible that there is also a red component in the spectrum shifting the red photometry to higher values such that the reddening is overestimated. This might also explain the absorption features which can be seen on the C IV line at $5801\,\text{Å}$ and the N IV line at around $7100\,\text{Å}$. But even if the reddening is smaller it cannot explain the observed UV photometry. This suggests that there are many more hot stars in the proximity one of them being M33-WR157.

With $2000\,\mathrm{km\,s^{-1}}$ this star has a terminal velocity that differentiates from the usually adopted $1600\,\mathrm{km\,s^{-1}}$ although its temperature of about $71\,\mathrm{kK}$ and luminosity of $\log(L/L_\odot) = 5.70$ are quite similar to other WN3 stars.

**M33-WR157** is classified as WN3. As already mentioned, it is also part of the region where M33-WR155 is located. Because they are so close together, they share the same GALEX UV photometry. Although there are absorption features visible, it was treated as single star because the spectrum in Fig. 8.50 can be reproduced quite good. Thus, the contribution from other sources might not be too strong. Moreover, a composite spectrum fit would introduce other uncertainties.

For the star, a luminosity of $\log(L/L_\odot) = 5.60$ and a temperature of about $77\,\mathrm{kK}$ were obtained.

**M33-WR158** is classified as WC4. The spectrum in Fig. 8.51 is most likely heavily contaminated because the emission lines are rather weak for a WC4 star. Since no companion can be clearly identified it was still analysed as single star. From the model a temperature of only $60\,\mathrm{kK}$ was obtained, which seems to be too small. The luminosity was found to be $\log L/L_\odot = 5.9$.

**M33-WR162** is classified as WN4. According to the criteria of Neugent & Massey (2014), it could be a close binary. However, the spectrum is not suffering from strong contamination and therefore it was treated as single star. From the spectrum in Fig. 8.52 a luminosity of $\log(L/L_\odot) = 5.55$ and a temperature of $66\,\mathrm{kK}$ were derived.

**M33-WR163** was already discovered by Humphreys & Sandage (1980) and re-observed several times later (Spiller 1992; Corral 1996; Massey et al. 1996; Mochejska

et al. 2001). Humphreys & Sandage (1980) classified it as an LBV candidate but Massey et al. (1996) reclassified it as Of/WN9 stars, which are also called slash stars. These are believed to be quiescent LBVs but it cannot be excluded that they become active again. Therefore, the appearance can drastically change over a period of a few years. By comparing the V band brightnesses through the years one can see that it slightly changed. While it was at around 18.03 mag in November 1993 (Massey et al. 1996) it increased to 17.91 in October/November 1999 (Mochejska et al. 2001). Until September 2000 it was still at 17.95 mag (Neugent & Massey 2011) so it did not change significantly during this year.

Fig. 8.53 shows the spectrum that was taken by Neugent & Massey (2011). From the spectral fit a luminosity of $\log(L/L_\odot) = 5.50$ and a temperature of 24.5 kK were derived. In Fig. 8.54 an older spectrum of M33-WR163 is shown from Corral (1996), which was taken in January 1994. Unfortunately, it is difficult to compare the spectra because the y axis is not labelled. Nevertheless, the line ratio can be compared. On a first glance the two spectra are quite similar but the He I feature between 4400 and 4500 Å is stronger in the spectrum from Neugent & Massey (2011). Thus, mass-loss rate and/or temperature have slightly changed between the two observations.

**M33-WR164** is classified as WC6 and the spectral fit is shown in Fig. 8.55. It has a luminosity of $\log(L/L_\odot) = 5.70$ and a temperature of 60 kK. The unexpected low temperature might be caused by the high mass-loss rate such that $\tau_{\mathrm{Ross}} = 20$ is still located inside the wind of the star. Thus, the given temperature here is not representing the stellar surface. Moreover, there are indications that the star could have a close companion according to the method from Neugent & Massey (2014). If it is a compact object, it might accrete material from the stellar wind, which could lead to the emission of X-Rays.

**M33-WR167** is classified as WN3 and he spectrum displayed in Fig. 8.56. The star has a temperature of 63 kK and a luminosity of $\log(L/L_\odot) = 5.70$. The terminal velocity is 1500 km s$^{-1}$, which is slightly lower than the usually adopted 1600 km s$^{-1}$. Neugent & Massey (2014)found strong evidence that the star could have a close companion.

**M33-WR168** is the second variable star that was identified in M33 nearly 100 years ago (Duncan 1922). It is classified as Of/WN9 and its spectrum in Fig. 8.57 looks similar to the spectrum of M33-WR205. The star has a temperature of 27.5 kK and a luminosity of $\log L/L_\odot = 5.55$.

**M33-WR170** is classified as WN3. Its spectrum is shown in Fig. 8.58. The star has a temperature of 76 kK and a luminosity of $\log(L/L_\odot) = 5.55$. It was also part of the analysis from Neugent & Massey (2014) but from their analysis it is unclear if the star has a close companion.

**M33-WR171** is classified as WN7. The spectrum in Fig. 8.59 has absorption lines but these are reproduced by the model thus, it was treated as single star. Nevertheless, *Spitzer* infrared measurements in the catalogue from Khan et al. (2015) detected a source which is located in a radial distance of 0″48 away from M33-WR171. Thus, it could be possible that the observed optical spectrum suffers from contamination. The increase in flux beyond 8 μm could come from PAH and dust

emissions from a near H II nebula (Humphreys et al. 2014). From the optical photometry, a luminosity of $\log(L/L_\odot) = 5.45$ and a temperature of 38 kK were derived. The observed GALEX UV photometry cannot be generated by the star alone. From Fig. 5.2 it can be concluded that the star is located inside a cluster. In their analysis, Neugent & Massey (2014) could not find evidence for the existence of a close companion.

**M33-WR172** is a broad lined WN3 star that was fitted as composite spectrum to account for contamination. Neugent & Massey (2014) have not found indicators for the presence of a close companion. The star has a temperature of about 75 kK and a luminosity of $\log(L/L_\odot) = 5.20$. Noteworthy is the high terminal velocity of 2000 km s$^{-1}$. It could be possible that the star has a non-negligible rotational velocity but due to the low signal-to-noise of the spectrum in Fig. 8.60, this cannot be confirmed.

**M33-WR173** is the second WN5 star in the sample. In contrast to M33-WR143, there are no signatures of another source in its spectrum in Fig. 8.61 but *Spitzer* observations in the catalogue from Khan et al. (2015) contain another source in a radius of 0.″33 from M33-WR171. The model was calculated without hydrogen because the He II feature at H$\alpha$ is already overestimated. However, the infrared source might lead to a contamination of the red part of the spectrum. This could explain why the line located at H$\delta$ is underestimated, which points to the presence of hydrogen. According to the model the star has a temperature of 52 kK and a luminosity of $\log(L/L_\odot) = 5.55$

**M33-WR174** is classified as WN4. To match the observed photometry a reddening of $E(\text{B} - \text{V}) = 0.3$ mag was assumed. The spectrum in Fig. 8.62 has an absorption component but the shape of the lines is peculiar indicating that probably more than just one additional sources is creating them. *Spitzer* observation from Khan et al. (2015) reveal an infrared source in a radius of 0.″28. Nonetheless, a single star model was used because the quality of the single star fit seems reasonable. A luminosity of $\log(L/L_\odot) = 5.70$ and a temperature of 54 kK are obtained for the star.

**M33-WR175** is classified as WN3. The spectrum in Fig. 8.63 was analysed using a two component fit. The secondary component was fitted using an O star grid model with a temperature of 40 kK. The Wolf-Rayet star has a luminosity of $\log(L/L_\odot) = 5.80$ and a temperature of around 61 kK.

The Gaia satellite measured a G band magnitude of 18.31 mag for this star, which is slightly fainter than the observed values from Neugent & Massey (2011). Additionally, the star was observed by San Roman et al. (2010) using g r i z filter and an adjusted u filter that reaches further into the UV. Their measurements confirm the observed values from Neugent & Massey (2011).

**M33-WR177** is another WN4 where the spectrum in Fig. 8.64 has a clearly visible secondary component. Therefore, it was analysed as binary. To account for the absorption lines, a B star grid model with a temperature of 24 kK was used. The Wolf-Rayet star model has a temperature of 62 kK and a luminosity of $\log(L/L_\odot) = 5.80$.

The G band luminosity of 19.61 mag from Gaia (Gaia Collaboration et al. 2018) supports the measurements from Neugent & Massey (2011).

**M33-WR178** is a very good example for a WN3 star. The spectrum is presented in Fig. 8.65. Neugent & Massey (2011) flagged it as isolated star which is further supported by the UV photometry perfectly covered by the model. Moreover, the star was observed by the Gaia satellite that measured a brightness of 21.09 mag for the G band (Gaia Collaboration et al. 2018), which is in line with the observed optical photometry. The star has a temperature of about 83 kK and a luminosity of $\log(L/L_\odot) = 5.70$. Furthermore, it has a terminal velocity of $1700\,\mathrm{km\,s^{-1}}$, which is slightly higher than usually adopted for early type WN stars. Future UV observations will be used to estimate the metallicity of this star.

**M33-WR179** is classified as WN4.5. To account for the absorption lines of He I and He II in the blue part of the spectrum in Fig. 8.66, it was analysed using a binary fit. The O star component was reproduced using a 32 kK grid model. The Wolf-Rayet star has an estimated temperature of 60 kK and a luminosity of $\log(L/L_\odot) = 5.55$.

**M33-WR180** is textbook example of a WN3 star. Its spectrum in Fig. 8.67 is best reproduced using a model with a temperature of 70 kK and a luminosity of $\log(L/L_\odot) = 5.50$. From the UV photometry it seems that the star is rather isolated.

**M33-WR182** is one the few Wolf-Rayet stars with round line profiles. To account for the shape of the lines in the spectrum in Fig. 8.68, a rotational velocity of $v_{\mathrm{rot}} \sin i = 2000\,\mathrm{km\,s^{-1}}$ was assumed. Furthermore, it has a temperature of 68 kK and a luminosity of $\log(L/L_\odot) = 5.90$. If the star is indeed a fast rotator, it might explains its enhanced terminal velocity and mass-loss rate compared to other WN3 stars.

**M33-WR191** is the last WN7 in the sample. Its spectrum in Fig. 8.69 has a small absorption component which is covered by the model using a temperature of 37 kK and a luminosity of $\log(L/L_\odot) = 5.90$. The detected UV flux is nearly covered by the star.

**M33-WR193** is classified as WC4 and the spectrum is shown in Fig. 8.70. It suffers most likely from strong contamination but it is also an extreme case of strong nebula emissions. Thus, the star is probably embedded in a dense nebula. In fact, the nebula emissions are looking very similar to observed spectra from planetary nebulae (Magrini et al. 2004). The star is part of the star forming region NGC604 and according to Drissen et al. (1993) its spectrum is highly reddened. Additionally, there are photometric marks available for the J, H and K band from Fariña et al. (2012). Combining all data, the value of $E(\mathrm{B-V}) = 0.6$ mag was estimated for the reddening resulting in a very high luminosity of $\log(L/L_\odot) = 6.40$ for the star. For the temperature a value of 56 kK was derived, which is too small for a WC4.

**M33-WR195** is the last WN5 star of the sample. The spectrum in Fig. 8.71 has no signatures of a companion. The UV photometry suggests that the star is rather isolated because it is reproduced by the model. To match all photometric marks a reddening of $E(\mathrm{B-V}) = 0.25$ mag had to be assumed. From the model a temperature of 57 kK and a luminosity of $\log L/L_\odot = 5.45$ were obtained.

**M33-WR197** is classified as WN4. Its spectrum in Fig. 8.72 includes several absorption features, which are reproduced using a grid model with a temperature of 24 kK. The Wolf-Rayet star has a temperature of 68 kK and a luminosity of $\log(L/L_\odot) = 5.50$. Compared to the single WN4 stars of the sample it has a smaller terminal velocity of $1300\,\mathrm{km\,s^{-1}}$.

According to Ivanov et al. (1993) the star is a member of an association, which they assigned the number 86. This would explain why the model is not covering the UV photometry from GALEX.

**M33-WR198** is classified as WN4. The blue end of the spectrum in Fig. 8.73 is too noisy to clearly identify absorption lines. Thus, it was analysed as single star although Neugent & Massey (2011) assigned it a crowding index of S. The optical and far UV photometry marks are covered by a model with a luminosity of $\log(L/L_\odot) = 5.60$ and a temperature of 70 kK but interestingly the near UV mark suggests that there should be another UV source. Additionally, the star was observed by Gaia and there it has a brightness of 20.86 mag in the G band, which is similar to the optical photometry.

**M33-WR199** is classified as WN3-4. The spectrum in Fig. 8.74 could be contaminated but there are no clear absorption features indicating the presence of another O or B type star. Thus, it was analysed as single star, although Neugent & Massey (2014) found evidence pointing to the existence of a close companion. According to the model, M33-WR199 has a luminosity of $\log(L/L_\odot) = 5.45$ and a temperature of 68 kK.

**M33-WR200** is classified as WC5-6. The spectrum in Fig. 8.75 contains many emission lines. From the spectral fit a temperature of 79kK and a luminosity of $\log L/L_\odot = 5.4$ were obtained. It was also observed by the Gaia satellite where the observed G band magnitude of 20.32 is in line with observed photometry.

**M33-WR201** was classified as WN3-4 star but a closer look reveals that it is a WN3. The spectrum in Fig. 8.76 is reproduced using a model with a temperature of 69 kK and a luminosity of $\log(L/L_\odot) = 5.60$. Additionally, the model contains $20\,\%$ hydrogen by mass to get the observed feature at H$\alpha$.

In the Gaia DR2 catalogue the star has a G magnitude of 20.90 mag and a BP magnitude of 20.75 mag supporting the measurement from Neugent & Massey (2011).

**M33-WR204** is the last WC star in the sample. It is classified as WC4 and the spectral fit in Fig. 8.77 gives a temperature of 100 kK and a luminosity of $\log(L/L_\odot) = 5.35$. Compared to the rest of the lines the C III/C IV feature at around $4680\,\text{Å}$ and the C IV at around $5800\,\text{Å}$ have a much stronger intensity due to the high mass-loss rate.

The observed value for the G band of 20.33 mag and the BP band of 19.94 mag are in accordance with the optical photometry from Neugent & Massey (2011).

**M33-WR205**

M33-WR205, also known as Romano's star, is the only star in the sample that was analysed before. It got its name from the Italian astronomer Giuliano Romano who observed a strong variability of the star between 1961 and 1978 (Romano 1978).

Due to its strong variability, the star was further monitored and is still observed today. The available photometric data cover a time span of more than 100 years as can be seen in Fig. 8.2. The light curve shows a strong increase in brightness at
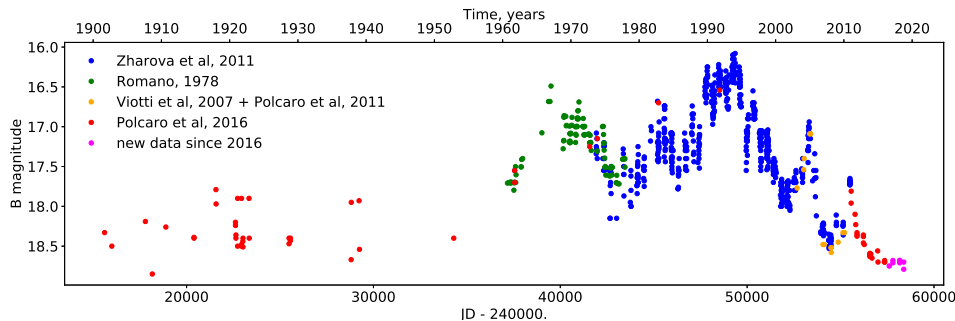


**Fig. 8.2** Lightcurve of M33-WR205 from Maryeva et al. (2019). The photometric data cover more than 100 years and show a strong increase in brightness at the beginning of the 1960s. Since the mid of the 1990s the brightness is decreasing but in 2005 and 2011 there were small outbursts again.

the beginning of the 1960s. Over a period of more than 30 years the star was very active but since the mid of the 1990s the brightness is decreasing again with two small outbursts in 2005 and 2011. During these times several spectra were taken and extensively analysed (Clark et al. 2012; Maryeva & Abolmasov 2012; Maryeva et al. 2015; Polcaro et al. 2016; Maryeva et al. 2018, 2019). Thus, it is the only star in the sample that was analysed before.

For the optical photometry the measurement from Neugent & Massey (2011) was taken but it should be emphasised again that these values were obtained in September 2001 whereas the spectra were taken in October 2010. Photometry from 2010 is given in Polcaro et al. (2016) in their Table 2 but only for the V filter. The next B band photometry that is closest to the observation is from the third January 2011. However, the V and B values differ only by 0.1 mag from the data obtained in 2001. The infrared photometry was taken from Humphreys et al. (2014) and was observed by *Spitzer* and 2MASS.

Independently of Neugent & Massey (2011), Clark et al. (2012) observed a spectrum of M33-WR205 at the end of September 2010. Thus, the two spectra are quite similar and the analysis should reveal the same parameters. For their analysis, they adopted the optical photometry from Sholukhova et al. (2011) and infrared photometry from Valeev et al. (2009). The infrared values are brighter by more than 1 mag compared to the values published in Humphreys et al. (2014) while the V band values differ by 0.2 to 0.3 mag. Additionally, they adopted a distance of 964 kpc. All these factors can be the reason why their estimated luminosity of $\log(L/L_\odot) = 5.85$ is higher compared to the luminosity derived from the spectral fit in Fig. 8.78 which is $\log(L/L_\odot) = 5.65$. The terminal velocity of $265\,\mathrm{km\,s^{-1}}$ was taken from them. The estimated temperature of 27 kK is higher by 1 kK. Hydrogen and nitrogen abundance are very similar but for the mass-loss rate I found a higher value.

**M33-WR206**

M33-WR206 is probably the most interesting WN early star of the sample. Neugent & Massey (2011) classified it as WN2pec because it has a very strong O VI line at 3811 Å as can be seen in Fig. 8.79. In contrast to the strong oxygen line, the C IV

line at 5801 Å is barely visible in the spectrum. Already Neugent & Massey (2011) noted that it would challenge our current understanding of single star evolution if the oxygen abundance is higher than the carbon abundance. The star was also A part of the sample from Neugent & Massey (2014) where they searched of close companions to Wolf-Rayet stars in M31 and M33. From their analysis, there is no evidence that the star is a close binary. Furthermore, there is a GALEX UV measurement available supporting that the seems to be isolated because the photometric observations are covered by a model with a temperature of 185 kK and a luminosity of $\log(L/L_\odot) = 5.90$. However, it should be noted that the star is in the region of parameter degeneracy between temperature and mass-loss rate. The extremely high temperature is comparable to the temperatures of the two Galactic WO2 stars WR102 and WR142, which both have 200 kK (Sander et al. 2019). In contrast to these two stars, M33-WR206 has a much smaller terminal velocity of $2000 \, \mathrm{km \, s^{-1}}$ whereas the Galactic WO2 stars have $5000 \, \mathrm{km \, s^{-1}}$. More interesting are the abundances of carbon and oxygen in M33-WR206. From the first glance by taking a look at the spectrum, one would expect a higher oxygen abundance but the spectral analysis reveals a carbon abundance by mass of around $3\% \pm 1\%$ and an oxygen abundance of only $0.9\%$. For the oxygen abundance it is difficult to estimate the uncertainty because the O VI line reacts very sensitive to temperature, mass-loss rate and abundance. The upcoming UV observation by the Hubble Space Telescope should help to get a better estimate of the oxygen and carbon abundance because the UV spectrum in Fig. 8.79 contains more of these lines. For now, the uncertainty of the oxygen abundance is about $\pm 0.2\%$. Additionally, the model includes neon because during the onset of helium burning nitrogen is transformed into neon (Iben & Tutukov 1985) but since there are no optical neon lines we will have to wait until the UV spectrum is available to estimate the neon fraction.

For this star, it might be interesting to think about its further evolution. Obviously, the star is in a transition phase right now from either WN to WC or directly from WN to WO. This phase should last for only several 10 000s years (Meynet & Maeder 2005). Afterwards, the mass-loss rate will decide its spectral appearance. If the wind becomes very thick, the spectrum might shift to a WC star spectrum because the hotter inner part is hidden by the wind. If the wind stays somewhat thin, the hot inner part is not completely covered such that the strong O VI line could remain. According to Fig. 8.3 from Georgy et al. (2009), the star is located in a region where it should evolve to a WO star before it becomes a black hole.
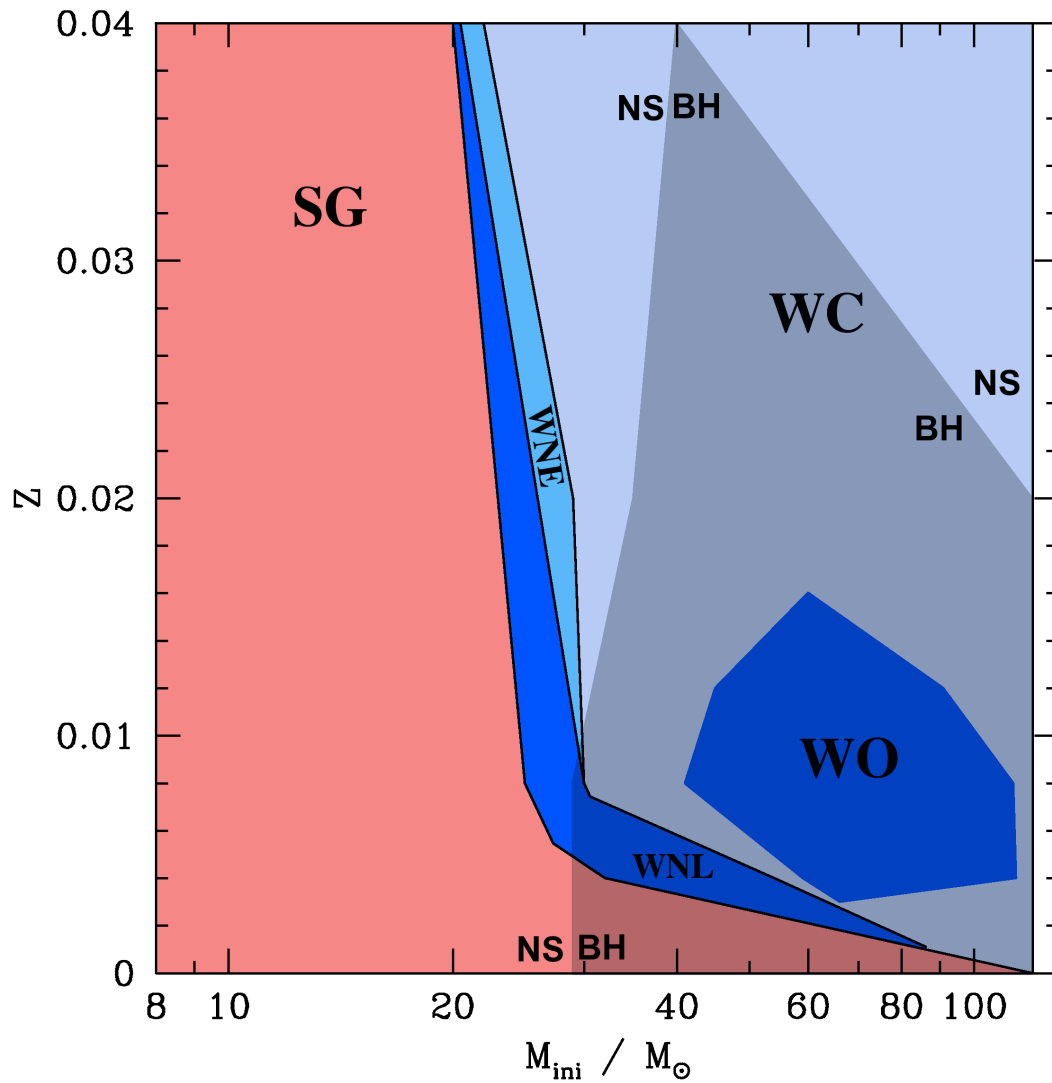
**Fig. 8.3** The final fate for massive stars shown for different metallicities from Georgy et al. (2009). M33-WR206 should evolve to a WO star before it becomes a black hole.

## 8.2 Spectral fits
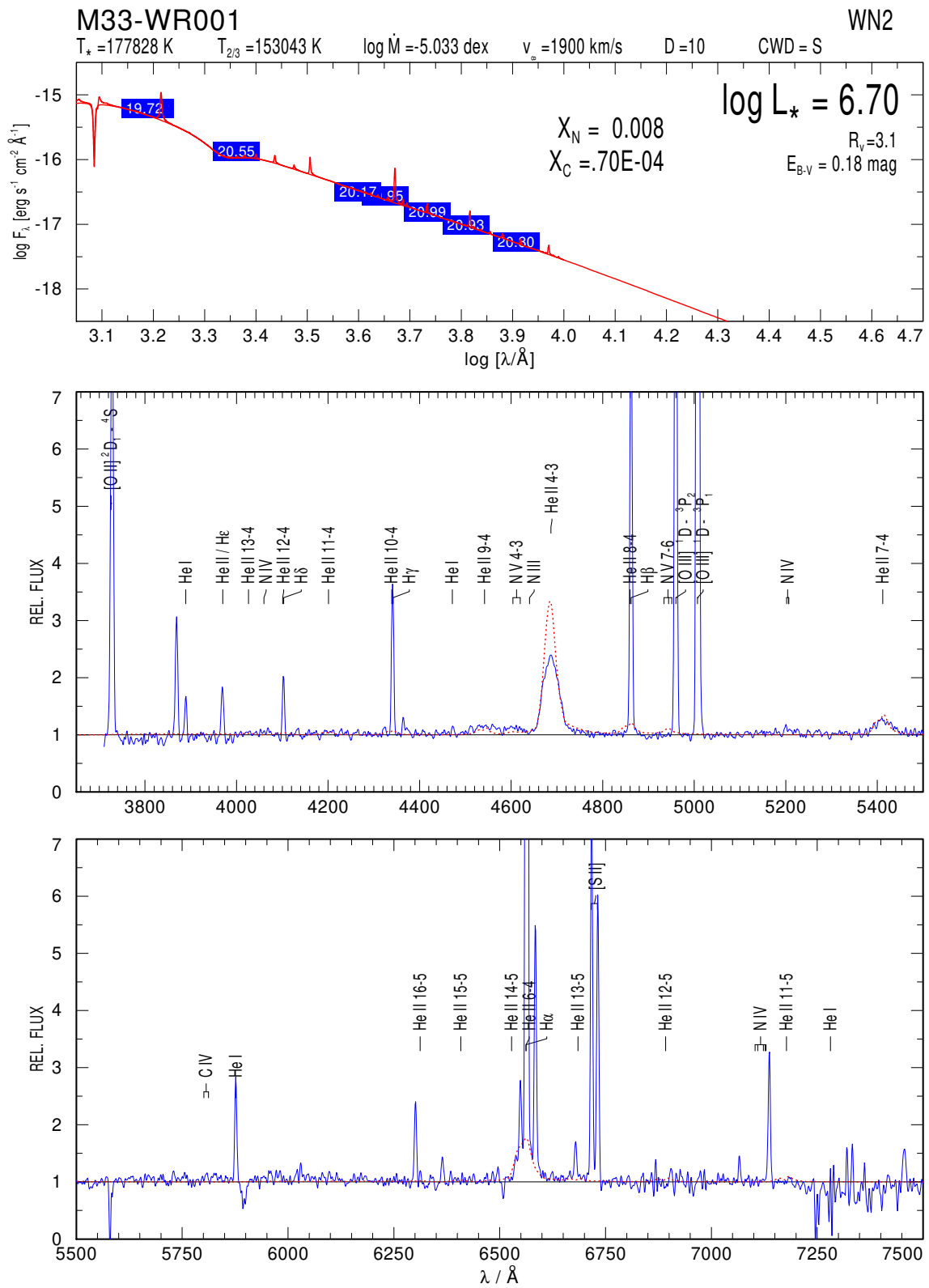
**Fig. 8.4** M33-WR001
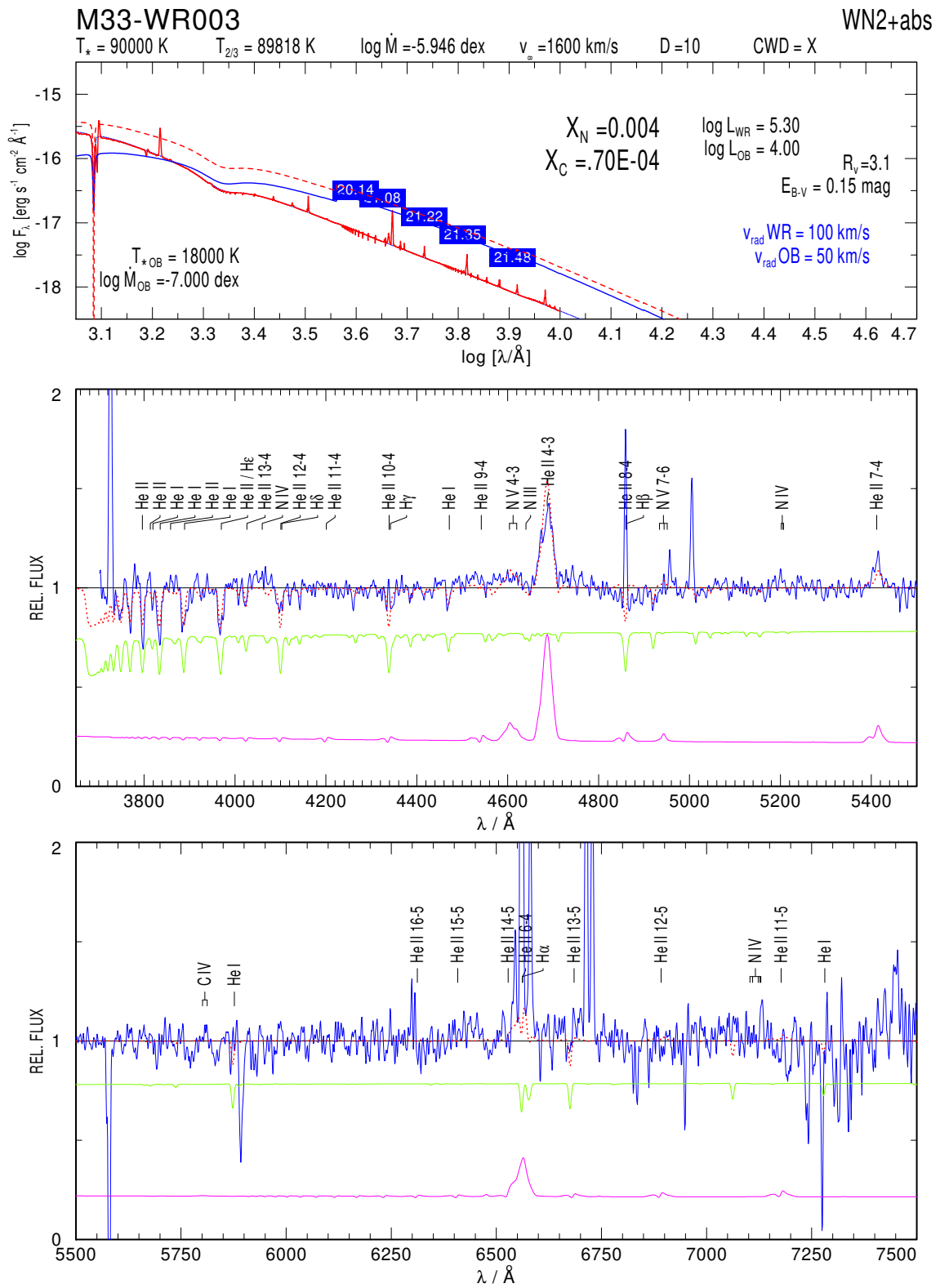
**Fig. 8.5** M33-WR002

**Fig. 8.6** Composite fit for M33-WR003
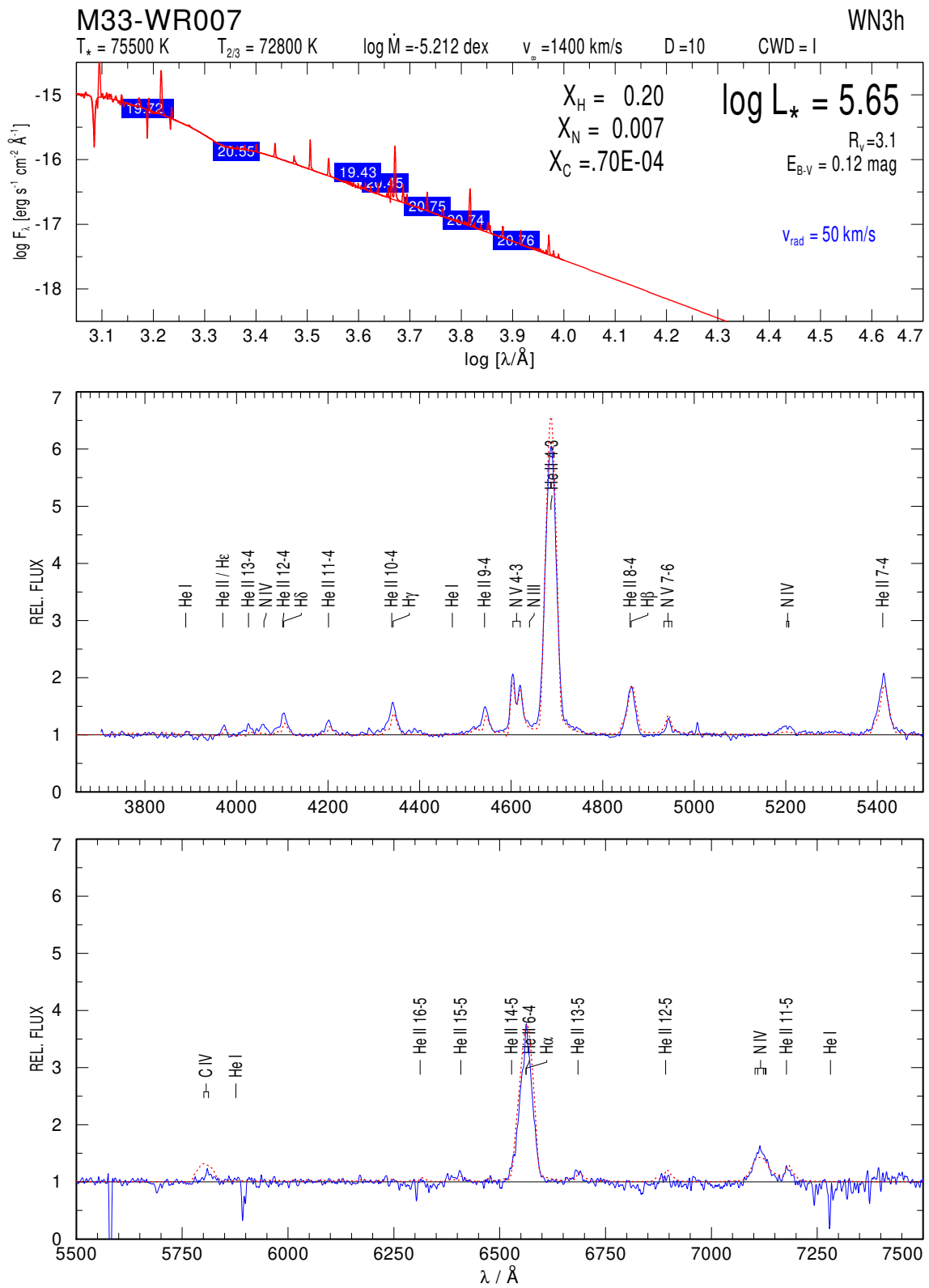
**Fig. 8.7** M33-WR007
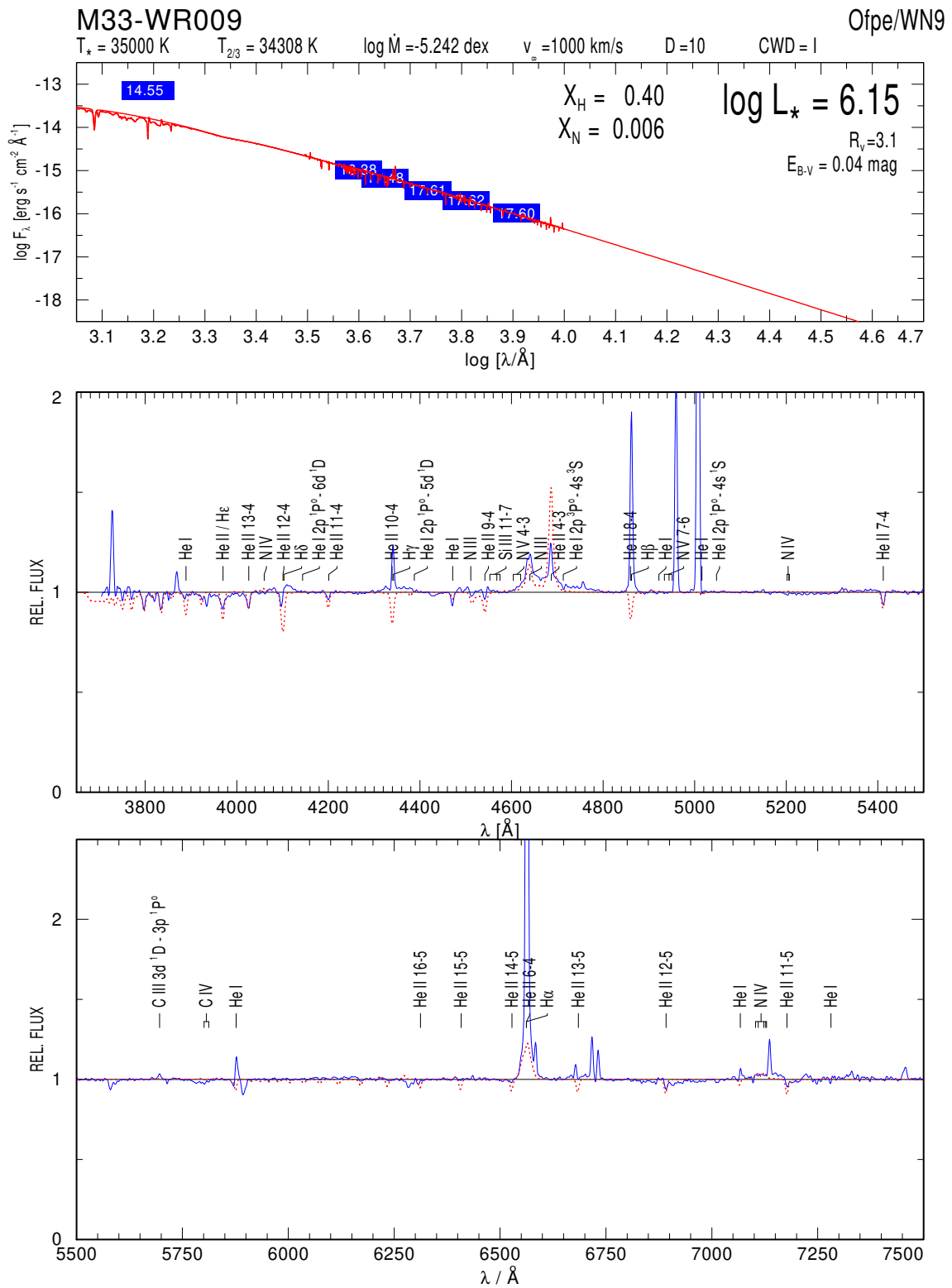
**Fig. 8.8** M33-WR009
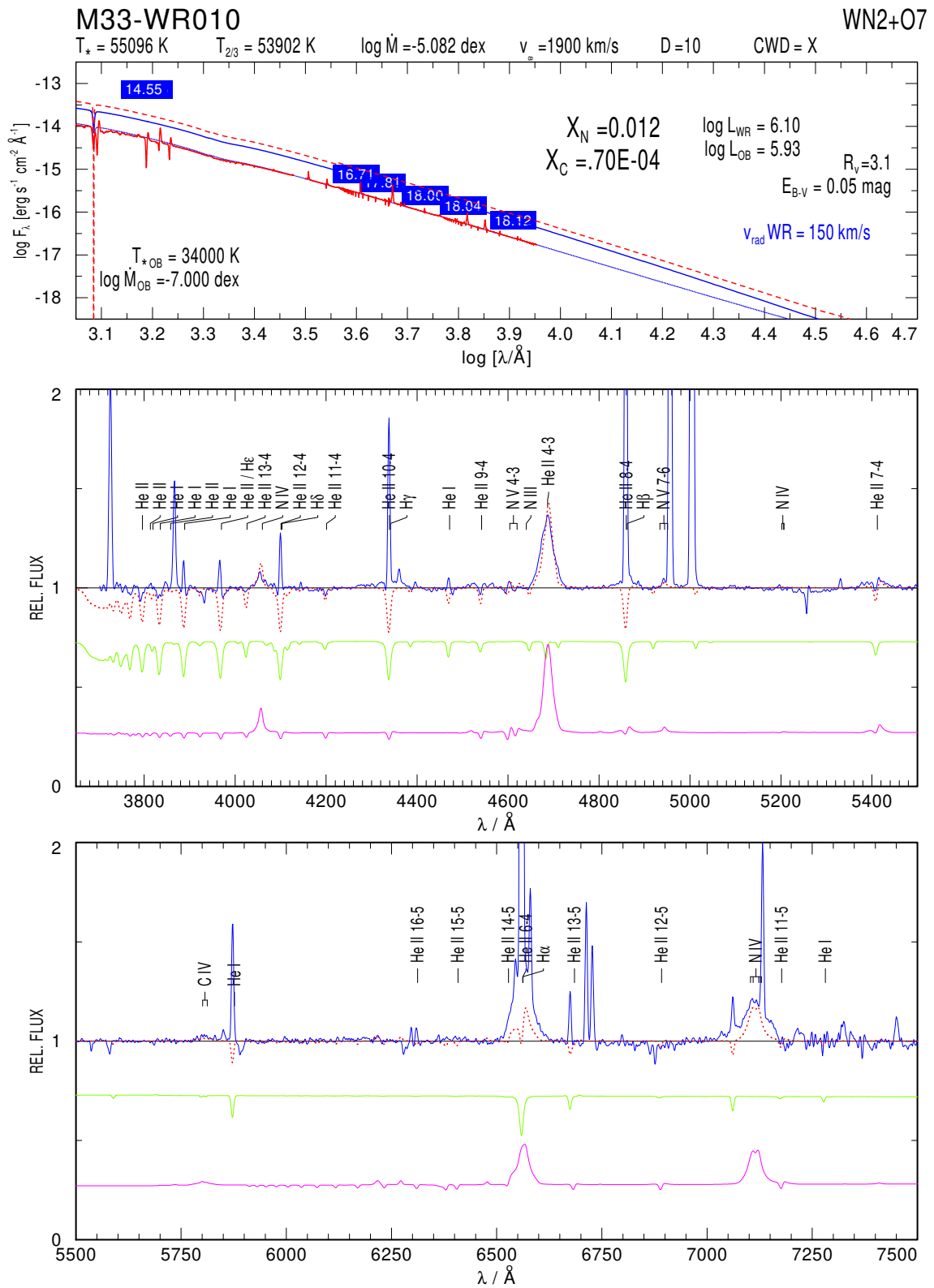
**Fig. 8.9** Composite fit for M33-WR010
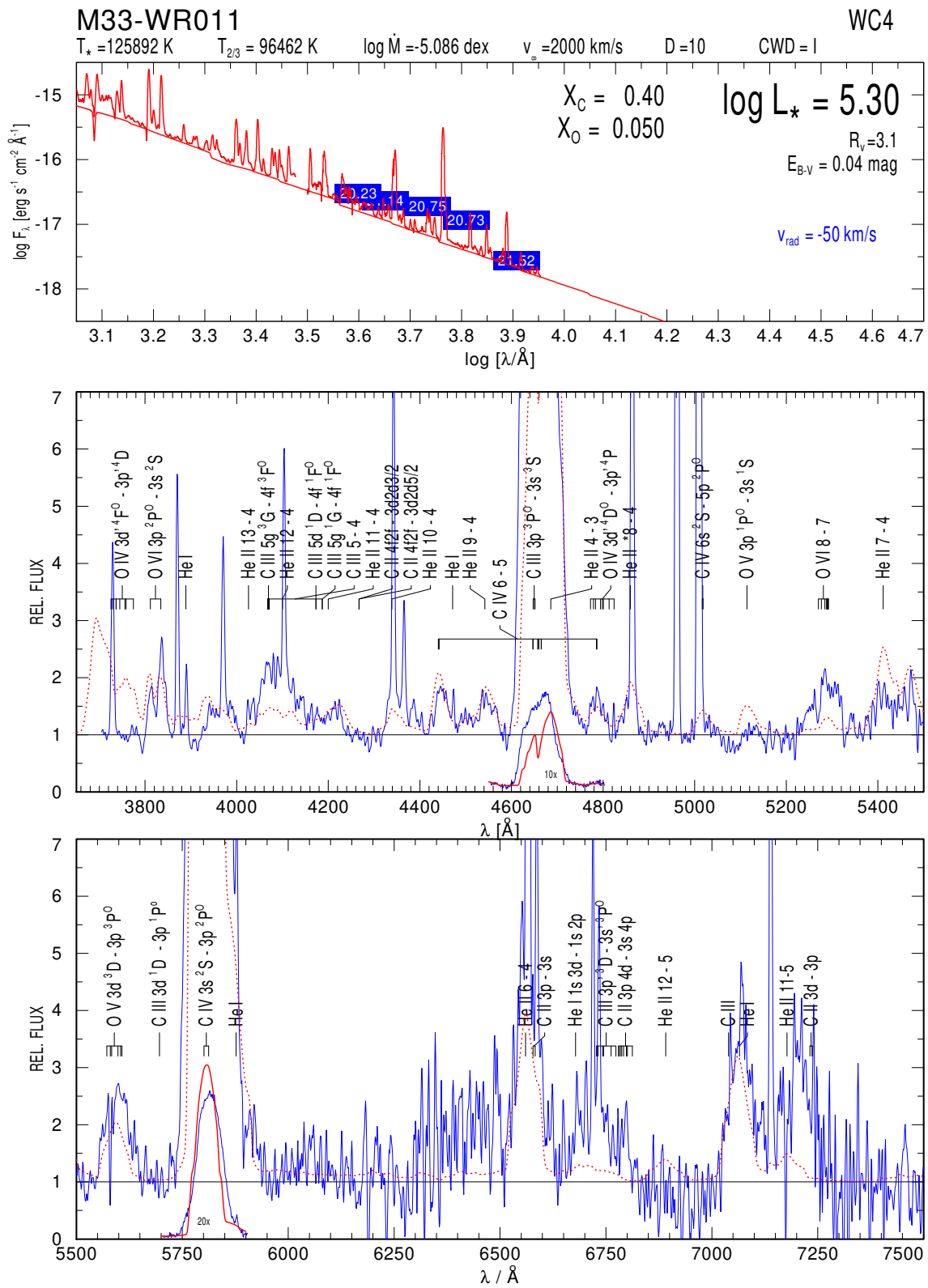
**Fig. 8.10** M33-WR011

**Fig. 8.11** M33-WR013
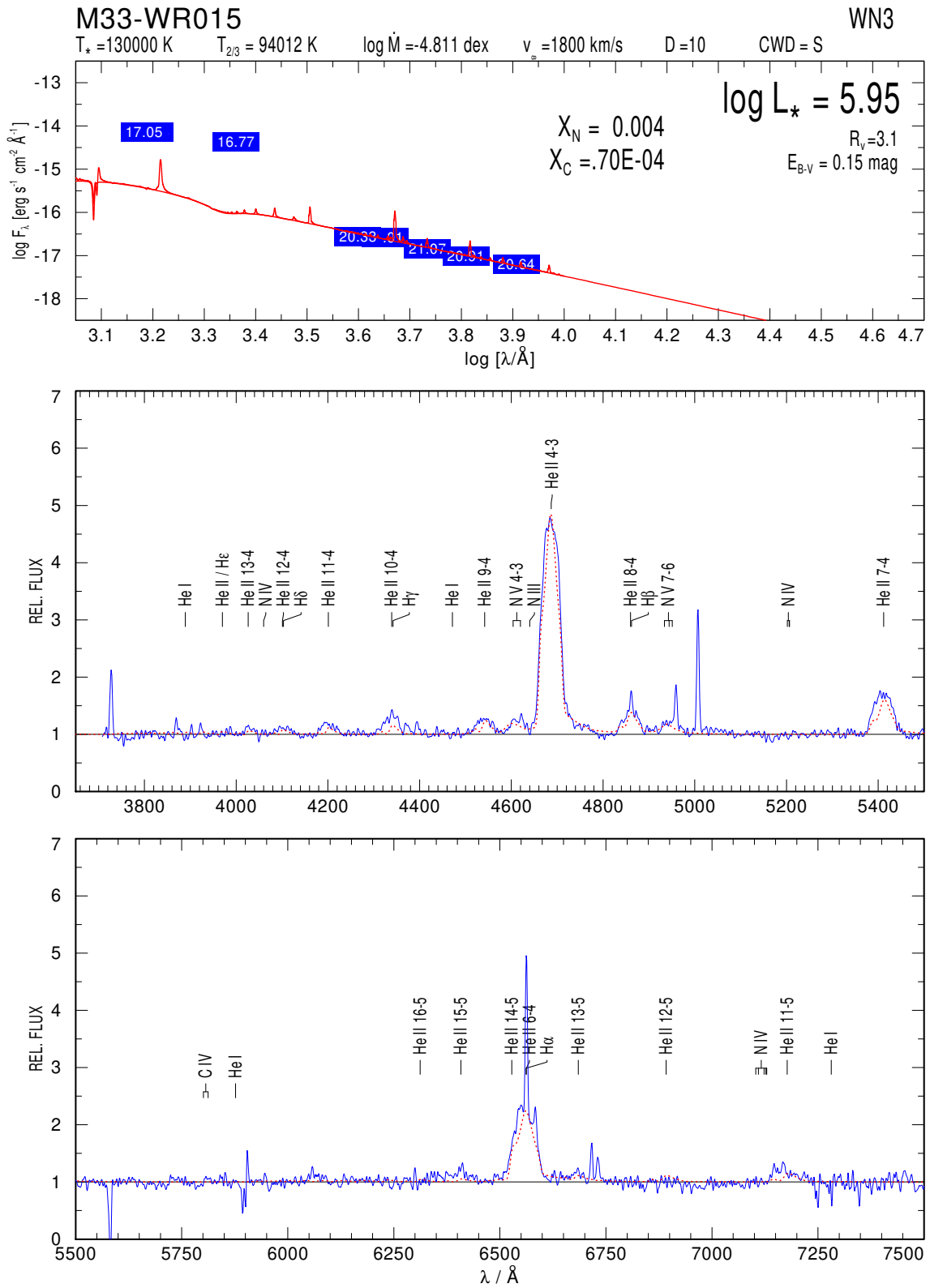
**Fig. 8.12** M33-WR015
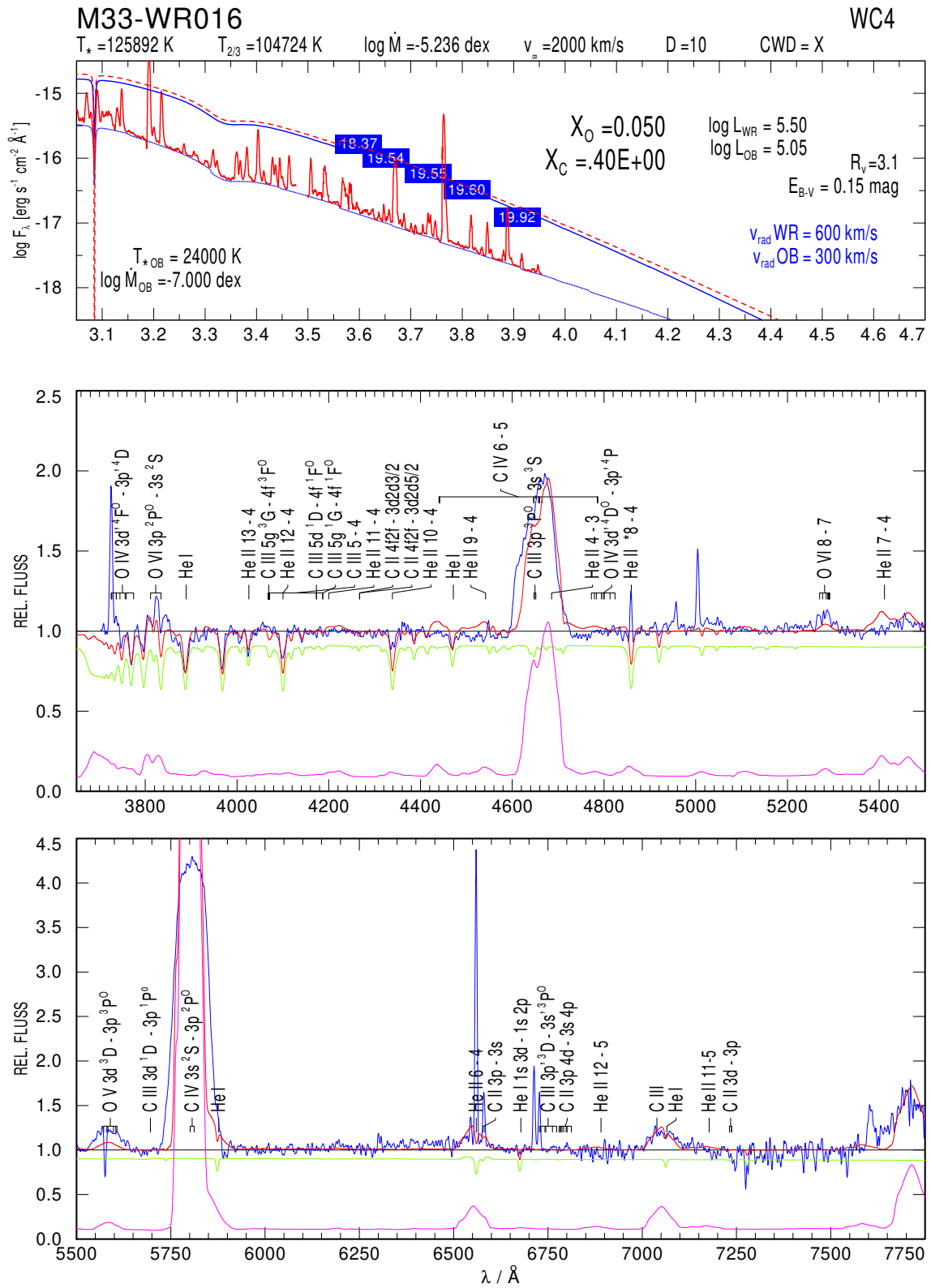
**Fig. 8.13** Composite fit for M33-WR016
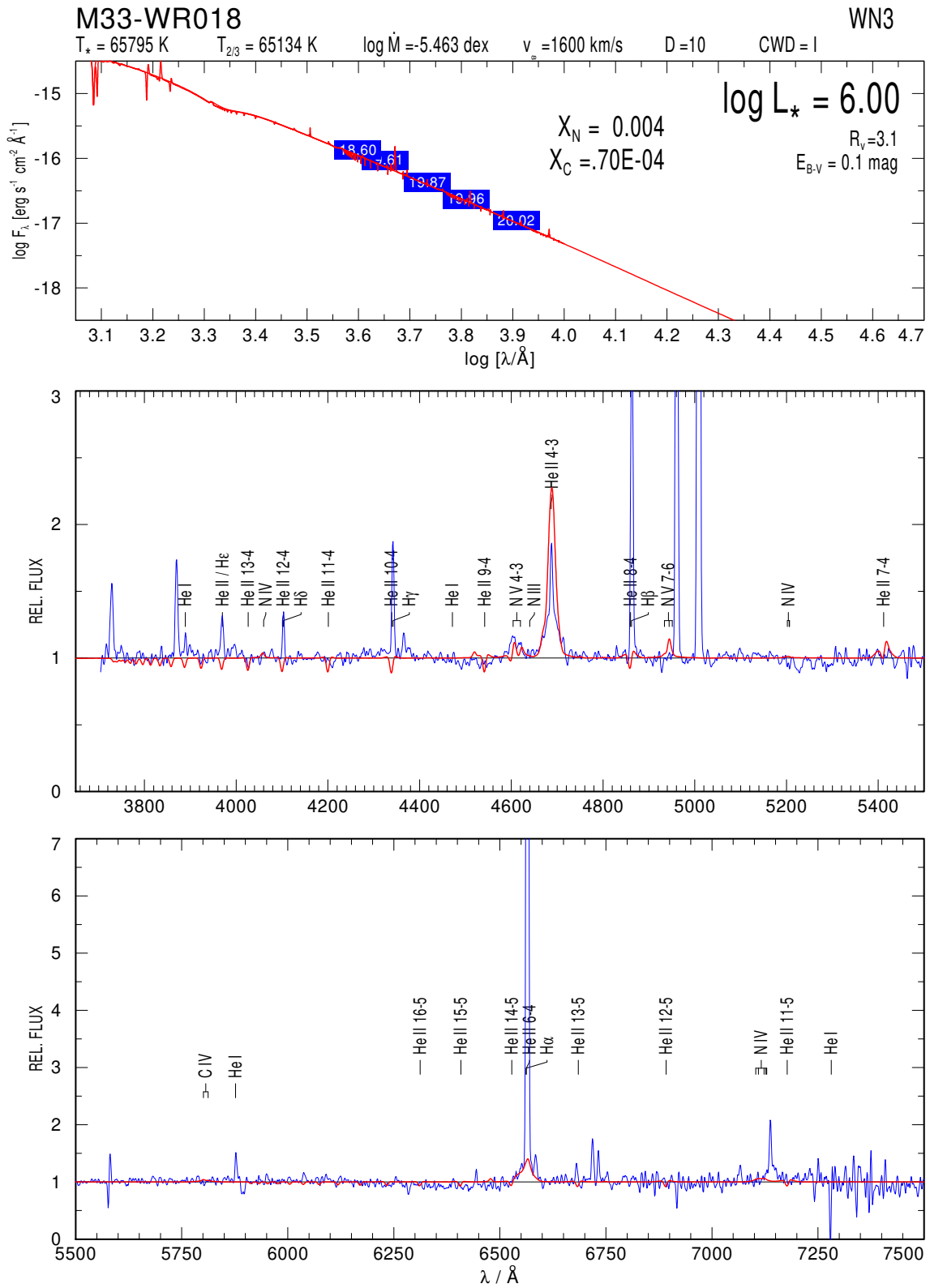
**Fig. 8.14** M33-WR018
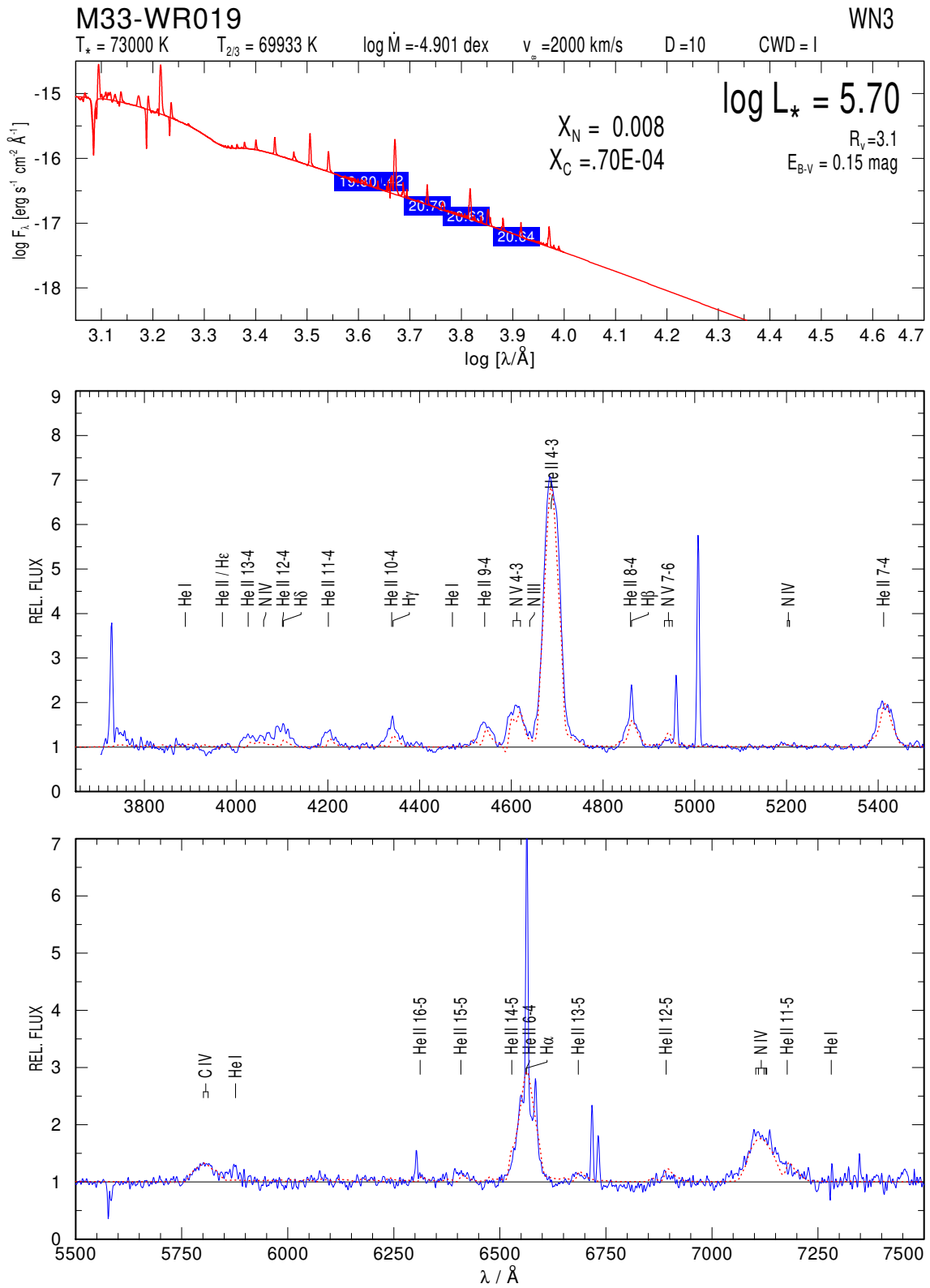
**Fig. 8.15** M33-WR019

**Fig. 8.16** M33-WR022

**Fig. 8.17** Composite fit for M33-WR027

**Fig. 8.18** M33-WR032

91
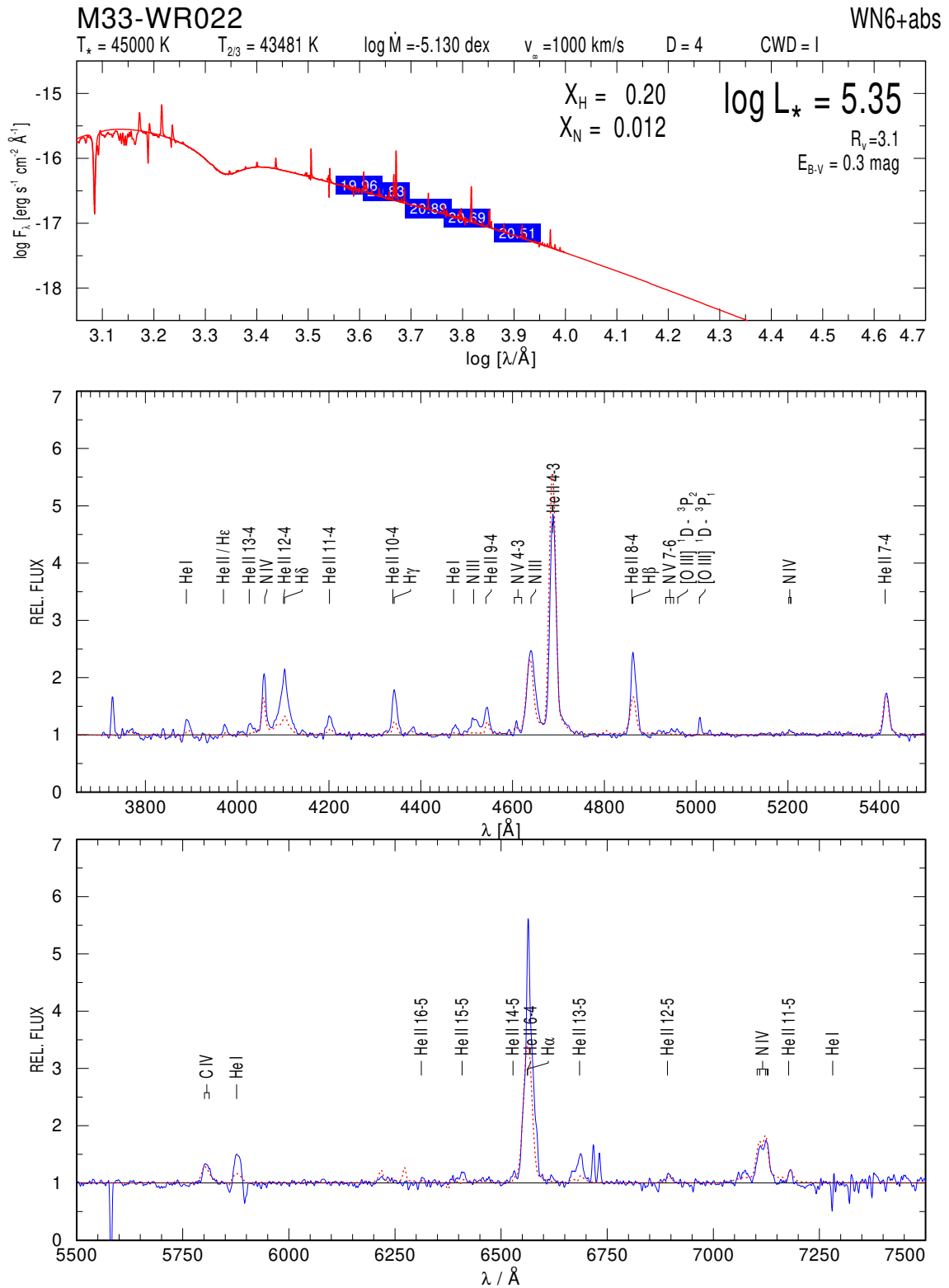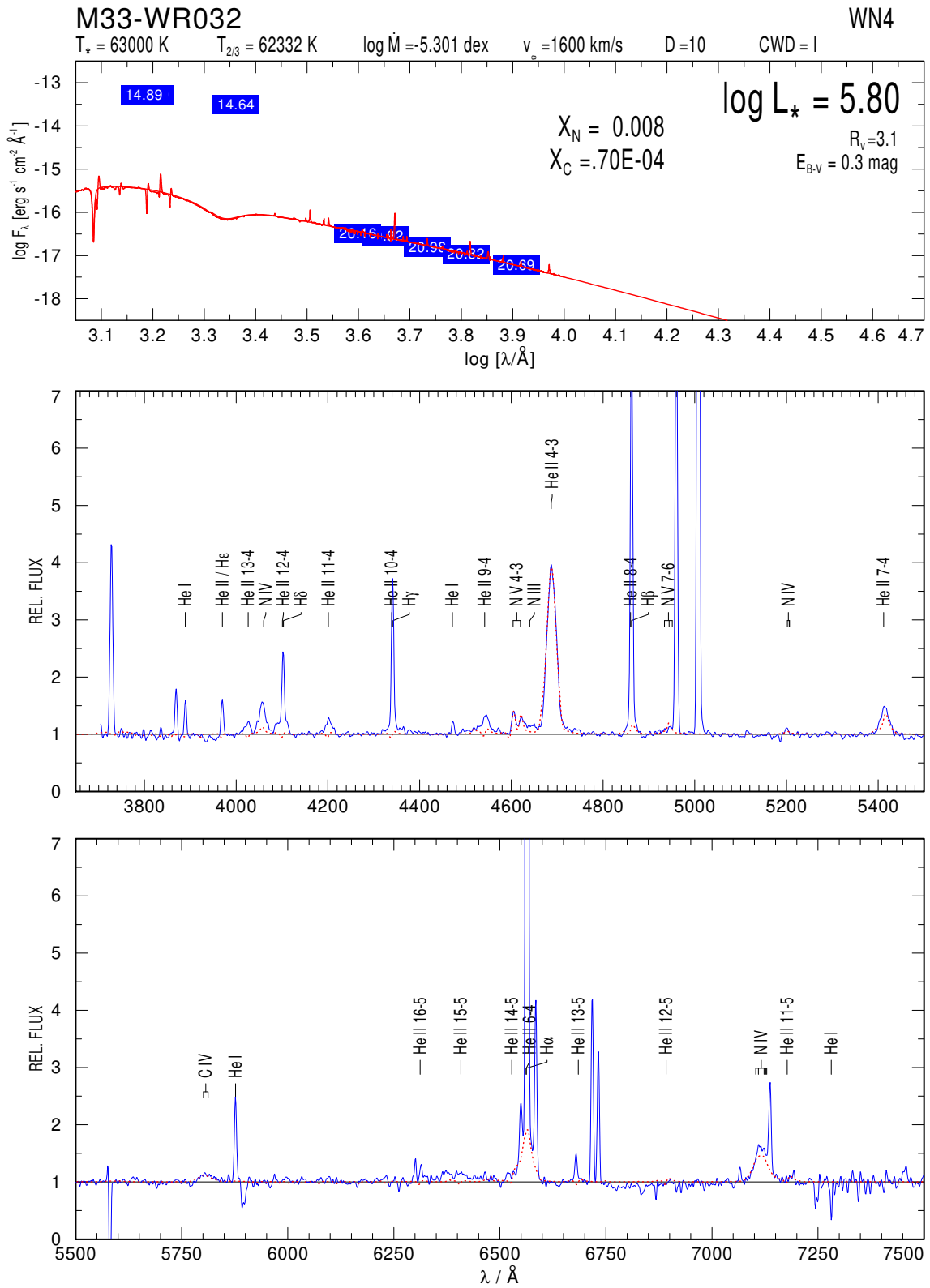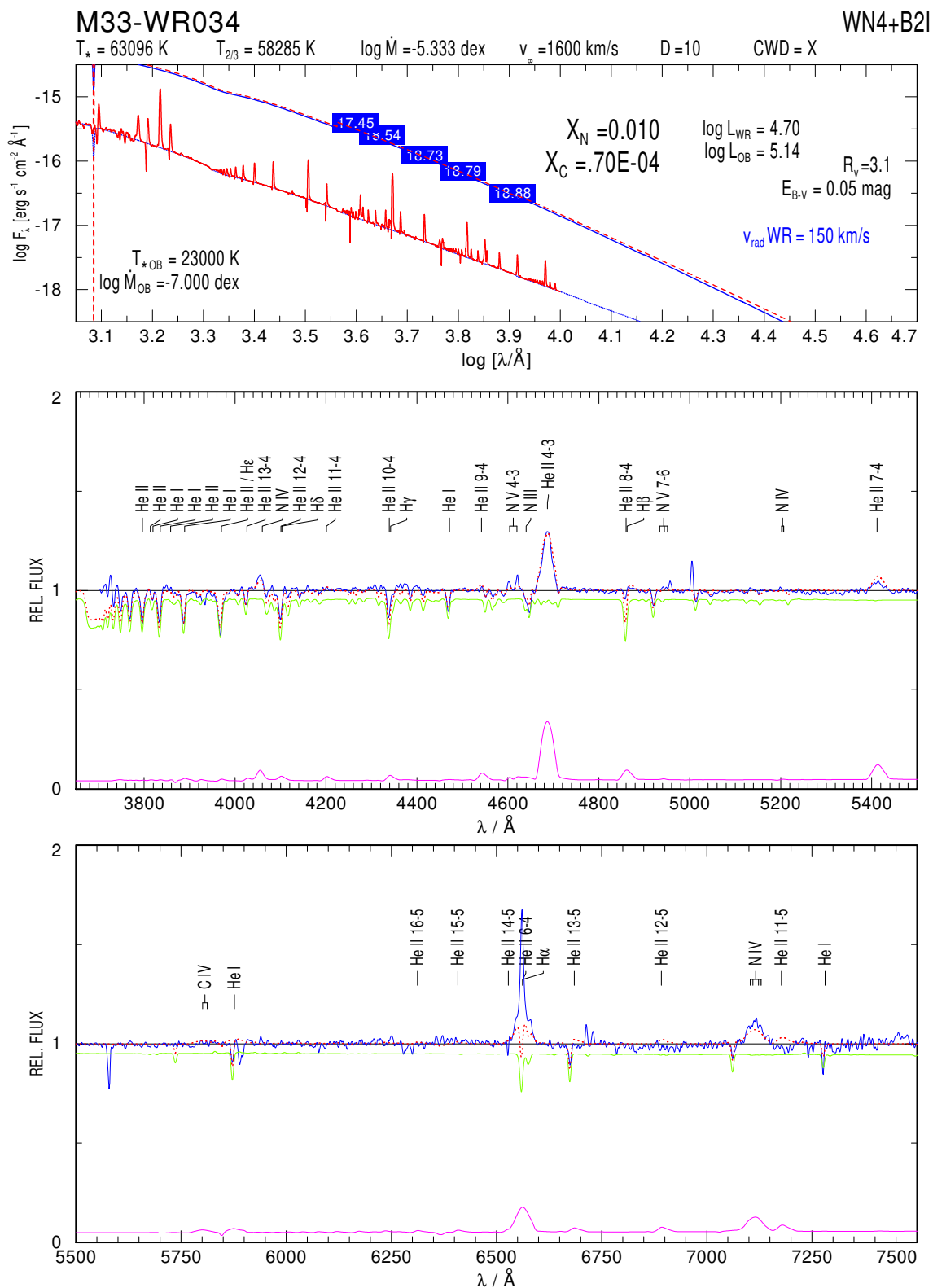
**Fig. 8.19** Composite fit for M33-WR034
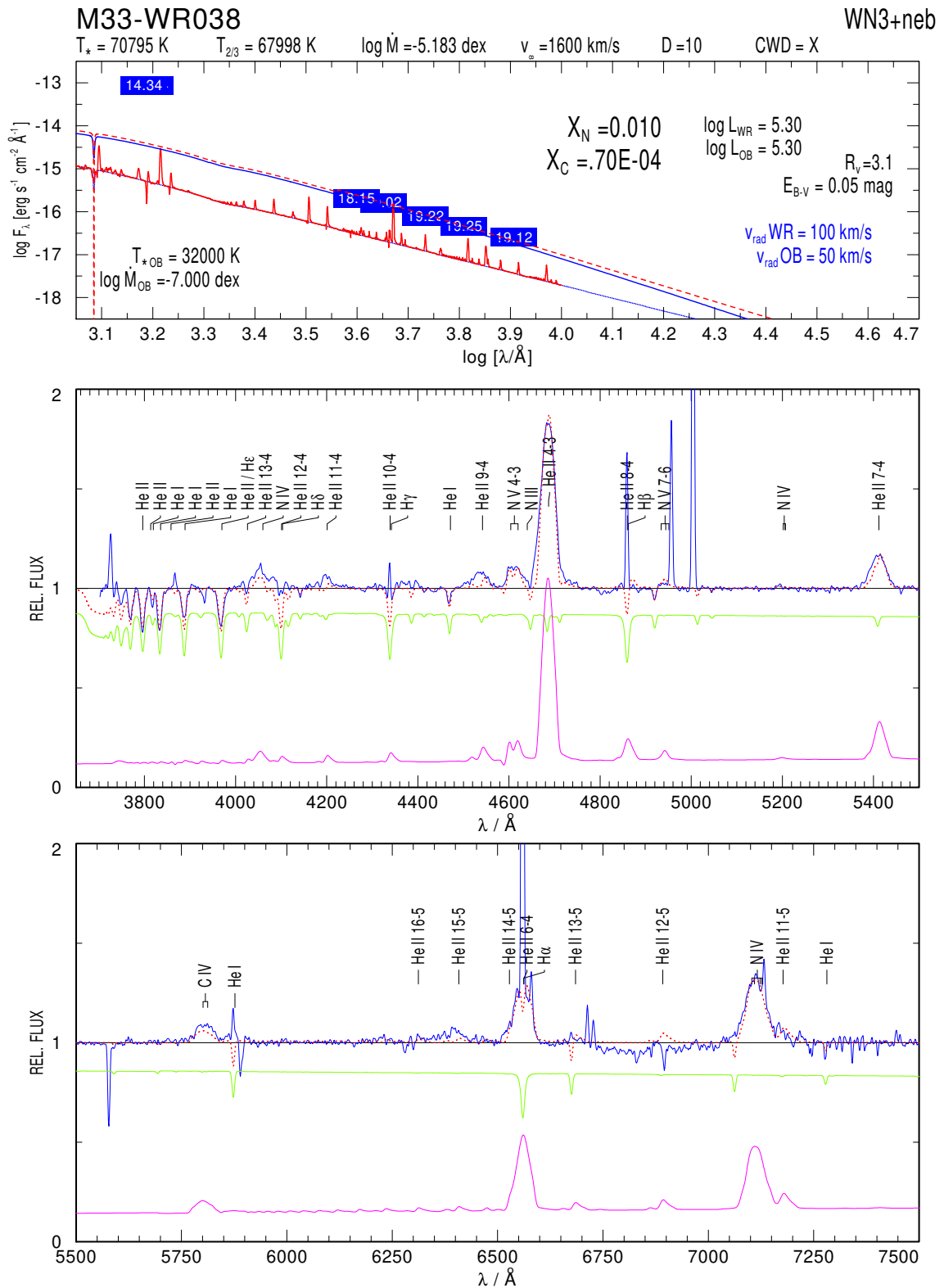
**Fig. 8.20** Composite fit for M33-WR038
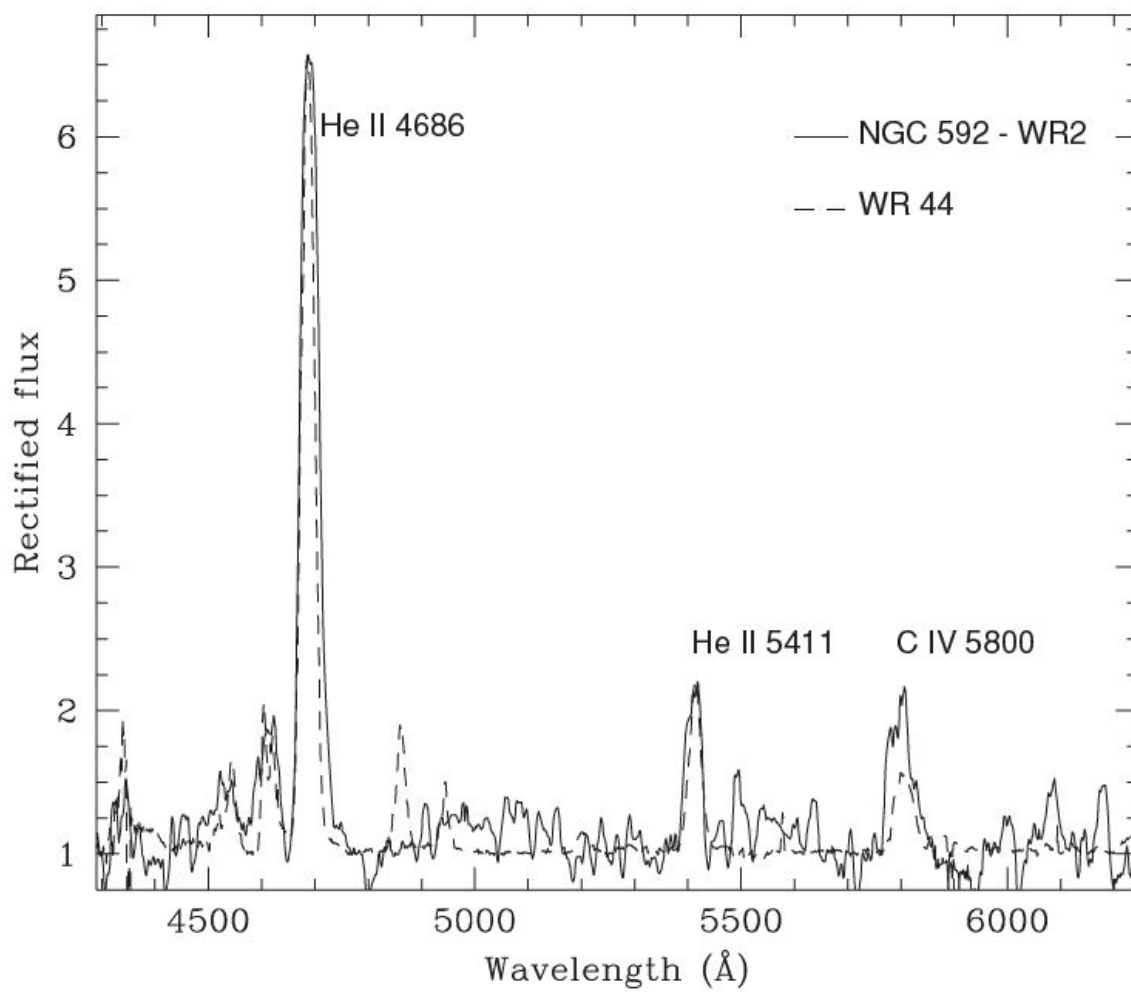
**Fig. 8.21** Spectrum of M33-WR038 from Drissen et al. (2008). It is shown together with the spectrum of the Galactic star WR44 (dotted line).
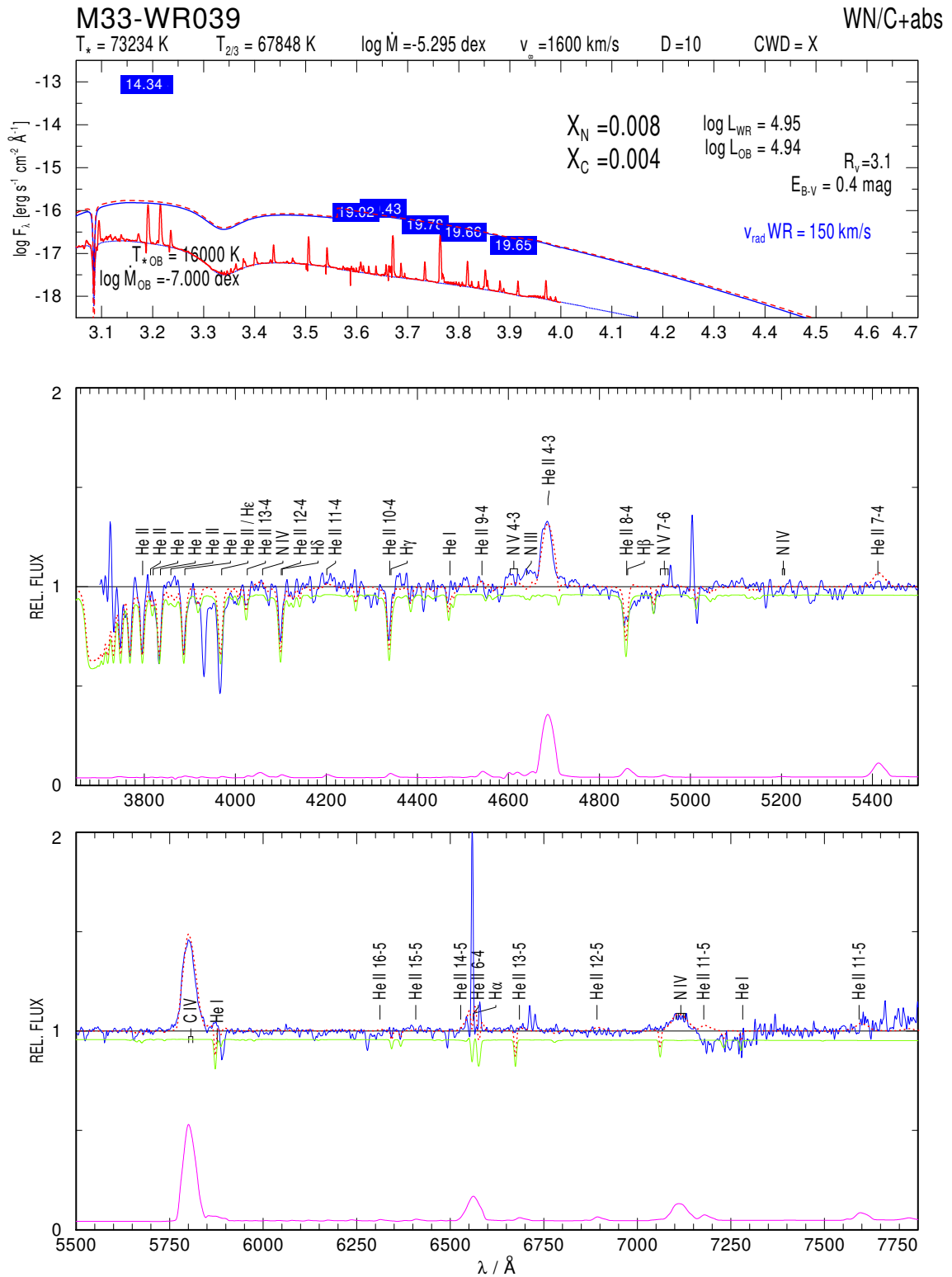
**Fig. 8.22** Composite fit for M33-WR039

**Fig. 8.23** Single star fit for M33-WR040
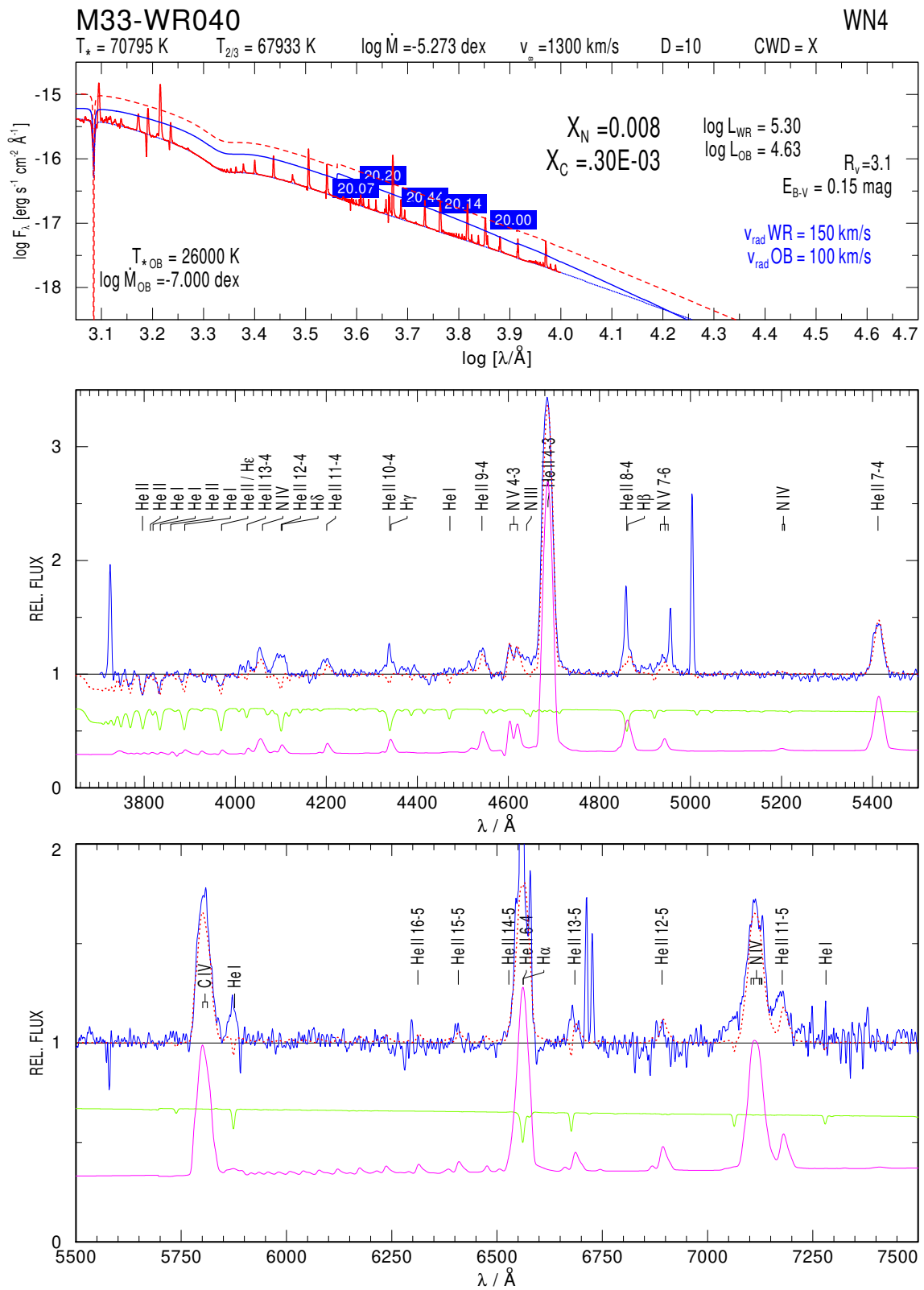
**Fig. 8.24** Composite fit for M33-WR040
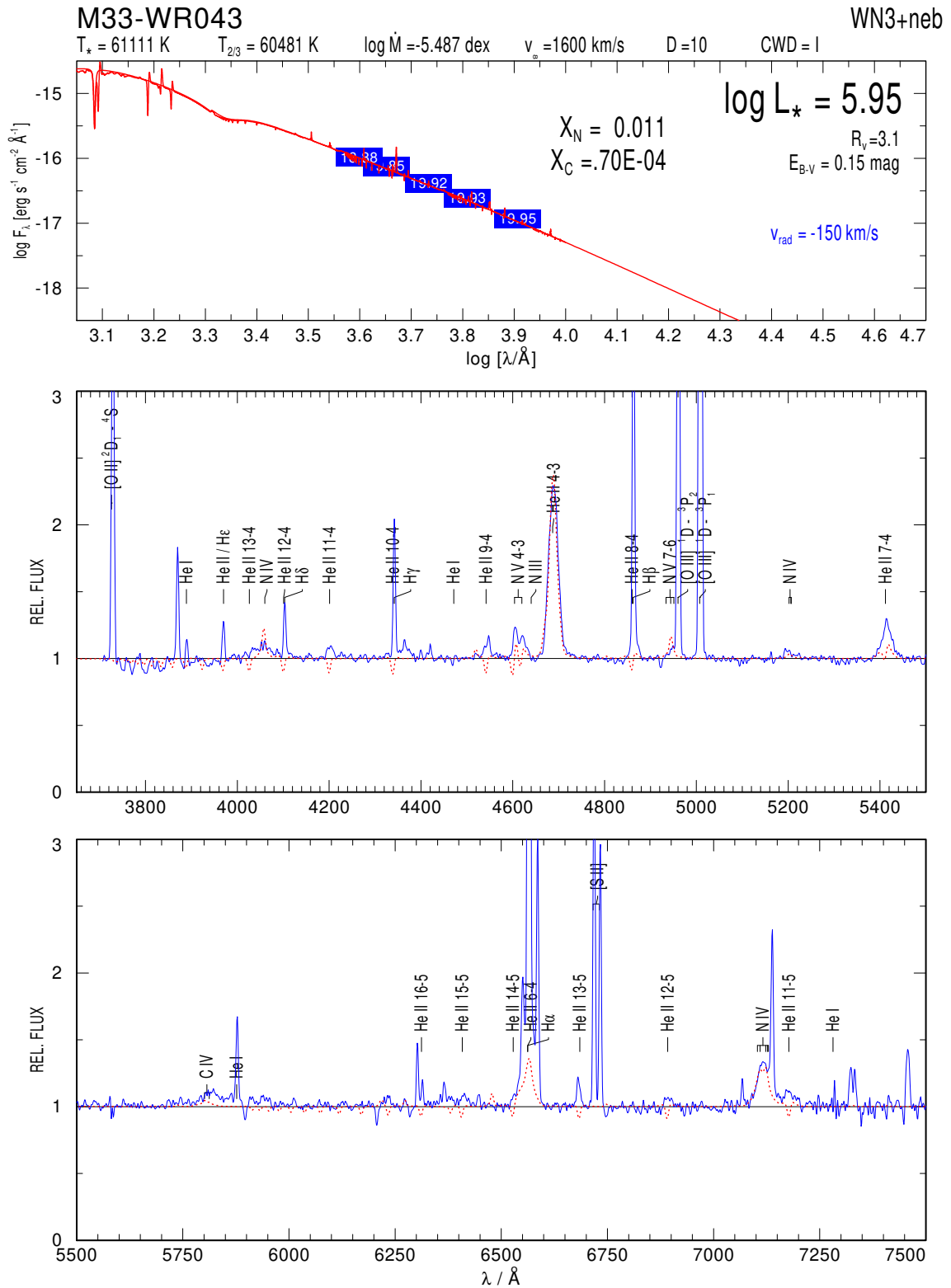
**Fig. 8.25** M33-WR043

**Fig. 8.26** M33-WR046

Fig. 8.27 M33-WR047
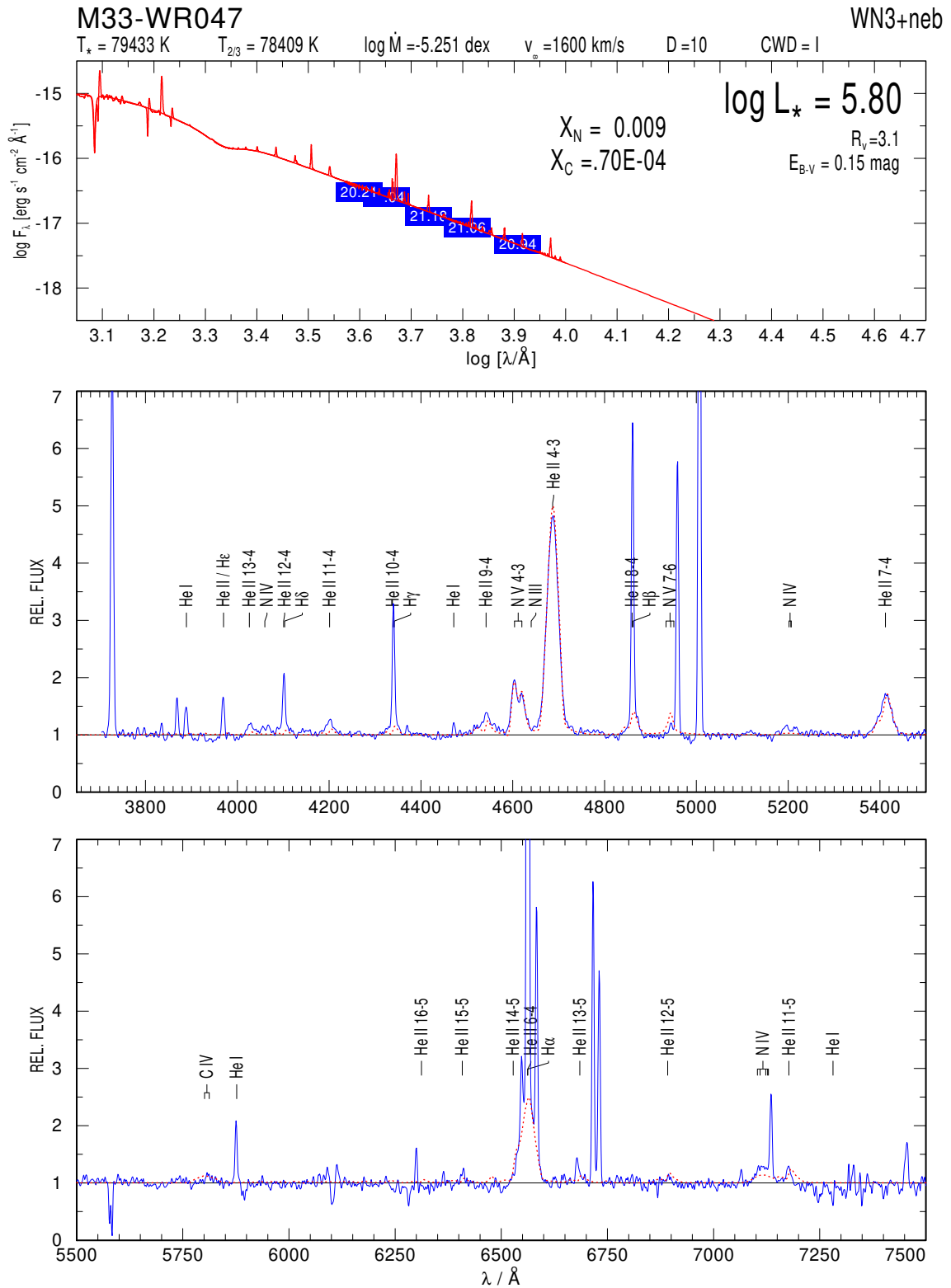
**Fig. 8.28** Composite fit for M33-WR048
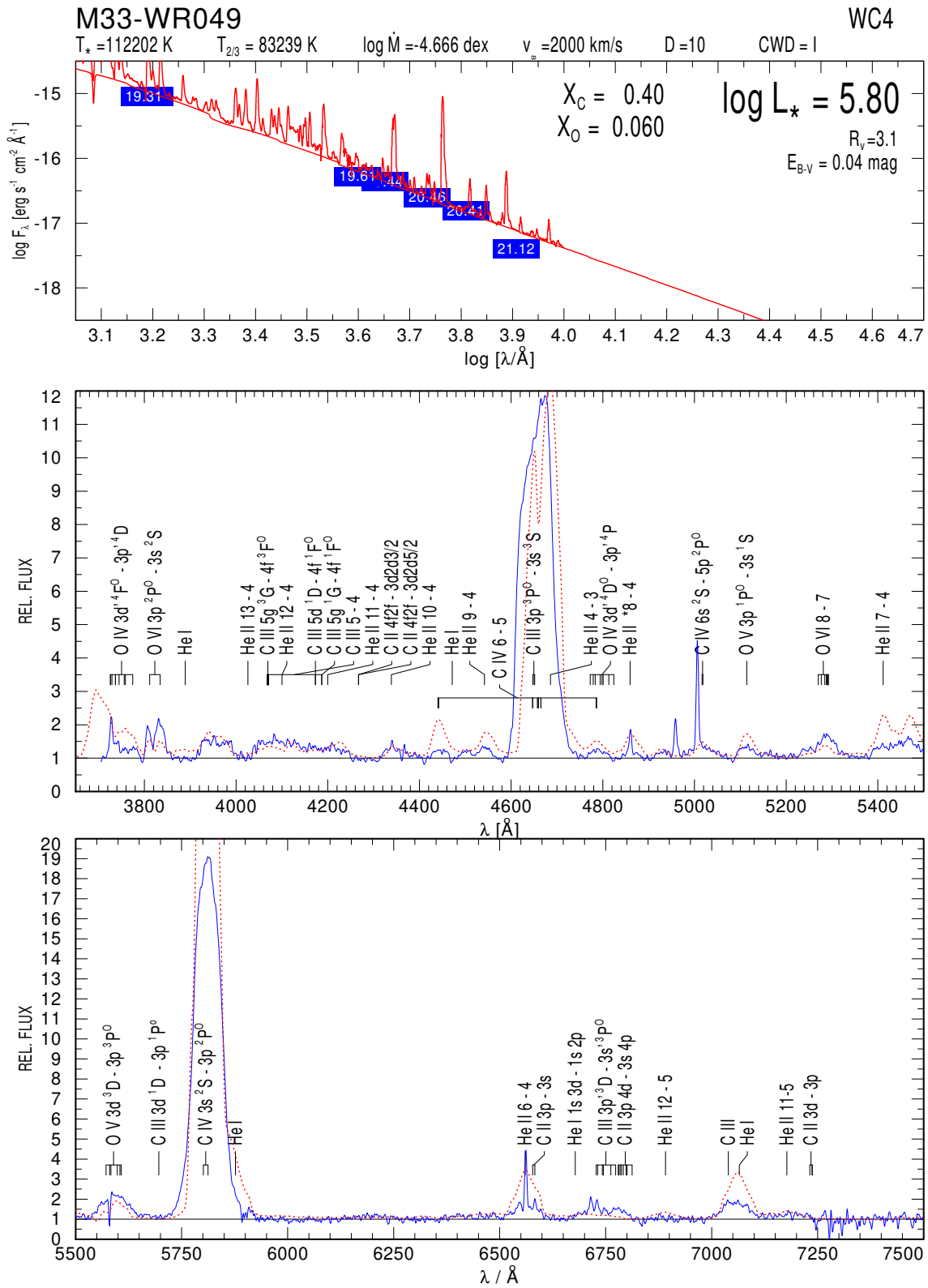
**Fig. 8.29** M33-WR049
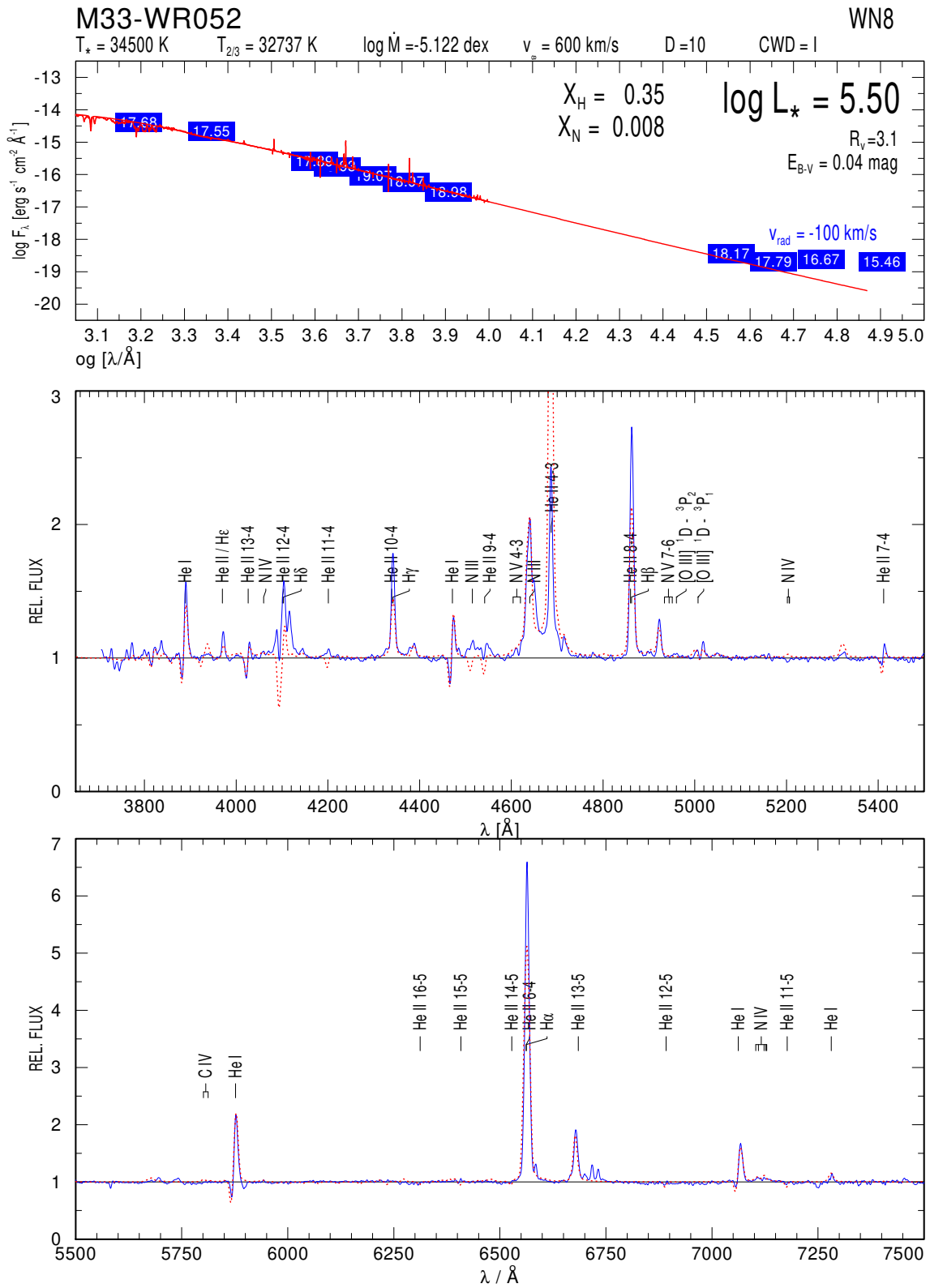
**Fig. 8.30** M33-WR052
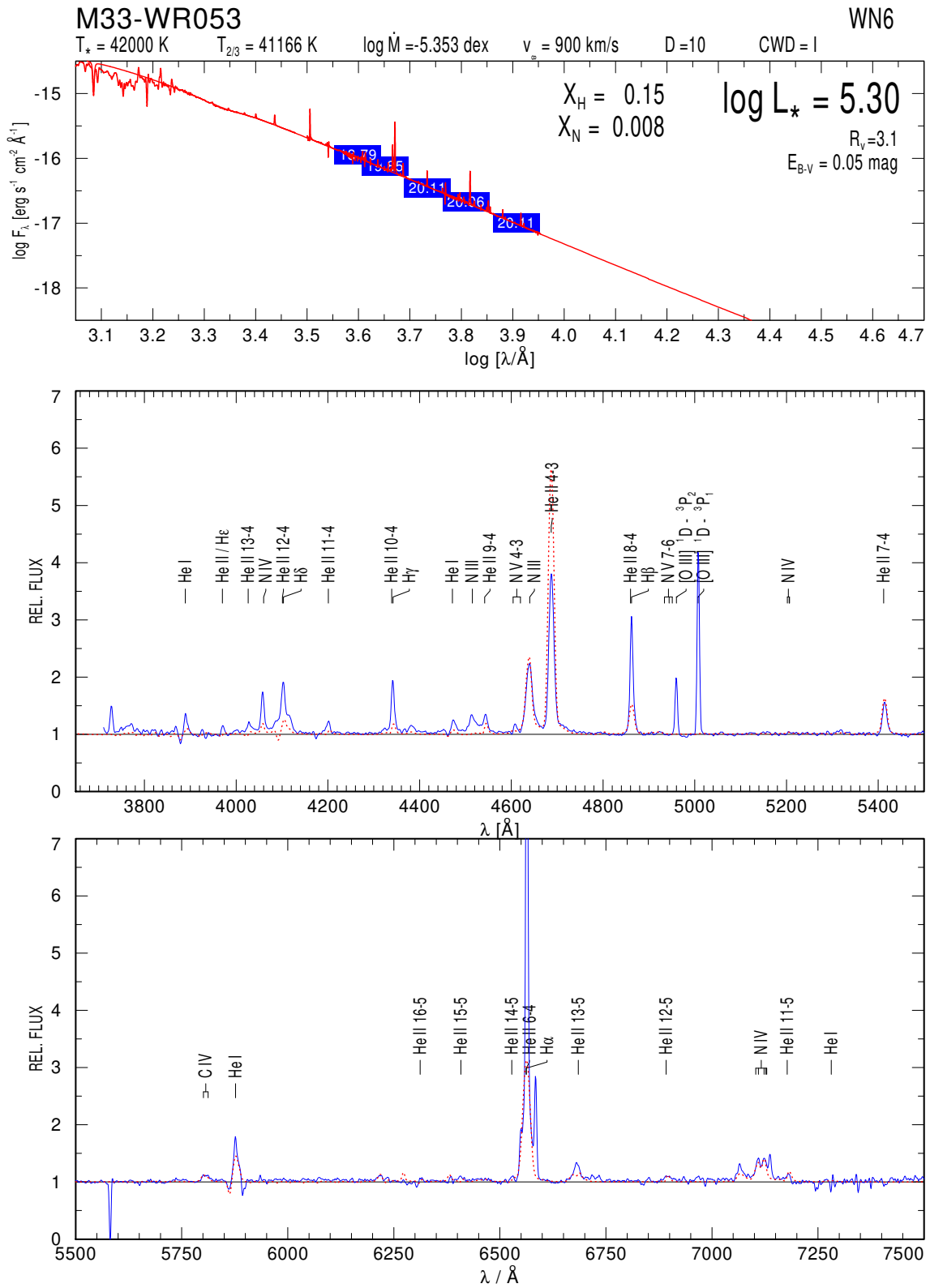
**Fig. 8.31** M33-WR053
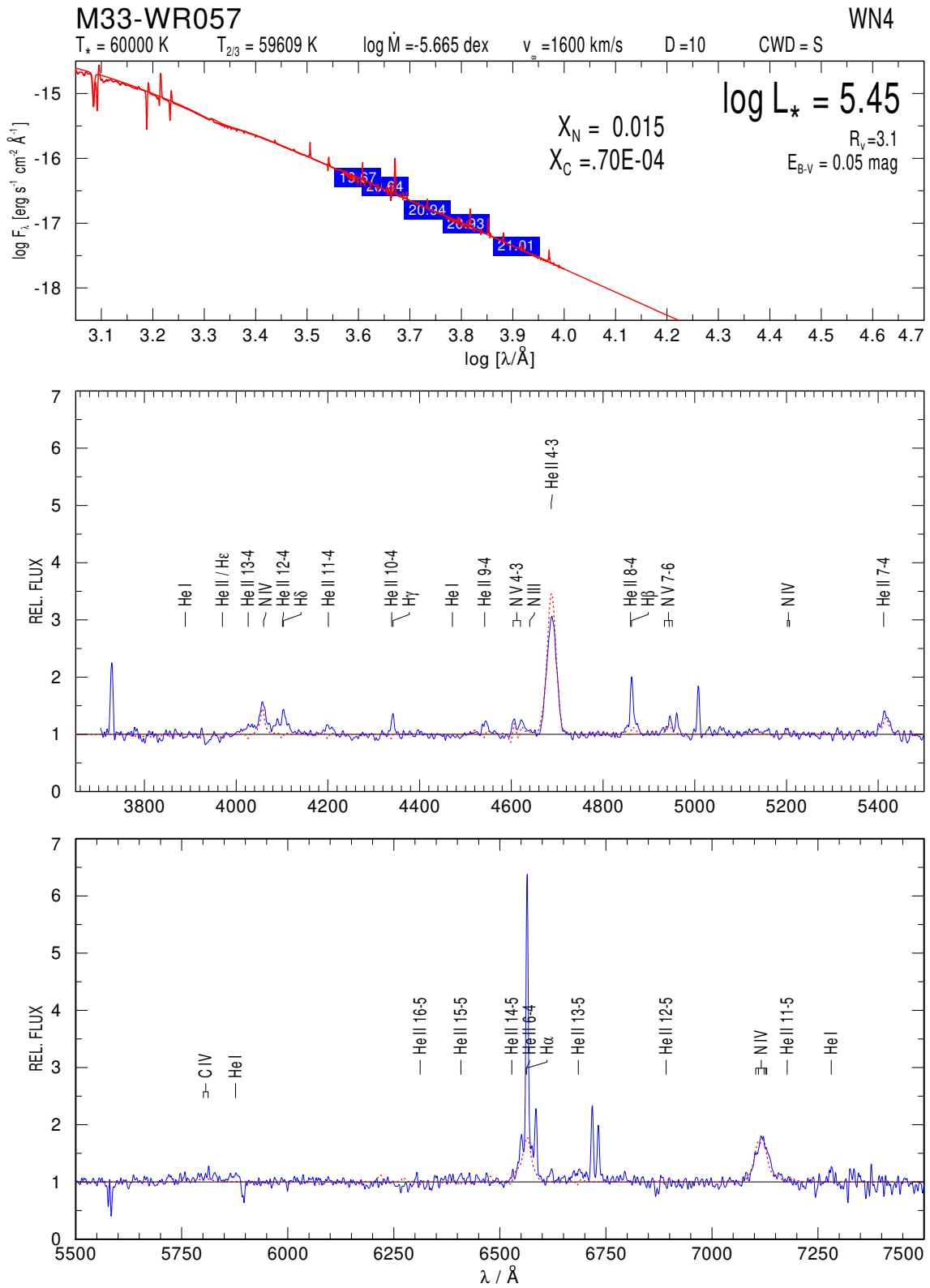
**Fig. 8.32** M33-WR057
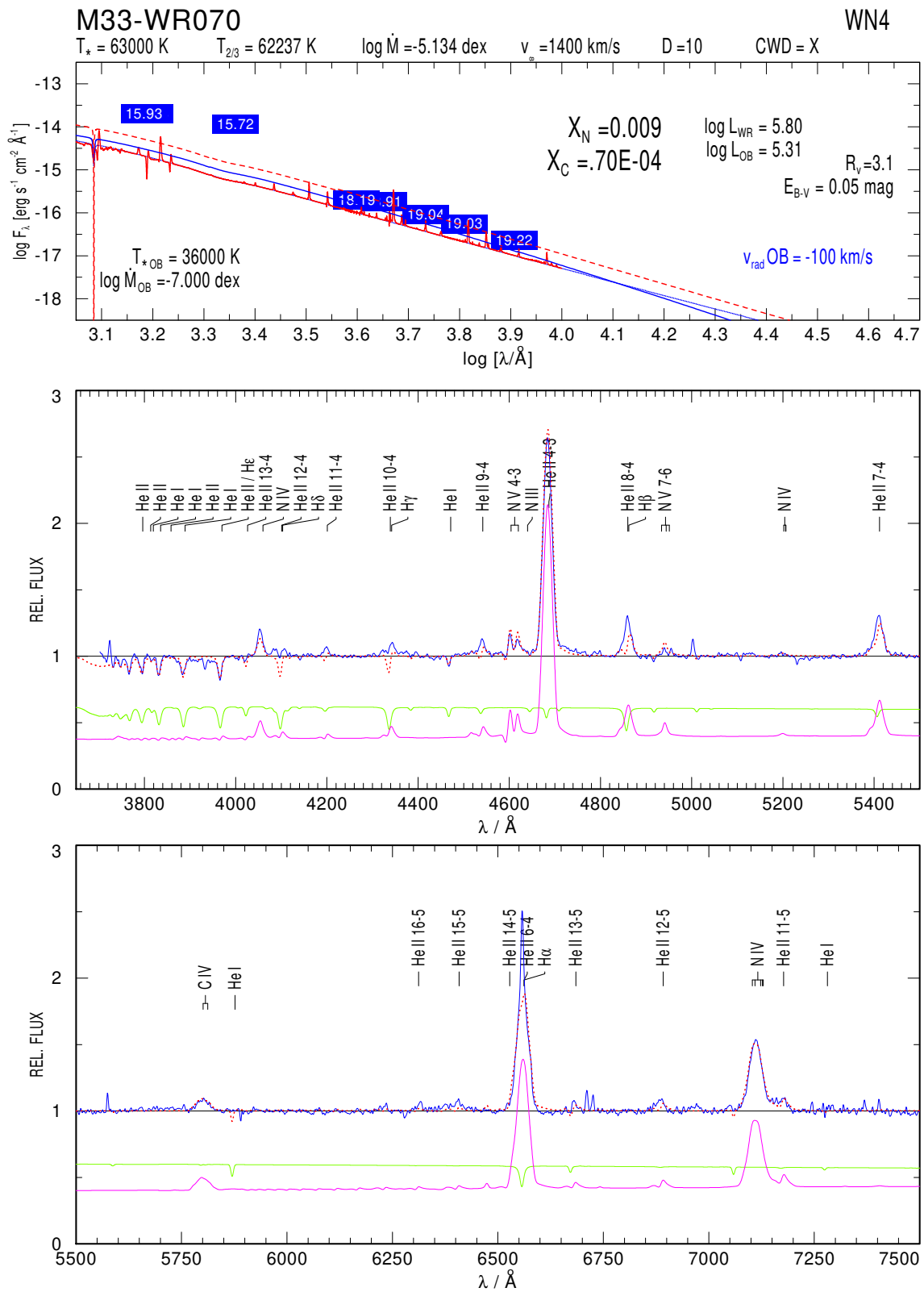
**Fig. 8.33** Composite fit for M33-WR070

**Fig. 8.34** M33-WR071

**Fig. 8.35** Composite fit for M33-WR074

**Fig. 8.36** Composite fit for M33-WR075bin
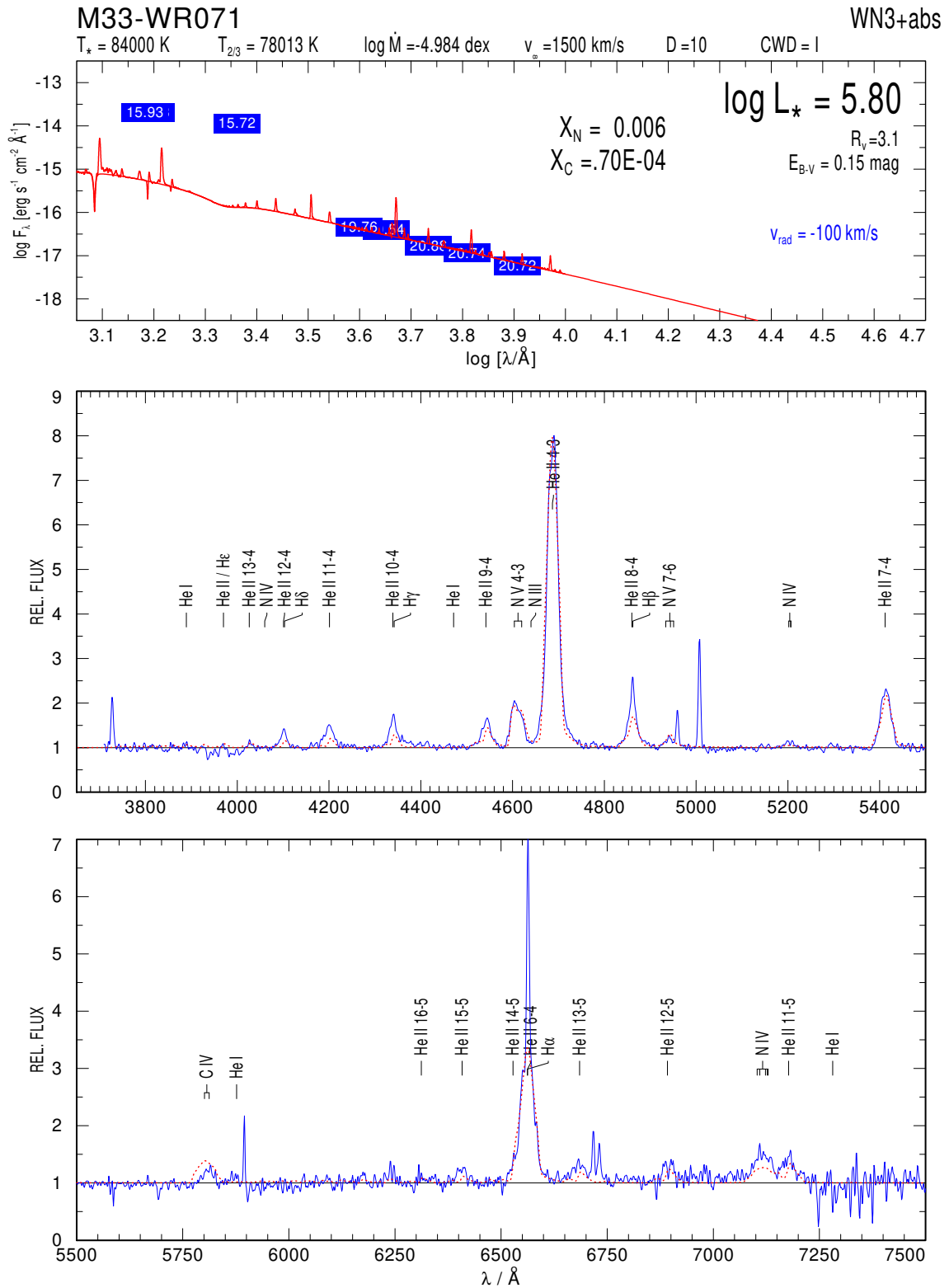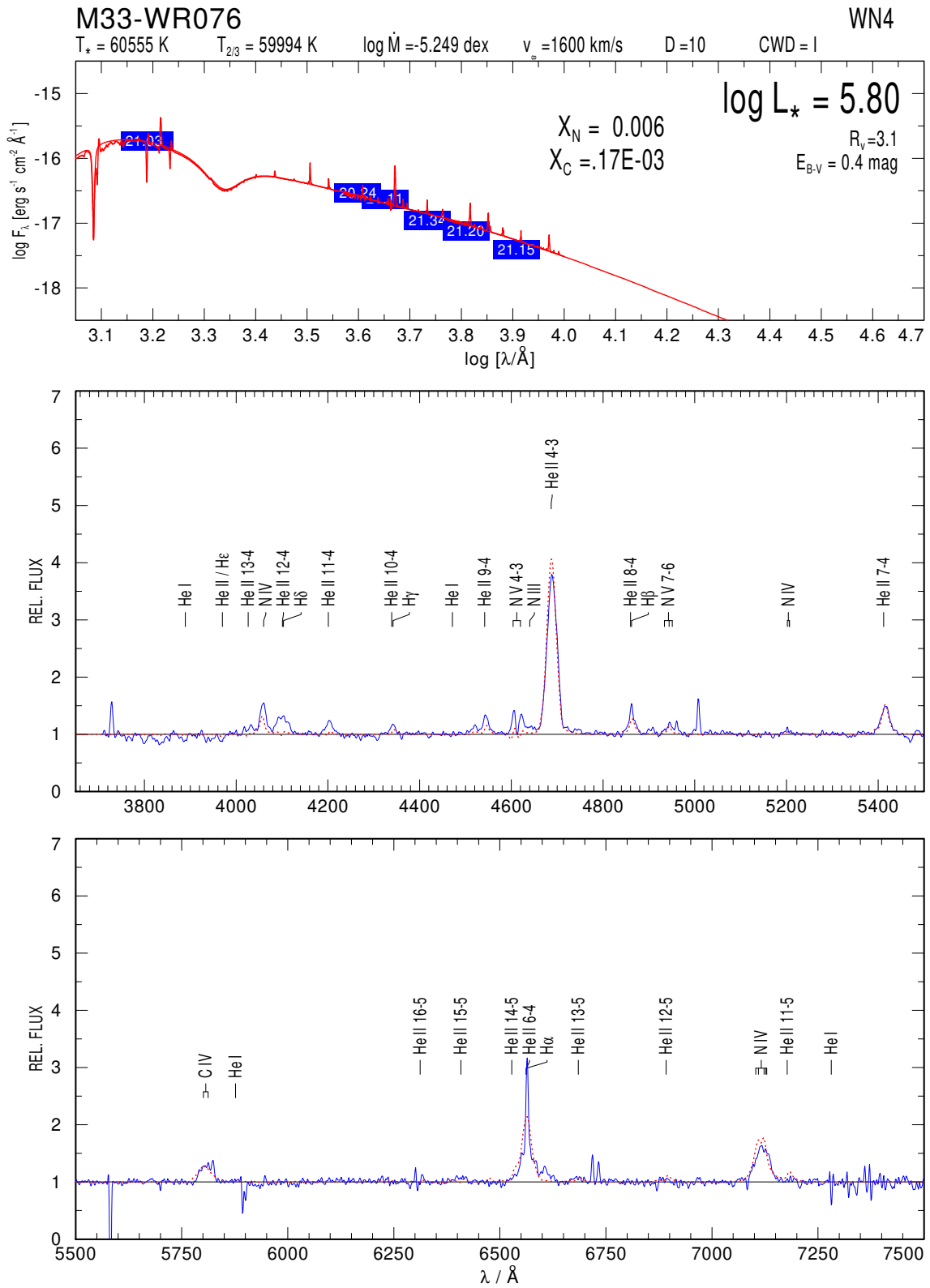
**Fig. 8.37** M33-WR076

**Fig. 8.38** M33-WR088
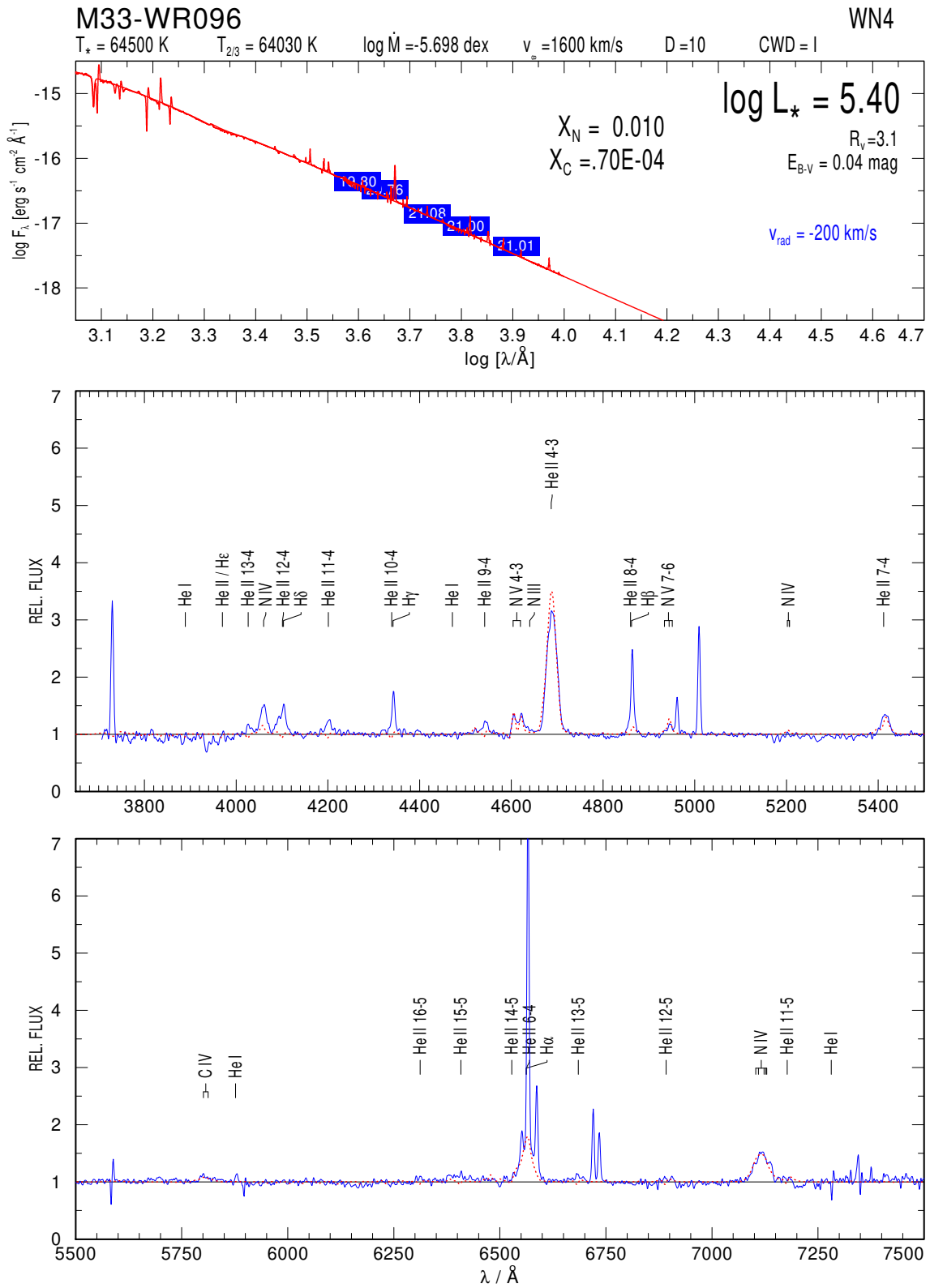
**Fig. 8.39** M33-WR096
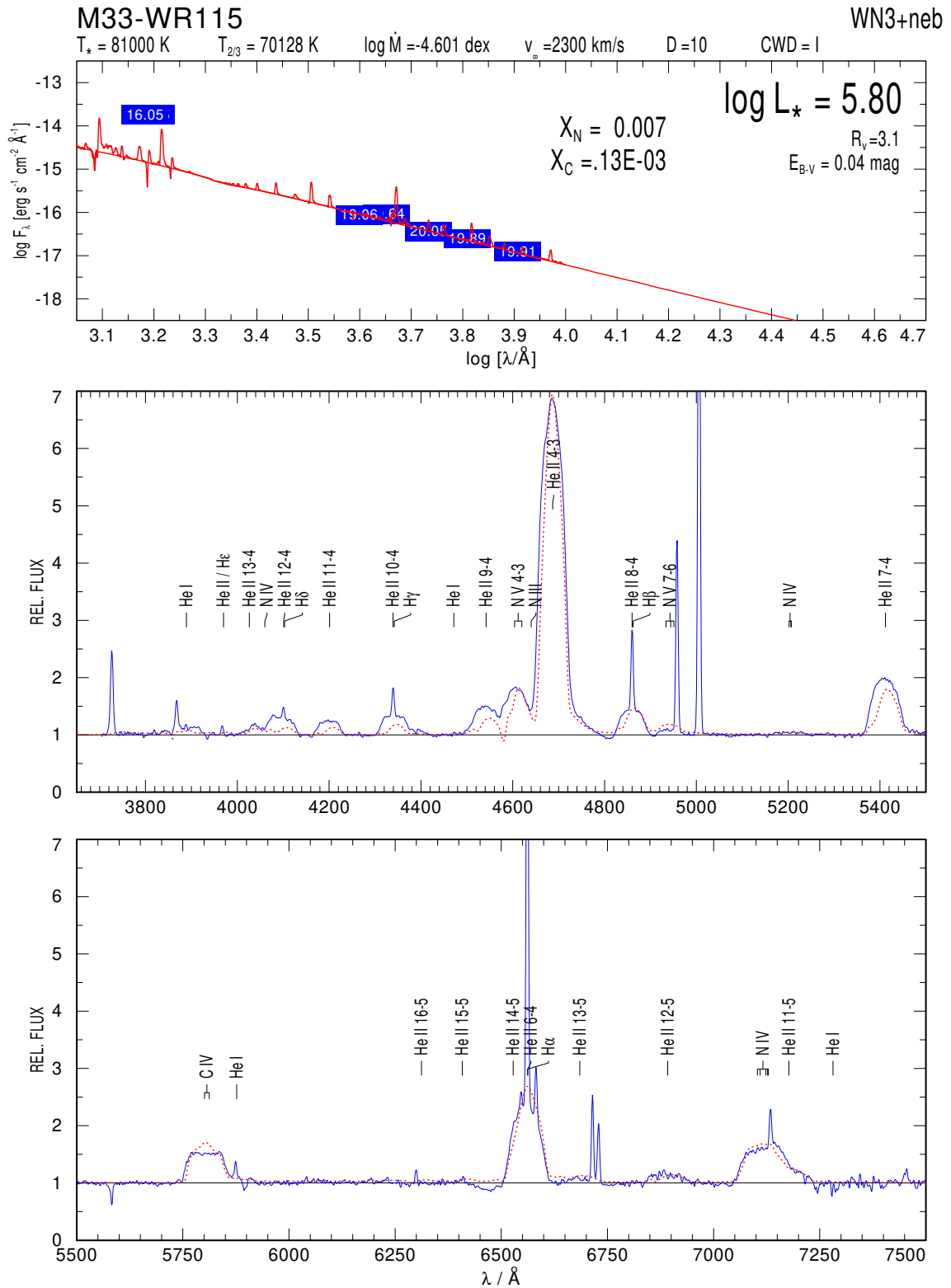
**Fig. 8.40** M33-WR115

**Fig. 8.41** M33-WR119

**Fig. 8.42** Composite fit for M33-WR133

**Fig. 8.43** Composite fit for M33-WR136
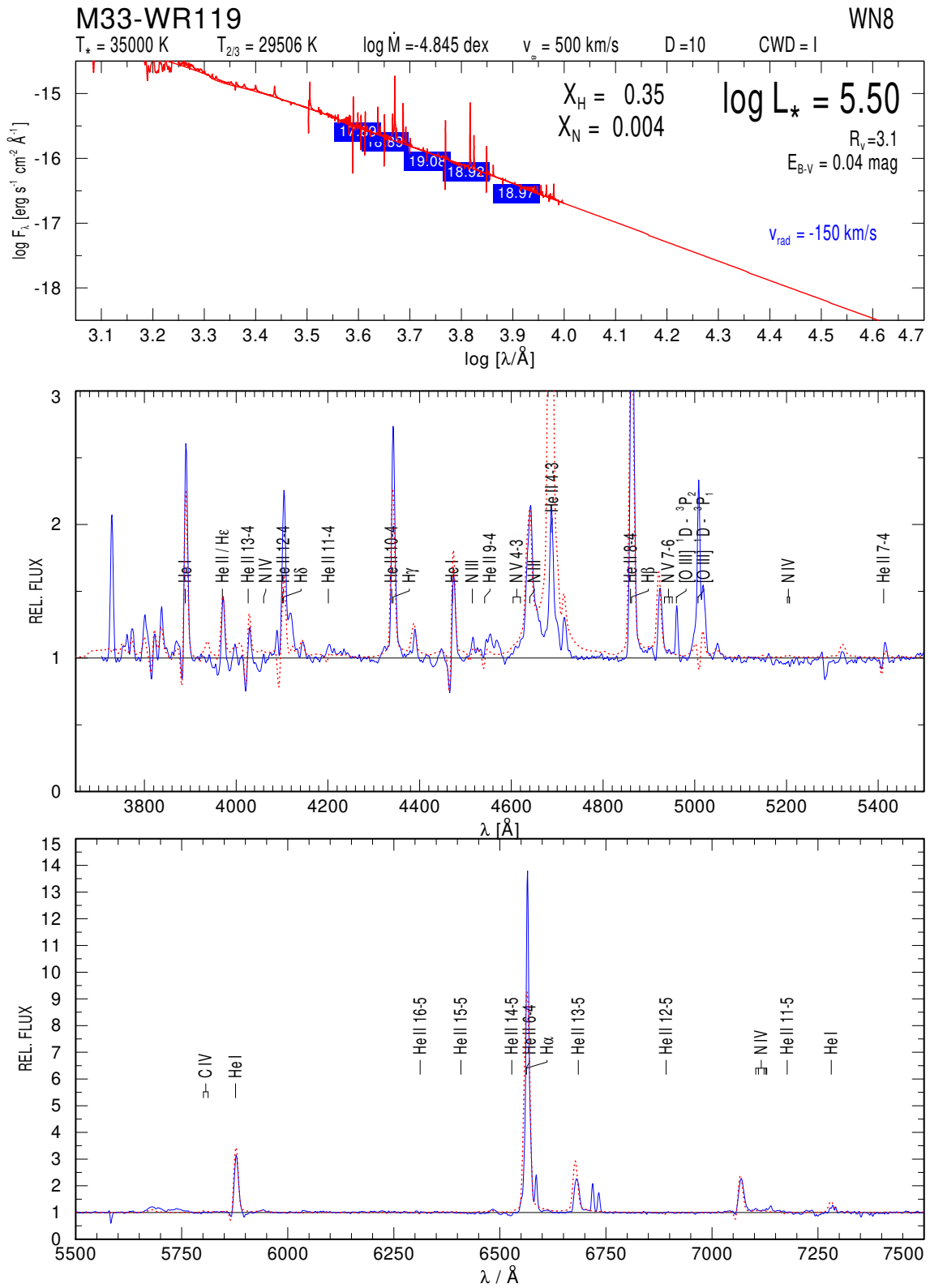
Fig. 8.44 Composite fit for M33-WR143
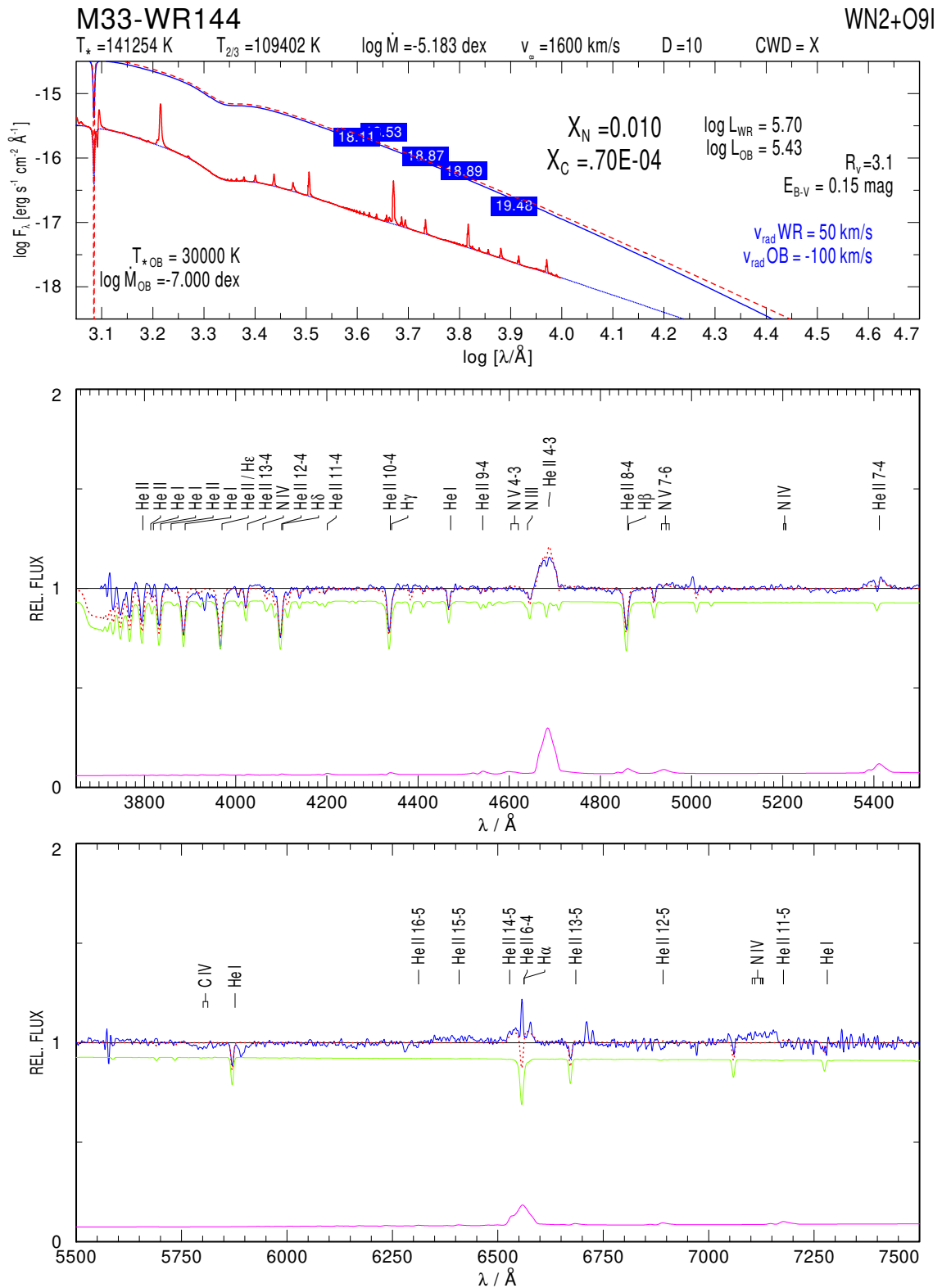
**Fig. 8.45** Composite fit for M33-WR144
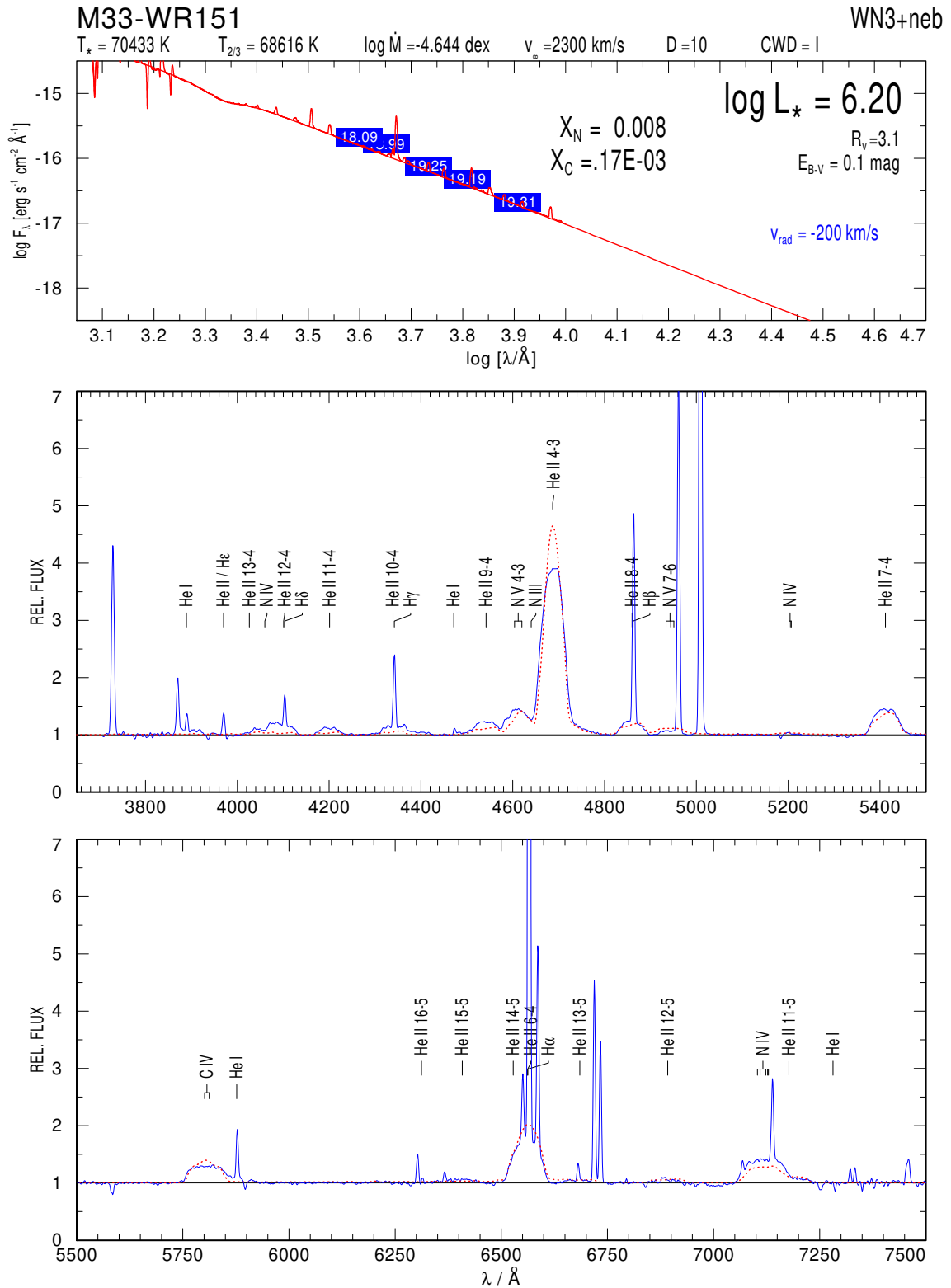
**Fig. 8.46** M33-WR151
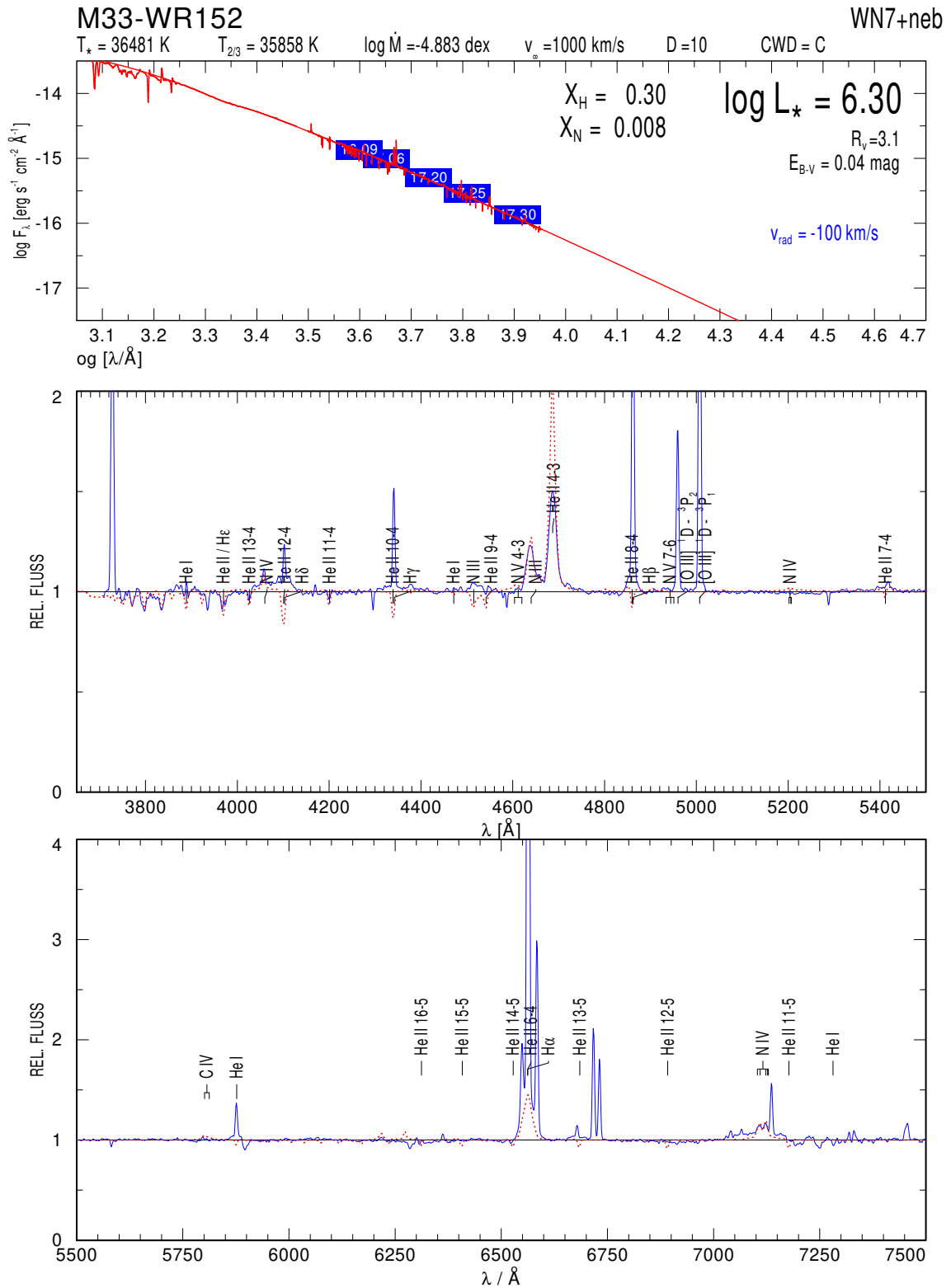
**Fig. 8.47** M33-WR152

**Fig. 8.48** M33-WR154

121

**M33-WR155**                                                                WN3+abs

$T_* = 70795$ K      $T_{2/3} = 68669$ K      $\log \dot{M} = -4.936$ dex      $v_\infty = 2000$ km/s      $D = 10$      CWD = X

$X_N = 0.012$

$X_C = .20E-03$

$\log L_{WR} = 5.70$

$\log L_{OB} = 4.15$

$R_v = 3.1$

$E_{B-V} = 0.6$ mag

$v_{rad}$OB $= 50$ km/s

$T_{OB} = 15000$ K

$\log M_{OB} = -7.000$ dex

**Fig. 8.49** Composite fit for M33-WR155

122
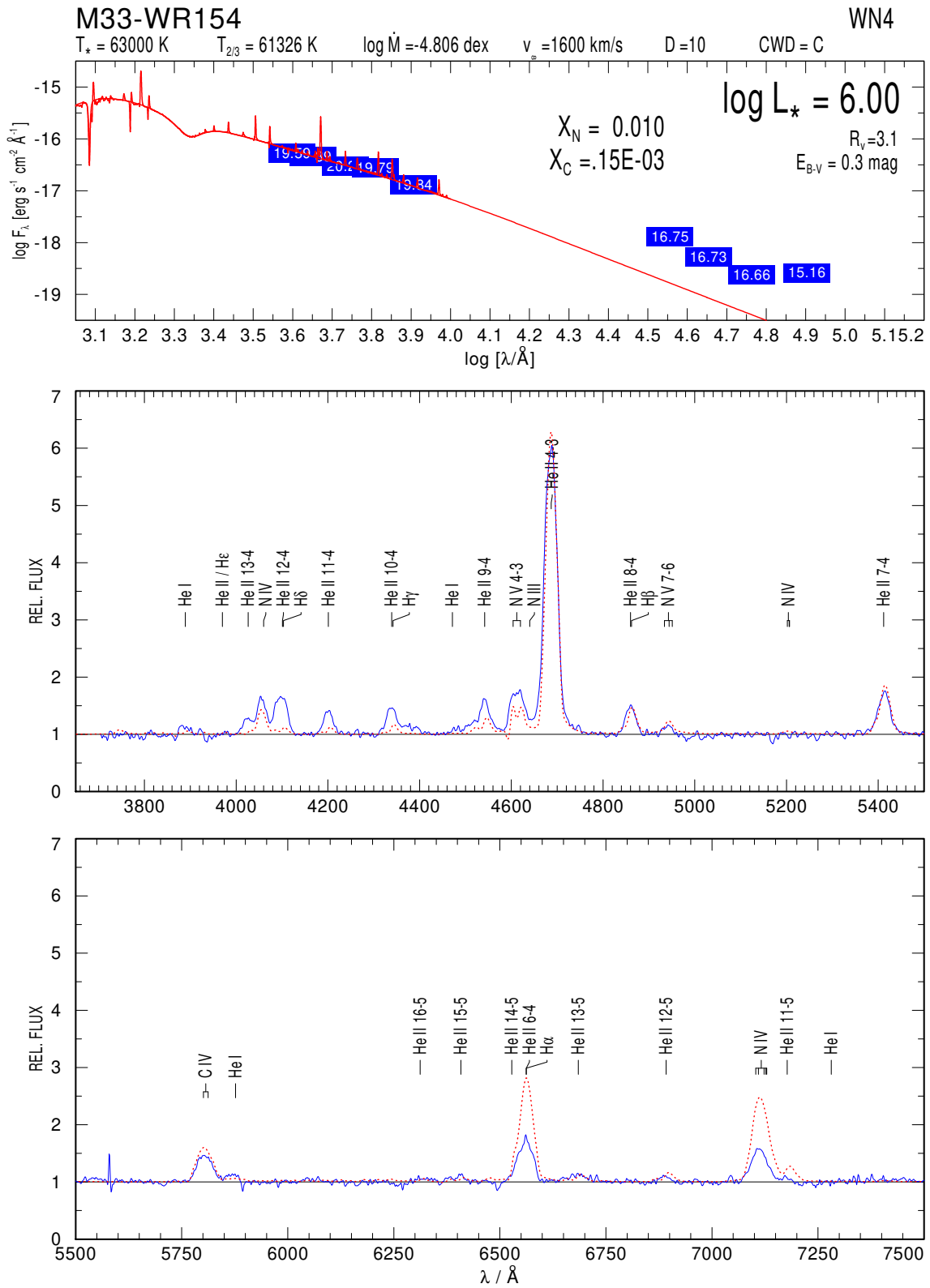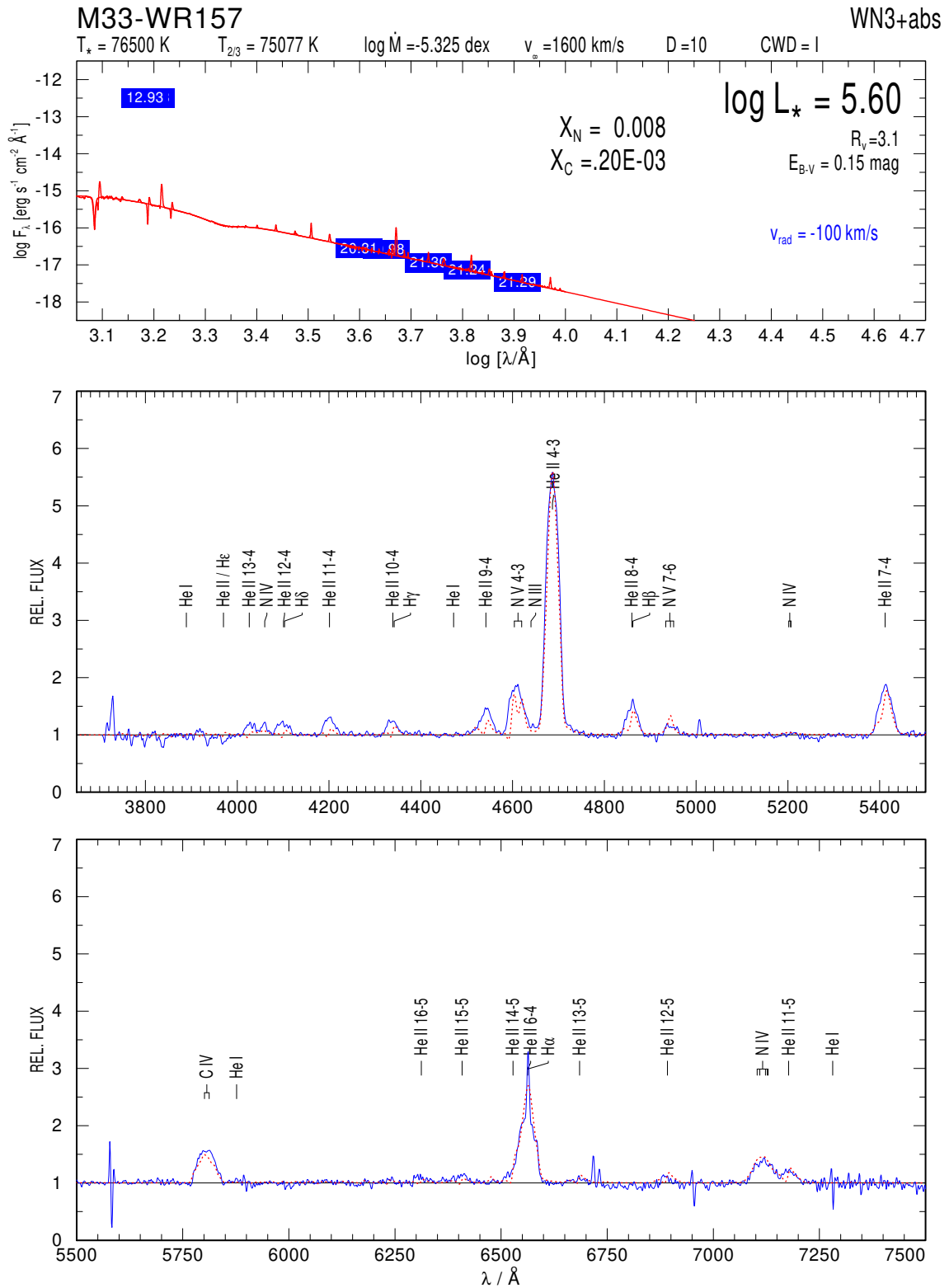
**Fig. 8.50** M33-WR157
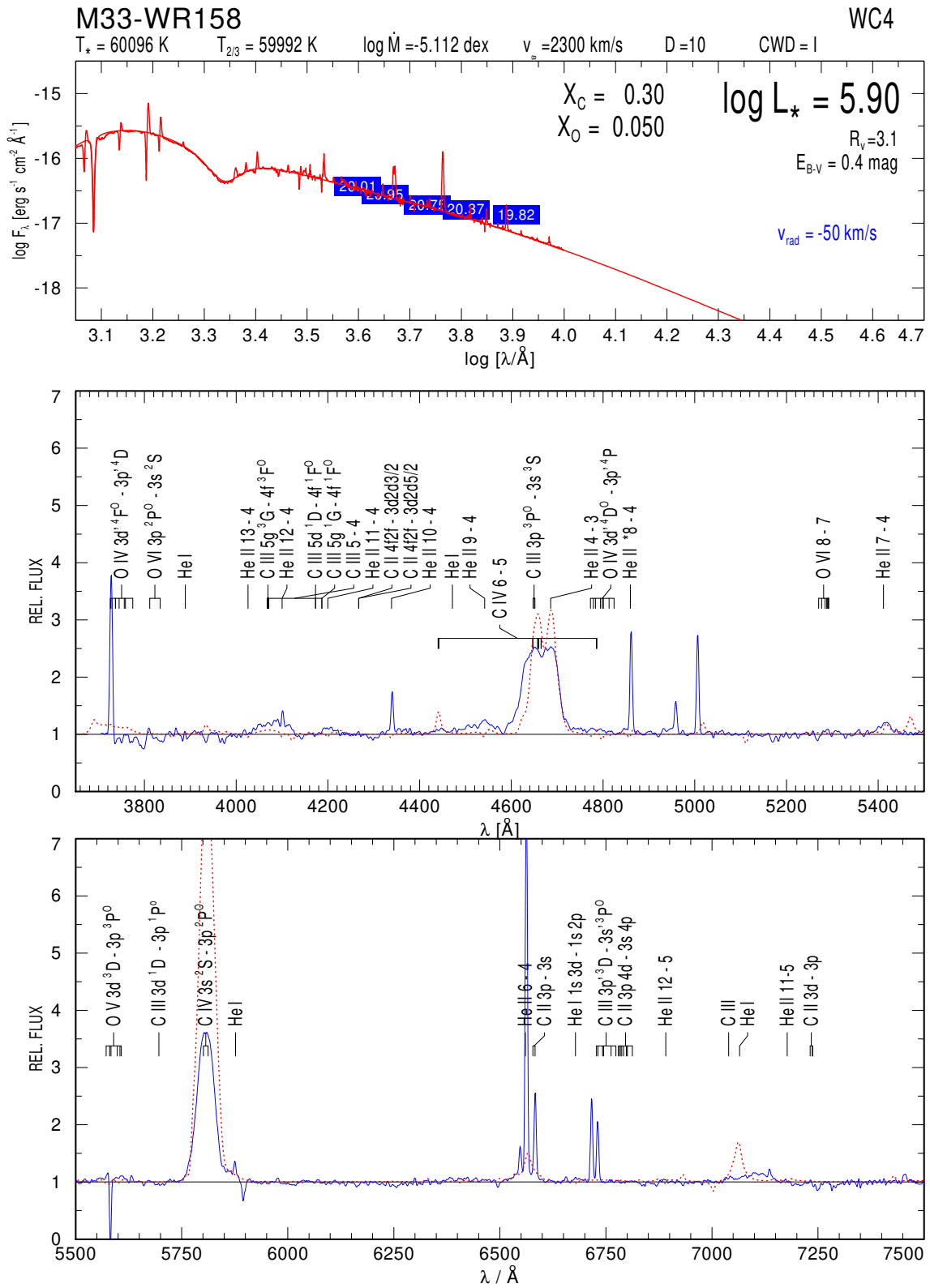
**Fig. 8.51** M33-WR158
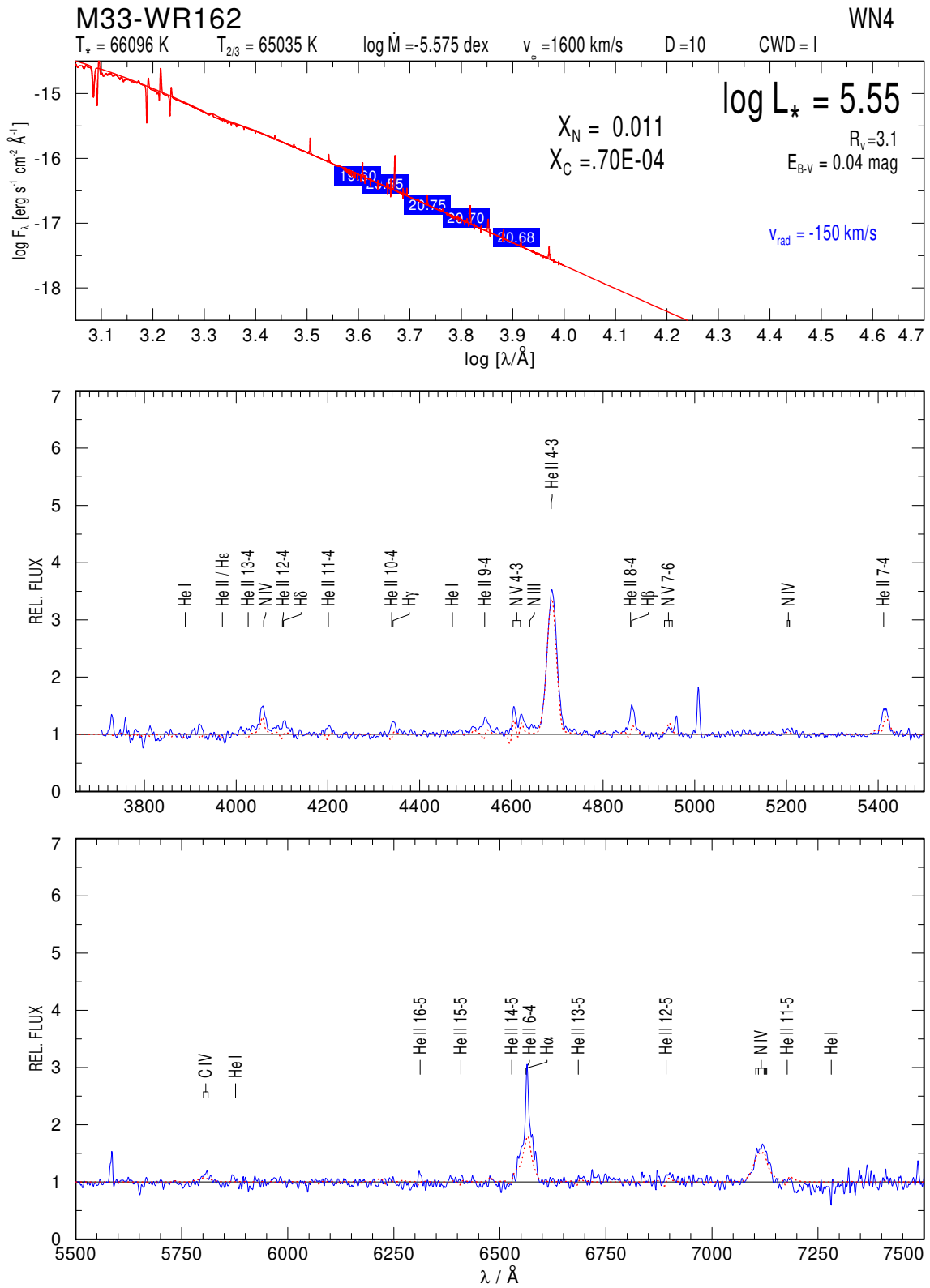
**Fig. 8.52** M33-WR162
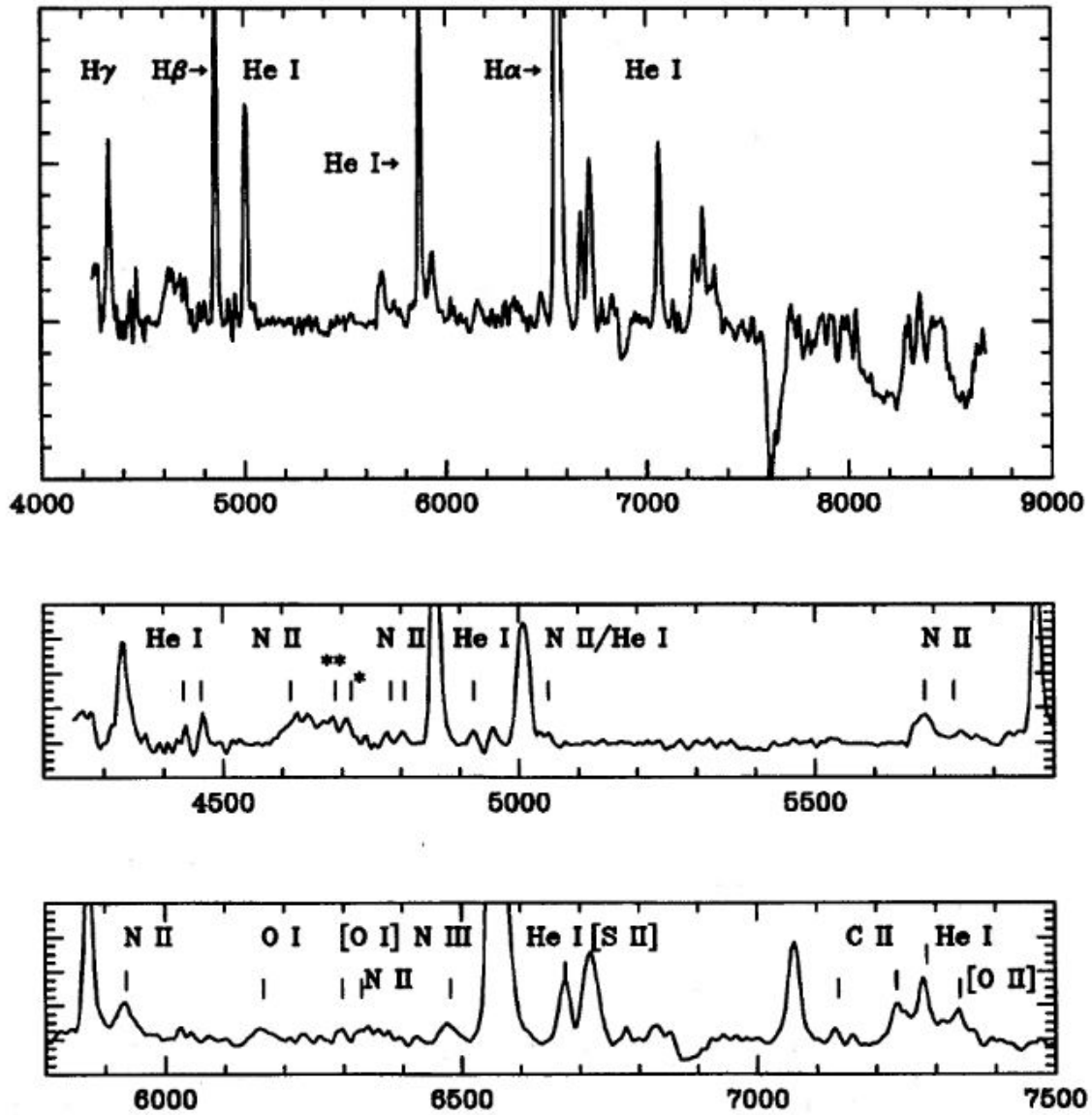
**Fig. 8.53** M33-WR163

**Fig. 8.54** M33-WR163 observed in January 1994 with a resolution of 25 Å from Corral (1996).
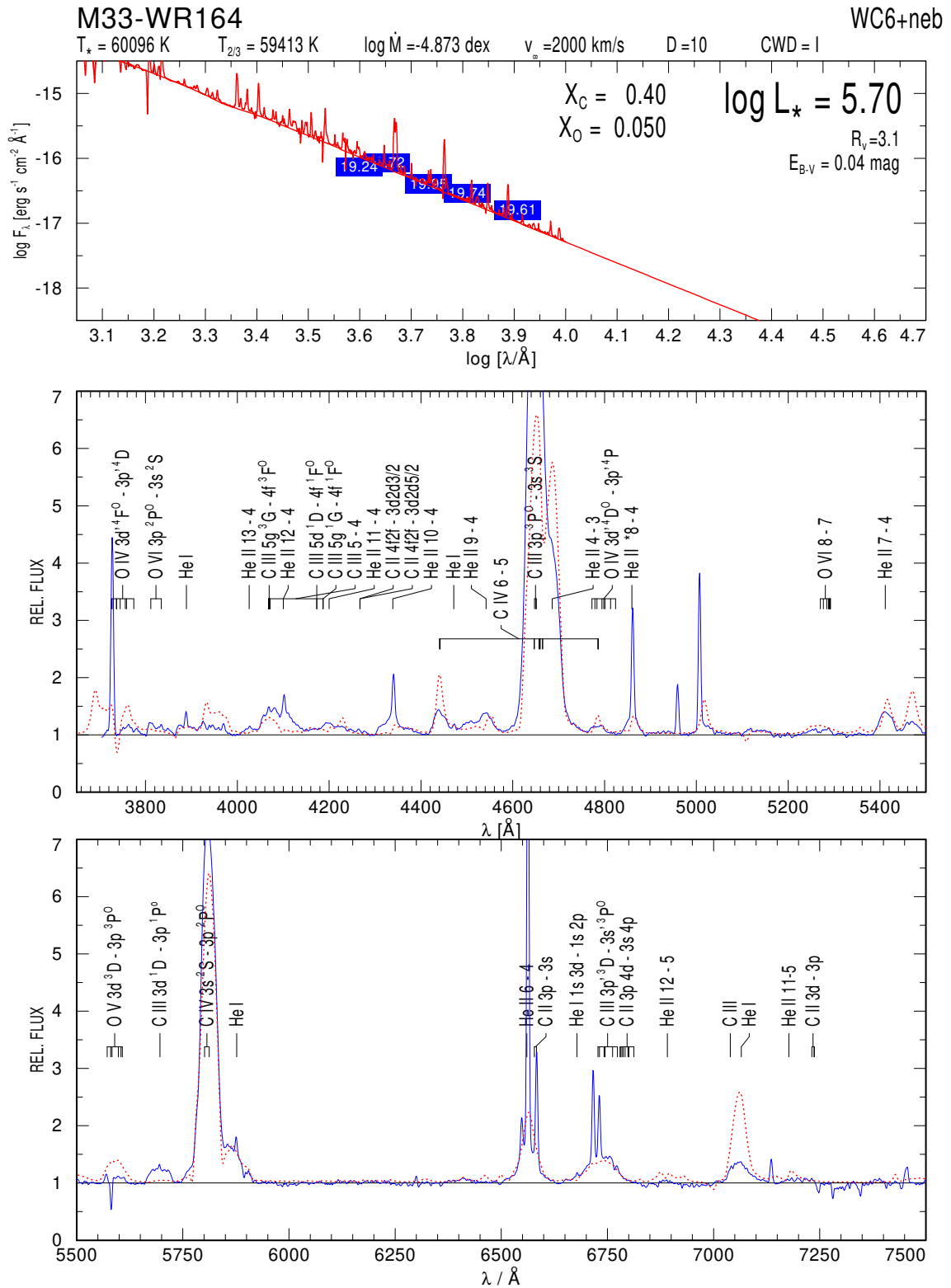
**Fig. 8.55** M33-WR164
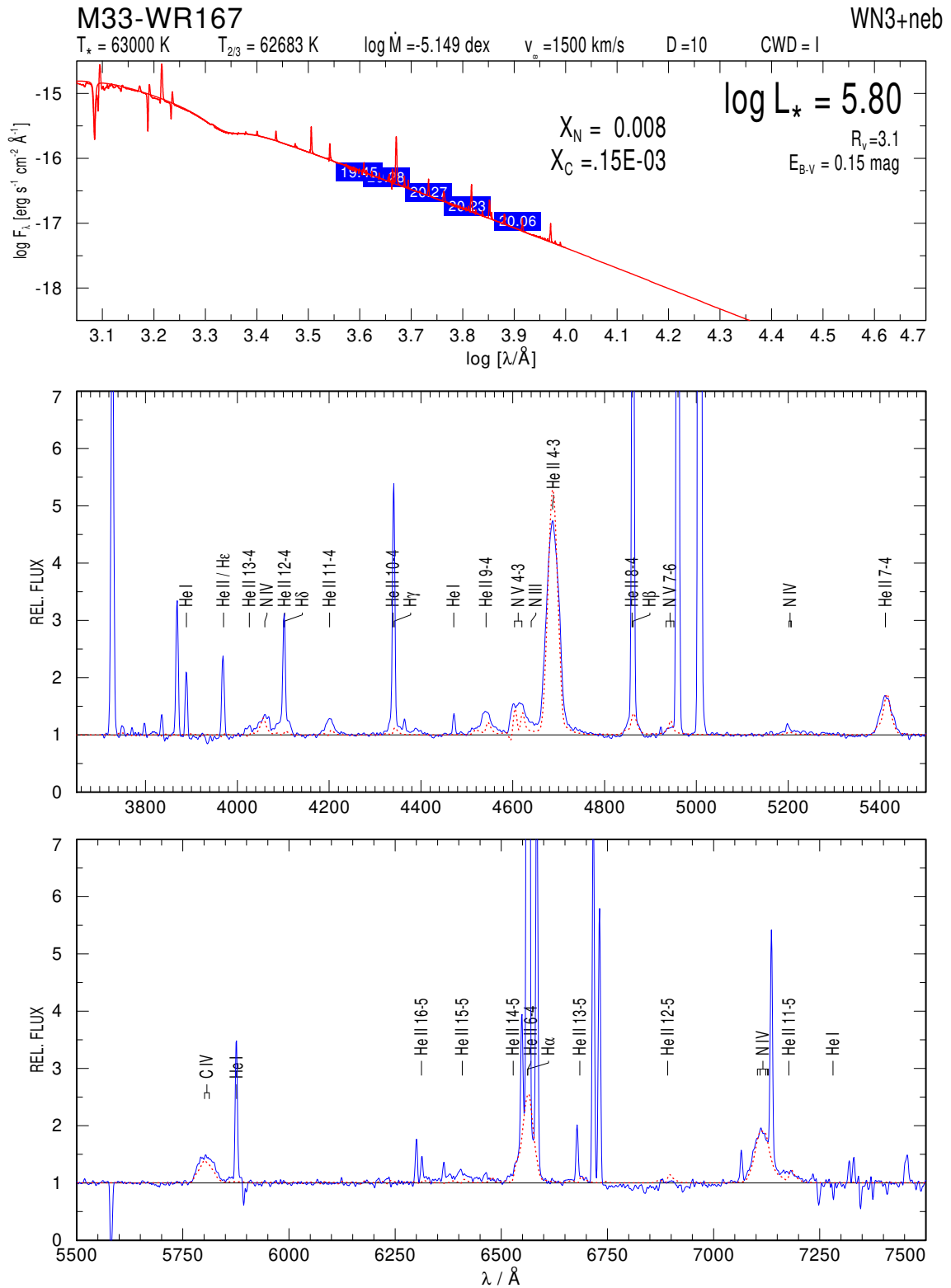
**Fig. 8.56** M33-WR167
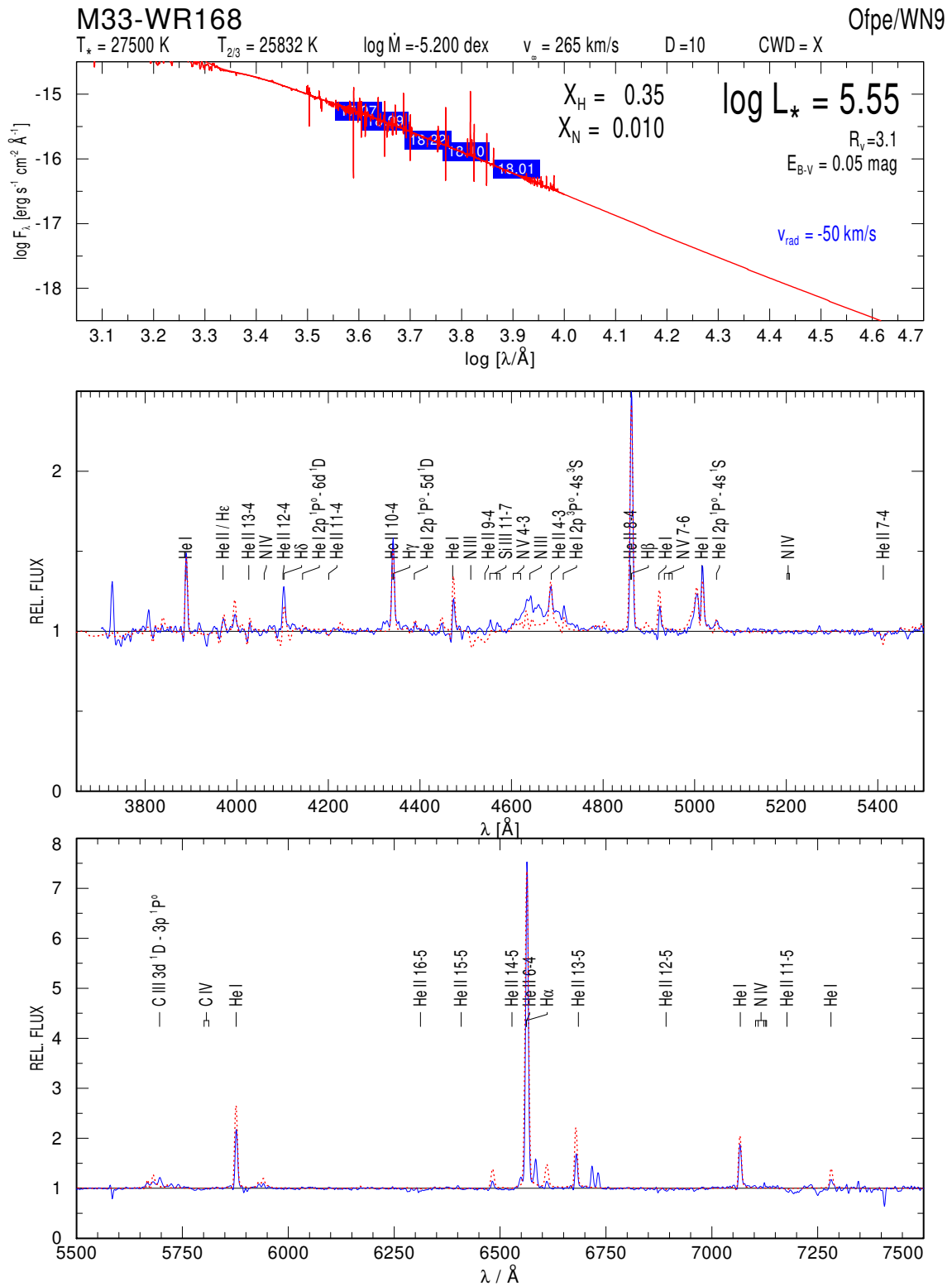
**Fig. 8.57** M33-WR168
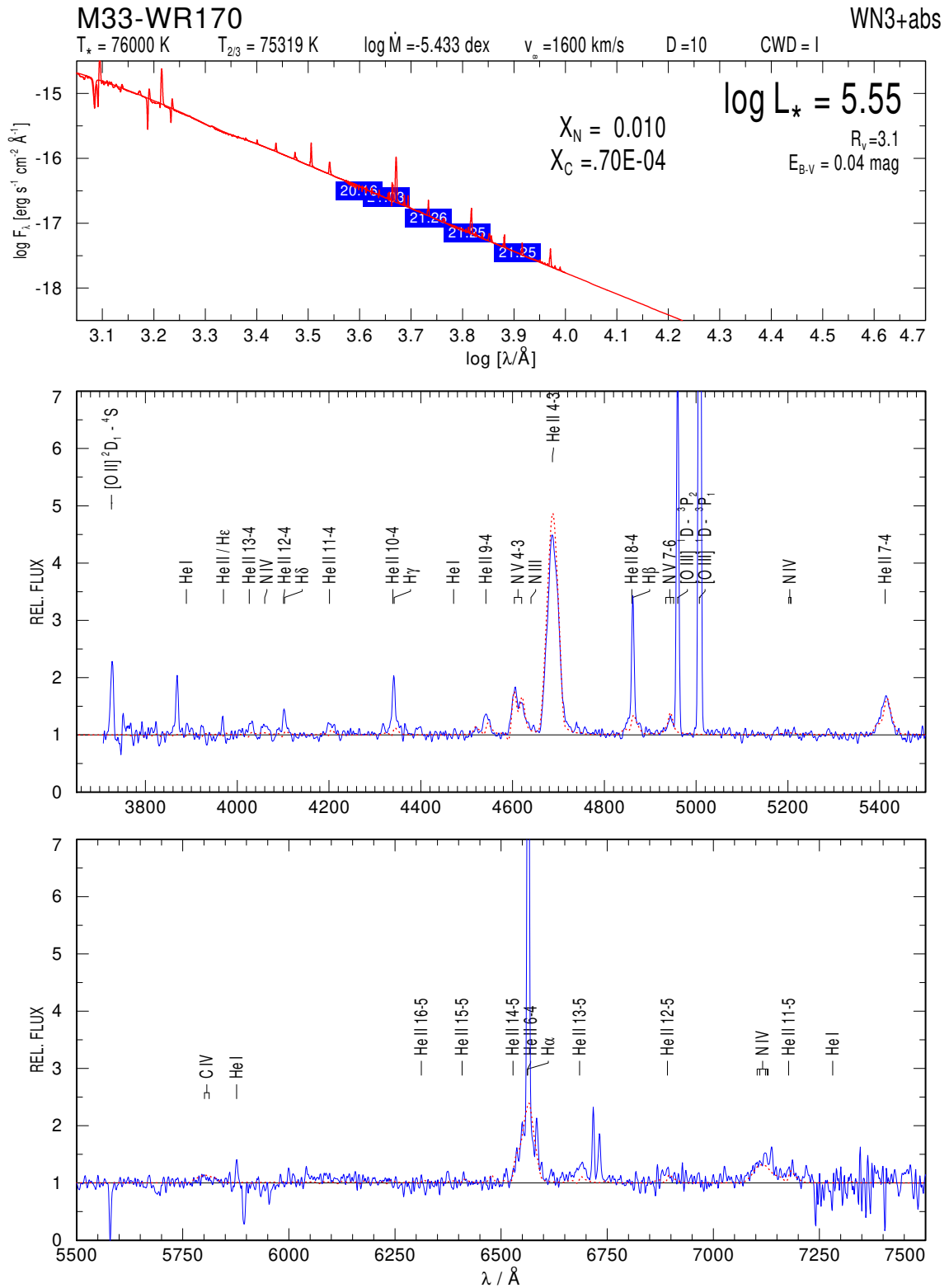
**Fig. 8.58** M33-WR170
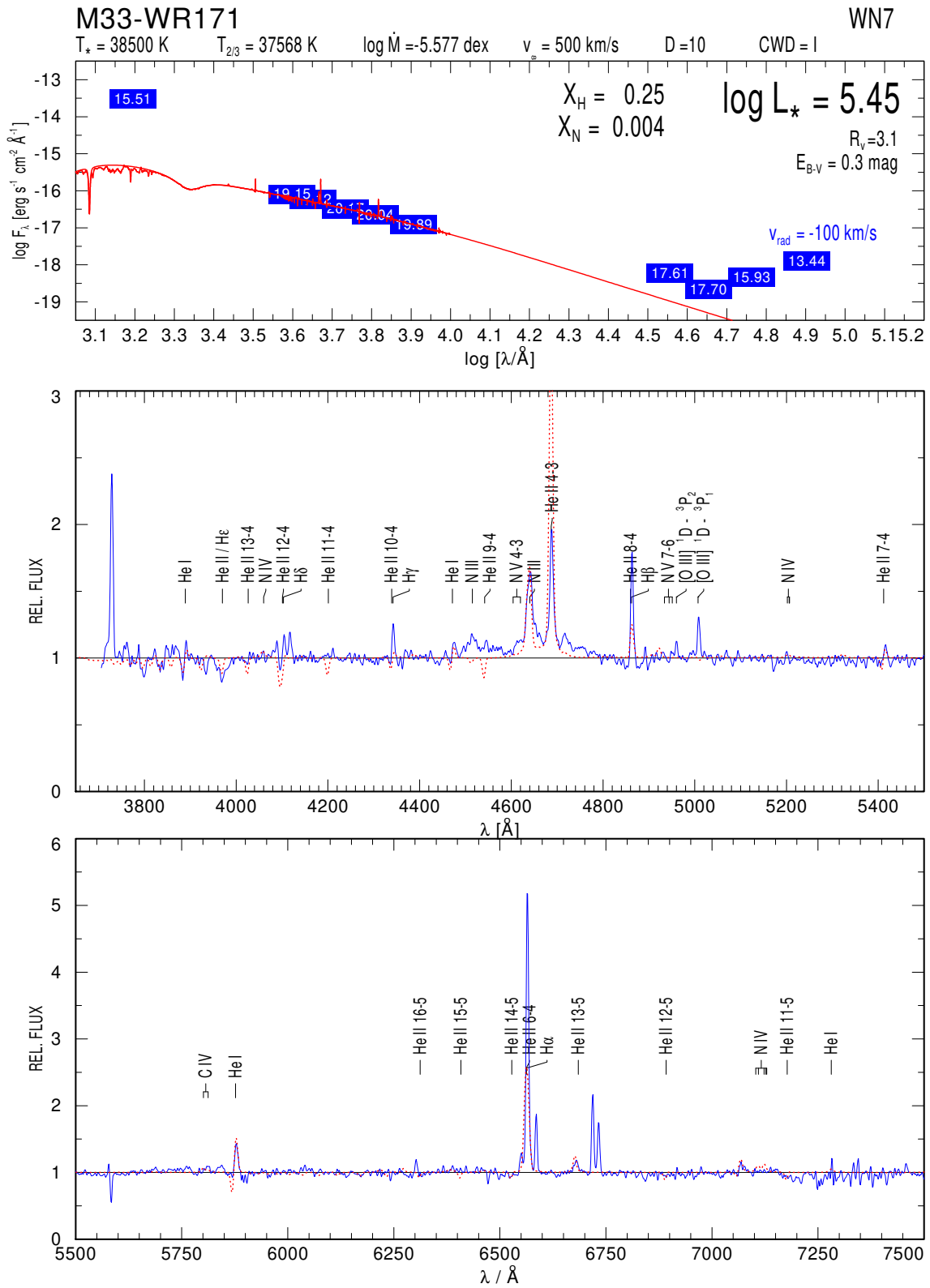
**Fig. 8.59** M33-WR171
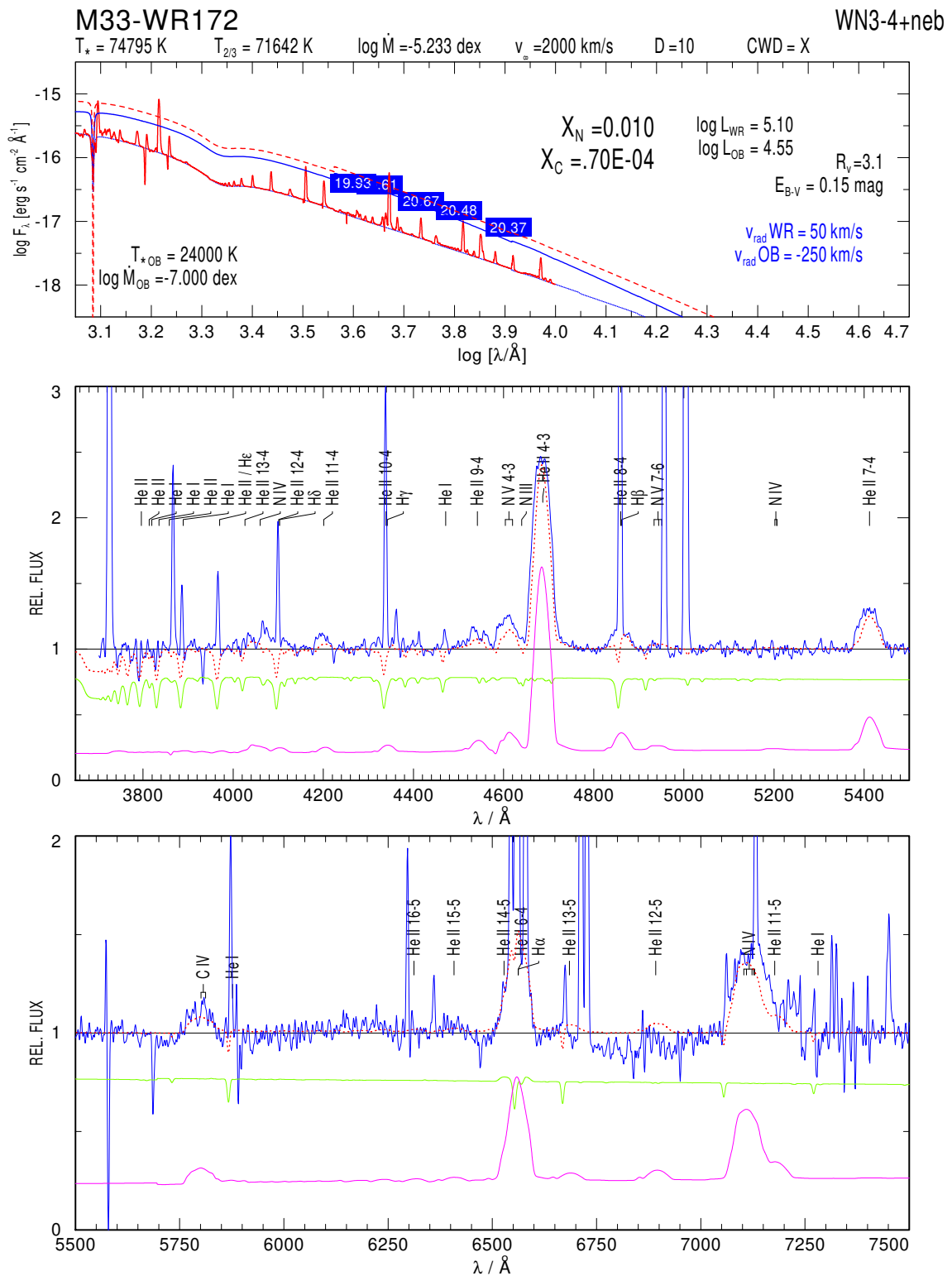
**Fig. 8.60** Composite fit for M33-WR172
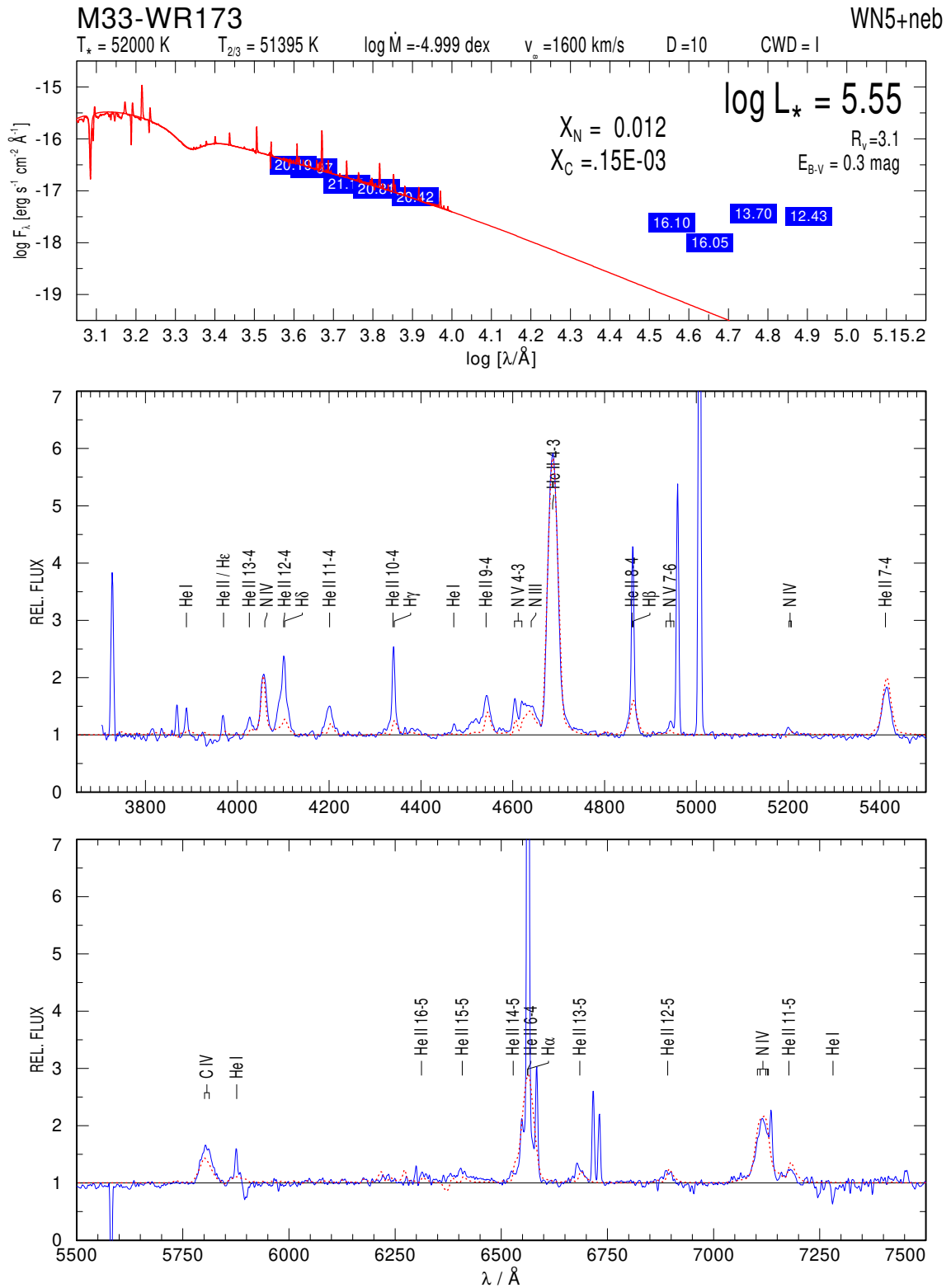
**Fig. 8.61** M33-WR173
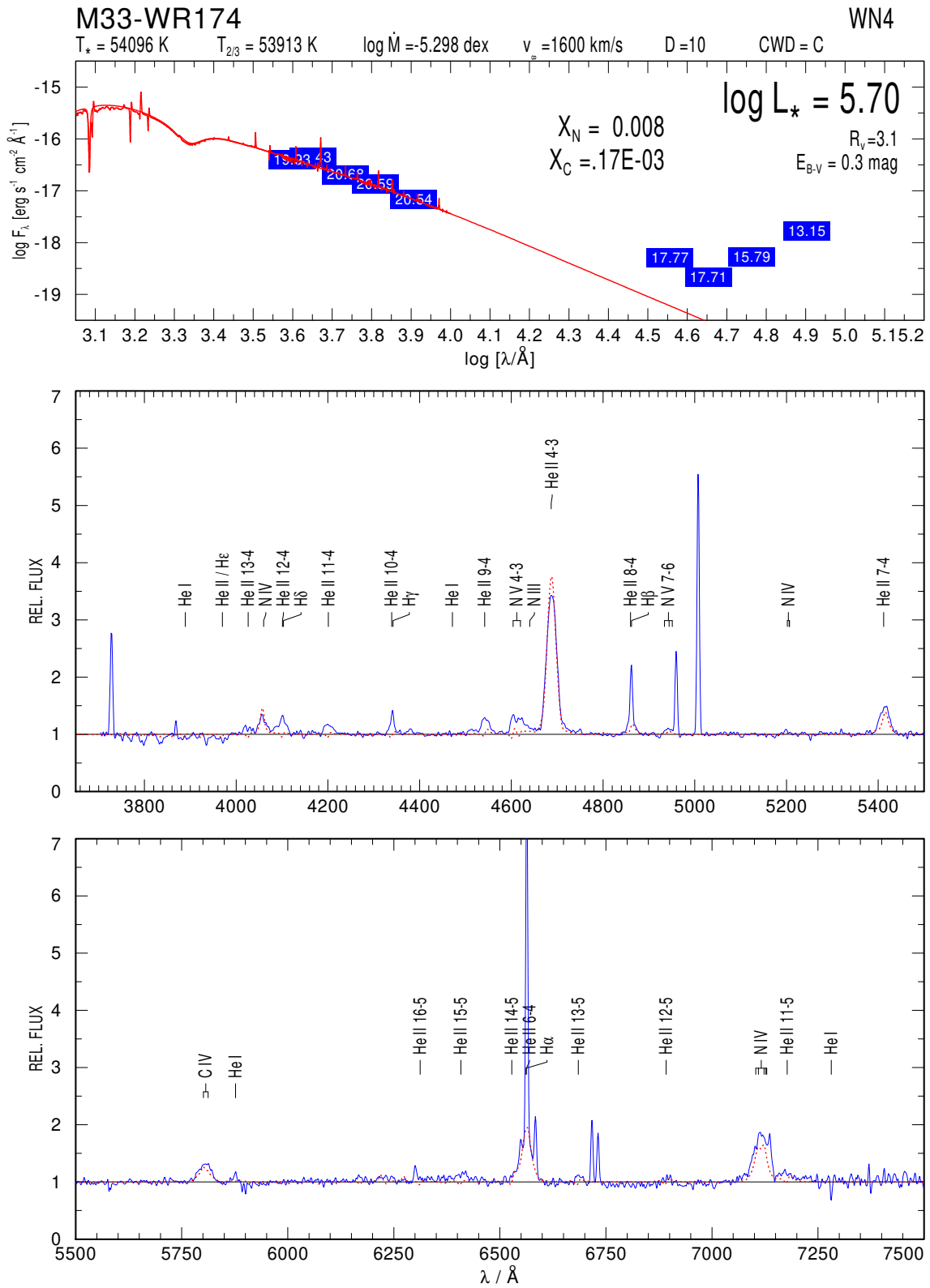
**Fig. 8.62** M33-WR174
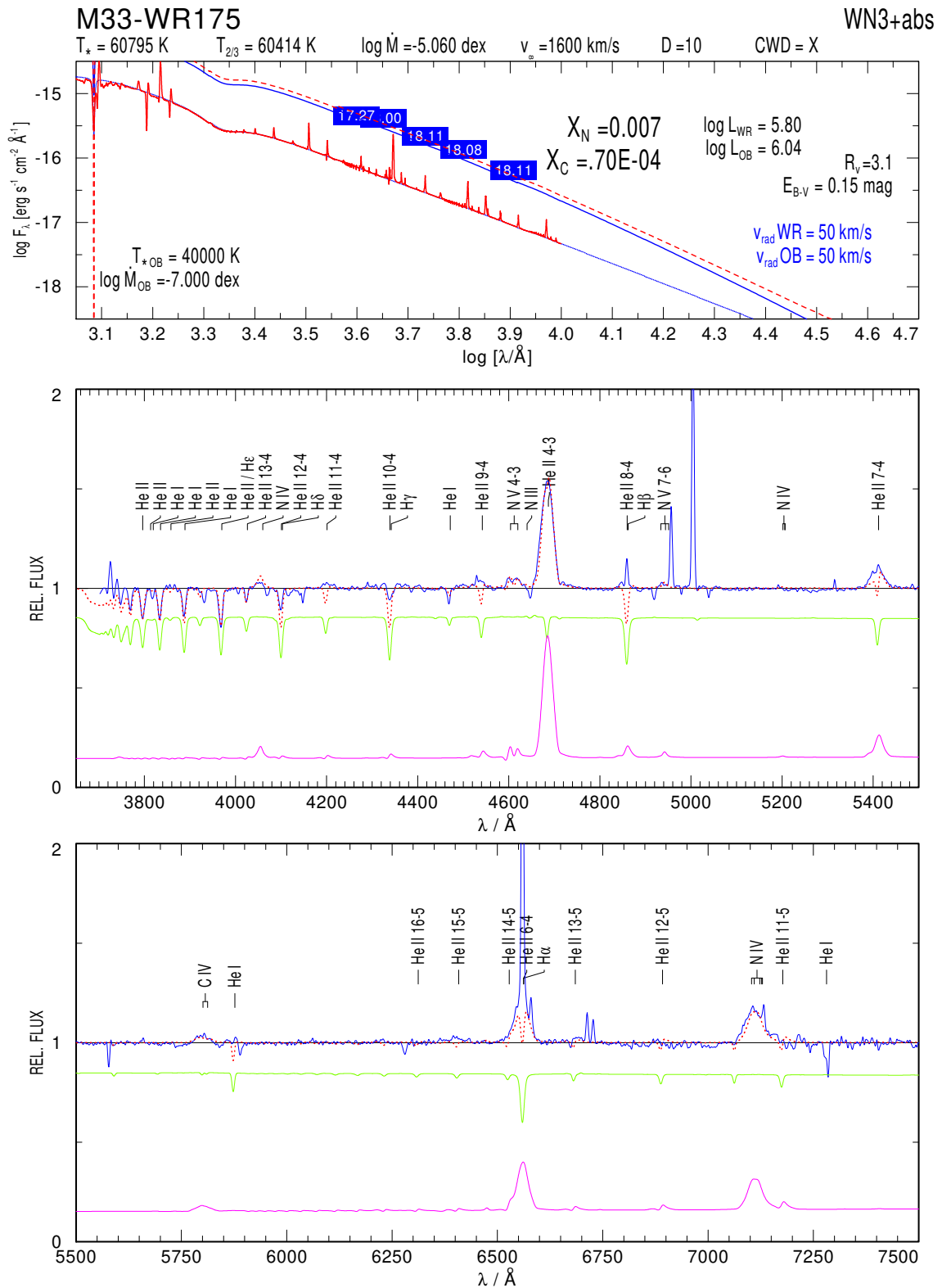
**Fig. 8.63** Composite fit for M33-WR175
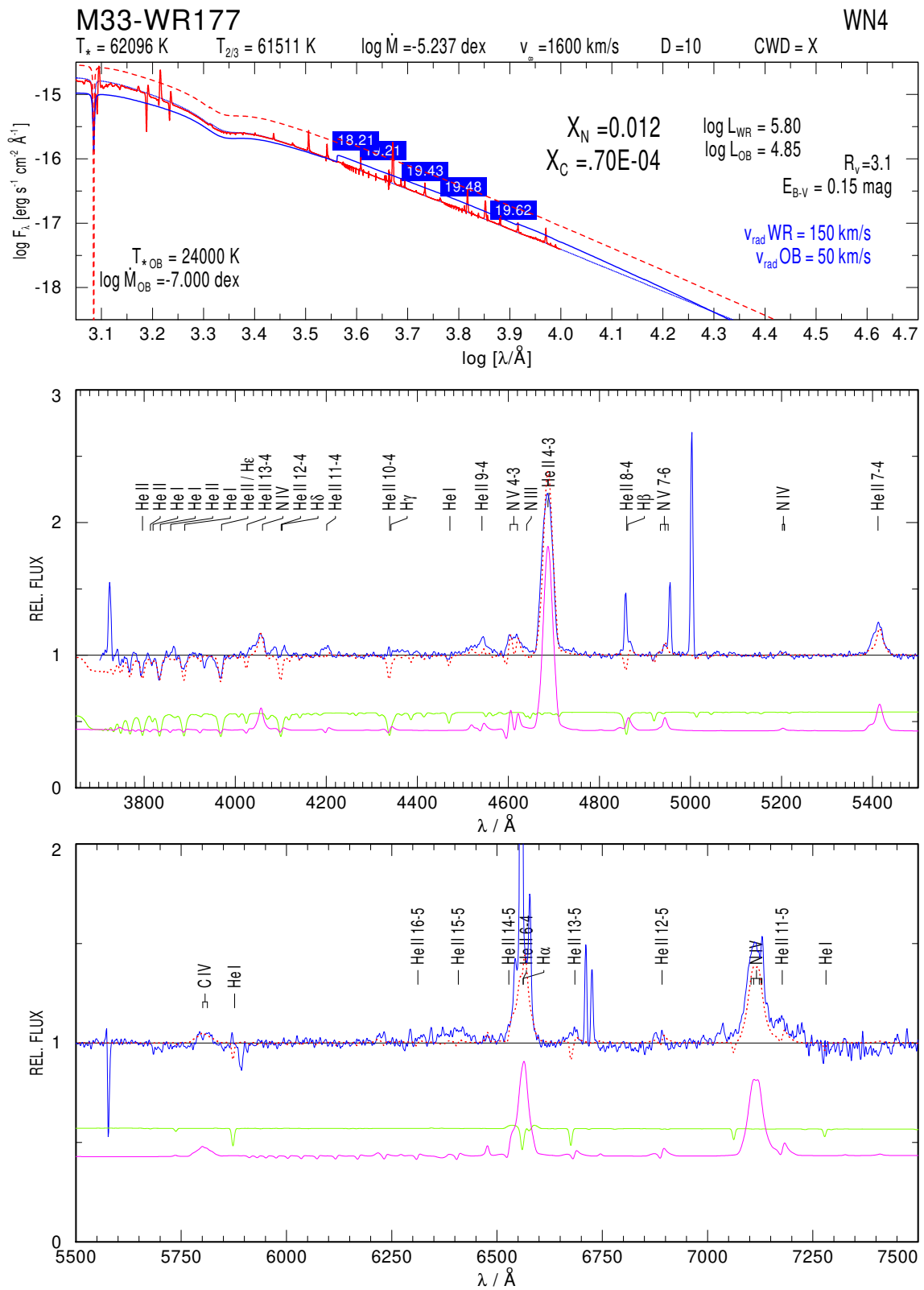
**Fig. 8.64** Composite fit for M33-WR177

**Fig. 8.65** M33-WR178

**Fig. 8.66** Composite fit for M33-WR179
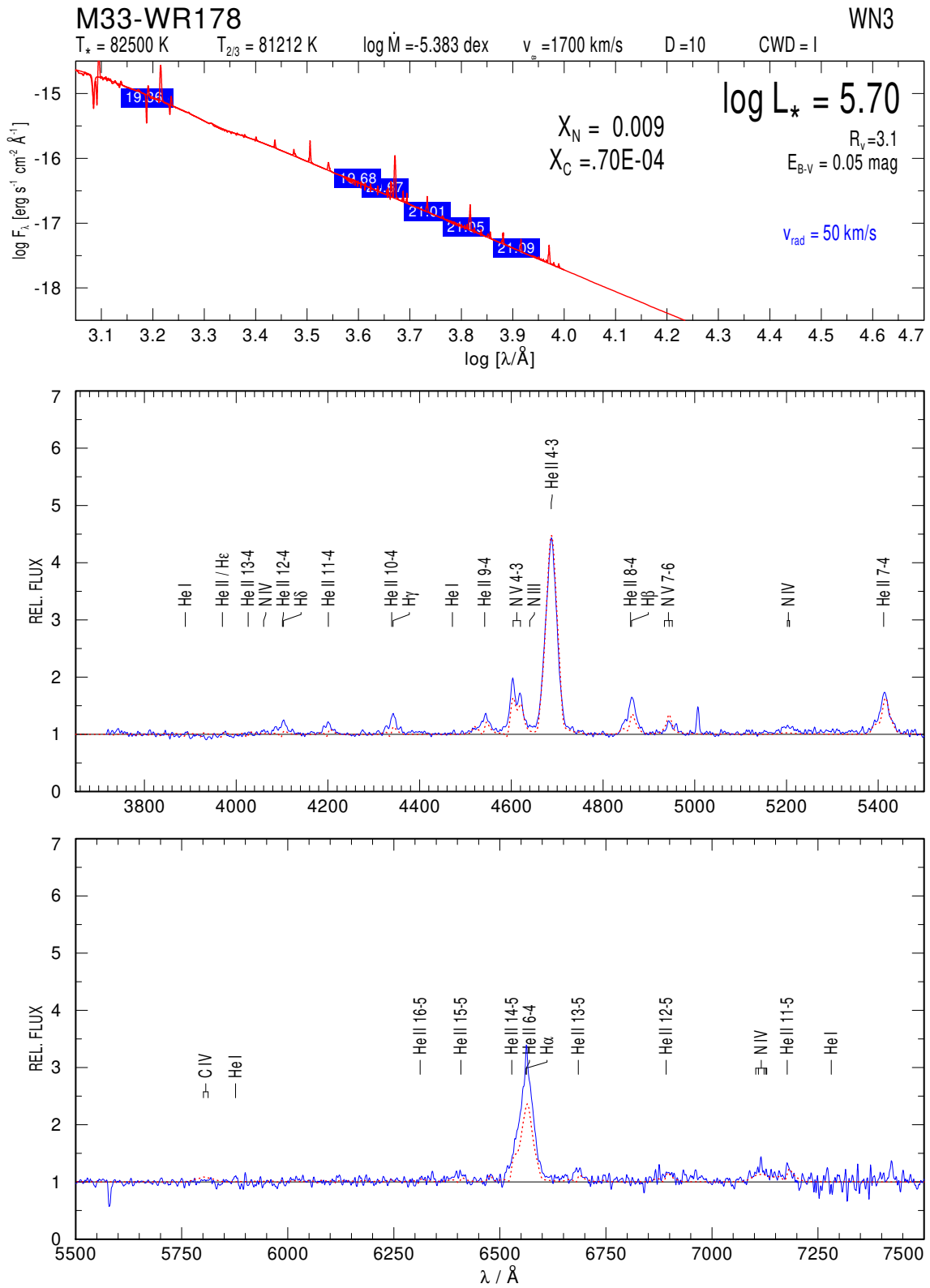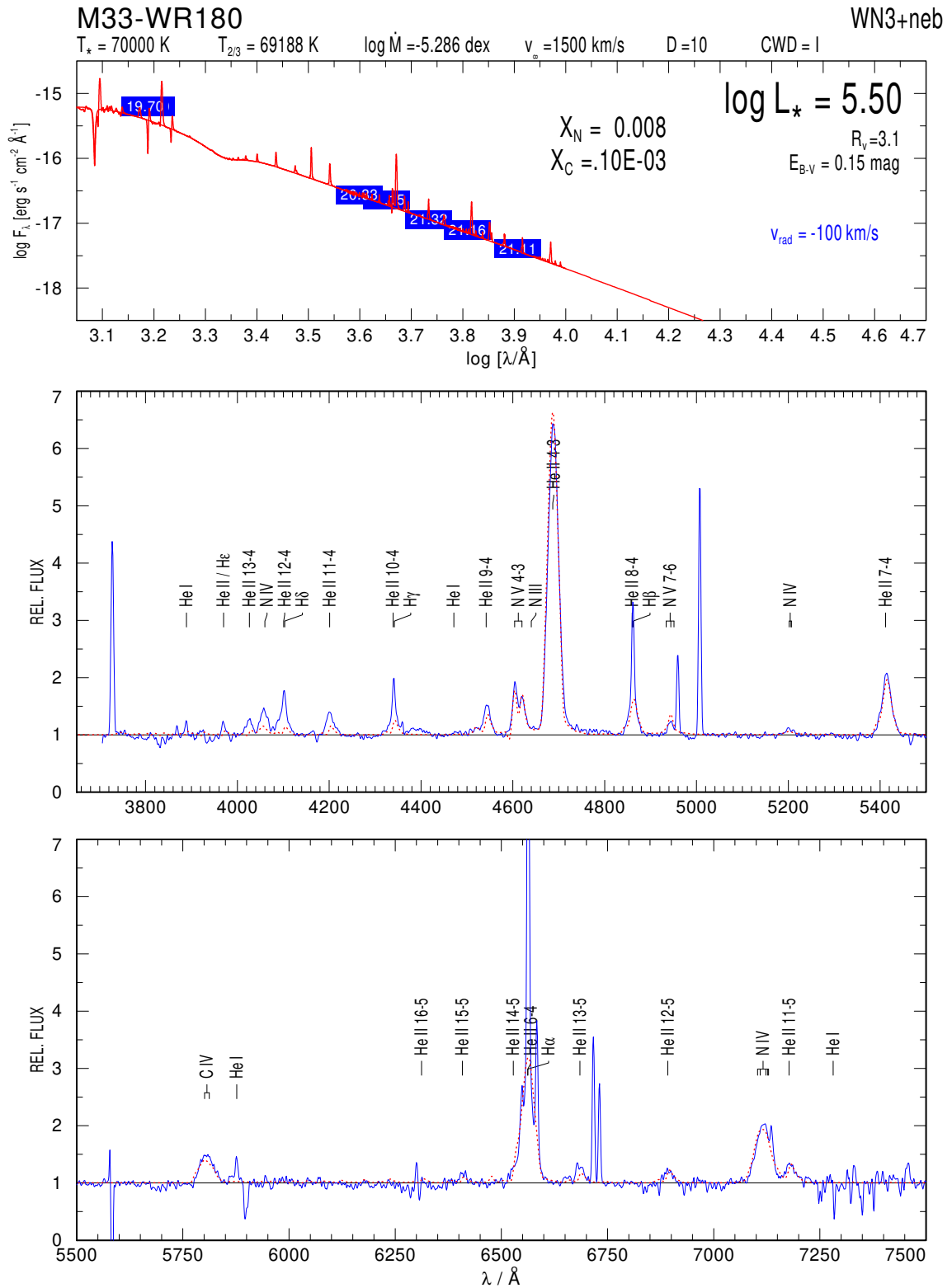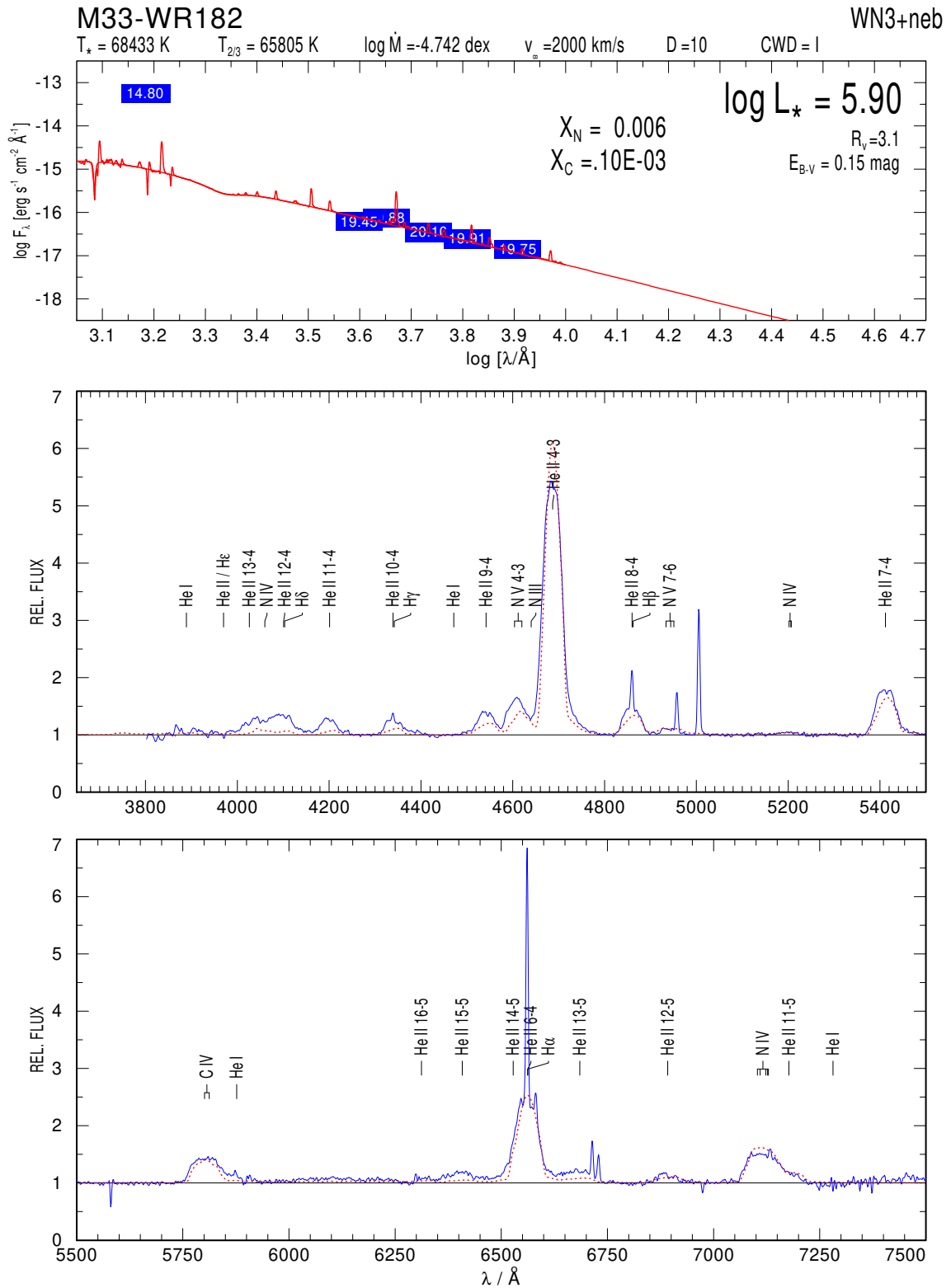
**Fig. 8.67** M33-WR180

**Fig. 8.68** M33-WR182
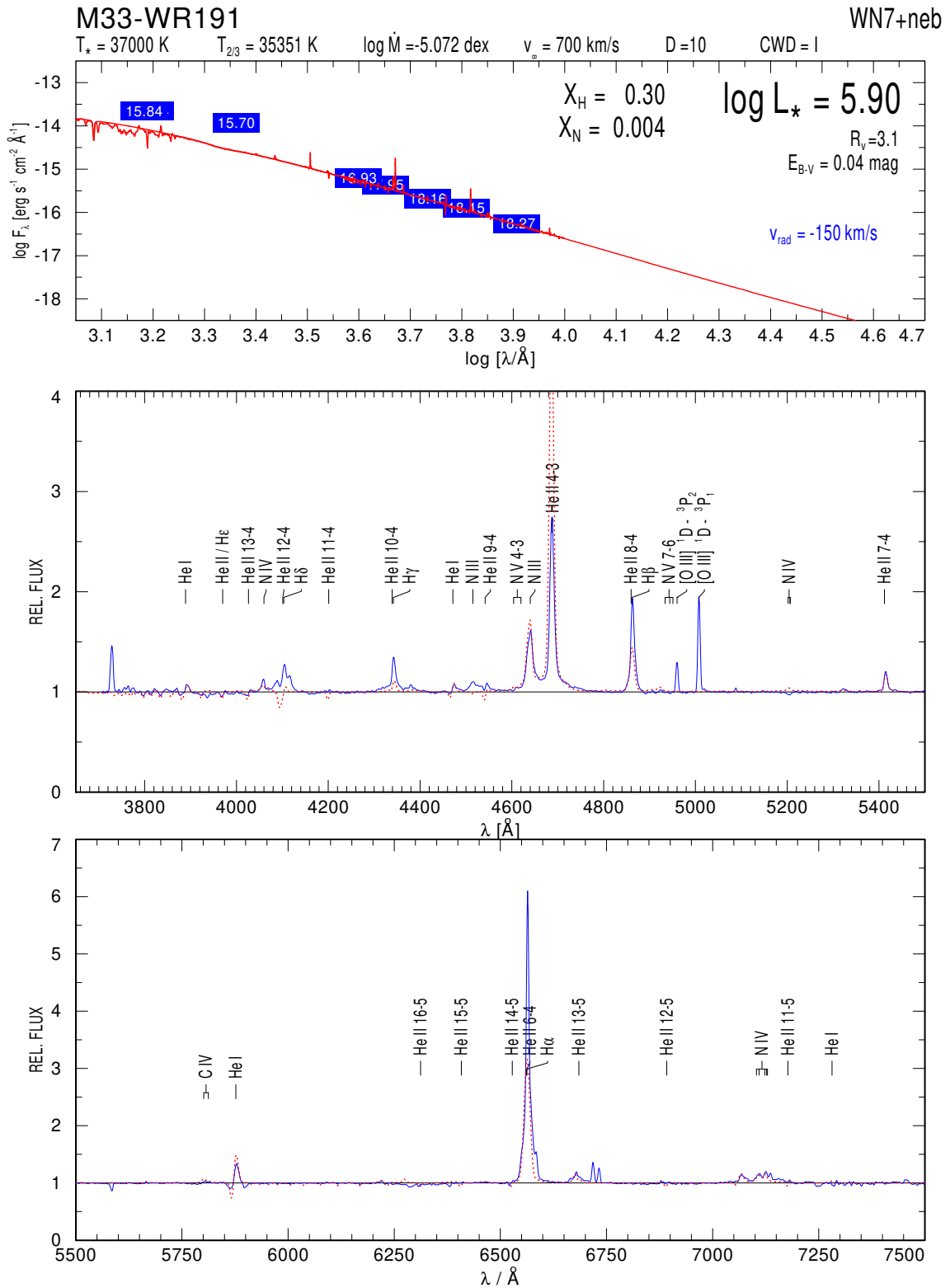
**Fig. 8.69** M33-WR191

**Fig. 8.70** M33-WR193

**Fig. 8.71** M33-WR195

144

**Fig. 8.72** Composite fit for M33-WR197

145
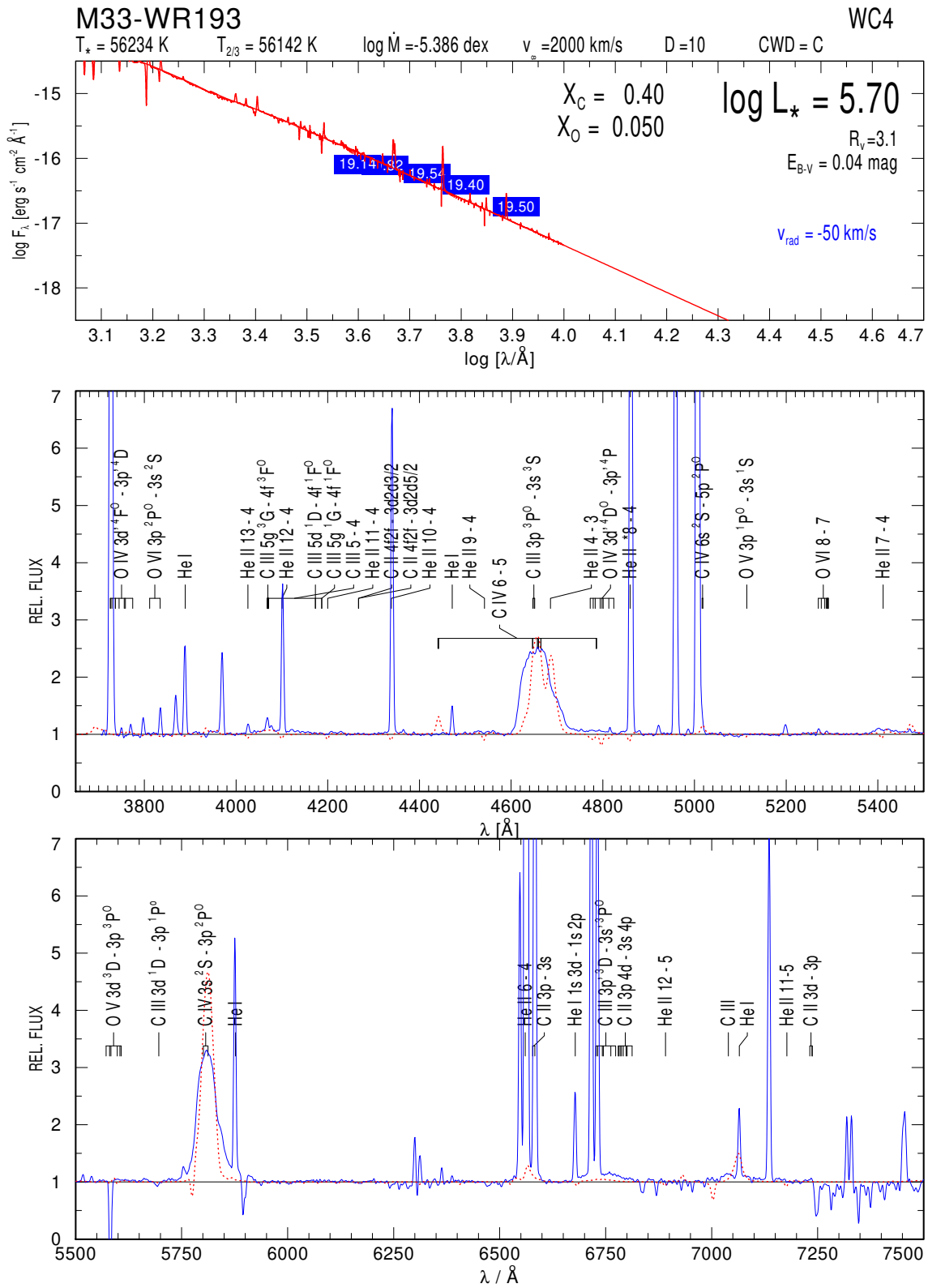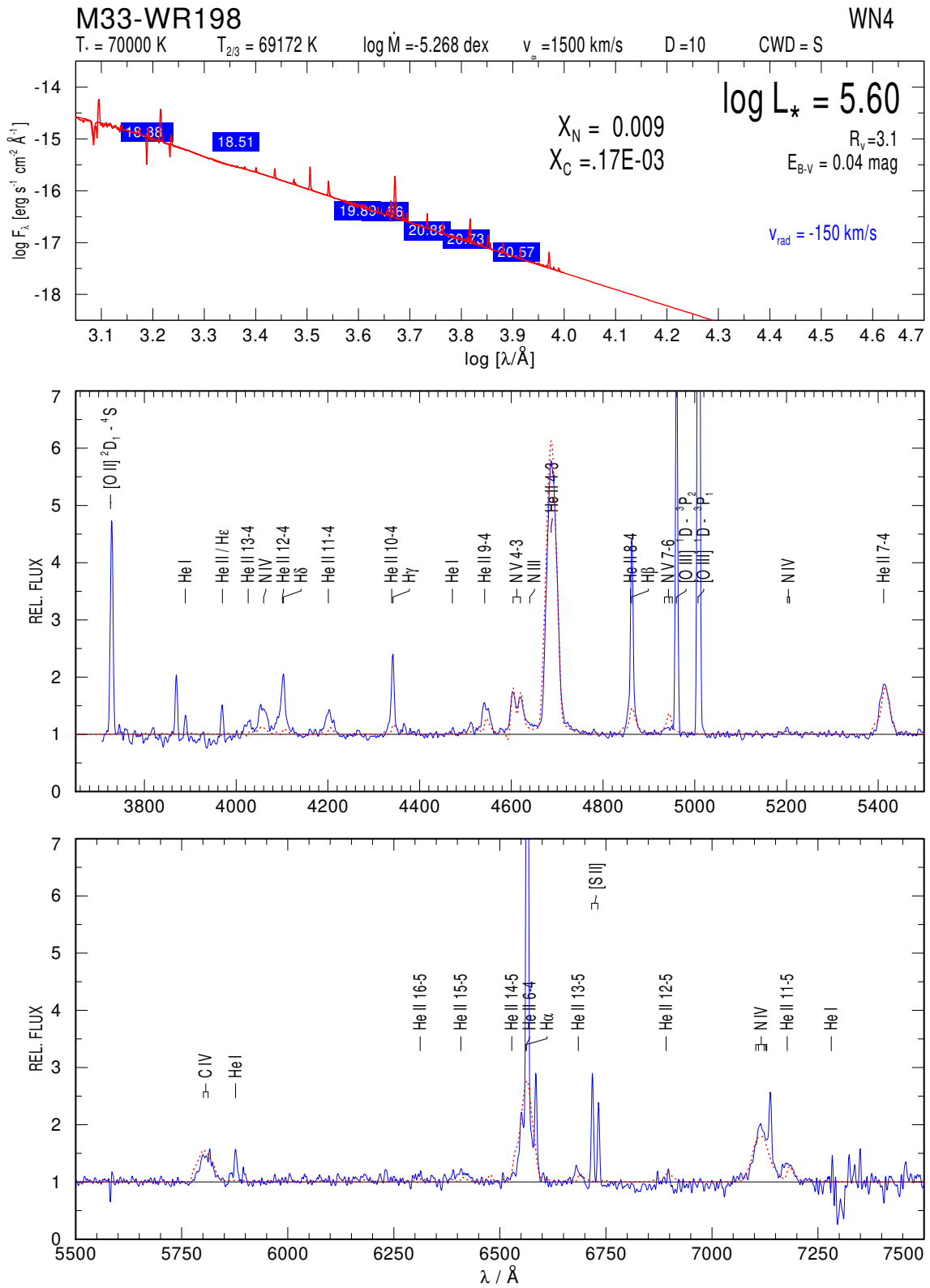
**Fig. 8.73** M33-WR198
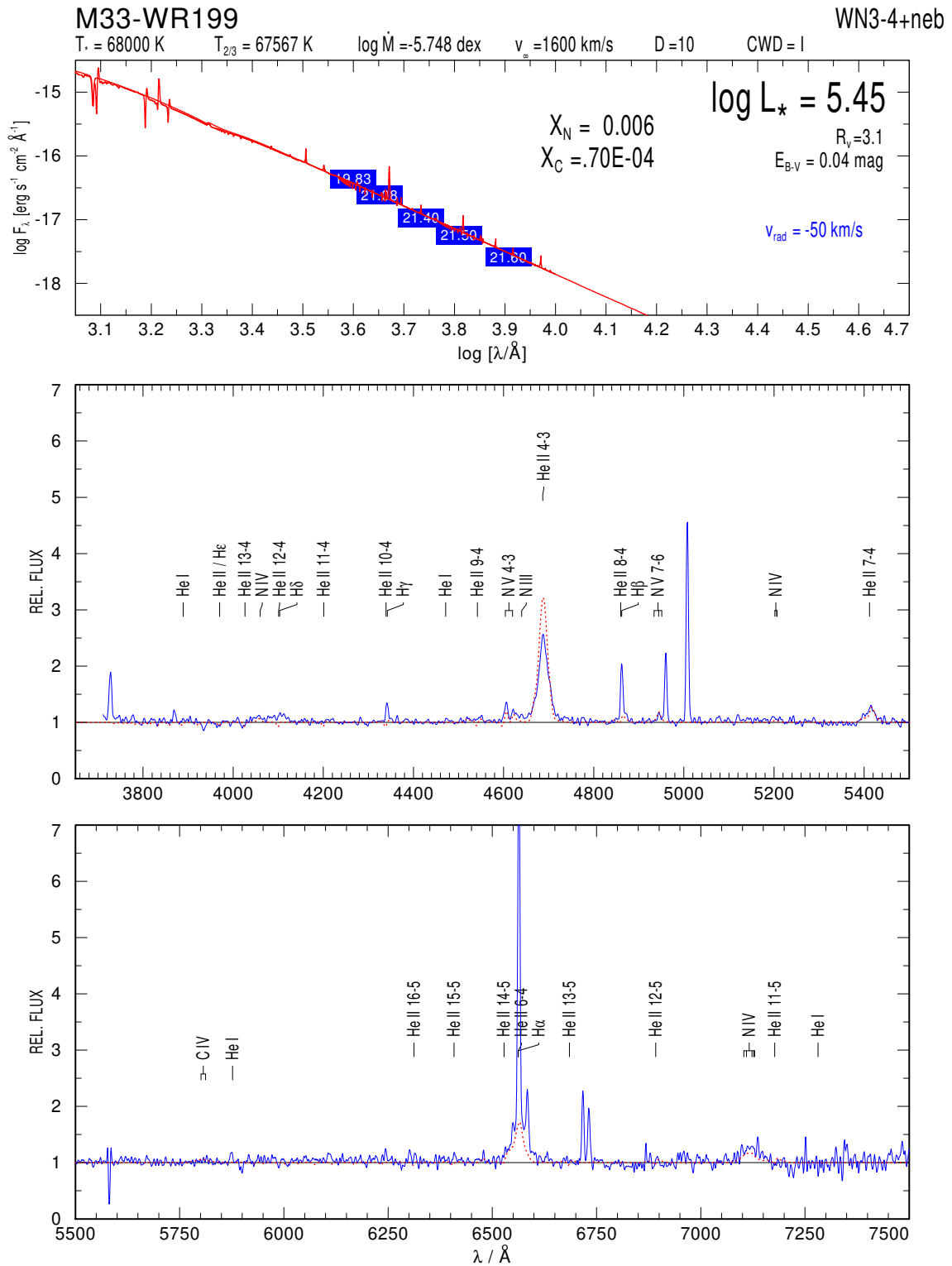
**Fig. 8.74** M33-WR199
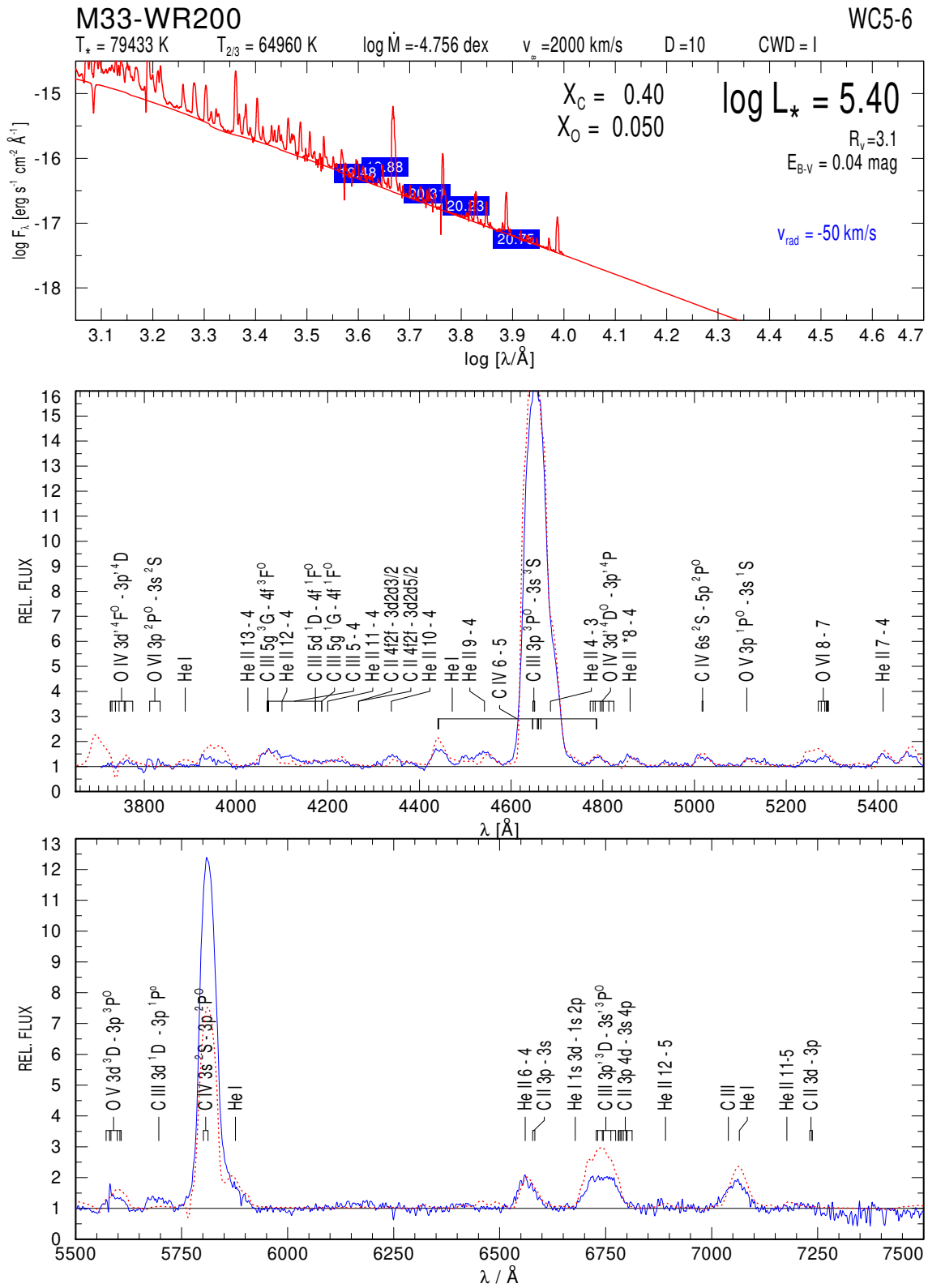
**Fig. 8.75** M33-WR200
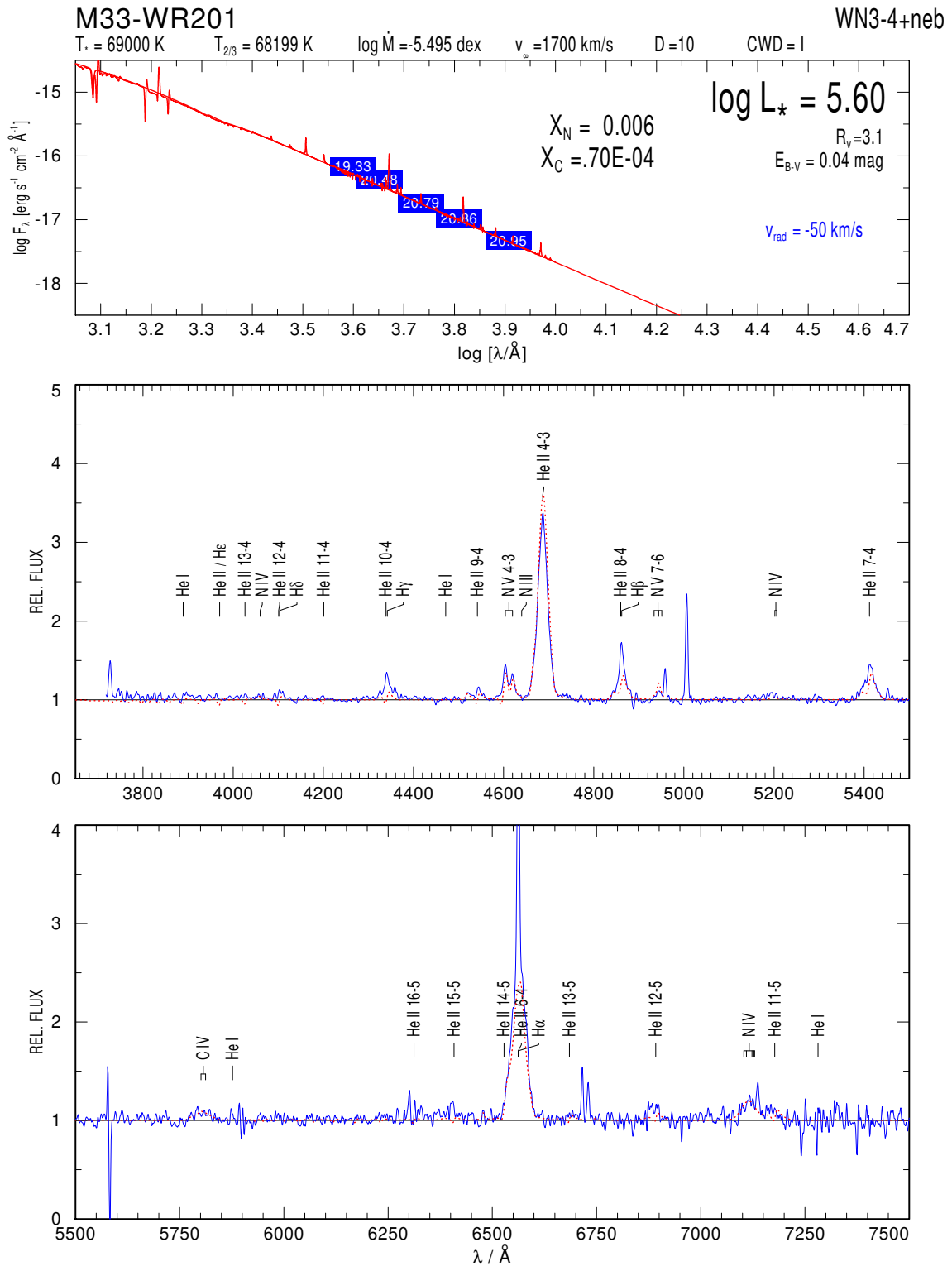
**Fig. 8.76** M33-WR201
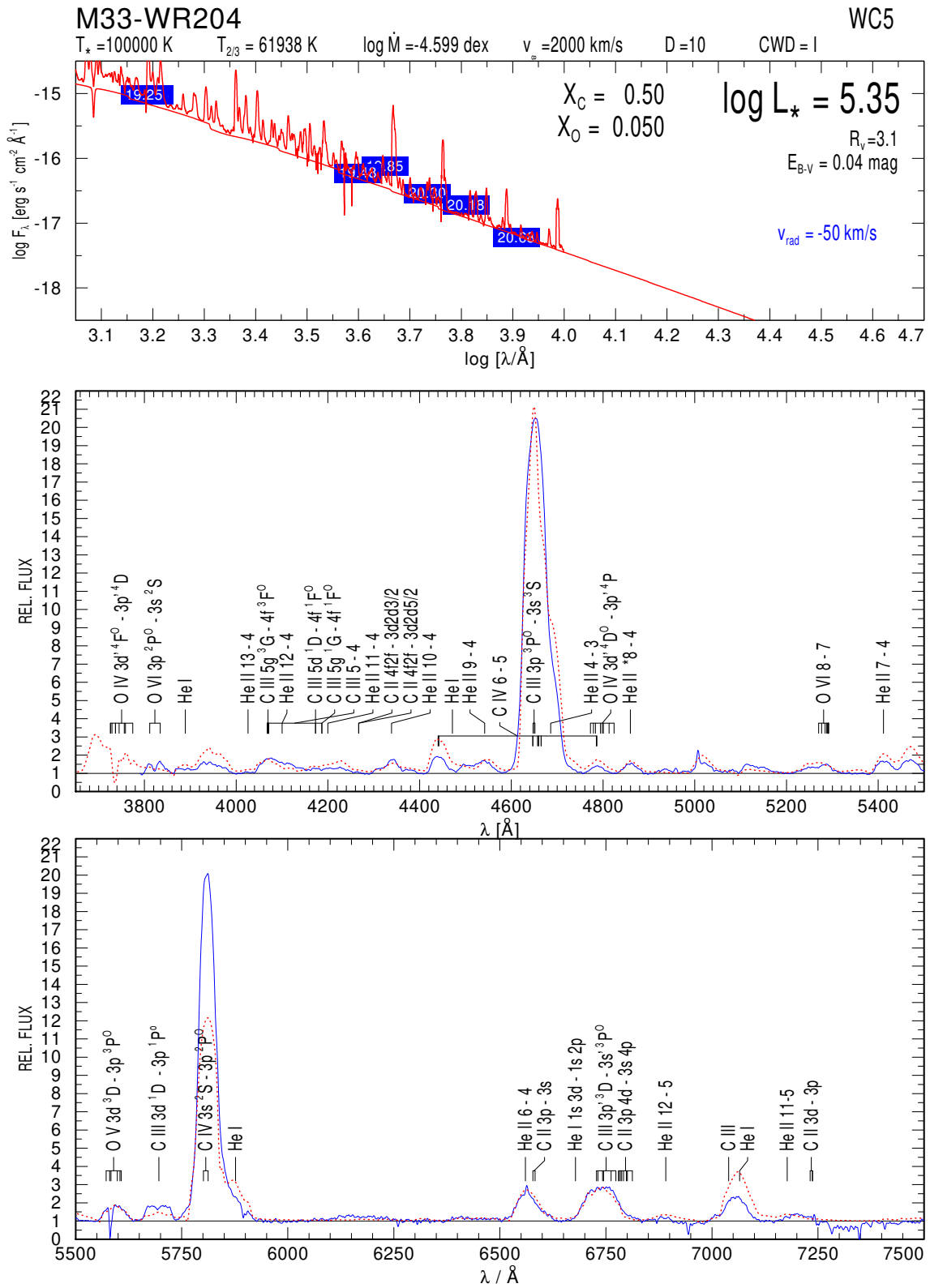
Fig. 8.77 M33-WR204
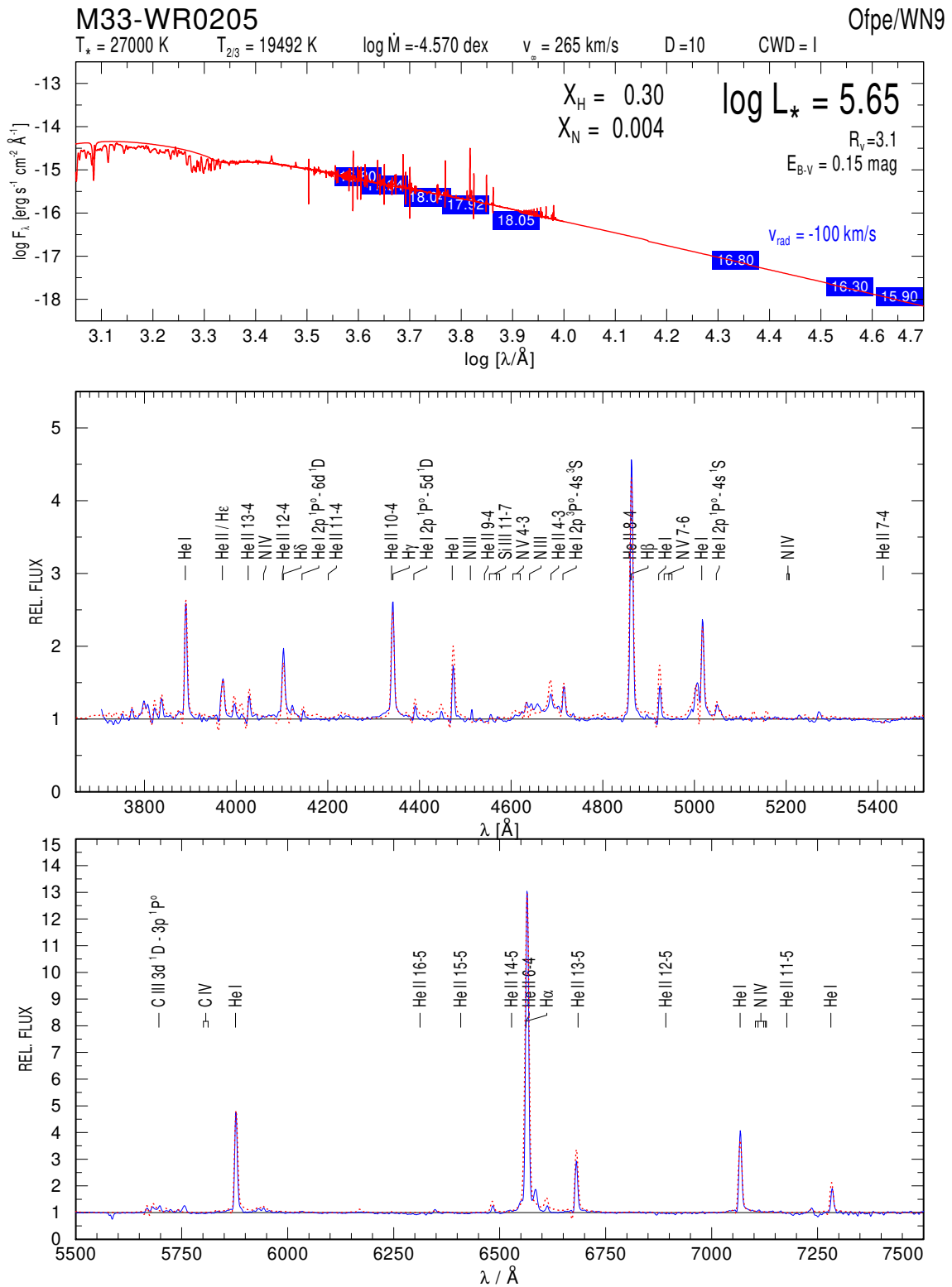
**Fig. 8.78** M33-WR205
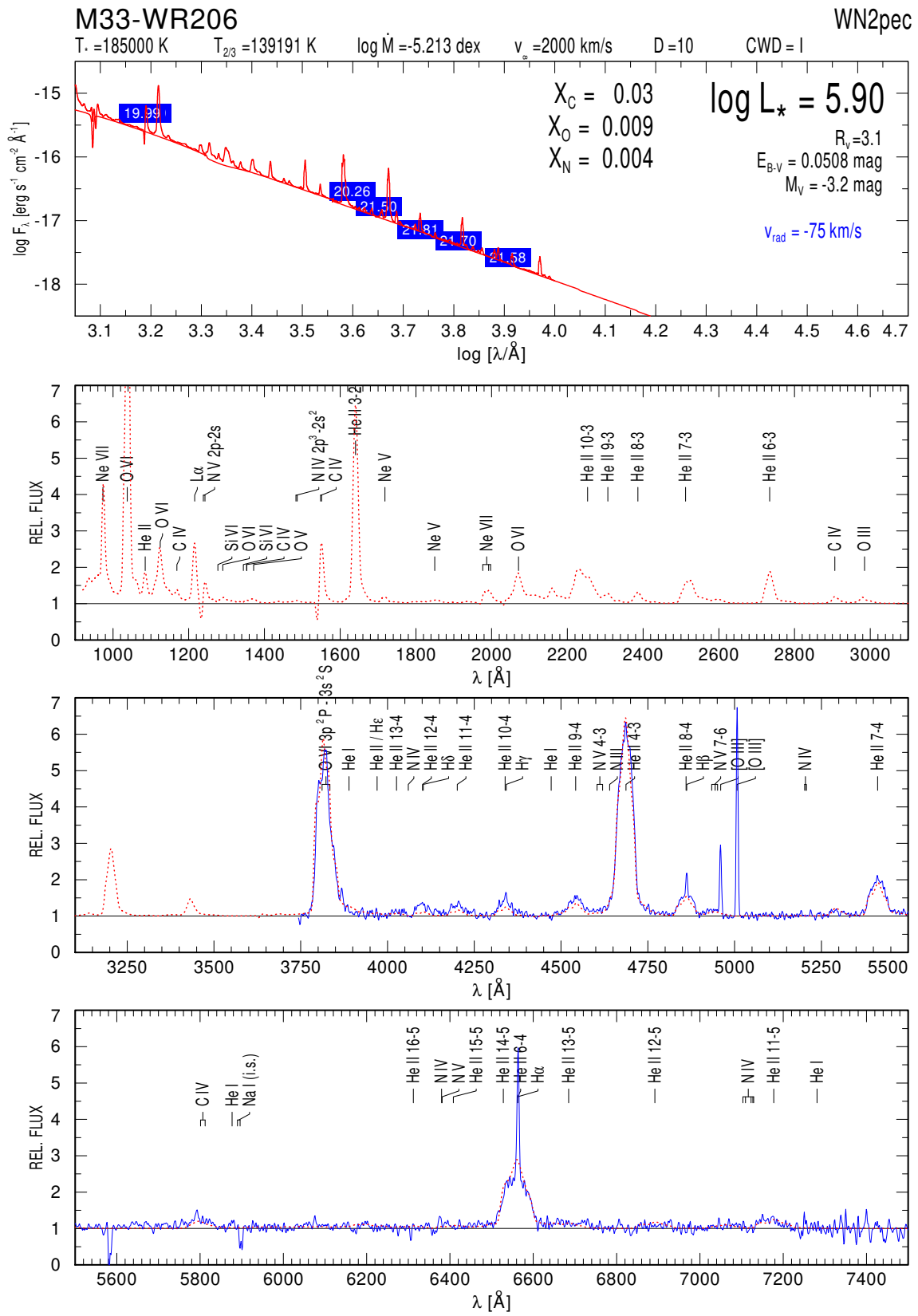
**Fig. 8.79** M33-WR206

## 8.3 List of all Wolf-Rayet stars in M33

**Table 8.1** List of all known Wolf-Rayet stars in M33

| Number | RAJ200 | DEJ2000 | Star | Classification | Number | RAJ200 | DEJ2000 | Star | Classification |
|---|---|---|---|---|---|---|---|---|---|
| 1 | 23.13362 | 30.58956 | J013232.07+303522.4 | WN2 | 107 | 23.44929 | 30.56058 | J013347.83+303338.1 | WN4 |
| 2 | 23.13387 | 30.58731 | J013232.13+303514.3 | WN3+neb | 108 | 23.44983 | 30.75183 | J013347.96+304506.6 | WN |
| 3 | 23.1385 | 30.44786 | J013233.24+302652.3 | WN2+abs | 109 | 23.45354 | 30.66378 | J013348.85+303949.6 | WN |
| 4 | 23.15675 | 30.66786 | J013237.62+304004.3 | WC | 110 | 23.45867 | 30.63858 | J013350.08+303818.9 | WN+O8-9 |
| 5 | 23.15717 | 30.66825 | J013237.72+304005.7 | Ofpe/WN9 | 111 | 23.45867 | 30.64894 | J013350.08+303856.2 | WC7+abs |
| 6 | 23.17008 | 30.41508 | J013240.82+302454.3 | WNE | 112 | 23.45929 | 30.56178 | J013350.23+303342.4 | WN8-9 |
| 7 | 23.17246 | 30.57117 | J013241.39+303416.2 | WN3h | 113 | 23.45942 | 30.69297 | J013350.26+304134.7 | WC5-6 |
| 8 | 23.17479 | 30.6735 | J013241.95+304024.6 | WCE | 114 | 23.46008 | 30.64283 | J013350.42+303834.2 | B1 |
| 9 | 23.18921 | 30.64953 | J013245.41+303858.3 | Ofpe/WN9 | 115 | 23.46129 | 30.94353 | J013350.71+305636.7 | WN3+neb |
| 10 | 23.19058 | 30.64844 | J013245.74+303854.4 | WN2+O7 | 116 | 23.46367 | 30.63661 | J013351.28+303811.8 | WC7+abs |
| 11 | 23.191 | 30.33875 | J013245.84+302019.5 | WC4+neb | 117 | 23.466 | 30.55789 | J013351.84+303328.4 | WC6 |
| 12 | 23.23296 | 30.53219 | J013255.91+303155.9 | WC4 | 118 | 23.46671 | 30.67319 | J013352.01+304023.5 | WC4+abs |
| 13 | 23.23479 | 30.59317 | J013256.35+303535.4 | WN6+abs | 119 | 23.46846 | 30.73103 | J013352.43+304351.7 | WN8 |
| 14 | 23.23683 | 30.45692 | J013256.84+302724.9 | WN | 120 | 23.46962 | 30.65203 | J013352.71+303907.3 | WNE |
| 15 | 23.23883 | 30.73836 | J013257.32+304418.1 | WN3+neb | 121 | 23.46962 | 30.75056 | J013352.71+304502.0 | WC4 |
| 16 | 23.24117 | 30.59717 | J013257.88+303549.8 | WC4 | 122 | 23.46979 | 30.74567 | J013352.75+304444.4 | WN |
| 17 | 23.25083 | 30.50425 | J013300.20+303015.3 | WN8 | 123 | 23.47012 | 30.72994 | J013352.83+304347.8 | WNE |
| 18 | 23.2595 | 30.18864 | J013302.28+301119.1 | WN3+neb | 124 | 23.47187 | 30.73711 | J013353.25+304413.6 | WC |
| 19 | 23.26112 | 30.52225 | J013302.67+303120.1 | WN3 | 125 | 23.47333 | 30.64767 | J013353.60+303851.6 | Ofpe/WN9 |
| 20 | 23.26225 | 30.18967 | J013302.94+301122.8 | WNE | 126 | 23.47417 | 30.59131 | J013353.80+303528.7 | WNE |
| 21 | 23.26329 | 30.19006 | J013303.19+301124.2 | WNE | 127 | 23.47667 | 30.58144 | J013354.40+303453.2 | WC6 |
| 22 | 23.26337 | 30.56906 | J013303.21+303408.6 | WN6 | 128 | 23.47854 | 30.53967 | J013354.85+303222.8 | WN9-10 |
| 23 | 23.26546 | 30.39064 | J013303.71+302326.3 | WC | 129 | 23.48054 | 30.33361 | J013355.33+302001.0 | WN3+neb |
| 24 | 23.27075 | 30.53328 | J013304.98+303159.8 | WNE | 130 | 23.48167 | 30.75969 | J013355.60+304534.9 | WN |
| 25 | 23.27362 | 30.48267 | J013305.67+302857.6 | WNE | 131 | 23.48212 | 30.75036 | J013355.71+304501.3 | WN7 |
| 26 | 23.28125 | 30.71625 | J013307.50+304258.5 | WN2 | 132 | 23.48279 | 30.75789 | J013355.87+304528.4 | WN7 |
| 27 | 23.282 | 30.55428 | J013307.68+303315.4 | WN4 | 133 | 23.48308 | 30.45892 | J013355.94+302732.1 | WN3+B2I |
| 28 | 23.2825 | 30.49753 | J013307.80+302951.1 | WNE | 134 | 23.48308 | 30.56878 | J013355.94+303407.6 | WC4-5 |
| 29 | 23.28567 | 30.46822 | J013308.56+302805.6 | WNE | 135 | 23.48429 | 30.54489 | J013356.23+303241.6 | WC |

**Table 6.1** continued.

| Number | RAJ200 | DEJ2000 | Star | Classification | Number | RAJ200 | DEJ2000 | Star | Classification |
|---|---|---|---|---|---|---|---|---|---|
| 30 | 23.28808 | 30.83181 | J013309.14+304954.5 | Ofpe/WN9 | 136 | 23.48471 | 30.57244 | J013356.33+303420.8 | WN3 |
| 31 | 23.29475 | 30.65006 | J013310.74+303900.2 | WN | 137 | 23.48492 | 30.58208 | J013356.38+303455.5 | WC5 |
| 32 | 23.29487 | 30.4595 | J013310.77+302734.2 | WN4 | 138 | 23.48833 | 30.58667 | J013357.20+303512.0 | WNL |
| 33 | 23.29637 | 30.65467 | J013311.13+303916.8 | WN3+abs | 139 | 23.49063 | 30.57119 | J013357.75+303416.3 | WN |
| 34 | 23.29704 | 30.52969 | J013311.29+303146.9 | WN4+B2I | 140 | 23.49379 | 30.57539 | J013358.51+303431.4 | WNL |
| 35 | 23.29767 | 30.81581 | J013311.44+304856.9 | WNE+B3 I | 141 | 23.49454 | 30.59069 | J013358.69+303526.5 | B1 Ia+WNE |
| 36 | 23.29937 | 30.64797 | J013311.85+303852.7 | WNL | 142 | 23.49746 | 30.56042 | J013359.39+303337.5 | WC6 |
| 37 | 23.30087 | 30.46125 | J013312.21+302740.5 | WN | 143 | 23.49833 | 30.5765 | J013359.60+303435.4 | WN5 |
| 38 | 23.30183 | 30.64667 | J013312.44+303848.0 | WN3+neb | 144 | 23.49912 | 30.86389 | J013359.79+305150.0 | WN2+O9I |
| 39 | 23.30225 | 30.65008 | J013312.54+303900.3 | WN/C+abs | 145 | 23.49921 | 30.56867 | J013359.81+303407.2 | WNL |
| 40 | 23.30254 | 30.75861 | J013312.61+304531.0 | WN4 | 146 | 23.50238 | 30.63592 | J013400.57+303809.3 | WN? |
| 41 | 23.30396 | 30.74983 | J013312.95+304459.4 | WN | 147 | 23.50375 | 30.65506 | J013400.90+303918.2 | WN5 |
| 42 | 23.30975 | 30.49869 | J013314.34+302955.3 | WN | 148 | 23.50542 | 30.66797 | J013401.30+304004.7 | WC6 |
| 43 | 23.31067 | 30.88878 | J013314.56+305319.6 | WN3+neb | 149 | 23.50721 | 30.60558 | J013401.73+303620.1 | WC4+abs |
| 44 | 23.31258 | 30.65192 | J013315.02+303906.9 | WC5-6 | 150 | 23.50958 | 30.6305 | J013402.30+303749.8 | WN3-4+abs |
| 45 | 23.31379 | 30.75097 | J013315.31+304503.5 | WN3 | 151 | 23.51221 | 30.85728 | J013402.93+305126.2 | WN3+neb |
| 46 | 23.31429 | 30.38336 | J013315.43+302300.1 | WN3 | 152 | 23.52833 | 30.79083 | J013406.80+304727.0 | WN7+neb |
| 47 | 23.31479 | 30.75392 | J013315.55+304514.1 | WN3+neb | 153 | 23.53271 | 30.69586 | J013407.85+304145.1 | WN |
| 48 | 23.31592 | 30.94578 | J013315.82+305644.8 | WN4.5+O | 154 | 23.53429 | 30.87617 | J013408.23+305234.2 | WN4 |
| 49 | 23.31737 | 30.79772 | J013316.17+304751.8 | WC4 | 155 | 23.53708 | 30.79222 | J013408.90+304732.0 | WN3 |
| 50 | 23.31867 | 30.53925 | J013316.48+303221.3 | WNL | 156 | 23.538 | 30.652 | J013409.12+303907.2 | WC |
| 51 | 23.32708 | 30.4495 | J013318.50+302658.2 | WC4-5 | 157 | 23.54467 | 30.87797 | J013410.72+305240.7 | WN3 |
| 52 | 23.35017 | 30.84186 | J013324.04+305030.7 | WN8 | 158 | 23.54642 | 30.77708 | J013411.14+304637.5 | WC4 |
| 53 | 23.36083 | 30.59731 | J013326.60+303550.3 | WN6 | 159 | 23.56408 | 30.57311 | J013415.38+303423.2 | WN |
| 54 | 23.36112 | 30.67786 | J013326.67+304040.3 | WC6 | 160 | 23.56462 | 30.5625 | J013415.51+303345.0 | WN(E) |
| 55 | 23.36358 | 30.65253 | J013327.26+303909.1 | Ofpe/WN9 | 161 | 23.56554 | 30.56686 | J013415.73+303400.7 | WNL |
| 56 | 23.36567 | 30.53081 | J013327.76+303150.9 | WN | 162 | 23.56604 | 30.92303 | J013415.85+305522.9 | WNL |
| 57 | 23.3765 | 30.52461 | J013330.36+303128.6 | WN4 | 163 | 23.56696 | 30.61169 | J013416.07+303642.1 | Ofpe/WN9 |
| 58 | 23.386 | 30.69089 | J013332.64+304127.2 | WNL/LBV | 164 | 23.56783 | 30.61289 | J013416.28+303646.4 | WC6+neb |

**Table 6.1** continued.

| Number | RAJ200 | DEJ2000 | Star | Classification | Number | RAJ200 | DEJ2000 | Star | Classification |
|---|---|---|---|---|---|---|---|---|---|
| 59 | 23.38675 | 30.69611 | J013332.82+304146.0 | WN7 | 165 | 23.56813 | 30.62008 | J013416.35+303712.3 | WN7 |
| 60 | 23.38737 | 30.69336 | J013332.97+304136.1 | WNL | 166 | 23.57154 | 30.54744 | J013417.17+303250.8 | WC4-5 |
| 61 | 23.38879 | 30.69158 | J013333.31+304129.7 | WC6 | 167 | 23.57171 | 30.55964 | J013417.21+303334.7 | WN3+neb |
| 62 | 23.38954 | 30.69261 | J013333.49+304133.4 | WNL? | 168 | 23.57654 | 30.64361 | J013418.37+303837.0 | Ofpe/WN9 |
| 63 | 23.39062 | 30.69278 | J013333.75+304134.0 | WNLx2?? | 169 | 23.57808 | 30.56994 | J013418.74+303411.8 | Ofpe/WN9 |
| 64 | 23.39087 | 30.69156 | J013333.81+304129.6 | WN7 | 170 | 23.57983 | 30.52436 | J013419.16+303127.7 | WN3 |
| 65 | 23.39183 | 30.68811 | J013334.04+304117.2 | WN | 171 | 23.58158 | 30.63375 | J013419.58+303801.5 | WN7 |
| 66 | 23.39275 | 30.69392 | J013334.26+304138.1 | WN7 | 172 | 23.582 | 30.56194 | J013419.68+303343.0 | WN3-4+ne |
| 67 | 23.39279 | 30.69353 | J013334.27+304136.7 | WNL+neb | 173 | 23.58837 | 30.63283 | J013421.21+303758.2 | WN5+neb |
| 68 | 23.39283 | 30.56319 | J013334.28+303347.5 | WN5 | 174 | 23.59154 | 30.55397 | J013421.97+303314.3 | WN4 |
| 69 | 23.39296 | 30.69178 | J013334.31+304130.4 | WN8 | 175 | 23.59321 | 30.55381 | J013422.37+303313.7 | WN3+abs |
| 70 | 23.39554 | 31.01189 | J013334.93+310042.8 | WN4 | 176 | 23.59392 | 30.55475 | J013422.54+303317.1 | WN |
| 71 | 23.39679 | 31.01044 | J013335.23+310037.6 | WN3 | 177 | 23.59592 | 30.78056 | J013423.02+304650.0 | WN4 |
| 72 | 23.39779 | 30.70558 | J013335.47+304220.1 | WC4 | 178 | 23.60462 | 30.33064 | J013425.11+301950.3 | WN3 |
| 73 | 23.39888 | 30.60808 | J013335.73+303629.1 | WC | 179 | 23.61233 | 30.88242 | J013426.96+305256.7 | WN4.5 |
| 74 | 23.40279 | 30.71739 | J013336.67+304302.6 | WN4+O | 180 | 23.61375 | 30.87478 | J013427.30+305229.2 | WN3+neb |
| 75 | 23.40558 | 30.59086 | J013337.34+303527.1 | WN4 | 181 | 23.62317 | 30.69583 | J013429.56+304145.0 | WC4 |
| 76 | 23.40754 | 30.47553 | J013337.81+302831.9 | WN4 | 182 | 23.63104 | 30.95464 | J013431.45+305716.7 | WN3+neb |
| 77 | 23.40917 | 30.52022 | J013338.20+303112.8 | WC6 | 183 | 23.63379 | 30.78494 | J013432.11+304705.8 | WN6 |
| 78 | 23.41375 | 30.59858 | J013339.30+303554.9 | WN4 | 184 | 23.63408 | 30.81769 | J013432.18+304903.7 | WC4 |
| 79 | 23.41467 | 30.76125 | J013339.52+304540.5 | B0.5Ia+WNE | 185 | 23.63433 | 30.78408 | J013432.24+304702.7 | Of/WNL |
| 80 | 23.41542 | 30.35033 | J013339.70+302101.2 | WNE | 186 | 23.63467 | 30.78325 | J013432.32+304659.7 | WCE |
| 81 | 23.41646 | 30.52736 | J013339.95+303138.5 | WN4b | 187 | 23.63542 | 30.78431 | J013432.50+304703.5 | WN10 |
| 82 | 23.41683 | 30.52258 | J013340.04+303121.3 | WNE+abs | 188 | 23.63583 | 30.78497 | J013432.60+304705.9 | WNL |
| 83 | 23.41696 | 30.71067 | J013340.07+304238.4 | WC5 | 189 | 23.6365 | 30.78811 | J013432.76+304717.2 | Ofpe/WN9 |
| 84 | 23.41746 | 30.52625 | J013340.19+303134.5 | WC4 | 190 | 23.63658 | 30.78431 | J013432.78+304703.5 | WC6 |
| 85 | 23.41754 | 30.59772 | J013340.21+303551.8 | WC4-5 | 191 | 23.63842 | 31.00536 | J013433.22+310019.3 | WN7+neb |
| 86 | 23.41762 | 30.68389 | J013340.23+304102.0 | WN | 192 | 23.64008 | 30.78461 | J013433.62+304704.6 | WN8+neb |
| 87 | 23.41783 | 30.6815 | J013340.28+304053.4 | WC | 193 | 23.64092 | 30.78231 | J013433.82+304656.3 | WC4 |

**Table 6.1** continued.

| Number | RAJ200 | DEJ2000 | Star | Classification | Number | RAJ200 | DEJ2000 | Star | Classification |
|---|---|---|---|---|---|---|---|---|---|
| 88 | 23.418 | 30.76692 | J013340.32+304600.9 | WN3+neb | 194 | 23.64196 | 30.78175 | J013434.07+304654.3 | WNE |
| 89 | 23.41954 | 30.71492 | J013340.69+304253.7 | WN | 195 | 23.65908 | 30.83144 | J013438.18+304953.2 | WN5 |
| 90 | 23.42354 | 30.64867 | J013341.65+303855.2 | WN | 196 | 23.66242 | 30.68883 | J013438.98+304119.8 | WC4 |
| 91 | 23.42429 | 30.69856 | J013341.83+304154.8 | WC6-7 | 197 | 23.66842 | 30.72275 | J013440.42+304321.9 | WN4+neb |
| 92 | 23.42462 | 30.70075 | J013341.91+304202.7 | WN | 198 | 23.68129 | 30.82206 | J013443.51+304919.4 | WN4 |
| 93 | 23.42721 | 30.55408 | J013342.53+303314.7 | WC4-5 | 199 | 23.6845 | 30.63256 | J013444.28+303757.2 | WN3 |
| 94 | 23.42996 | 30.65172 | J013343.19+303906.2 | WN | 200 | 23.68587 | 30.74594 | J013444.61+304445.4 | WC5-6 |
| 95 | 23.43004 | 30.65014 | J013343.21+303900.5 | WC5 | 201 | 23.69717 | 31.13022 | J013447.32+310748.8 | WN3 |
| 96 | 23.43054 | 30.74736 | J013343.33+304450.5 | WN4 | 202 | 23.74537 | 30.69139 | J013458.89+304129.0 | WC4 |
| 97 | 23.43058 | 30.59281 | J013343.34+303534.1 | WN4.5+O6-9 | 203 | 23.77237 | 30.68747 | J013505.37+304114.9 | WC4-5 |
| 98 | 23.435 | 30.64608 | J013344.40+303845.9 | WC4 | 204 | 23.78017 | 30.75025 | J013507.24+304500.9 | WC5 |
| 99 | 23.4385 | 30.64475 | J013345.24+303841.1 | WN7 | 205 | 23.79054 | 30.69925 | J013509.73+304157.3 | Ofpe/WN9 |
| 100 | 23.43992 | 30.58108 | J013345.58+303451.9 | WNL | 206 | 23.79279 | 30.75636 | J013510.27+304522.9 | WN2pec |
| 101 | 23.44163 | 30.60075 | J013345.99+303602.7 | WN4b | 207 | 23.26125 | 30.19208 | J013302.73+301131.6 | WN2.5 |
| 102 | 23.4425 | 30.57681 | J013346.20+303436.5 | WNE | 208 | 23.51683 | 30.78283 | J013404.07+304658.3 | WN6 |
| 103 | 23.44396 | 30.61681 | J013346.55+303700.5 | WC6 | 209 | 23.48492 | 30.58208 | J013411.45+303637.3 | WN4 |
| 104 | 23.445 | 30.55958 | J013346.80+303334.5 | WN6/C4 | 210 | 23.64263 | 30.77714 | J013434.26+304637.8 | WN6 |
| 105 | 23.44646 | 30.61744 | J013347.15+303702.8 | WC6 | 211 | 23.67658 | 30.83858 | J013442.41+305019.0 | WN4.5 |
| 106 | 23.44862 | 30.73092 | J013347.67+304351.3 | WN6 | | | | | |

157